Characterisation of locally pumped active waveguide components for optical integrated circuits

Karim, Abid

Award date:
1993

Awarding institution:
University of Bath

Characterisation Of Locally Pumped Active Waveguide Components For Optical integrated Circuits

Submitted by

Abid Karim

For the degree of Ph.D

of the University of Bath

1993

ProQuest LLC
789 East Eisenhower Parkway
P.O. Box 1346
Ann Arbor, MI 48106-1346

DEDICATED TO

MY

PARENTS

WITH LOVE AND RESPECT

SUMMARY

Optical integrated circuit (OIC) technology is breaking down barriers in a manner similar to the semiconductor integrated circuits. The increased packing densities of electronic components on a single substrate have increased the amount of information processing capacity at ever decreasing cost. But in the case of the OIC, the fabrication of several active components on a single substrate raises the difficult question of how the optical signals can be routed, as light generated in the one part of the active device could be absorbed in other parts. One solution to this problem is to locally inject carriers in the waveguides to provide an active integrated optic waveguide (AIOW). This would not only overcome the inherit losses found in passive waveguides, but it would also provide gain. With such technology, several components, such as optical amplifiers, detectors, switches, couplers as well as waveguide sections to join these components, can be now fabricated.

In this thesis, the characteristics of two particularly important components of an active OIC, the active waveguide optical detector (AWOD) and the active waveguide optical amplifier (AWOA) are investigated thoroughly. The structure is based on the GaAs rib waveguide laser structure. Throughout the research presented in this thesis, wherever necessary, a hybrid configuration is compared with the monolithic configuration in order to have a complete understanding of light propagation in locally pumped active waveguides. The flexibility being offered by the use of discrete components in the hybrid approach, is used to point out the underlying limitations, such as the generation and amplification of spontaneous emission, feedback between two coupled components and leakage of optical flux in the locally pumped active waveguide. Detuning caused by the feedback of optical radiation between two components and the injection of input optical radiation from the source laser into the AWOA is used to investigate frustrated instabilities, which appear as a train of self sustained pulsations and eventually leads to chaos. This unwanted phenomena of chaotic dynamics is exploited to investigate the route to chaos and two new routes to chaos in AWOA are demonstrated.

Despite some limitations in locally pumped AIOW which have discussed in the thesis, the results presented show the general feasibility of using AIOWs in OIC structures.

TABLE OF CONTENTS

Acknowledgements

I am grateful for the custom that limits acknowledgements only to those directly involved in the work. Otherwise, a complete acknowledgement would be an impossible task.

First, I would like to thank Dr. Richard F. Ormondroyd, my supervisor for his help during the experimental work and for his guidance and experience in the presentation of the thesis. Secondly I would like to thank the officials of the Ministry of Science and Technology, Government of Pakistan and the Education Division, High Commission for Pakistan in the U.K. for financial and moral support. Finally, I would like to thank the members of staff and colleagues at School of Electrical Engineering, University of Bath for their support through out the work.

List of main symbols and abbreviation

a_{TE},a_{TM}	asymmetric factor for TE and TM modes
A_{21}	Einstien coefficient of spontaneous emission
A_i	area of ith layer
b	normalised guide index
b_I,b_O	normalised guide indices for inside and outside regions
B	AWOD bandwidth
B	±3dB frequency or spectral bandwidth
B_{12}	Einstien coefficient of stimulated absorption
B_{21}	Einstien coefficient of stimulated emission
c	free space light velocity
C	total capacitance
C	coupling efficiency
C_{11},C_{12},C_{21},C_{22}	complex scattering 'matrix elements'
C_A	velocity of optical radiation in the amplifying medium
C_j	junction capacitance
C_p	laser submount parasitic capacitance
D_{min}	minimum spot size of light beam
e	electronic charge
$E_{1,2}$	Energy states
E_1,E_2,E_i,E_o,E'_1,E'_2	electric field components
E_g	Bandgap energy
f	frequency
$f_{1,2}$	Fermi distribution functions
f_{ext}	external cavity modes separation
F	noise figure
F_P,F_N	quasi-Fermi levels for the valence and the conduction bands under non-equilibrium conditions
g	local optical gain
g_m	material gain
g_o	unsaturated local gain
g_{th}	threshold gain

G	signal gain
G_s	single pass gain
$G(x)$	rate of hole-electron pair generation
h	Plank constant
$h\nu$	photon energy
I	pumping current
I'	average photodetector current
I_b	background current
I_d	dark current
I_L	current contribute to the laser emission above threshold
I_{ph}	photogenerated current
I_s	signal shot noise current
I_{sth}	stripe geometry laser threshold current
I_{th}	threshold current
$I(z)$	Light intensity in the z-direction
J	current density
J_{bth}	broad area laser threshold current density
J_{diff}	diffusion current density
J_{dr}	drift current density
J_e,J_h	leakage current densities due to electron and hole leakage currents
J_{nom}	nominal current density
$J_{(nom)o}$	transparency current density
J_o	leakage current density
J_{oth}	threshold leakage current density
J_{sth}	stripe geometry laser threshold current density
J_{th}	threshold current density
J_{tot}	total current density
k	Boltzmann constant
k_c	coupling coefficient
k_o	Free space vector
L	device length
L_g	etched gap length
L_s	bonding pad inductance
m	number of guided modes supported by a guide
m_l	number of longitudinal modes
m_t	number of effective transverse modes
n_1,n_2	Population of energy state E_1 or E_2

n_i	refractive index, where i=1,2,3,4,5
n_{sp}	population inversion factor
N	carrier density
N'	effective carrier density
N_D	impurity concentration in the active layer
N_e	injected carrier density
N_{eff}	effective refractive index
N_{fc}	free carrier concentration
N_I,N_O	effective indices of inside and outside region
N_o	transparency carrier density
N_{th}	injected carrier density at threshold
P	optical power output
P_{act}	rate of heat generation in the active region
P_{in}	total input power
P_N	total mean noise power
P_o	input optical power
$<P_o>$	mean input optical power
P_{sat}	saturated output power
r_{12},r_{21}	upward and downward transition rate
r_2,r_3	amplitude reflection coefficient
R	total resistance
$\mathcal{R}$	responsitivity of the photodetector
R_1,R_2	facet reflectances of input and output facet of a device
R_B	bias resistance
R_i	incremental resistance
R_L	load resistance
R_s	series resistance
R_{th}	thermal resistance
R_x	composite sheet resistance
s	the effective thickness of optical distribution
S	photon density
t	time
t_g	complex round-trip transmission coefficient
T	temperature
T_m	steady-state temperature
T_o	characteristic temperature parameter
T_r	reference temperature

v_g	group velocity
v_p	phase velocity of guided modes
v_s	saturation drift velocity.
V	V-number or the normalised active layer thickness
V_D	diffusion potential of the junction
V_I, V_O	V-number for inside and outside regions
V_L	voltage contributes to the laser emission
V_o	optical mode volume
V_{th}	voltage at laser threshold
V_w	normalised width
W	device width
W_{max}	maximum width
x	aluminium content
α	total internal radiation losses
α_a	Absorption coefficient
α_c	coupling loss
α_{end}	end mirror loss
α_{fc}	free carrier absorption
α_{ib}	interband absorption
α_s	scattering loss
β_g	complex propagation constant
β_s	spontaneous emission or saturation parameter
β_v	exponential junction parameter
β_z	propagation constant
Δ	normalised detuning parameter
ΔN_{eff}	effective refractive indices difference
ΔT_j	temperature of the active layer
ΔV	voltage drop other than the junction voltage drop
$\Delta\nu_1$	equivalent noise bandwidth of the spontaneous emission shot noise components
$\Delta\nu_2$	equivalent noise bandwidth of the spontaneous emission beat noise components

ε_o	free space permitivity
ε_r	dielectric constant of the active layer
Γ	radiation confinement factor
η	differential quantum efficiency of the photodetector
η_D	external or differential quantum efficiency
η_{in}	internal quantum efficiency
η_T	total quantum efficiency or Henry factor
θ_c	critical angle
θ_d	incident angle
λ	wavelength of optical radiation
ν	frequency of optical radiation
ν_o	resonant mode frequency
ξ	fraction of electron-pair contribute to the photocurrent
ρ_i	electrical resistivity of *i*th layer
$\rho(\nu_{21})$	Photon density at frequency ν
ρ_w	winding number
σ_i	thermal conductivity of *i*th layer
σ_{out}	variance of the photon number
τ	thermal rise time
$\tau_{21,s}$	spontaneous lifetime
τ_d	transient time of the AWOD
τ_p	photon lifetime
υ	peak-trough
χ	excess noise factor
ω	angular velocity
ω_i	frequency of the external signal
ω_o	dressed intrinsic frequency of the system

AIOW	active integrated-optic waveguide
A.R	antireflection
AWOA	active waveguide optical amplifier

AWOD	active waveguide optical detector
CW	continuous wave
EIM	effective index method
FEM	finite element method
FPA	Fabry-Perot amplifier
LAD	large area detector
NTWA	near travelling wave amplifier
OIC	optical integrated circuit
SIM	spectral index method
SSP	self-sustained pulsation
SVM	scalar variational method
TTV	transient temperature variation
TWA	travelling wave amplifier
WIM	weighted index method

Chapter-1

Introduction

> "Before exploring the boundaries of this intriguing new discipline, we have to remind ourselves that the field of integrated optics is still in its infancy, still in its research stage, and is still searching for its proper role. At this early stage, when many discoveries are yet to be made, it may appear somewhat futile to attempt to forecast the limitation of this infant technology, and it is certainly premature to try detail comparison with established technologies such as silicon integrated circuits. Yet, there are some crude patterns emerging that indicate limits in the size, speed, and power consumption of integrated devices and circuits. It may be worthwhile to trace some of these patterns in order to derive pointers for potential future progress in this field."
>
> *(Kogelnik, reference-1)*

1.1- Optical integrated circuits

The wide-spread application of microprocessor-based technology in modern day society is evidence of the success of semiconductor based technology. After transistors and micro-electronic devices, which process information in the form of electronic signals, the next technological era is likely to be in the area of laser and integrated optical circuits (OIC) which use light-wave signals to process the information. This represents a device technology with potential to meet a broad range of future telecommunication and computing systems needs.

The importance of the optical means of data transmission and processing has increased due to its advantages such as high data transmission speed, the freedom from electromagnetic noise, interchannel cross-talk, electrical isolation and due to its improved reliability, small size, light weight and potential low cost.

An optical integrated circuit is an optical circuit designed to implement certain functions by integrating active and passive optical, electro-optical or acousto-optical devices on a suitable substrate. A few of the optical devices that may be integrated on a single substrate include light generation devices, photodetectors, optical-waveguides, modulators, spatial and temporal switches, amplifiers and beam formers.

There are two approaches to the fabrication of an integrated optical circuit. The first approach is to use hybrid integration. This combines the best passive and active components from different materials. For example, the source may be fabricated from III-V semiconductors, whilst the waveguide may be made of GaAs (for operation at 1.3μm and 1.55μm) or $LiNbO_3$ and the detector made up of Si or Ge, as shown in figure 1.1. Such an approach improves the individual device performance and provides the flexibility of using different materials. But, it also places severe limitations on the alignment of the different optical components. The second approach is to use monolithic integration. This requires that all the component are fabricated on a single substrate, essentially from the same material. For example, figure 1.2 shows a proposed future integrated optical circuit made from GaAs. This approach is considered to be more accurate and more attractive because it simplifies the device fabrication considerably.

Although monolithic integration is an ideal approach for the integration of several optical components on a single substrate, the integration of many components on a single substrate raises the question of routing the signals, because light generated in one part of the device will be strongly absorbed in other parts of the device where there is no pumping unless sophisticated wafers are fabricated with localised compositional changes to overcome the inherent absorption of the photons. This problem can be solved by injecting local carriers, as shown in figure 1.3, to provide active integrated-optic waveguide (AIOW) [4]. This would not only

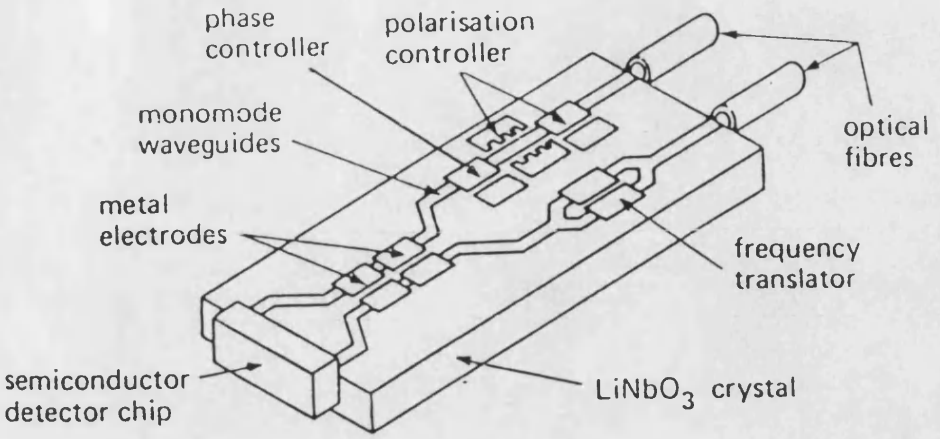

Figure 1.1. Hybrid optical integrated circuit [3].

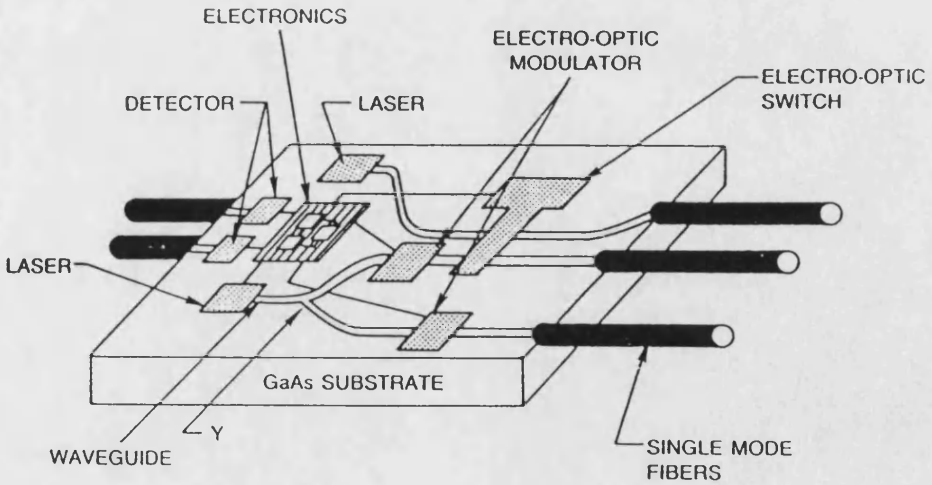

Figure 1.2. GaAs based future monolithic integrated optical circuit [2].

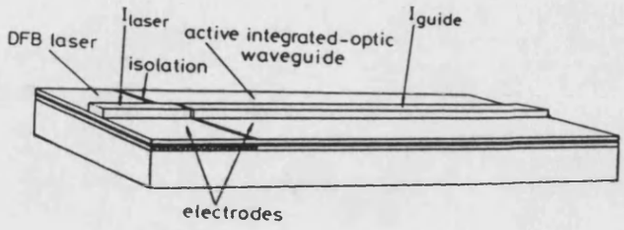

Figure 1.3. The schematical representation of locally pumped AIOW integrated with a DFB laser [4].

overcome the inherent losses (which occur when radiation at wavelengths equal or shorter than the absorption edge of the material is used) but it could be used to provide the local gain as well.

1.2- Materials for optical integrated circuits

The main requirements of the material for an OIC are; transparency and good optical properties in the appropriate part of electromagnetic spectrum (such as generation and detection of light in that part of electromagnetic spectrum), feasibility of fabrication of low loss thin film waveguides and compatibility with electronic components. Most of the research in OIC technology has been centred on lithium niobate and III-V semiconductors. Lithium niobate has relatively low absorption losses typically of the order of 1dB/cm but it is impossible to have light emitting action in this material and photodetectors in this material are not possible either. Consequently, it can only be used as a passive waveguide component in hybrid integration. On the other hand, III-V semiconductors and their alloys are thought to be the best materials to achieve true monolithic integration. The fabrication of discrete lasers [5-7], detectors [8], switches and modulators [9] and optical amplifiers [10,11] were achieved quite a long time ago. Also, several attempts have been made to use this material as waveguide material (e.g. references-12 and 13). The transparence condition in III-V semiconductors (at or shorter than their emission wavelengths) can only be satisfied by local pumping to create AIOW, however. Consequently, although GaAs has low loss at wavelengths longer than 860-890nm, where it is essentially a passive component, near to its lasing wavelength it has a very high loss.

The early research in integrated optics using III-V semiconductors has focused on GaAs and its alloys, which emit the light around 0.85μm. Recently devices made from InP based materials have become of increasing significance due to their potential application in longer wavelength optical fibre communication systems, because optical fibre exhibits lower loss around 1.3μm and 1.55μm (emission

wavelength of InP based materials) and also lower chromatic dispersion. However, the work reported in this thesis is based on GaAs active waveguide due to availability of this material.

1.3- Historical background

The use of light as a means of communication goes back centuries with methods such as signal fires, reflecting mirrors, beacon tower etc being used. The history of modern optical communication systems started when Graham Bell performed his famous experiment using the photophone in 1880. The present interest in integrated optical circuits has its roots in the invention of Maiman's ruby laser [14] in 1960. With this invention the future of optical communication started to look bright. In 1961 laser action in semiconductors was proposed by Basov *et al* [15] and in the same year, Bernard and Durafforg [16] presented a quantitative description of laser action in semiconductors. 1962 was the year when different groups [5-7] reported experimental observation of laser action in GaAs p-n junctions. Since then, p-n junction lasers have been the subject of extensive research because of their potential applications in optical communication. The invention of the GaAs/AlGaAs heterojunction laser [17] brought a turning point in that area of research by allowing continuous room temperature operation of semiconductor lasers. In parallel with this, optical fibres as signal carrying media received a lot of attention from many groups (for details see reference-18) and which had a breakthrough when fibre with an attenuation of 20dB/km was produced in the 0.85μm wavelength region, appropriate for GaAs lasers [19]. Since then, research in optical communications has received considerable attention. In return, the threshold current of laser sources has been reduced to as low as 3mA [20] and optical fibre losses lower than 0.2dB/km have been achieved at longer wavelengths [21].

During this period of early research only optical fibre was considered as a suitable optical waveguide medium and monolithic optical waveguide structures were largely ignored due to the limitation of fabrication technology at that time. In

1969, Miller [22] used the term "integrated optics" to describe such waveguide components and suggested that the comparatively slow electronic circuits should be replaced with these faster optical integrated circuits and to make optical system compatible with modern thin film technology. The idea was to build various optical devices on a common substrate and then to interconnect them by thin film waveguides. This idea was quickly followed by a paper by Marcatili [23] in which he discussed the mode patterns in integrated optical waveguides. Goell [24] then successfully fabricated a passive rib waveguide structure in glass using r.f. sputtering which proved the validity of miniature guiding structure which could be used to connect different optical components.

In the early days of research, hybrid type integration was widely accepted as the future substitute of electronic IC's. Stoll et al [25] fabricated an integrated epitaxial waveguide and an optical detector and brought the concept of monolithic integration. This was quickly followed by the fabrication of a passive waveguide with an integrated laser source [26]. First attempts to fabricate two active components on a single substrate was reported by Merz et al [8] when they fabricated an integrated laser source with a waveguide detector coupled via the passive waveguide.

Although the term "monolithic integration" was quickly accepted by other groups, this area of research was still largely ignored when compared with optical fibre research and laser diode research. The main breakthrough came when different groups [10,11,27,28] demonstrated the amplification of optical signals within a Fabry-Perot laser cavity and achieved unsaturated gain as high as 25dB. This result gave new life to research in this field and the optical integrated circuit began to be considered as a substitute for the electronic integrated circuit. During the early stages of research on optical amplifiers, it was realized that the facet reflectance was an obstacle to continued improvement of the broadband signal gain of the optical amplifier because it reduces the optical bandwidth of the amplifier and the effect of gain saturation is higher. The saturation optical output power, signal gain

and optical bandwidth of the optical amplifier were improved quite significantly by reducing the facet reflectivities. Several techniques have been proposed to reduce the facet reflectivity [29-34]. Of all these techniques, anti-reflection (A.R) coating is considered as being the most practical in terms of compatibility with all types of devices and structures. By combining different fabrication and facet reflectance reducing techniques, an internal gain of the optical amplifier as high as 40dB has been achieved to date [34].

Several different structures for active integration have been proposed in order to reduce the threshold current of the integrated optical source and to limit excess heating in optical IC's (for example references 8, 24, and 35-39). Among these ideas, the use of the buried heterostructure [36-37] provides the lowest current requirement for integrated sources and amplifiers, but the ridge waveguide structure [24] is probably more promising as a research structure for device development because it is easier to fabricate. This type of structure only needs one epitaxial growth step layer, and dry etching or ion milling technique can be used to fabricate different optical components. Moreover its open waveguiding structure provide easy coupling to the external signals.

As mentioned earlier, when several components are fabricated on a single substrate, the absorption of optical signals in the waveguide sections is a critical point. To avoid this problem several techniques have been suggested. These include impurity induced disordering [40], monolithic laser-waveguide butt coupling [41], monolithic integrated orthogonal facet laser and optical waveguide [42], laser and optical waveguide coupled via evanescent field [43] and multisegment pumped tandem stripe laser [44] as shown in figure 1.4. All these techniques are fairly difficult and complicated, the last one less so, where the individual segment can be pumped locally and independently to provide active integrated-optic waveguide [4]. This is the method adopted throughout this thesis.

Kucharska [45] has recently reported the experimental results of optical non-linearities in monolithic integrated devices, but there has long been interest in

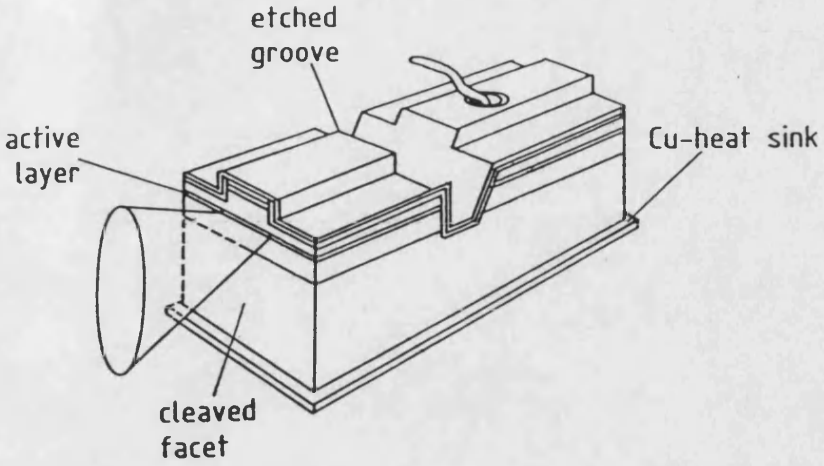

Figure 1.4. The sketch of multisegment ridge waveguide structure [44].

using the non-linearty of semiconductor materials for optical logic and switching, which goes back to early 1960's when Lasher [46] proposed an inhomogeneously pumped multisegment laser diode as an optical logic component. This device was later analysed by Perkins, Ormondroyd and Rozzi [47,48] and Perkins and Ormondroyd [49]. Since then, optical non-linearities have been observed in GaAs and other material systems [50-52] using a passive saturable absorber and this is termed as an absorptive non-linearity. Also the non-linearities in the refractive properties of the active medium which effects the frequency characteristic of the optical cavity (and hence the feedback mechanism) give rise to dispersive effects in the amplifier including bistable operation. These two types of active non-linearity have also been reported in external cavity lasers in the form of self-sustained pulsations (which leads to chaos) [53], optical bistability [54] or both phenomena [55]. On the one hand, the self-sustained pulsations (SSP) can be used to generate narrow picosecond pulses [56] and to perform logical and switching operation [57]. On the other hand, non-linearities in amplifiers introduce additional cross-talk and noise.

1.4- Purpose of the thesis

The main purpose of this study is to investigate the performance of monolithic active integrated circuit components (such as the active waveguide optical detector (AWOD) and the active waveguide optical amplifier (AWOA)), to incoming butt-coupled optical radiation. This has been done by;

1. Developing a reliable alignment technique to align different optical components used in optical integration.
2. Originating the optical leakage, which appears as an additional source of optical signals loss and noise in OIC.
3. Measuring the characteristics of monolithic integrated components and hybrid integrated components by using them as an active waveguide optical detector (AWOD) and an active waveguide optical amplifier (AWOA).

4. Examining the underlying non-linear mechanism in the active waveguide by measuring the input/output characteristics of the AWOA.

5. Investigating the dynamic response of active integrated optical waveguide components caused by the finite facet reflectance and the injection of external input radiation.

6. Using the existing theoretical background and technical facilities to achieve a comprehensive understanding of the internal working mechanism of active OIC's.

1.5- Scope of the thesis

The use of guided-wave optics for both optical communication systems and signal processing is now becoming very attractive and monolithic integration is expected to form the fabrication backbone of these complex integrated optical circuits. In practice, the integration of several components on a single substrate raises the very important question of routing the optical signals. A convenient and practical solution to this problem for experimental characterisation of integrated optical components is the use of multi-segment ridge waveguide structure where all the active components share the same active layer and are butt-coupled to each other via an etched gap and they are locally pumped to provide AIWO, as shown in figure 1.4. The active device shown in figure 1.4 can be used as the active waveguide optical detector (AWOD) or the active waveguide optical amplifier (AWOA), depending on particular application, just by changing the biasing condition (reverse bias or zero bias for AWOD and forward bias for AWOA).

Due to the simplicity and the ease of control of each component, the locally pumped multisegment approach is adopted in this thesis to investigate the light propagation characteristics of active waveguide. By using this approach, a novel four segments twin stripe device, as shown in figure 1.5, has been fabricated. All the segments can be used as an integrated waveguide detector, integrated optical amplifier or integrated laser source. With this structure good optical and electrical

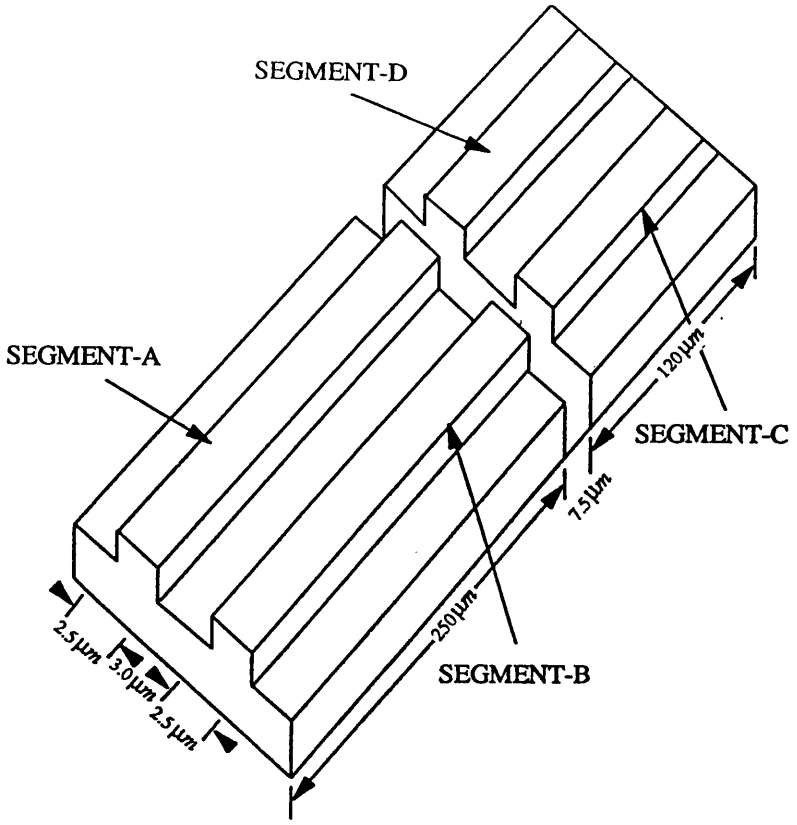

Figure 1.5. The structural view of monolithic integrated four-segment twin tandem stripe laser device.

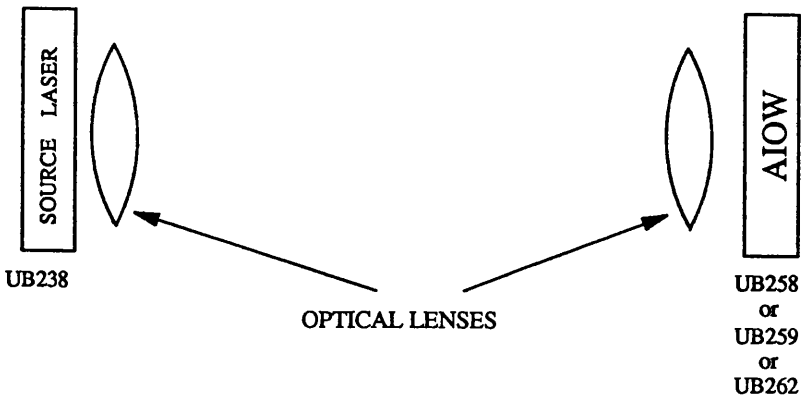

Figure 1.6. The achievement of the active optical waveguide in hybrid approach through optical lenses.

confinement is achieved, but the performance of the etched or milled facet laser can be poor due to problems with corrugated and non-vertical facets [58]. Moreover, the finite etched facet reflectance cannot be altered due to a narrow gap between two segments. So it is very difficult to establish a real understanding of the behaviour of the light propagation in monolithic integrated active components only by using this type of monolithic approach. Therefore, in order to have a more complete understanding of light propagation in active components, the hybrid approach, as shown in figure 1.6, whenever necessary is used to reinforce the monolithic integration results. In this case, no optical isolator is used to create real butt coupling conditions and the result can be applied directly to monolithic integrated components. For the hybrid approach, three different types of devices, UB258, UB259 and UB262 of similar structure but with different facet reflectances have been used as an AIOW to make the study more comprehensive and valid for variety of structural considerations. For the hybrid approach, a 5μm wide stripe laser, UB238 has been used as the source laser through the work reported in this thesis.

Figure 1.7 gives the general waveguide structure used in the tests and structural parameters of the various devices tested are listed in table 1.1.

Table 1.1. *Structural parameters for different devices used in hybrid approach.*

DEVICE NUMBER	*STRIPE WIDTH, W (μm)*	*R_1 (%)*	*R_2 (%)*
UB238	*5.0*	*30*	*30*
UB258	*2.5*	*30*	*4.48**
UB259	*2.5*	*4.48**	*4.48**
UB262	*2.5*	*30*	*30*

*- See section 2.6.5.

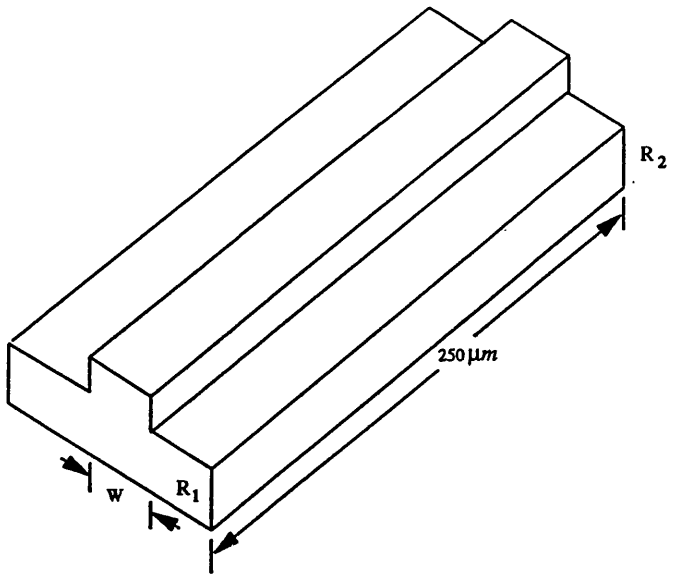

Figure 1.7. The structural representation of devices used in hybrid approach.

1.6- Organisation of the thesis

The integration of several active optical components on a single substrate still remains a significant technological challenge. Not the least of these problems is the lack of a clear understanding of the optical signal propagation mechanism in the active media. In order to gain a better understanding of light propagation in the active media, this thesis is divided into two main parts. The first part, consisting of chapters two and three, provides the basic theoretical and technical information about the laser devices which are later used in second part (chapters four, five and six), where the characteristics of monolithic OIC components are measured.

The investigation of wave propagation in OIC components needs a detailed understanding of light generation and propagation mechanisms in laser as they share similar structure and chapter-2 attempts to fulfil this need. This chapter is organized in such a way that it provides the necessary background of laser theory but it also discusses the practical laser characteristics such as the measurement of the laser Light-Current characteristic, the differential quantum efficiency, η_D, the internal quantum efficiency, η_{in}, the optical dissipation losses in the active region, α and the facet reflectivity.

It is a well established fact that the laser characteristics, such as optical gain saturation, the peak emission wavelength, total losses and the threshold current are temperature dependent. In chapter-3, some of these temperature dependent properties are investigated by originating the heat sources in a laser diode and by using a three channel temperature controller. A novel temperature dependent loss measurement technique is developed and is validated by comparing the loss values obtained in chapter-2 for $5\mu m$ wide stripe laser (UB238) and obtained by this new technique for same device. After establishing the validity of this temperature dependent loss measurement technique, the optical dissipation losses inside the $2.5\mu m$ wide stripe laser (UB262) are measured and this value is later used in chapter-5 to calculate the unsaturated local gain, g_o of the active medium. The effect of the temperature variation on the laser characteristics, such as the I-L and

spectral characteristics are investigated for several devices and the thermal rise time of FP devices is evaluated from the temperature dependent I-L characteristics. Also the thermal rise time of different devices (FP lasers and A.R. coated optical amplifiers) is evaluated from the temperature dependent spectral characteristic, for the first time.

The actual work on OIC components is described in chapter-4 by considering the use of an active waveguide structure as a waveguide detector both theoretically and experimentally. The characteristics of several devices with different structures, such as: the monolithic integrated waveguide detector; the Fabry-Perot laser waveguide detector with different stripe width and the A.R. coated waveguide detector are then measured and calibrated with respect to a standard detector. This provides the necessary background for using the monolithic optical detector to accurately measure the input power of any monolithic or hybrid component and in particular to align these optical components in a hybrid configuration. The leakage of optical flux is also observed in this chapter and is justified by originating the source of that leakage.

In chapter-5, the optical amplifier is considered as an essential part of an OIC. The internal signal gain of several amplifiers (Fabry-Perot (FP)) and near travelling wave (NTW) amplifier) is measured by a newly developed technique in which the saturated output characteristics are used. Also in this chapter, the nonlinear relationship between input and output of the active waveguide is measured and compared with the results of reference-4.

The investigation of nonlinear characteristics of the active waveguide is further extended in chapter-6 to include the effect of the facet reflectance on the output when two integrated components are butt coupled. The effect of the facet reflectance is observed in the form of the frustrated instabilities which appear as a train of self-sustained pulsations (SSP) at the output and which eventually leads to chaos. By exploiting the SSP in different devices, two new routes to chaos are identified.

Chapter-7, which is the concluding chapter, is devoted to the general discussion of the work presented in this thesis. Also in this chapter, conclusions are made with remarks on system limitations and suggestions for future work are presented.

References

1. Kogelnik, H., 'Limits in integrated optics', Proc. of the IEEE, vol.69, p.232, 1981.
2. Leonberger, F.J., and Dounelly, J.P., 'Semiconductor integrated optic devices', in Guided-wave optoelectronics, Tamir, T (Ed.), p.317, Springer-Verlag, 1990.
3. Stallard, W.A., Hodgkinson, T.G., Preston, K.R., and Booth, R.C., 'Novel $LiNbO_3$ integrated-optic component for coherent optical heterodyne detection', Electron. Lett., vol.21, p.1077, 1985.
4. Ormondroyd, R.F., Pennington, P.N., and Perkins, M.C., 'Nonlinear static characteristics of monolithic integrated-optic waveguides, IEE Proc-J, vol.136, p.56, 1989.
5. Hall, R.N., Fenner, G.E., Kingsley, J.D., Soltys, T.J., and Carlson, R.O., 'Coherent light emission from GaAs junction', Phys. Rev. Lett., vol.9, p.366, 1962. Reprinted in Semiconductor devices: Poineering papers, Sze, S.M. (Ed.), p.890, 1991.
6. Nathan, M.I., Dumke, W.P., Burns, G., Dill, F.H., and Lasher, G., 'Stimulated emission of radiation from GaAs *p-n* junctions', Appl. Phys. Lett., vol. 1, p.62, 1962. Reprinted in Semiconductor devices: Poineering papers, Sze, S.M. (Ed.), p.893, 1991.
7. Quist, T.M., Rediker, R.H., Keyes, R.J., Krag, W.E., Lax, B., Whorter, A.L., and Zeigler, H.J., 'Semiconductor maser of GaAs', Appl. Phys. Lett., vol.1, p.91, 1962.
8. Merz, J.L., and Logan, R.A., 'Integrated GaAs-$Al_xGa_{1-x}As$ injection lasers and detectors with etched reflectors' Appl. Phys. Lett., vol.33, p.530, 1975.
9. Ikeda, M., 'Switching characteristics of laser diode switch', IEEE J. of Quant. Electron., vol. QE-19, p.157, 1983.
10. Schicketanz, D., and Zeidler, G., 'GaAs double-heterostucture lasers as amplifiers', IEEE J. of Quant. Electron., vol. QE-11, p.65, 1975.
11. Kobayashi, S., and Kimura, T., 'Gain and saturation power of resonant AlGaAs laser amplifier', Electron. Lett., vol.16, p.230, 1980.
12. Garmire, E., Stoll, H., Yariv, A., and Hunsperger, R.G., 'Optical waveguiding in photon implanted GaAs', Appl. Phys. Lett., vol.21, p.87, 1972.
13. Somekh, S., Garmire, E., Yariv, A., Garvin, H.L., and Hunsperger, R.G., 'Channel optical waveguides and directional couplers in GaAs-imbedded and ridged', Appl. Optics, vol.13, p.327, 1974.
14. Miaman, T.H., 'Stimulated optical radiation in ruby lasers', Nature, vol.187, p.493, 1960.
15. Basov, N.G., Kroklin, O.N., and Papov, Y.M., 'Production of negative temperature states in p-n junctions of degenerate semiconductors', Sov. Phys., JETP, vol.13, p.1320, 1961.

16. Bernard, M.G.A., and Duraffourg, G., 'Laser conditions in semiconductors', Phys. Status Solidi, vol.1, p.699, 1961. Reprinted in Semiconductor devices: Poineering papers, Sze, S.M. (Ed.), p.880, 1991.
17. Alferov, Z.L., Andreev, V.M., Korel'kov, V.I., Portnoi, E.L., and Tret'yakov, D.N., 'Injection properties of n-$Al_xGa_{1-x}As$ p-heterojunctions', Sov. Phys., Semicond., vol.2, p.843, 1969.
18. Synder, A.W., and Love, J.D., 'Optical waveguide theory', Chapman and Hall, 1983.
19. Kapron, F.P., Keck, D.B., and Mavrer, R.D., 'Radiation losses in glass optical waveguides', J. Appl. Phys., vol.38, p.5419, 1967.
20. Thornton, R.L., Burnham, R.D, Paoli, T.L., Holonyak, N., and Deppe, D.G., 'Low threshold planar buried heterostructure lasers fabricated by impurity induced disordering', Appl. Phys. Lett., vol.47, p.1239, 1985.
21. Miya, T., Terunuma, Y., Hosaka, T., and Miyashita, T., 'Ultimate low-loss single-mode fibre at 1.55μm', Electron. Lett., vol.15, p.106, 1979.
22. Miller, S.E., 'integrated optics; An introduction', B.S.T.J., vol.48, p.2059, 1969.
23. Marcatili, E.A.J., 'Directional rectangular waveguide and directional coupler for integrated optics', B.S.T.J., vol.48, p.2071, 1969.
24. Goell, J.E., 'Electron-resist fabrication of bends and couplers for integrated optical circuits', Appl. Optics, vol.12, p.729, 1973.
25. Stoll, H., Yariv, A., Hunsperger, R.G., and Tangoman, G.L., 'Proton-implanted optical waveguide detectors in GaAs' Appl. Phys. Lett., vol.23, p.664, 1973.
26. Hurwitz, C.E., Rossi, J.A., Hsieh, J.J., And Wolfe, C.M., 'Integrated GaAs-AlGaAs double heterostructure lasers', Appl. Phys. Lett., vol.27, p.241, 1975.
27. Chang, M.B., and Garmire, E., 'Amplification in cleaved-substrate lasers', IEEE J. Quantum Electron., vol. QE-6, p.997, 1980.
28. Yamamoto, Y., 'Characteristics of AlGaAs Fabri-Parot cavity type laser amplifiers', IEEE J. Quantum Electron., vol. QE-16, p.1047, 1980.
29. Mukai, T., Yamomoto, Y., and Kimura, T., 'S/N and error rate performance in AlGaAs semiconductor laser pre-amplifier and linear repeater systems', IEEE J. Quantum Electron., vol. QE-18, p.1560, 1982.
30. Zah, C.E., Osinki, J.S., Caneau, C., Menocal, S.G., Reith, L.A., Salzman, J., Shokoohi, F.K., and Lee, T.P., 'Fabrication and performance of 1.5μm GaInAsP travelling-wave laser amplifiers with angled facets', Electron. Lett., vol.23, p.990, 1987.
31. Farries M.C., Buus, J., and Robbins, D.L., 'Analyses of antireflection coatings on angled facet semiconductor laser amplifiers', Electron. Lett., vol.26, p.381, 1990.
32. Cha, I., Kitamura, M., and Mito, I., '1.5μm band travelling-wave semiconductor optical amplifiers with window facet structure', Electron. Lett., vol.25, p.242, 1989.

33. Cha, I., Kitamura, M., Honmou, M., and Mito, I., '1.5μm band travelling-wave semiconductor optical amplifiers with window facet structure', Electron. Lett., vol.25, p.1241, 1989.

34. Rideout, W., Holmstrom, R., LaCourse, J., Meland, E., and Pawazinik, W., 'Ultra-low-reflectivity semiconductor optical amplifiers without antireflection coatings', Electron. Lett., vol.26, p.36, 1990.

35. Tsukada, T., 'GaAs-$Ga_{1-x}Al_xAs$ buried-heterostructure injection lasers', J. Appl. Phys., vol.45, p.4899, 1974.

36. Brillouet, F., Rion, J., Trotte, M., Azoulay, R., and Dugrand, L., 'Low threshold and low dispersion MOCVD-LPE buried-heterostructure GaAs/GaAlAs lasers', Electron. Lett., vol.20, p.857, 1984.

37. Ishii, M., Kamon, K., Shimagu, M., Mihara, M., Kumabe, H., and Isshiki, K., 'Planar TSJ lasers fabricated in embedded GaAs-AlGaAs layers grown by low pressure organometallic vapour phase epitaxy', Optoelectronics Devices Tech., vol.2, p.83, 1987.

38. Aiki, K., Nakamura, M., Kuroda, T., and Umeda, J., 'Channelled-substrate planar structure (AlGa)as injection laser', Appl. Phys. Lett., vol.30, p.649, 1977.

39. Ishida, K., Matsui, K., Fakunaga, T., Takamori, T., and Nakashima, H., 'Fabrication of index-guided AlGaAs multiquantum well lasers with buried optical guide by Si-induced disordering', Jap. J. of Appl. Phys., vol.25, p.L690, 1986.

40. Thornton, R.L., Epler, J.E., and Paoli, T.L., 'monolithic integration of a transparent dielectric waveguide into an active laser cavity by impurity induced disordering', Appl. Phys. Lett., vol.51, p.1983, 1987.

41. William, P.J., Charles, P.M., Griffith, L., Considine, L., and Carter, A.C., 'High performance buried ridge DFB lasers with monolithically integrated with butt coupled stripe loaded passive waveguide for OEIC', Electron. Lett., vol.26, p.142, 1991.

42. Ribot, H., Sansonetti, P., Brandon, J., Carre, M., Menigaux, L., Azoulay, R., and Bouadma, N., 'Monolithic integration of GaAs/GaAlAs buried-heterostructure orthogonal facet laser and optical waveguide', 'Appl. Phys. Lett., vol.54, p.475, 1989.

43. Ribot, H., Sansonetti, P., and Carenco, A., 'Improved design for the monolithic integration of a laser and an optical waveguide coupled by an evanescent field', IEEE J. of Quant. Electron., vol. QE-26, p.1930, 1990.

44. Bouadma, N., Correc, P., and Brillouet, F.P., 'GaAS:GaAlAs ridge waveguide laser and their monolithic integration using the ion beam etching process', IEEE J. of Quant. Electron., vol. QE-25, p.2219, 1989.

45. Kurcharska, A.I., Blood, P., Fletcher, E.D., and Hulyer, P.J., 'Bistability in inhomogeneously pumped quantum well laser diodes', IEE Proc-J, vol.135, p.31, 1988.

46. Lasher, G.J., 'Analysis of a proposed bistable injection laser', Solid State Electron., vol.7, p.707, 1964.

47. Perkins, M.C., Ormondroyd, R.F., and Rozzi, T.E., 'Effect of photon lifetime on absorptive bistability in inhomogeneously pumped lasers' Electron. Lett., vol.21, p.857, 1985.

48. Perkins, M.C., Ormondroyd, R.F., and Rozzi, T.E., 'Analysis of absorptive bistability characteristics of multisegment lasers' IEE Proc.-J, vol.33, p.283, 1986.

49. Perkins, M.C., and Ormondroyd, R.F., 'Transient analysis of optical bistability in inhomogeneously pumped lasers' IEE Proc.-J, vol.135, p.133, 1988.

50. Gibbs, M., McCall, S.L., Venkatesan, T.N.C., Gossard, A.C., Passuer, A., and Weigmann, W., 'Optical bistability in semiconductors', Appl. Phys. Lett., vol.35, p.451, 1979.

51. Miller, D.A.B., Smith, S.D., and Johnston, A., 'Optical bistability and signal amplification in a semiconductor crystal: Application of new low-power non-linear effect in InSb', Appl. Phys. Lett., vol.35, p.658, 1979.

52. Poole, C.D., and Garmire, E., 'Optical bistability at the band gap in InAs', Appl. Phys. Lett., vol.44, p.363, 1984.

53. Mukai, T., and Otsuka, K., 'New route to optical chaos: Successive-subharmonic-oscillation in a semiconductor coupled to an external cavity', Phys. Rev. Lett., vol.55, p.1711, 1985.

54. Otsuka, K., and Kobayashi, S., 'Optical bistability and non-linear resonance in a resonant-type semiconductor laser amplifier', Electron. Lett., vol.19, p.262, 1983.

55. Liu, H.F., and Kamiya, T., 'Observation of chaos in an inhomogeneouly pumped self-pulsating semiconductor laser', Jap. J. of Appl. Phys., vol.28, 1600, 1989.

56. Morton, P.A., Helkey, R.J., Corzine, S.W., and Bowers, J.E., 'Subpicosecond multiple pulse formation in actively mode-locked semiconductor lasers', Proc. OSA Topical meeting on picosecond electronics and optoelectronics, Salt Lake city, p.87, March-1989.

57. Warren, M.E., Koch, S.W., and Gibbs, H.M., 'Optical bistability, logic gating, and waveguiding operation in semiconductor etalon', IEEE Computer, p.68, Dec.1987.

58. Carter, A.J., Thomas, B., Morgan, D.V., Bhardwaj, J.K., McQuarrie, A.M., and Stephen, M.A., 'Dry etching of GaAs and InP for optoelectronic devices', IEE Proc-J. vol.136, p.2, 1989.

Chapter-2

Light emission process in semiconductor active media

2.1- Introduction

The laser consists of three main elements: an external energy source or pump, an amplifying or active medium and an optical cavity or resonator to provide the necessary feedback to sustain the oscillation at optical frequencies. In the case of the semiconductor laser, the *p-n* junction provides the active region where the injection of external carriers provides the necessary optical gain by means of achieving population inversion and feedback is achieved either by reflection at naturally cleaved facets (to form a Fabry-Perot resonator) or via an external Bragg grating.

The discussion of basic laser theory begins in section 2.2 with the Einstien relations, which connect the rates of absorption, spontaneous emission and stimulated emission in a two-energy-level system by considering blackbody radiation as the radiation field. Also in section 2.2, necessary conditions for lasing action in the two energy level system are derived. Similar relationships for the lasing conditions are derived in section 2.3 for the more complicated band structure of semiconductor. In section 2.4, the different types of semiconductor lasers are considered briefly. Waveguiding is central to the low threshold operation of semiconductor lasers. Consequently waveguiding mechanisms in the slab and rib waveguides using the effective index concept is analysed in section 2.5. In section 2.6, basic parameters which are necessary to analyse the light propagation process in active waveguides are measured experimentally. Section 2.7 provides the summary of main point.

2.2- Light amplification in two-energy-level systems

2.2.1- Einstien relations

Consider the two energy-level system of figure 2.1 (typical of a gas). The populations n_1 and n_2 of the two energy levels E_1 and E_2, in thermal equilibrium, are related via Boltzmann's equation;

$$\frac{n_2}{n_1} = e^{\frac{-(E_2-E_1)}{kT}} \tag{2.1}$$

where T is the equilibrium temperature and k is the Boltzmann constant. The negative exponent in equation (2.1) indicates that $n_2 << n_1$ at equilibrium; i.e. most electrons are in the lower energy level.

When an electron in an atom undergoes a transition between two energy states, it either emits or absorbs a photon having an energy;

$$\Delta E = h\nu \tag{2.2}$$

where $\Delta E = E_2 - E_1$ is the energy difference between two energy levels, h is Plank's constant and ν is the frequency of the photon.

Suppose an electron in the lower level E_1, interacts with a photon and is excited to the higher energy level E_2, as shown in figure 2.1(a) where it is out of thermal equilibrium. Very soon after being excited to the higher energy level, the atom will undergo a downward transition and emit a photon of energy $h\nu = E_2 - E_1$. This emission process may occur in two ways:

1. a spontaneous emission process, in which the electron drops to the lower energy level in an entirely random way, as shown in figure 2.1(b).

2. a stimulated emission process in which the electron is 'triggered' to undergo the transition by the presence of a photon of energy $h\nu = E_2 - E_1$, as shown in figure 2.1(c).

Under normal circumstances (i.e. under thermal equilibrium conditions), the stimulated process is not observed because the probability of a spontaneous process occurring is much higher than that of stimulated emission because n_2 is less than

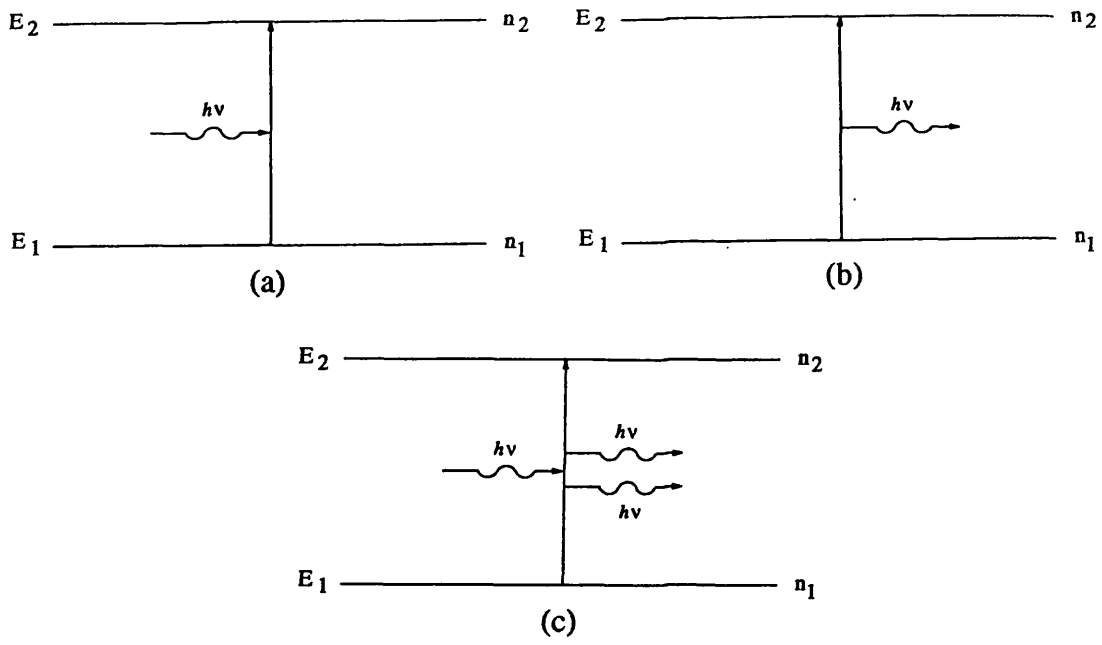

Figure 2.1. A schematic representation of different processes for simplified two level system (a) absorption, (b) spontaneous emission and (c) stimulated emission.

n_1. The average time the electron exists in the excited state before making a spontaneous transition from E_2 to E_1 is called the spontaneous lifetime and is defined as;

$$\tau_s = \frac{1}{A_{21}} \tag{2.3}$$

where A_{21} is the spontaneous transition rate and '21' indicates a transition from level '2' to level '1'.

Because the spontaneous emission radiation from any electron is emitted randomly, the radiation by a large number of atoms clearly will be incoherent. In contrast, the stimulated emission process results in coherent and monochromatic radiation. This latter process was first explained by Einstien in 1917.

In a two level system, the probability that an electron will undergo a spontaneous emission from energy level E_2 of population n_2 within a time interval dt is given by;

$$-\frac{dn_2}{dt} = n_2 A_{21} \tag{2.4}$$

The probability of the stimulated emission process is dependent upon the density of electrons at level E_2 and the intensity of the optical field interacting with the excited electrons, that is;

$$-\frac{dn_2}{dt} = n_2 B_{21} \rho(\nu_{21}) \tag{2.5}$$

where $\rho(\nu_{21})$ is the photon density at a frequency ν_{21}.

Absorption also depends on the strength of the photon field. In effect, stimulated absorption and stimulated emission are inverse processes. Therefore;

$$\frac{dn_1}{dt} = n_1 B_{12} \rho(\nu_{21}) \tag{2.6}$$

where A_{21}, B_{12} and B_{21} are the Einstien coefficients of spontaneous emission, stimulated absorption and stimulated emission respectively.

For a system in thermal equilibrium, absorption must be equal to the total emission of photons;

$$n_1 B_{12}\rho(\nu_{21}) = n_2 B_{21}\rho(\nu_{21}) + n_2 A_{21} \tag{2.7}$$

and the photon density which achieves this condition is given by;

$$\rho(\nu_{21}) = \frac{\frac{A_{21}}{B_{21}}}{\frac{B_{12}}{B_{21}}\frac{n_1}{n_2} - 1} \tag{2.8}$$

By comparing equations (2.1) and (2.8), we have;

$$\rho(\nu_{21}) = \frac{\frac{A_{21}}{B_{21}}}{\frac{B_{12}}{B_{21}}\exp\frac{E_2 - E_1}{kT} - 1} \tag{2.9}$$

Since the system is in a thermal equilibrium condition, it would give rise to radiation which is identical to that of the blackbody distribution inside an enclosure described by Plank's blackbody law for energy about the frequency, ν as;

$$\rho(\nu) = \frac{8\pi h\nu^3}{c^3\left[\exp\frac{h\nu}{kT} - 1\right]} \tag{2.10}$$

where c is the velocity of light in a vacuum.

By equating equations (2.9) and (2.10) for energy density $\rho(\nu) = \rho(\nu_{21})$ (as the system is in thermal equilibrium), results in;

$$B_{21} = B_{12} \tag{2.11}$$

$$\frac{A_{21}}{B_{21}} = \frac{8\pi h\nu^3}{c^3} \tag{2.12}$$

and

$$B_{21} = \frac{c^3}{8\pi h\nu^3\tau_s} \tag{2.13}$$

Equations (2.11) to (2.13) are called Einstien relations. Taken together, they tell the following.

1. The fundamental Einstein coefficients A_{21}, B_{12} and B_{21} all are inter-related. If one is known by measurement or calculations, all are known.
2. Although, the derivation of Einstein relations was based on the condition of thermal equilibrium, they are valid under any conditions because they are characteristics of the atom and are equally valid whether the atom is in an intense radiation field or in an enclosure that can be treated as a blackbody in thermal equilibrium.
3. As B_{21}/A_{21} is proportional to the reciprocal of the frequency, ν_{21}, the higher the frequency, the smaller B_{21} becomes in comparison with A_{21}. Since B_{21} is related to the stimulated emission and A_{21} is related to spontaneous emission, it indicates that lasers of short wavelength radiation would be difficult to build and operate.

The above discussion indicates that the process of stimulated emission competes with the processes of spontaneous emission and absorption. If one wants to amplify a beam of light by stimulated emission, then the rate of this process must increase the other two processes. It is clear from equation (2.7) that to achieve this for a given pair of energy levels, one must increase the radiation density and the population density, n_2 of the upper level in relation to population density n_1 of the lower energy level (so that $n_2 > n_1$): that is, one must create a so called condition of population inversion.

2.2.2. Population inversion and optical gain

Consider a collimated beam of light passing through an absorbing material which is travelling in the direction z, as shown in figure 2.2. For the sake of simplicity, it is assumed that there is only a single radiative transition between energy levels E_1 and E_2. The change in the irradiance of the beam as a function of distance is given by;

$$\Delta I(z) = I(z + \Delta z) - I(z) \tag{2.14}$$

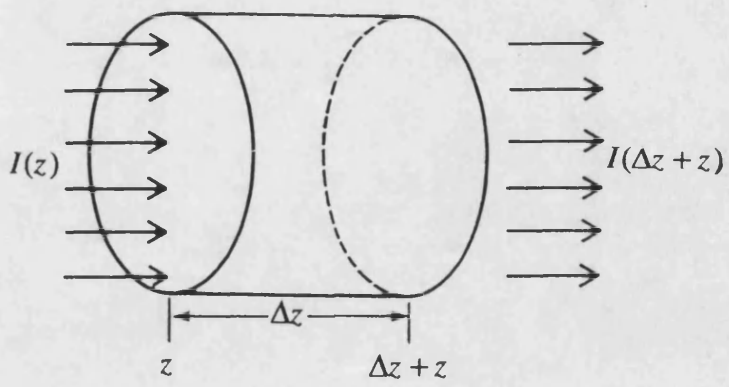

Figure 2.2. Radiation passing through an absorbing medium.

For a homogeneous medium $\Delta I(z)$ is proportional both to the distance travelled, Δz and $I(z)$, that is;

$$\Delta I(z) = -\alpha_a I(z)\Delta z \tag{2.15}$$

where the constant of proportionality, α_a is the absorption coefficient. The minus sign indicates the reduction in beam irradiance brought about by absorption as α_a is taken to be a positive quantity.

For a small value of Δz, equation (2.15) can be written as;

$$\frac{dI(z)}{dz} = -\alpha_a I(z) \tag{2.16}$$

This can be solved to give;

$$I(z) = I(o)\exp\{-\alpha_a z\} \tag{2.17}$$

where $I(o)$ is the irradiance of the beam at the input, z=0.

The degree of absorption of the beam will depend on how many electrons are in energy state E_1 and how many electrons are in energy level E_2. If n_2 is zero, then the absorption would be maximum. If all of the electrons were in the upper state, the absorption would be zero and the probability of stimulated emission would be large and there would be net gain.

From the discussion of section 2.2.1 and making the use of equations (2.5) and (2.6), an expression for the net rate of loss of photons per unit volume, $-\frac{dS}{dt}$ can be written as;

$$-\frac{dS}{dt} = n_1 B_{12}\rho(\nu_{21}) - n_2 B_{21}\rho(\nu_{21}) \tag{2.18}$$

Here, photons generated by spontaneous emission are neglected as they are emitted randomly in all directions and only a small fraction of them contributes to collimated beam.

Using equation (2.11), equation (2.18) can be re-written as;

$$-\frac{dS}{dt} = (n_1 - n_2)B_{21}\rho(\nu_{21}) \tag{2.19}$$

The irradiance, $I(z)$, of the beam along the length, z, is the energy crossing unit area in unit time and therefore is given by the energy density times the speed of light in the medium, that is;

$$I(z) = \rho \frac{c}{n} \tag{2.20a}$$

where n is the refractive index of the medium.

For photons of frequency ν_{21}, the irradiance of the beam is given by;

$$I(z) = \rho(\nu_{21}) \frac{c}{n} \tag{2.20b}$$

where the energy density, $\rho(\nu_{21})$ is the product of number of photons, S and energy of each photon, $h\nu_{21}$. Therefore equation (2.20b) can be re-written as;

$$I(z) = \frac{Sh\nu_{21}c}{n} \tag{2.21}$$

The change in photon density within the beam between boundaries z and $(z + \Delta z)$ is;

$$-dS = [I(z) - I(z + \Delta z)] \frac{n}{h\nu_{21}c} \tag{2.22}$$

For small values of Δz

$$-dS = -\frac{dI(z)}{dz} \cdot \frac{\Delta z n}{h\nu_{21}c} \tag{2.23}$$

and the rate of decay of photon density in a time interval $dt = \frac{\Delta z n}{c}$ is;

$$\frac{dS}{dt} = \frac{dI(z)}{dz} \cdot \frac{1}{h\nu_{21}} \tag{2.24}$$

Consequently;

$$\frac{dS}{dt} = -\alpha_a I(z) . \frac{1}{h\nu_{21}} \tag{2.25}$$

and by substituting the value of $I(z)$ from equation (2.20b);

$$\frac{dS}{dt} = -\alpha_a \rho(\nu_{21}) . \frac{c}{n} \cdot \frac{1}{h\nu_{21}} \tag{2.26}$$

By comparing the equations (2.19) and (2.26), one can have;

$$\alpha_a = (n_1 - n_2)\frac{B_{21} h \nu_{21} n}{c} \qquad (2.27)$$

Equation (2.27) provides the link between the absorption coefficient and the population difference for the two transition states. Normally, n_1 is greater than n_2, as shown in figure 2.3(a). In this case α_a is a positive quantity and absorption occurs. If one creates a condition where n_2 is greater than n_1 (figure 2.3(b)), then α_a is negative and irradiance of the beam grows with distance.

2.2.2.1. Attainment of population inversion

Population inversion for light amplification is a non-equilibrium condition. In order to create this non-equilibrium condition, one has to supply external energy to excite the electrons into the upper level E_2 in the two-level system. This excitation process is called pumping.

In two-level systems, once electrons are excited into upper level the probabilities of further stimulated absorption or emission are equal. Even with very intense pumping, the best that can be achieved with the two level system, considered so far, is the equality of populations of two levels. Only the equality of the coefficients B_{21} and B_{12} is the necessary condition for lasing action to occur, although it is not sufficient in a practical system because of the losses occurring in the laser cavity. In order to achieve true population inversion, three or four energy levels systems are used. In both systems, there exist a central metastable state (as shown in figures 2.4(a) and (b)) in which the electron spend unusually long time before decaying to ground state.

The three level system consists of a ground level, E_o, a metastable level, E_1 and third level, E_2, above the metastable level. Under the influence of suitable pumping, electrons may be excited from ground, E_o level to the level E_2. As E_2 is a normal level, electrons will rapidly decay by non-radiative process to either E_o or to E_1. Hence empty states will always be provided in E_2. The metastable level always exhibits a much longer time than E_2, so it will allow a large number of

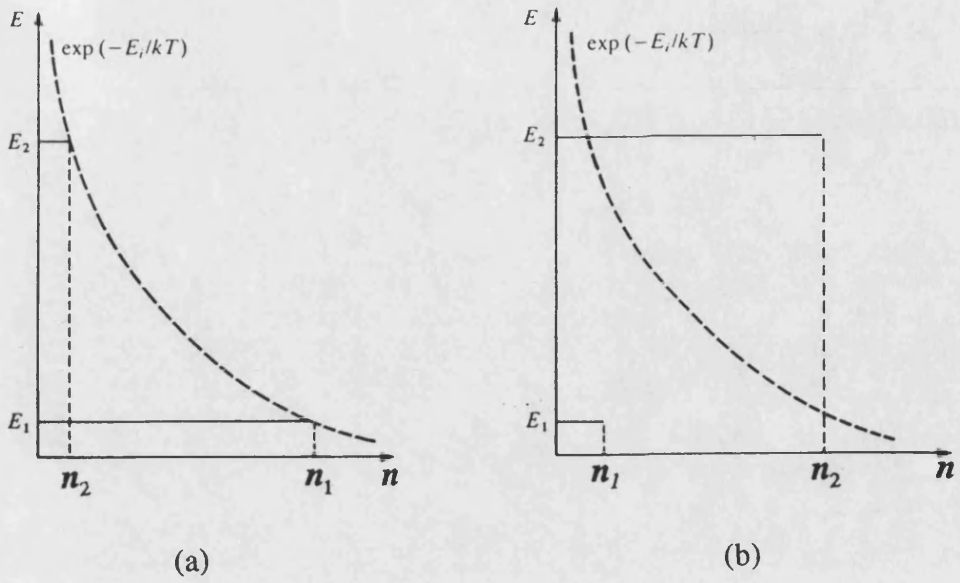

Figure 2.3.Population of two level energy system (a) in thermal equilibrium and (b) after pumping.

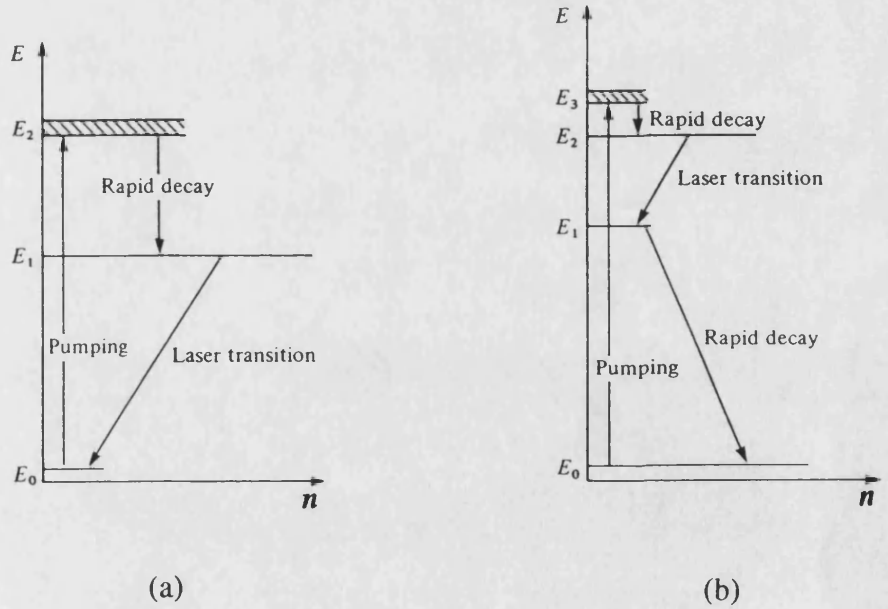

Figure 2.4. Population inversion in (a) three energy level system and (b) four level system.

electron to accumulate. With sufficiently intense pumping, a significant number of electrons can be pumped to level E_1. A population inversion between E_o and E_1 occurs when the population of E_1 exceeds that of ground level and lasing action may occur as a result of radiative transition between E_1 and E_o.

The main drawback with the three level system is that it requires very high pumping power because the level E_o is the ground state. This problem can be solved by using four level system (figure 2.4(b)). In this case, electrons are excited from ground level E_o to the level E_3. They decay rapidly to the metastable level E_2. The population of E_3 and E_1 remain unchanged as a result of fast decay of electron, a small increase in the population of level E_2 creates population inversion and lasing takes place between E_2 and E_1.

Although, population inversion may be obtain in three or four energy levels systems more efficiently. However, the study of two level system is helpful in understanding the laser action and can be extended to semiconductor band structure. Therefore here we restrict ourselves to two level system.

2.2.3. Optical feedback

The laser, despite its acronym, is usually interpreted to mean an oscillator than an amplifier. The laser is basically a Fabry-Perot etalon in which the space between the two mirrors contains an amplifying medium with an inverted population. The initial stimulus is provided by any spontaneous transition between appropriate energy levels in which the emitted photon travel along the optical axis. The generated light is amplified when it passes through the medium. The net gain per unit length of most active medium is so small that very little amplification of light beam results from a single pass through the active medium. However, the arrangement of mirror surfaces forms a Fabry-Perot cavity (or resonator), which provides total internal reflection. The light of a particular frequency can be reflected back

and forth within the resonant cavity in a reinforcing (coherent) manner, if an integral number of half wavelength fit between the end mirrors, such that;

$$L = \frac{m\lambda}{2} \tag{2.28}$$

where L is the cavity length, m is an integer and λ is the wavelength.

In practice, the distance in a half-wavelength of visible or near infrared light is so small that equation (2.28) is automatically satisfied over some portion of real mirror spacing. Therefore, many values of m will fit the resonant condition. After multiple passes, the net gain can be substantial as a result of positive feedback and when the optical gain exactly matches the losses, a stable output is obtained. However, only those modes for which there is no net loss can oscillate in a stable manner.

The minimum gain necessary for the operation of a laser can be determined by considering the increase of irradiance undergone by a beam of light at the resonance frequency in travelling a roundtrip path inside a FP resonator of length, L, as shown in the figure 2.5. Because of the gain of the material, the radiation intensity grows exponentially with distance, z. According to Beer's law it can be given by;

$$I(z) = I(o)\exp\{(g_{21} - \alpha)z\} \tag{2.29}$$

where $I(o)$ is incident irradiance, $I(z)$ is light intensity at a point z, g_{21} is the gain and α is the absorption coefficient which is sum of losses due to free-carrier, coupling losses, band edge absorption losses and scattering losses.

After a round-trip, the intensity is given by;

$$I(2L) = I(o)R_1R_2\exp[2L(g_{21} - \alpha)] \tag{2.30}$$

At the lasing threshold, $I(2L) = I(o)$. Therefore;

$$R_1R_2\exp[2L(g_{th} - \alpha)] = 1 \tag{2.31}$$

or

$$g_{th} = \alpha + \frac{1}{2L}\ln\frac{1}{R_1R_2} \tag{2.32}$$

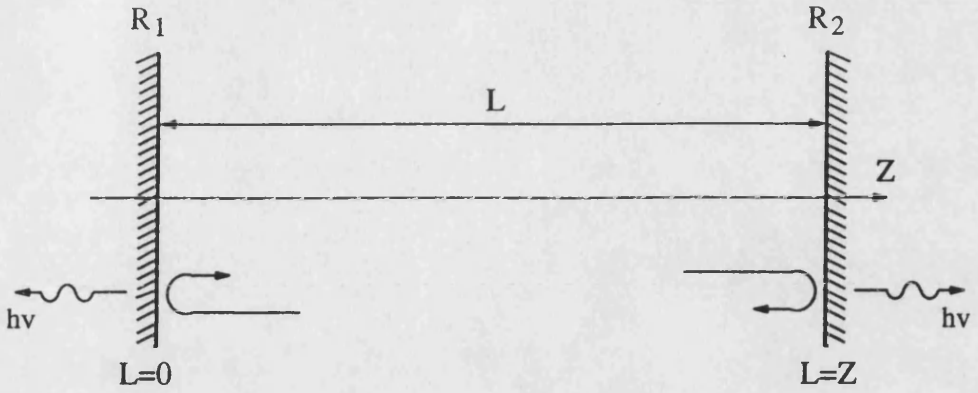

Figure 2.5. The geometry of the Fabry-Perot resonator.

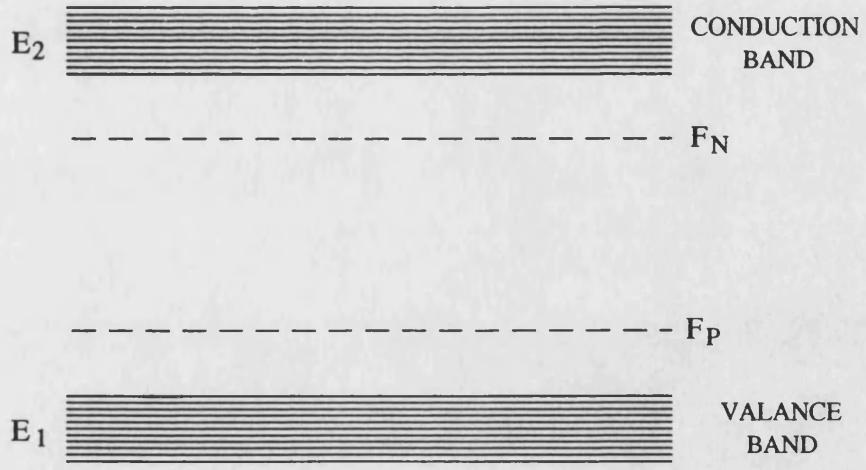

Figure 2.6. The schematic representation of available energy states within the conduction and the valence bands.

where $\frac{1}{2L}\ln\frac{1}{R_1R_2}$ is the mirror loss.

Equation (2.32) indicates that g_{th} can have a wide range of values, depending on the cavity length, the absorption coefficient of the material, the facet reflectivities and the structure of the laser which also effects α.

2.3. Optical absorption and emission in semiconductors

2.3.1. Necessary condition for lasing action in semiconductors

The energy level structure inside a semiconductor is much more complicated than that of simple atomic system considered above. According to the Pauli exclusion principle, the available electron states in the semiconductor can be represented by a continuous band of states within the valence and conduction band, as shown in figure 2.6. The probability that the state E_1 contains an electron is given by Fermi-Dirac statistics, rather than Boltzmann statistics, as;

$$f_1 = \frac{1}{\exp\frac{E_1 - F_P}{kT} + 1} \tag{2.33}$$

And the probability that the energy state, E_2 is occupied by an electron is;

$$f_2 = \frac{1}{\exp\frac{E_2 - F_N}{kT} + 1} \tag{2.34}$$

where F_P and F_N represent the quasi-Fermi levels for the valence and conduction bands under non-equilibrium conditions respectively. The quasi-Fermi level represents the points where the states would be 50% occupied in non-equilibrium conditions.

The rate at which electrons in an energy state E_1 in the valence band can be excited up to the state E_2 in the conduction band depend on several factors including the probability that the transition can occur (B_{12}), the probability that the state E_1 contains an electron (f_1), the probability that the state E_2 is empty $[1-f_2]$ and

the density of the photons of frequency ν_{21}, $\rho(\nu_{21})$. The upward transition rate may be then written as;

$$r_{12} = B_{12} f_1 [1 - f_2] \rho(\nu_{21}) \tag{2.35}$$

In addition to being absorbed, these photons can also stimulate the emission of similar photons by the transition of an electron from E_2 to E_1. Therefore, the downward transition rate is given by;

$$r_{21} = B_{21} f_2 [1 - f_1] \rho(\nu_{21}) \tag{2.36}$$

where $[1 - f_1]$ is the probability that the state E_1 is empty.

If stimulated emission is to occur, then the rate of downward transition must exceed the rate of upward transition, that is;

$$B_{12} f_1 [1 - f_2] \rho(\nu 21) < B_{21} f_2 [1 - f_1] \rho(\nu 21) \tag{2.37}$$

but

$$B_{12} = B_{21}$$

Therefore;

$$f_1 [1 - f_2] < f_2 [1 - f_1] \tag{2.38}$$

requiring that;

$$f_2 > f_1 \tag{2.39}$$

This is analogous to the population inversion condition in an atomic system i.e. $n_2 > n_1$. On substituting equation (2.33) and (2.34) into equation (2.38), the following important relation for net stimulated light output can be obtained;

$$\exp\left[\frac{F_N - F_P}{kT}\right] > \exp\left[\frac{E_2 - E_1}{kT}\right] \tag{2.40}$$

Equation $E_2 - E_1 = h\nu$ can only be satisfied if

$$h\nu < F_N - F_P \tag{2.41}$$

This equation states that net stimulated emission occurs for all transitions where the photon energy $h\nu$ is less than the separation of the two quasi-Fermi levels. If the material which is being used as an active medium has a definite

energy gap, E_g, then $F_N - F_P$ must be greater than E_g before any stimulated emission can occur. This condition was first derived by Bernard and Duraffour [1]. Equation (2.41) shows why the unpumped semiconductor in thermal equilibrium cannot lase as there is no separation between the quasi-Fermi levels. Basov *et al* [2] suggested that the condition for the separation of quasi-Fermi levels in semiconductor could be achieved by the injection of carriers across a *p-n* junction. Also equation (2.41) tells us either one or both of the quasi-Fermi levels must lie outside the band edge, when the junction is forward biased in the valence and/or conduction band. This mean that the *p-n* junction must be degenerately doped to achieve this, or alternatively a heterojunction must be used.

When the junction is forward biased, the electrons are injected across the junction from the *n*-type material into the *p*-type material and holes are injected from the *p*-type material into the *n*-type material. Once these carriers cross the junction where they exist as minority carriers, they are out of thermal equilibrium and they recombine with majority carriers. This recombination process may be of several different types and it will be discussed below.

2.3.2. Recombination mechanisms in semiconductors

The electron-hole recombination process can in general be divided into two groups, radiative and non-radiative recombination.

2.3.2.1 Radiative recombination

The radiative recombination occurs when an electron in the conduction band recombines with a hole in the valence band and the excess energy is emitted in the form of a photon. The radiative recombination is thus the radiative transition of an electron in the conduction band to an empty state (i.e. hole) in the valence band. The optical process associated with the radiative recombination of electron-hole pair in semiconductors are spontaneous emission and stimulated emission.

The rates of the recombination processes in a semiconductor are related to

each other through the Einstein relations. In order to achieve net stimulated emission, the downward transition must be equal or greater than the upward transition. Therefore, the net rate of stimulated emission r_{st} can be written as;

$$r_{st} = r_{21} - r_{12}$$

$$r_{st} = B_{21}\rho(\nu_{21})[f_2 - f_1] \tag{2.42}$$

Spontaneous emission in semiconductors is characterised by the spontaneous lifetime. The net spontaneous emission rate can be written as;

$$r_{sp} = \frac{f_2[1 - f_1]}{\tau_{sp}} \tag{2.43}$$

The absorption rate, which is the difference between upward and downward transition rates, just the opposite of stimulated emission, is given by;

$$r_{abs} = r_{12} - r_{21}$$

$$r_{abs} = B_{21}[f_1 - f_2]\rho(\nu_{21}) \tag{2.44}$$

2.3.2.2. Non-radiative recombination

The non-radiative recombination of an electron-hole pair is characterised by the absence of an emitted photon in the recombination process. This includes surface recombination, the recombination at defects and Auger recombination.

In lasers, the cleaved facet surfaces are exposed to the ambient temperature and in general, a surface is a strong perturbation of crystal lattice, creating many bonds that could act as centres of non-radiative recombination. These defects can be reduced by coating the mirror facet surfaces to enhance the facet reflectance.

Defects in the active layer of an injection laser can be formed in several different ways. In most of the cases, they are grown in during epitaxial process and can be avoided by growing defect-free materials.

The Auger recombination process is an intrinsic process. Physically speaking, during the Auger recombination process, the energy released by the electron-hole recombination is taken by a third charge carrier and eventually lost to the lattice

phonons. The rate of the Auger recombination is higher for long wavelength devices, whereas material with wider bandgap, such as GaAs, the Auger recombination process becomes significant only above a carrier concentrations of $10^{19}/cm^3$.

2.3.2.3. Direct and indirect bandgap semiconductors

The ratio between radiative and non-radiative recombination processes eventually defines the internal quantum efficiency, η_{in} of the emission process and this parameter needs to be made as large as possible. In optical sources, the radiative recombination process is obviously preferred to the non-radiative recombination process. The most useful type of material for this purpose is the so called direct-bandgap semiconductor material, such as GaAs, InP and GaSb, in which the minimum of the conduction band and maximum of the valence band occur at same crystal momentum value as shown in figure 2.7(a).

Figure 2.7(b) shows energy momentum diagram of direct-bandgap material where the maximum and minimum of the valence band and the conduction bands respectively occur at different values of crystal momentum.

2.3.3. The lasing threshold

The expression for the gain coefficient for the two-energy-level system in equation (2.32) can, in principle, be applied to semiconductor lasers directly. However, in the situation where the optical wave extends in both the transverse and lateral directions, only the fraction of power which remains within the active layer can participate in stimulated emission. The proportion of the optical intensity confined to the active layer, relative to the total optical power in active layer, is called the confinement factor, Γ. The efficiency of the confinement of electromagnetic field mainly depends on the order of the transversal mode confinement which is given by the thickness of active layer and the increments by which the refractive index changes at the heterojunction edges (heterojunction laser are discussed in

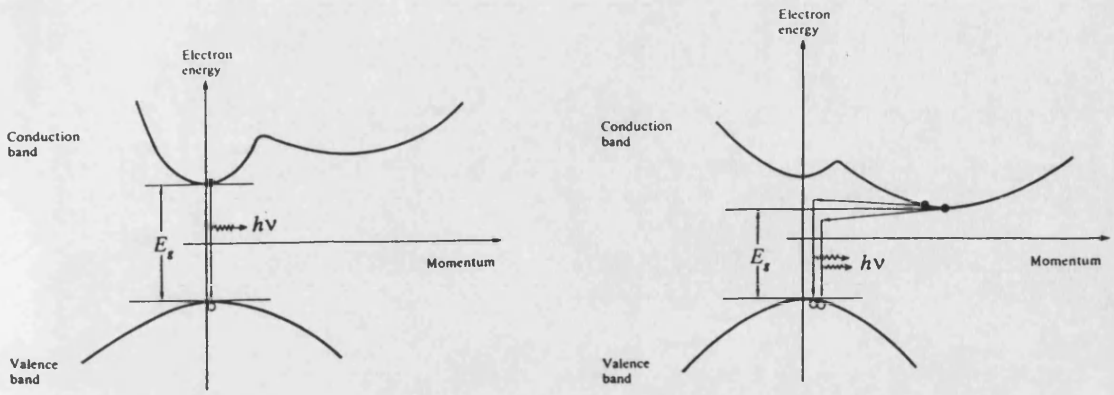

(a) (b)

figure 2.7. Schematic energy-momentum diagram for (a) direct band-gap and (b) indirect band-gap materials.

section 2.4). Analytically, the confinement factor for the fundamental TE and TM mode in heterostructure lasers is given by [3];

$$\Gamma_{TE} = \frac{V^2}{2+V^2} \tag{2.45}$$

and

$$\Gamma_{TM} = \frac{\left(\frac{n_3}{n_2}\right)^2 V^2}{2+\left(\frac{n_3}{n_2}\right)^2 V^2} \tag{2.46}$$

where V is the normalized active layer thickness (see section 2.5).

The effect of Γ changes the lasing condition of equation (2.32) to;

$$g_{th} = \frac{1}{\Gamma}\left[\alpha + \frac{1}{2L}\ln\frac{1}{R_1 R_2}\right] \tag{2.47}$$

In semiconductor lasers, usually $R=R_1=R_2$ and equation (2.47) can be re-written as;

$$g_{th} = \frac{1}{\Gamma}\left[\alpha + \frac{1}{L}\ln\frac{1}{R}\right] \tag{2.48}$$

The facet reflectance, R_1 of the laser facet for the plane wave can be calculated by the Fresnel relation, that is;

$$R_1 = \left(\frac{n_3 - 1}{n_3 + 1}\right)^2 \tag{2.49}$$

The threshold gain, g_{th}, also defined as [4,5];

$$g_{th} = \beta[J_{nom} - J_{(nom)_o}] \tag{2.50}$$

where β is the slope of the g vs J_{nom} curve [6]. J_{nom} is the current density required to maintained excitation rate of $1\mu m$ thick active layer device for unity internal quantum efficiency [5]. $J_{(nom)_o}$ is the transparency current density ($J_{(nom)_o}$ is the value of J_{nom} where gain just overcome losses). J_{nom} is given by;

$$J_{nom} = \frac{\eta_{in} J}{d_3} \tag{2.51}$$

where η_{in} is the internal quantum efficiency, d_3 is the thickness of the active layer and J is the current density. The internal quantum efficiency of a semiconductor diode is given by [7];

$$\eta_{in} = \eta_D \left\{ 1 + \frac{2\alpha L}{\ln \frac{1}{R_1 R_2}} \right\} \tag{2.52}$$

where η_D is the differential quantum efficiency, which is the slope of the I-L characteristic (section 2.6) in lasing region, that is;

$$\eta_D = \frac{\Delta P}{\Delta I} \tag{2.53}$$

The current density which is necessary to achieve the threshold gain for broad area lasers is given by [8];

$$J_{th} = J_t + J_e + J_h \tag{2.54}$$

where J_t is the total current density. J_e and J_h are the leakage current densities due to electron and hole leakage currents. J_e and J_h in equation (2.54) can be ignored at low the level of doping (as in DH lasers) and at the higher level of Al concentration in passive layers [9]. Therefore, from equations (2.48)-(2.51), at threshold;

$$J_{th} = \frac{d_3}{\eta_{in}} \left\{ \frac{1}{\Gamma\beta} \left(\alpha + \frac{1}{L} \ln \frac{1}{R} \right) + J_{(nom)_o} \right\} \tag{2.55}$$

The lowest threshold current density possible for a laser diode is given by [10];

$$J_{th} = \frac{d_3}{\eta_{int}} \left\{ \frac{1}{\beta} (g_{th}) \right\} \tag{2.56}$$

J_{th} can further be reduced by increasing the length of the device and increasing the facet reflectivity. For a fixed optical loss, J_{th} is determined by the waveguide parameter, Γ and by the gain constant, β.

2.3.4. Optical radiation losses in semiconductor lasers

There are three main contributions to laser losses. They can all be important,

in different circumstances, in contributing to the total loss, α in equation (2.47). The three loses may be defined as [5,11];

$$\alpha = \Gamma\alpha_{fc} + (1-\Gamma)\alpha_{fc} + \alpha_s + \alpha_c \tag{2.57}$$

where α_{fc} is the free carrier absorption, $\alpha_s$is the scattering loss and α_c is the coupling loss.

The cause for free carrier absorption losses is the direct interaction between optical waves and electrical carriers (electrons and holes) in the conduction band. It is approximately proportional to the square of the wavelength and directly proportional to the carrier concentration [11]. For energies close to the bandgap energy, the free carrier absorption can be defined as [12];

$$\alpha_{fc} = b_{fc}N_{fc} \tag{2.58}$$

where the N_{fc} is the free carrier concentration. The coefficient b_{fc} is a constant. For GaAs, b_{fc} is $3\text{x}10^{-18}/\text{cm}^2$ for electrons and $7\text{x}10^{-18}/\text{cm}^2$ for holes [9].

In the active layer, the propagating mode spreads outside the active layer and α_{fc} is reduced by the confinement factor Γ in the same manner as the active layer gain coefficient. $\Gamma\alpha_{fc}$ accounts for the free carrier losses in the active layer. In the adjacent AlGaAs layers, the losses are generally only free carrier losses, but they can also be band-to-band absorption losses if a low energy tail exists on the absorption spectrum of that material. Since the fraction $(1-\Gamma)$ of the propagating mode is within the AlGaAs layers, this contribution to the α is inserted in equation (2.57) as $(1-\Gamma)\alpha_{fc}$.

Free carrier absorption in the passive layers of heterojunction lasers can be reduced by reducing the doping level and it becomes insignificant at carrier concentrations of 10^{17} cm^{-3} or lower [13] in GaAs. Decreasing the doping level in the active layer may be of some benefit in reducing free carrier losses, but it is the concentration of injected carriers at lasing threshold that must be considered because the gain increases with injected carrier concentration proportionally more than does the loss.

The scattering losses in the heterojunction laser are due to irregularities in the

heterojunction surface. Epitaxial technology has developed to such a level where these imperfections can largely be minimised during layer growth. However, in poor samples, this loss has been reported as high as 12/cm [14].

The coupling losses, α_c can occur only whenever the optical field spreads beyond the wider energy gap confining layers. The coupling losses due to the leakage of radiation beyond the cladding layers are usually insignificant because the cladding layers are designed to be thick enough, typically $1\mu m$, to allow the optical field to decay.

For most practical purposes, the total losses in the heterojunction laser are dominated by the free carrier absorption losses. Thus equation (2.57) can be written as;

$$\alpha = \alpha_{fc} \tag{2.59}$$

2.4. Types of semiconductor lasers

2.4.1. Homojunction lasers

As mentioned before, the *p-n* junction provides the active medium and population inversion is achieved by forward biasing the *p-n* junction formed from heavily doped (degenerate) *p* and *n* type semiconductors. Heavy *p*-type doping with acceptor impurities causes a lowering of the Fermi level into the valence band. Similarly degenerative *n*-type doping causes the Fermi level to enter the conduction band. In thermal equilibrium, the Fermi energy has the same value throughout the material as shown in figure 2.8(a).

When the junction is forward biased with a voltage nearly equal to the bandgap voltage, electrons and holes are injected across the junction. At the high injection current, a region of inversion is created where the Fermi levels split into the two quasi-Fermi levels and they are separated by more than the bandgap energy (figure 2.8(b)). This inverted region is usually referred to as the active region. This region contains simultaneously electrons and holes as shown in figure 2.8(c). For

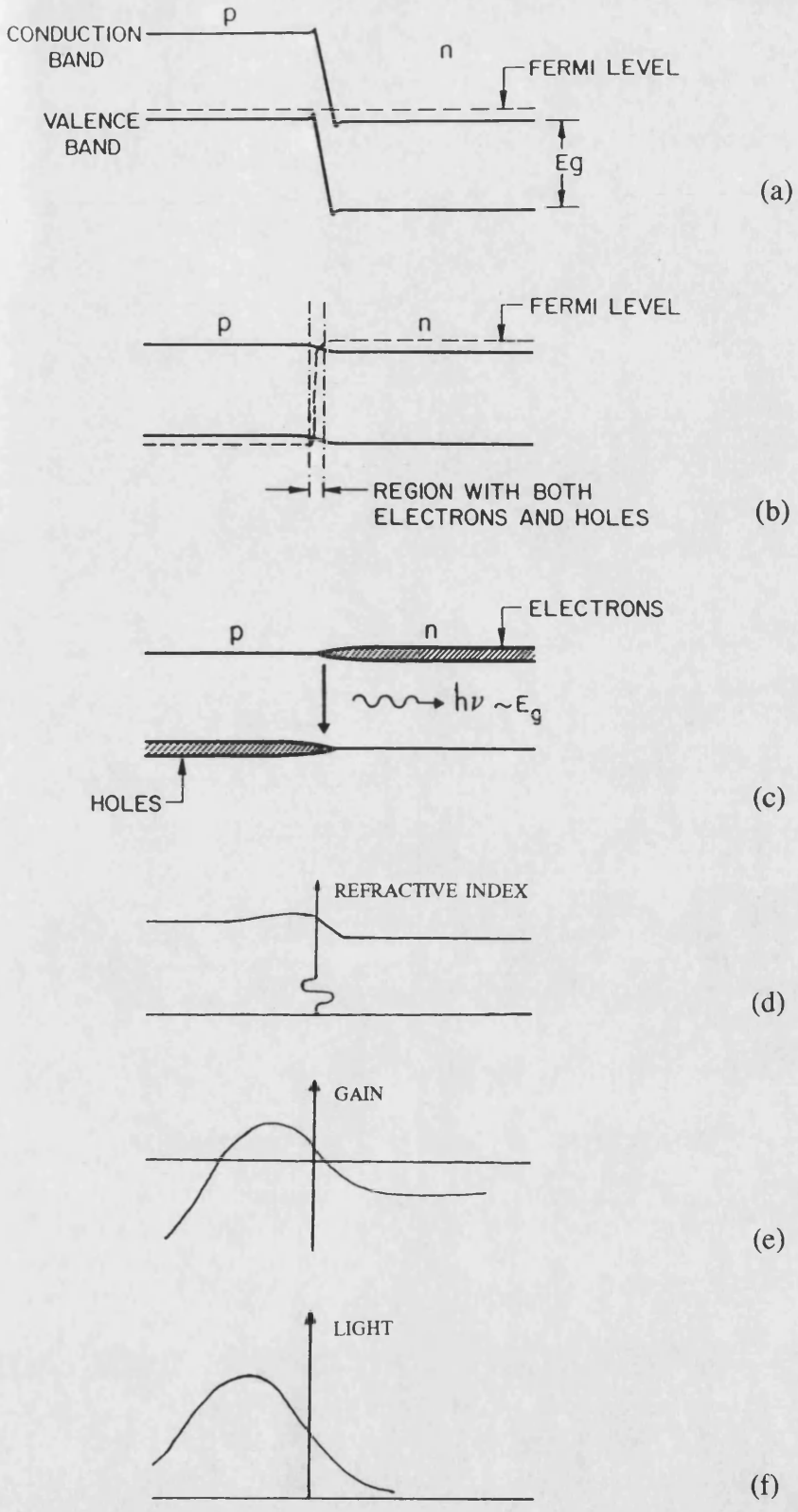

Figure 2.8. Energy band diagram of *p-n* junction at (a) zero bias (b) forward bias (c) schematic representation of the electron and hole densities under forward bias (d), (e) and (f) distribution perpendicular to the junction plane of the refractive index, gain and light intensity.

this region, the condition of equation (2.41) is satisfied for the radiation of frequency $\frac{E_g}{h} < \nu < \frac{(F_N - F_P)}{h}$. Any radiation of this frequency which is confined to the active region, will be amplified. Lasers which are made of single *p-n* junction, are known as homojunction laser. If, for example, the semiconductor is not degenerately doped and the quasi-Fermi levels are within the energy gap, then lasing cannot take place.

In homojunction lasers, however, the active region, where the gain is sufficiently high for lasing to take place is restricted to a narrow region near the junction, where the carriers are recombining. This perturbation in carrier density perturb the complex refractive index as shown in figure 2.8(d) and light generated can be guided by the resulting waveguiding effects (since refractive index of the active region is slightly higher than the surrounding area and this creates an internal built waveguide, see section 2.5). However, the guidance provided by this mechanism is very weak and the confinement of photons to the region of highest gain is very poor (figures 2.8(e) and (f)). Due to the poor confinement of the optical field, only the proportion of optical field confined to the active region will undergo amplification and the proportional of light not confined to the active region would be strongly attenuated. As a consequence, a very large current density would be required to achieve lasing action. Early homojunction laser required to be operated at liquid nitrogen temperature to maximise the gain.

2.4.2. Heterojunction lasers

The successful operation of the laser requires that both the carriers and the generated optical field should remain confined to the vicinity of the active region. This is achieved by fabricating double heterojunction (DH) lasers. Figures 2.9(a) and (b) shows the energy band diagram of a DH laser under thermal equilibrium and forward bias, where a thin layer of GaAs (lower energy gap and higher refractive index) is sandwich between relative thick layers of AlGaAs (higher bandgap and lower refractive index material). The thin GaAs layer acts as the active layer

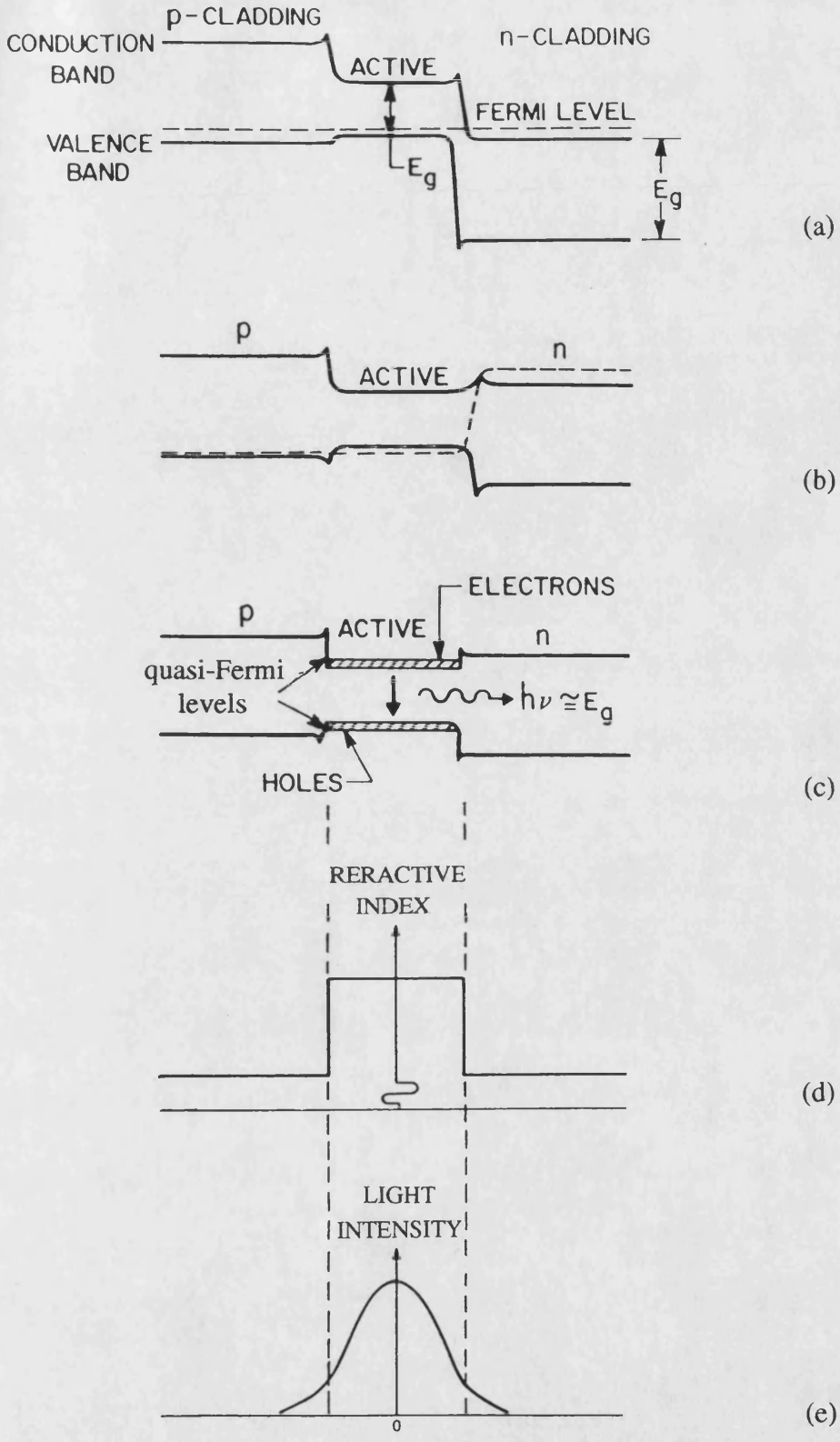

Figure 2.9. Energy band diagram of double-heterostructure laser at (a) zero bias (b) forward bias (c) area satisfying the condition $E_g<F_N-F_P$ under forward bias (d) and (e) the distribution of the refractive index and light intensity.

where electrons and holes move freely under forward bias (figure 2.9(b) and (c)). However, once there, they cannot cross over to the other side because of the potential barrier resulting from the bandgap difference. This region, as shown in figure 2.9(c), satisfies the condition of equation (2.41) for the radiation of frequency $\frac{E_g}{h} < \nu < \frac{(F_N - F_P)}{h}$ without the need for degenerative doping of either GaAs or GaAlAs.

In DH lasers, the optical confinement occurs by virtue of a fortunate coincidence. The lower bandgap active layer also has a higher refractive in comparison to the wider bandgap surrounding layers. The refractive index difference (figure 2.9(d)) creates an internally formed dielectric waveguide (dielectric waveguide will be discussed in section 2.5) which keeps the generated field in the vicinity of the gain region as shown in figure 2.9(e). Optical confinement deteriorates when the thickness of the active layer reduces below a certain value. The critical value can be made smaller by increasing the refractive index difference between active and passive confining layers. Typical critical value lie between 0.1 to 0.3μm, depending upon the refractive indices of active and passive layers.

The improved confinement of charge carriers results in a dramatic reduction in the required current density to achieve the threshold gain and this has made possible the operation of semiconductor lasers at room temperature in CW mode.

2.4.3. Stripe geometry DH lasers

The DH laser structure provides optical confinement in the transverse direction via the refractive index difference at the heterojunction interfaces, but lasing takes place across the whole width of the device. The field parallel to the device width is suppressed by making the sides rough, as shown in figure 2.10(a) for broad area DH laser, in order to reduce unwanted emission in these directions. Also, the broad emission area creates several problems including lasing from multiple non-uniform filaments in the relatively wide active area. In order to overcome this problem, usually a stripe geometry structure (as shown in figure 2.10(b)) of

such a width that only a single radiation filament can be excited is used. Such lasers, known as the stripe geometry lasers or stripe contact lasers have now become a dominant class of injection lasers. Generally, the stripe geometry is formed by creating high resistance areas on either side by techniques such as proton bombardment [15] or oxide isolation [16].

The restriction of the active region also provides the advantages such as;

* the reduction of the threshold current.

* the less exposure of the active region (only the area under the stripe) to surroundings, which slows down the process of gradual degradation of the laser and also it reduces the mirror facet heating effects, hence a less temperature sensitivity.

* an overall improvement in thermal properties.

The efficiency of the conversion of the electrical energy supplied from a source to the stripe laser is restricted by the three processes; (1) the spreading of electrical carriers in the lateral direction, (2) the lateral diffusion of minority carriers in the active layer after they pass through the *p-n* junction but prior to their recombination within the active region, and (3) the spreading of optical field in the lateral direction.

The spreading of current is shown schematically in figure 2.11. Because of the spreading of electrical carrier, the applied current also flows through an area close to the stripe region. The total current, J_s flowing from the stripe contact is divide into the two parts i.e. the current J_t flow into the active region just beneath the stripe and the currents J_o which flow into the region close to the stripe on both sides. Therefore [5];

$$J_s = J_t + 2J_o \tag{2.60}$$

where J_s, J_t and J_o are the stripe geometry laser's, total and the leakage current densities. J_o can be given as [9,17];

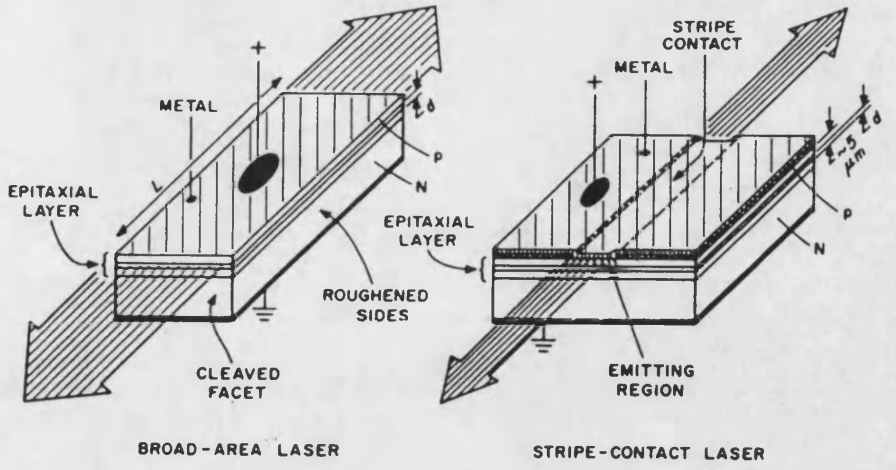

(a) (b)

Figure 2.10. DH semiconductor laser geometry (a) broad area contact laser and (b) stripe contact laser [4].

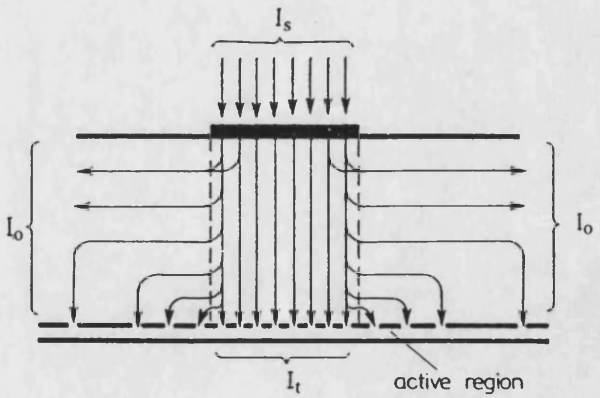

Figure 2.11. The phenomenon of current spreading in stripe geometry lasers. [12].

$$J_o = \left(\frac{2J_t}{\beta_v R_x W^2} \right)^{\frac{1}{2}} \tag{2.61}$$

where W is the width of the stripe. R_x is the composite sheet resistance. β_v is the exponential junction parameter. R_x is given by;

$$\frac{1}{R_x} = \frac{1}{\Sigma(d_i/\rho_i)} \tag{2.62}$$

here d_i and ρ_i are the thickness and the electrical resistivity of layers between the contact layer and the active layer. β_v is defined as [17];

$$\beta_v = \frac{e}{n_s kT} \tag{2.63}$$

where e is the electronic charge, n_s is a constant, k is the Boltzmann constant and T is the temperature. The value of constant n_s for GaAs/AlGaAs *p-n* junction is usually 2 [18].

In the stripe geometry laser, the total pumping current at threshold, I_{sth} and injected current density are related via equation as [17];

$$J_{sth} = \frac{I_{sth}}{WL} \tag{2.64}$$

In practice the distinction between the current spreading and the lateral diffusion of minority carriers becomes somewhat blurred in the process which take place in the active layer. Thus these two phenomenon should be consider together. However, in stripe geometry lasers, the lateral current spreading is the main contribution to the increase in the threshold current density [17]. For such lasers, it is reasonable to assume that lasing starts once the current density under the stripe, J_t reaches a value equal to the threshold current density for broad area DH lasers fabricated from the same material. Therefore equation (2.60) can be re-written as [17];

$$J_{sth} = J_{bth} + 2J_{oth} \tag{2.65}$$

where J_{bth} is the threshold current density of a broad area laser made from the same material as the stripe contact laser having threshold current density of J_{sth} and can be calculated from equation (2.55).

By combining equations (2.55) and (2.64), one can get;

$$I_{sth} = \left\{ \frac{1}{\eta_{int}} \left(\frac{g_{th}}{\beta} + J_{(nom)_o} \right) \right\} d_3 WL \tag{2.66}$$

This equation shows that I_{sth} increases with the length and the width of a device and, theoretically speaking, the lowest threshold current can be achieved with very small and narrow active layer. In practice, the current density will be very high, which could damage the device.

The degree of the current spreading depends upon the value of R_x and the stripe width. The effect of R_x and the stripe width on electrical carriers spreading is shown graphically in figure 2.12.

The restriction of the active region in stripe geometry lasers also produces a shallow maximum in the refractive index of the region under stripe, which forms a dielectric waveguide confining the optical field to a region below the stripe. The gain under the stripe varies continuously peaking at the center and falling away to a region of loss at edges. Therefore, in addition to the effects of the current spreading and the lateral diffusion in the active layer, J_{sth} can also be influenced by optical mode loss. This loss is due to optical radiation absorption losses in both active region and the surrounding $Al_xGa_{1-x}As$ layers and diffraction losses due to the optical field spreading outside the active region, both transverse and along the junction plane (optical radiation losses in the transverse direction are accounted in equation (2.47) by inserting the parameter Γ). Tsang [17] considered the effect of the lateral spreading processes on J_{sth} and he found that the influence of optical mode loss in the lateral direction is not as important as the current spreading and the lateral carrier diffusion in typical buried heterostructure stripe geometry lasers. The influence of optical mode loss on J_{sth} is shown in figure 2.13. It can be seen from figure 2.13 that the influence of optical mode loss (which includes optical

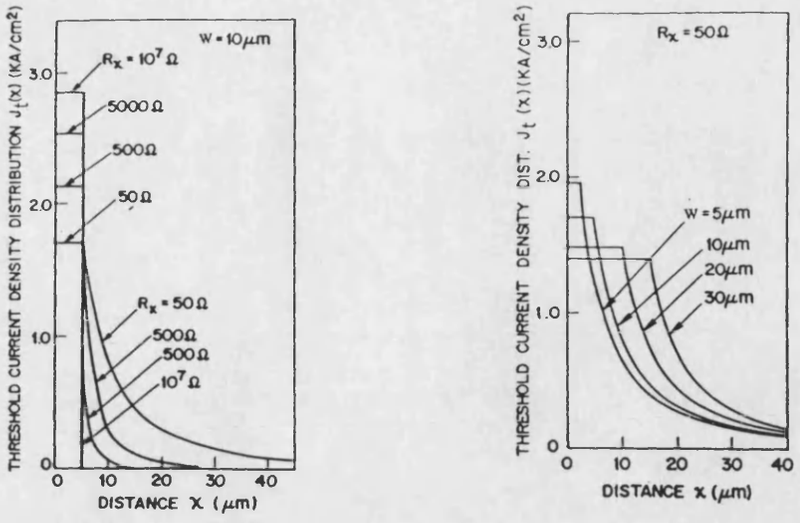

(a) (b)

Figure 2.12. The effect of (a) R_x and (b) the stripe width, W on carrier spreading [17].

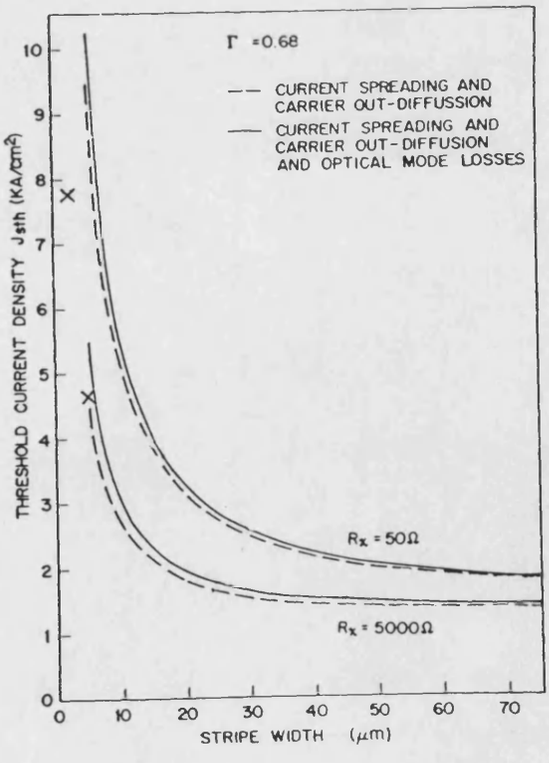

Figure 2.13. The effect of the stripe width on threshold current density J_{sth} [17].

radiation losses due to optical mode spreading in the lateral and transverse directions and due to the absorption of optical radiation, α) on J_{sth} is small as compare to other two phenomenon. If one takes account of optical mode loss due to the spreading of optical radiation in the transverse direction and α, then the influence of optical mode loss is expected to be significantly lower than that is shown in figure. However, in the rib waveguide structure (which is used during the work reported in this thesis and will be discussed in section 2.5.2), due to a small index step, the optical field is weakly guided in the lateral direction, and therefore the optical mode loss in the lateral direction is expected to have more influence on J_{sth} than for other laser geometries which have strong waveguiding (such as buried heterostructure laser) effects in the lateral direction. Furthermore, if the stripe gets narrower, the confinement of the optical field becomes poorer in the lateral direction. The value of Γ in equation (2.47) reduces and hence the required value of g_{th} increases. This actually results in a higher value of J_{sth} and hence higher I_{sth} for the rib waveguide laser since J_{sth} is determined by waveguide parameters Γ and β. The effect of optical mode loss in the lateral direction on J_{sth} will be discussed later in the experimental part of this chapter in more detail.

In both directions (parallel and perpendicular to the junction plane), waveguiding is the main phenomena which is responsible for wave propagation in the active layer of a stripe geometry laser and will be discussed in the next section.

2.5. Optical waveguides

A dielectric waveguide is a fundamental element that interconnects various components in integrated optical circuits. A waveguide may confine radiation in one or two directions, depending on the guiding structure. The simplest type of dielectric optical waveguide is the planar or slab waveguide which confines the optical radiation in only one direction. The study of the slab waveguide and its

properties is useful in gaining an understanding of the waveguiding mechanism in more complicated waveguides, such as rib waveguide (section 2.5.2). Thus, the slab waveguide is discussed below.

2.5.1. Slab waveguide

The structure of the slab waveguide is shown in figure 2.14. It is characterised by parallel planar boundaries in the y-direction and infinite in the lateral x-direction. Due to the infinite lateral dimensions, it can confine radiation in one direction. The physical mechanism behind the confinement is due to total internal reflection which occurs if the angle of incidence of a ray, θ_d, is greater than the critical angle, θ_c, which is given by;

$$\theta_c = \sin^{-1}\left(\frac{n_2}{n_1}\right) \tag{2.67}$$

A similar relation can be written for the layer 2 and layer 3 interface. Therefore, a fundamental requirement of the waveguide structure is that the refractive index of the guiding dielectric medium must be slightly higher than the surrounding medium in order to keep the propagating waves within guiding layers, i.e.

$$n_1 > n_3 \geq n_2 \tag{2.68}$$

The slab waveguide can be analysed by a rigourous EM field theory approach using Maxwell's equation as well as the conceptionally simpler ray optics approach. Both analyses are consistent and have been developed in several texts [19,20] and will not be considered in detail here. Both methods show that a slab waveguide can support a discrete number of modes confined within the guiding layer, plus a continuum of radiation modes.

According to EM-wave analysis (using Maxwell's equations), the guide can support a mode only when (see for example reference-21);

$$k_0 n_2, k_0 n_3 < \beta_z < k_0 n_1 \tag{2.69}$$

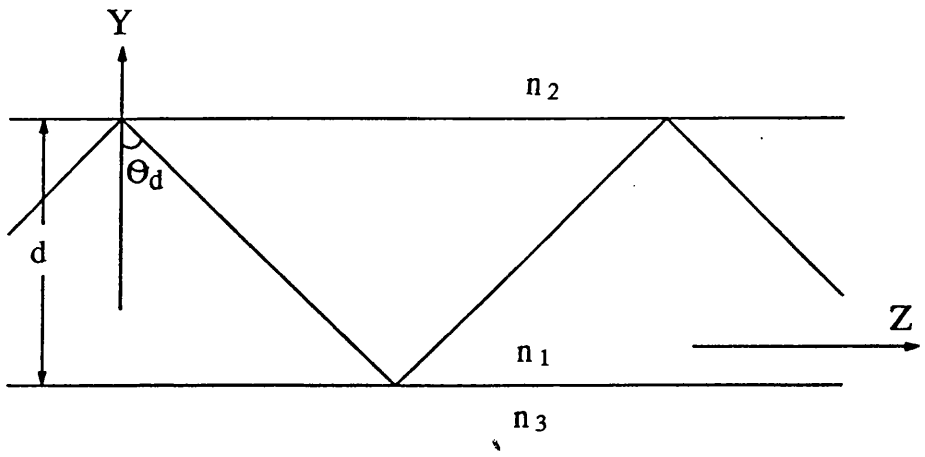

Figure 2.14. Zigzag wave propagation picture for the guided mode in the slab waveguide.

where the free space vector, $k_0 = \frac{2\pi}{\lambda_0}$ and β_z is the propagation constant in the z-direction.

The ray-optics analysis gives the relation for guided modes in the z-direction at a discrete angle, θ_d;

$$\beta_z = k_0 n_1 \sin\theta_d = \frac{\omega}{v_p} \tag{2.70}$$

where ω is the angular frequency and v_p is the phase velocity of the guided modes.

From equations (2.67) and (2.70), β_z is bounded by the propagation constant of the lower refractive index cladding layer and the guiding layer in such a way that;

$k_0 n_2, k_0 n_3 < \beta_z < k_0 n_1$

.

This condition is similar to equation (2.69).

The relationship between ω and β_z is shown in the sketch of the ω-β_z diagram [21] in figure 2.15 for the asymmetric slab waveguide. This figure explains some of the guiding characteristics of the slab waveguide. Only three guided modes are shown. This figure shows that an asymmetric guide cannot always support a guided mode. At the cut-off frequency, the propagation constant assumes the value of the lower bound $n_1 k_o$ and as ω increases, β_z approaches its upper bound $n_3 k_o$. As a result, more and more guided modes appear. Also in figure 2.15, the continuum spectrum of radiation modes (modes which do not satisfy equation (2.67) and lost in the substrate material or in waveguide surroundings) is shown.

In order to make the discussion simpler and to have more precise ω-β_z diagram, it is worthwhile to introduce normalization that combine the various guide parameters. Accordingly, the normalized guiding layer thickness V (oftenly called the V-number) is defined as;

$$V = k_0 d \sqrt{n_1^2 - n_3^2} \tag{2.71}$$

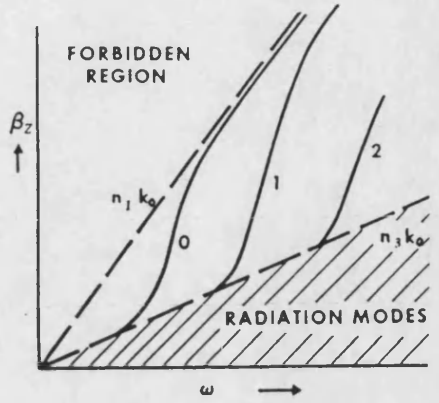

Figure 2.15. Simple $\omega - \beta$ diagram of a waveguide [21].

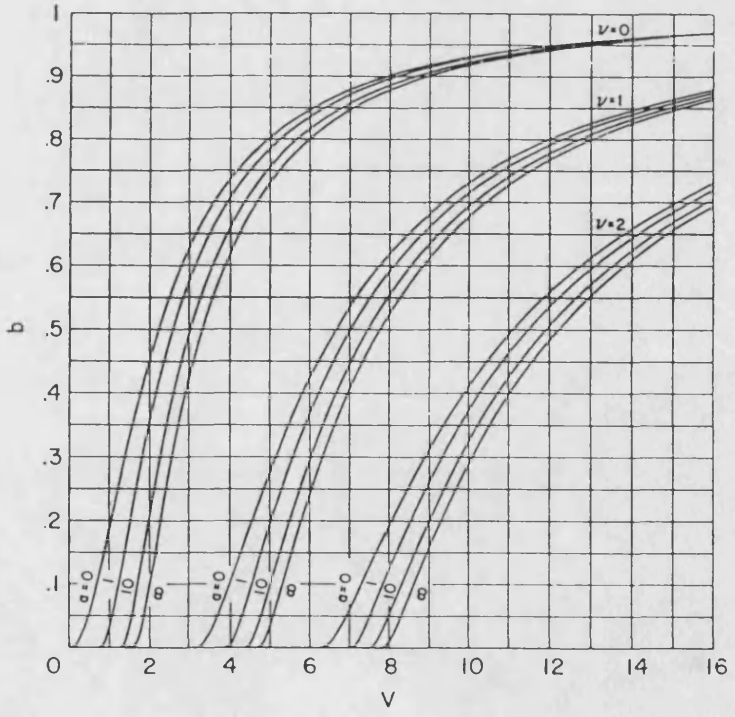

Figure 2.16. Normalised $\omega - \beta$ diagram as a function of asymmetric factor [22].

It is often convenient to use an effective index term by considering the slab waveguide as hypothetically homogeneous guiding structure and is defined as;

$$N_{eff} = \frac{\beta}{k_o} = n_1 \sin\theta_d \tag{2.72}$$

This is bounded by;

$$n_2, n_3 < N_{eff} < n_1 \tag{2.73}$$

Also a normalized guide index, b, can be defined as;

$$b = \frac{N_{eff}^2 - n_3^2}{n_1^2 - n_3^2} \tag{2.74}$$

For small index differences, N_{eff} can be given as;

$$N_{eff} = n_3 + b(n_1 + n_3) \tag{2.75}$$

Finally, an asymmetric factor (measure of asymmetry of the planar waveguide) for TE and TM modes can be defined as;

$$a_{TE} = \frac{n_3^2 - n_2^2}{n_1^2 - n_3^2} \tag{2.76}$$

$$a_{TM} = \frac{n_1^4(n_3^2 - n_2^2)}{n_2^4(n_1^2 - n_3^2)} \tag{2.77}$$

For symmetric guides, $n_2 = n_3$, a=0 and for asymmetric guides, $n_2 < n_3$, a>0.

The normalized $\omega - \beta_z$ diagram, which is achieved by using normalized parameters [22] is shown in figure 2.16 for four different values of asymmetric factor. This figure explains the similar propagation characteristics of a waveguide as explained by figure 2.15, but it also shows that a symmetrical waveguide can always support a propagating mode. This is generally the case for double heterostructure lasers, because the active layer is usually sandwiched between surrounded layers of the same material of higher energy gap and lower refractive index. In this case, a fundamental mode can always propagate, even in very thin layers, but the

confinement factor then decreases (see equations (2.45) and (2.46)). The number of guided modes which a guide can support is given by;

$$m = \frac{2 \times d(n_1^2 - n_3^2)}{\lambda} \tag{2.78}$$

Figure 2.16 along with equations (2.71) through (2.77) can directly be used to obtain the value of effective index of a waveguide.

2.5.2. Rib waveguide

The structure of the rib waveguide is shown in figure 2.17. This type of optical waveguide gives optical confinement in two directions, in contrast with the planar optical waveguide in which confinement occurs only in one direction. The modes which are supported by the rib geometry are not purely of the TE or TM type. However, they can be predominantly of these two types. For this reason, Marcatilli [23] refers to them as E_{pq}^{y} (with E_y and H_x components) and E_{pq}^{x} (with E_x and H_y components). Where p and q are the field extrema in x and y directions respectively.

For the case of the 2-D waveguide (such as the rib waveguide), no analytical method of solution exists. Accurate results can be obtained by using numerical methods such as the vector-H finite element method [24] and scalar variational method (SVM) [25,26], but this has a high computational overhead. For this reason several approximate analytical techniques, including effective index method (EIM) [27], the weighted index method (WIM) [28], the spectral index method (SIM) [29] and the equivalent index method [30] have been used. Among all analytical techniques, the EIM is a widely adopted analytical technique to determine propagation constant and the field distribution of a waveguide. This method has been used for passive optical rib waveguide [31] and also used by Buus [32] for laser cavity modes. The EIM makes it possible to replace the actual structure by a hypothetical homogeneous structure in the lateral and transverse directions. Instead of solving the two dimensional waveguide structure, the problem is split into two 1-D parts

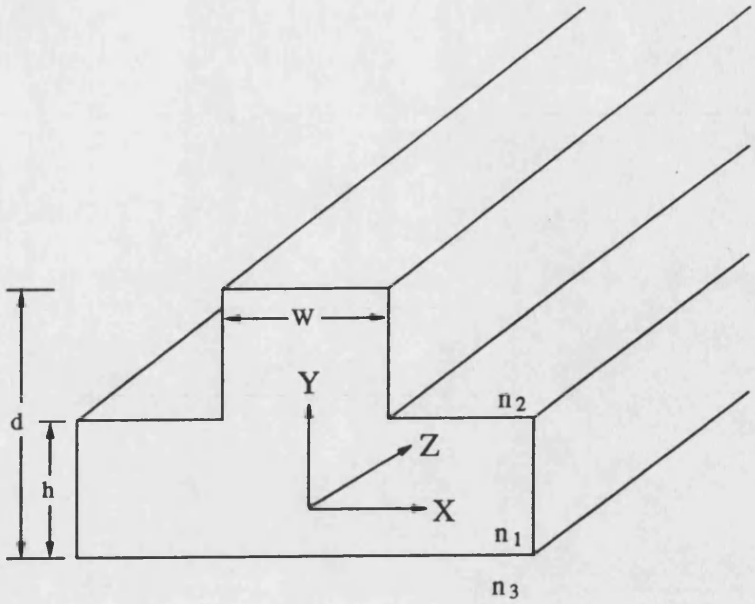

Figure 2.17. 2-D rib waveguide structure.

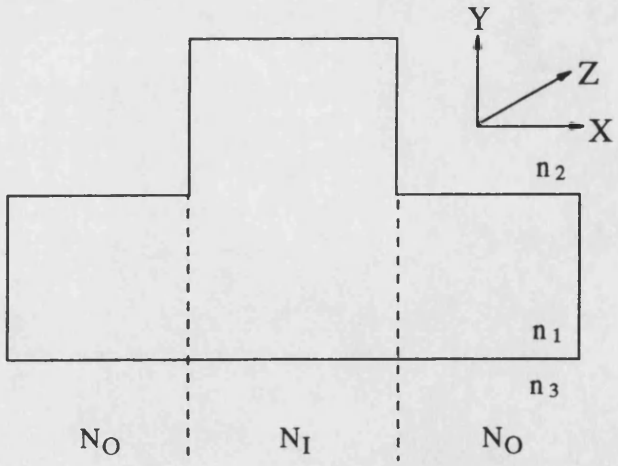

Figure 2.18. The application of effective index method to rib waveguide structure.

and the 1-D solution of the slab waveguide of last section can be applied.

For the waveguide structure under consideration, waveguide side walls appear as a step discontinuities, either in dielectric constant or in thickness. By applying the transverse resonance method [33] in the x-direction, the rib waveguide structure can be seen as inside and outside portions of a uniform dielectric structure [34], as shown in the figure 2.18. The inside region consists of the central rib of the effective refractive index, N_I, where guided modes can be supported. The two outside regions are identical and have the effective refractive index N_o. Each of the region (inside or outside) can be viewed as three layers planar waveguide.

The normalized thickness in terms of V-number in inside and outside regions in lateral direction are given by;

$$V_1 = k_0 d\sqrt{n_1^2 - n_3^2} \tag{2.79}$$

$$V_o = k_0 h\sqrt{n_1^2 - n_3^2} \tag{2.80}$$

and normalized width, V_w is also given in the same fashion as;

$$V_w = k_0 w\sqrt{N_I^2 - N_O^2} \tag{2.81}$$

where N_I and N_O are the effective indices which are given by

$$N_I^2 = n_3^2 + b_I(n_1^2 - n_3^2) \tag{2.82}$$

$$N_O^2 = n_3^2 + b_O(n_1^2 - n_3^2) \tag{2.83}$$

where b_I and b_O are the normalized guide indices and can be obtain from figure 2.16 if V-number is known.

In practical applications, single mode operation in the lateral direction is desirable and the maximum width for single mode operation for rib-guide structure is defined as [35];

$$W_{\max} = \frac{\lambda}{n_1\sqrt{2\Delta N_{eff}}} \tag{2.84}$$

where ΔN_{eff} is the refractive indices difference between N_I and N_O.

The accuracy of the effective index method and its agreement with the more accurate numerical solution becomes worse as the thickness of the outside region decreases (i.e. the rib becomes deeper) and it breaks down completely when the thickness of the slab adjacent to the rib is very close to or below the cut-off value (typically $0.5\mu m$ of GaAs) as shown in figure 2.19 where the results of the EIM are compared with more accurate numerical methods such as the scalar variational method (SVM) and the finite element method (FEM). It is clear from figure 2.19 that when the rib height is small, then the guide can be well approximated as a slab waveguide. The EIM breaks down when the rib height is larger than $0.5\mu m$ in GaAs based material because over this range, the slab adjacent to the rib waveguide is below cut-off. The top horizontal line represents the slab solution when the rib height is zero. The lower horizontal line shows the solution when slab height adjacent to the rib is zero. At this limiting stage, the solution of SVM is also limited in its application and accuracy. On the other hand, FEM gives accurate solution at all the values of slab thickness.

2.6. Experimental measurements

The purpose of this section is to measure the basic characteristics of a semiconductor laser such as the external or differential quantum efficiency η_D, the internal quantum efficiency η_{in}, optical radiation losses α and the facet reflectance of A.R. coated device. These parameters will be needed later in this thesis to evaluate the performance of active waveguide components.

For many applications in optical system and OIC, it is desirable to suppress the internal feedback. This is usually achieved by maximizing the end mirror losses by applying anti-reflection (A.R) coating. It is common practice to analyse the effectiveness of A.R. coating by looking at the laser output characteristics. In section 2.6.6 the output characteristics of the A.R. coated device are compared

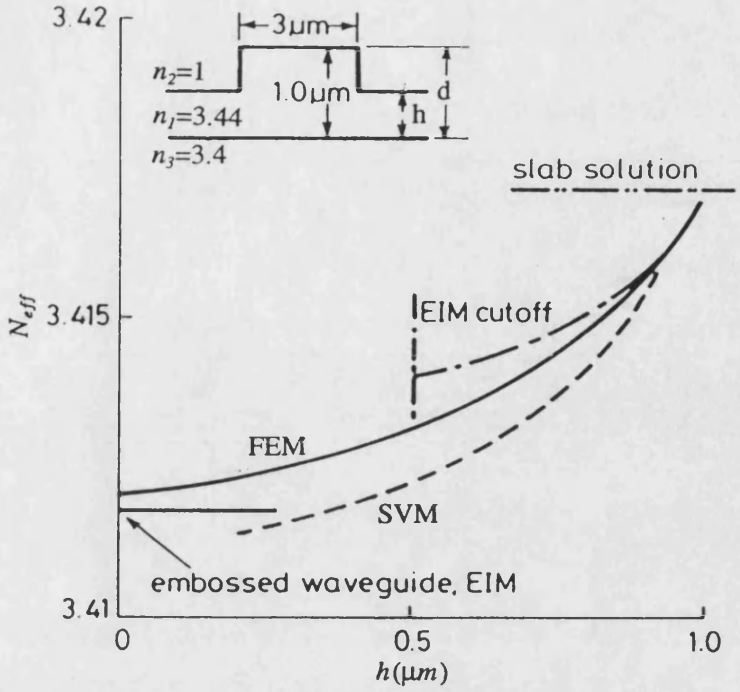

Figure 2.19. The comparison of the effective index method with more accurate numerical methods [24].

with the output characteristics of the same device prior to coating.

Before proceeding with the experimental measurements, it is worthwhile to consider errors associated with experimentally measured values.

2.6.1. Error analysis

All measurements, however careful and scientific, are subjected to some uncertainties or errors. Error analysis is the study and evaluation of these uncertainties or errors. Its two main functions are to allow an estimation of how large the errors are and to help to reduce them whenever necessary.

2.6.1.1. Sources of error in optical measurements

Generally, the radiation detection circuit consists of a photodiode which is followed by an amplification circuit and measuring instruments. There is unlikely to be in a situation where there is a single source of error and it is necessary to consider all the sources of error in an optical radiation detection measurement. These include;

1. *Instrumental errors:-*

   These errors are caused by imperfections in the construction and design or miscalibration of a the measuring instrument. The instruments used during the experimental work were pre-calibrated and have the error figure within manufacturer's specified error limits (typically 1-2%).

2. *Noise:-*

   Noise may be defined broadly as any signal that does not convey useful informations and may be classified in a number of ways. There are noise components which are clearly thermal in nature (called thermal noise) and those that arise from statical fluctuations in the flow of discrete carriers (called shot noise). The contributing sources of noise in active waveguide components are discussed in more detail in sections 4.6, 5.2.3.4 and 5.3.2.5.

3. *Response time:-*

The time of response of a measuring system to an input signal may also contribute to the uncertainty of measurement. However, during experimental measurements, this limitation was avoided by using pulses longer than the system response time and by sampling the output at the end of the pulse.

4. *Transmission:-*

In the transmission of information from sensing element to indicator, any (or all) of these types of errors may arise: (a). the signal may be attenuated by being absorbed or otherwise consumed in the communication channel (specially in a system with longer signal path), (b). it may be distorted by attenuation, resonance or delay phenomena and (c). it may suffer loss through the leakage of the signal current. In any of these circumstances, the signal reaching the indicator will differ in some respect from that at the primary sensing element. However, this problem can be avoided to some extent by careful design of an experiment, by shortening the signal path and by properly screening connecting wires (this approach was adopted throughout this thesis).

5. *Misalignment errors:-*

When the input light from the source laser is coupled to the AWOD or AWOA, a misalignment between the two components can cause a significant amount of error. During the work reported in this thesis, a novel alignment technique (as described in chapter-4) was used to align the two active components, therefore, misalignment between two active devices is expected to be relatively small.

6. *Back-reflection errors:-*

The multiple feedback between the two butt-coupled active components can cause a large amount of uncertainty in the output characteristic of an active

waveguide device. In fact, multiple feedback was found to be responsible for a measured 50% increase in the responsivity of the FP AWOD (chapter-4) and was a main reason for self-sustained pulsations (chapter-6).

7. *Errors due to optical flux leakage:-*

This source of error may be one of the important sources of error in OIC devices. During the experimental work, the effect of this source of error was eliminated by taking into account the leakage of optical flux while measuring the response of the AWOD or AWOA (see chapters 4 and 5).

8. *Ambient temperature influence on the measuring system:-*

Of the various ambient conditions that may alter the response of a device, temperature changes play an important part in the absolute values of the measurements. The influence of the change of temperature on the measuring instrument was minimised by performing nearly all measurements in a temperature controlled environment.

9. *Errors of observation and interpretation:-*

Errors in the observation, interpreting and recording of data must also be considered among the sources of uncertainty in measurements. These include parallax errors and personal bias of observer and can be reduced by making several observations of the same measurement.

2.6.1.2. Types of error

Errors can be divided into two classes.

a) systematic errors

b) random errors

An error, which in the course of a number of measurements made under the same conditions of the same value of a given quantity, and which either remains constant in absolute value and sign or varies according to a definite law when the

conditions change, is called a systematic error.

Sometimes, it is found that repeated readings under the same operating conditions are not identical, and these types of error are referred to as random errors. Random errors are caused by spontaneous fluctuation in certain physical quantities.

The limit to the sensitivity and accuracy of any measurement is usually set by fundamental physical fluctuations in the quantity itself which is being measured. Sometimes these fundamental fluctuations (which give rise to random error) can be directly displayed as noise in the measurements. In other cases, a lower semi-fundamental limit to the sensitivity of the measurement is set by systematic errors because of the non-ideal nature of the material, and these errors are hard to detect.

The distinction between random and systematic errors is not always clear-cut. For example, noise is inherently random in nature, but if the response of the indicating system is always in the same direction independent of the signal polarity, then, for a weak signal, the noise present may produce a positive indication that is larger on the average than would be produced in the absence of noise, by the signal being measured. Thus, for some systems, noise may give rise to a spurious signal that is always added to the measured value and its effect is systematic. Table 2.1 shows the breakdown of the sources of errors in a optical radiation detection set-up.

Table 2.1. *Breakdown of sources of errors.*

Source of error	**Type of error**	
	Random	*Systematic*
Instrumental errors	Seldom	Almost always
Noise	Generally	May be
Response time	Seldom	Almost always
Transmission	Sometimes	Usually
Misalignment errors	Seldom	Usually
Back-reflection errors	May be	Usually
Errors due to optical flux leakage	May be	Usually
Ambient influence on measuring system	Usually	May be
Errors of observation and interpretation	Usually	Sometimes

2.6.1.3. Characterisation of errors

In any experiment, there is never assurance that all systematic errors have been eliminated from a measurement or that proper correction has been made for those errors which are present. Therefore, during the work reported in this thesis, all the possible dominant sources of systematic error mentioned above (in section 2.6.1.1) were considered carefully and systematic errors were reduced to their lowest possible values. It is, however, always possible that significant systematic errors may remain unsuspected. On the other hand, random errors can be calculated and reduced reliably in statistical terms.

There are several statistical methods which are used to characterise the errors (depending upon the type of measurements), and expected to take account of small systematic errors. Normally, experiments involve the measurement of several values of two or more different physical variables in order to investigate the relationship between them. Probably the most important experiments of this type are those where the expected relation is linear and this is the case we are interested in here. We consider any two physical variables , x and y connected by a linear relation of the form;

$$y = A + Bx \tag{2.85}$$

where A and B are constants.

If the two variables x and y are linearly related as in equation (2.85), then a graph of y versus x should be a straight line which has a slope B and intersects the y-axis at $y=A$. But in practice, there are uncertainties and the most we can expect is that the distance of each point from the line will be reasonable compared to the uncertainties. If one has to measure N different values $x_1,.....,x_N$ and the corresponding values $y_1,.....,y_N$ and the measured values are subjected to uncertainties, then the interesting problem is to find the straight line which best fits the measurements. This problem can be treated analytically by means of the principle of maximum likelihood. This analytical method of finding the best straight line to fit a series of data points is called linear regression or the least-squares fit for a line.

2.6.1.4. Calculation of uncertainties

Let us consider the question of finding the best straight line $y = A + Bx$ to fit a set of measured points $(x_1,y_1),....,(x_N,y_N)$. In order to make the discussion simple and to the point, we assume that, although measurements of x suffer some uncertainty, the uncertainty in x is insignificant as compare to the uncertainty in the measurements of y. This is often a reasonable assumption, since the uncertainties in one variable are much smaller than those in the other, which can therefore safely be ignored [35]. We further assume that the measurements of all the values of y have uncertainties of same magnitude and the measurement of each y is governed by the same width parameter σ_y. This assumption is also a reasonable assumption in many experiments since the errors introduced by measuring instruments and human errors are expected to dominate the uncertainties. If A and B are known, the true value of y_i can be obtained by equation (2.85). The measurement of y_i is governed by a normal distribution centred on true value, with width parameter σ_y. The probability of obtaining the observed value y_i is;

$$P_{A,B}(y_i) \propto \frac{1}{\sigma_y} \exp\left[\frac{-(y_i - A - Bx_i)^2}{2\sigma_y^2}\right] \tag{2.86}$$

The probability of obtaining complete set of measurements $y_1,.....,y_N$ is the product;

$$P_{A,B}(y_1, ..., y_N) = P_{A,B}(y_1), ..., P_{A,B}(y_N) \tag{2.87}$$

The expression $(y_i - A - Bx_i)$ is the deviation of the measured value from its true value.

The measurement of each y_i is (as we are assuming) normally distributed about its true value $A+Bx_i$, with width parameter σ_y. Thus deviations $(y_i - A - Bx_i)$ are normally distributed, all with the same central value 0 and the same width σ_y. A good estimate for σ_y would be given by the square root of the average of the sum of the squares of the deviations of individual measurements, i.e. [35];

$$\sigma_y = \sqrt{\frac{1}{N}\sum_{i=1}^{N}(y_i - A - Bx_i)^2} \tag{2.88}$$

where A and B are given by;

$$A = \frac{(\Sigma x_i^2)(\Sigma y_i) - (\Sigma x_i)(\Sigma x_i y_i)}{N(\Sigma x_i^2) - (\Sigma x_i)^2} \tag{2.89}$$

and

$$B = \frac{N(\Sigma x_i y_i) - (\Sigma x_i)(\Sigma y_i)}{N(\Sigma x_i^2) - (\Sigma x_i)^2} \tag{2.90}$$

If we consider measuring just two pairs of data points (x_1,y_1) and (x_2,y_2), we can always find a line that passes exactly through both points and least square fit will give this line. That is, with just two pairs of data, we cannot possibly deduce anything about the reliability of measurements. Considering this reality in mind, equation (2.88) is corrected as [35];

$$\sigma_y = \sqrt{\frac{1}{N-2}\sum_{i=1}^{N}(y_i - A - Bx_i)^2} \tag{2.91}$$

Since systematic errors were reduced to their lowest possible value, total errors in the measurements are expected to be dominated by random errors and equation (2.91) can provide a reasonable estimate of error. Therefore, equation (2.91) will be used throughout the thesis to estimate the errors.

2.6.2. I-L Characteristic

There are two ways of measuring the optical output from a laser diode. One is the use of a lens system to focus the light from the LD to a small area optical detector. The main disadvantage is the possibility of a reduction in the measured light output due to the wide angle of radiation of the LD and this generally requires a lens of large numerical aperture and relatively short working distance. However, this method offers a fast response time due to the very high bandwidth of the small area detector. The other approach, probably the most commonly used method for measuring I-L characteristics is to place a calibrated large area detector (LAD) or optical power meter close to the laser diode facet to ensure large collection of output power. But the large area detector has slow response time due to the

large capacitance of the diode.

Here, the I-L characteristic of devices UB262 (a 2.5μm wide stripe laser) and UB238 (a 5μm wide stripe laser) were measured using the latter approach under pulsed current conditions using 200nS pulses to avoid excess heating. Figure 2.20 shows the I-L characteristics of laser diodes UB262 and UB238 at room temperature of 20°C. The external quantum efficiency of UB262 and UB238 can be measured from figure 2.20 by rewriting equation (2.53) as;

$$\eta_D = 2\frac{\Delta P}{\Delta I} \tag{2.92}$$

The factor 2 in equation (2.92) comes from the fact that the half of the light emitted by the laser is collected by the detector and for typical semiconductor laser with R_1=R_2, the value of the optical output from both facets is expected to be the same. The slope of each curve of figure 2.20 in lasing region gives the external quantum efficiency, η_D for UB262 and UB238 as 26% and 41% respectively. Kawaguchi *et al* [36] measured η_D as 33% and 38% for 4μm and 9μm wide stripe ridge waveguide lasers. Amann [37] has reported similar sort of value for ridge waveguide laser. The measured value of η_D of 41% for UB238 is better than the reported value in references-36 and 37. The measured value of η_D=26% for UB262 is justified because as the stripe gets narrower, η_D reduces due to the spreading of optical and electrical carriers in the lateral direction. The effect of carrier spreading and optical mode loss in the lateral direction are discussed in section 2.6.4.

2.6.3. Loss measurement in laser diode

There are several techniques [14,38,39] to measure the losses in a laser cavity which range from the simple cut-back technique [13] to the Fabry-Perot resonance measurement technique [38]. The former technique has been adopted here to measure the losses inside a laser cavity because of its simplicity. In this technique the output power from one facet of a laser diode is measured as a function of the

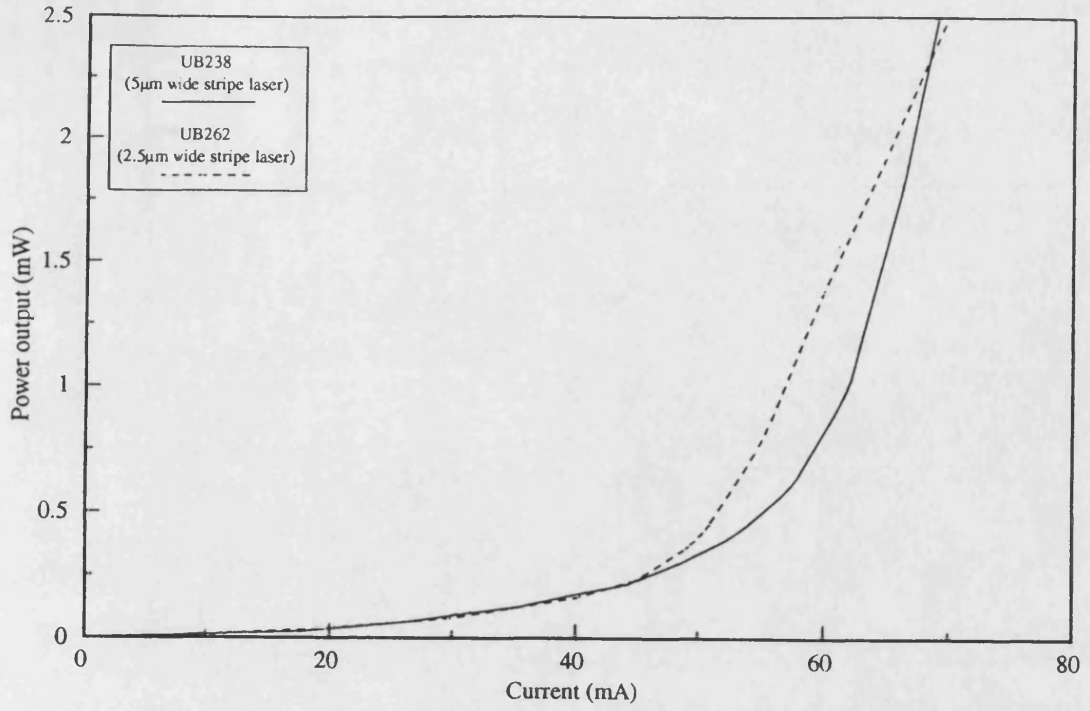

Figure 2.20. The measured I-L characteristics of UB238 (a 5μ*m* wide stripe laser) and UB262 (2.5μ*m* wide stripe laser).

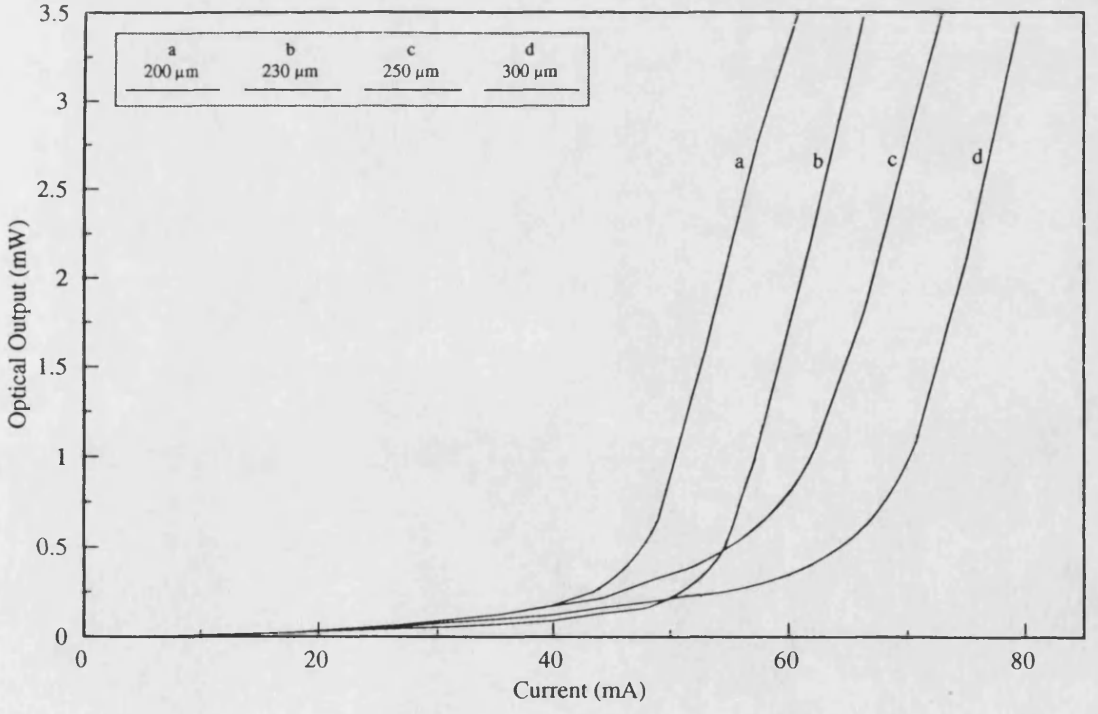

Figure 2.21. I-L characteristics as a function of length for 5μ*m* wide stripe devices.

device length. For this purpose, the I-L characteristics of four laser devices, with the same stripe width of 5μm but of different lengths of 200μm, 230μm, 250μm and 300μm were measured at 20°C. The results of these measurements are shown in figure 2.21. The differential quantum efficiencies for all devices were calculated from figure 2.21 using equation (2.92) and the reciprocal of η_D is plotted against the cavity length in figure 2.22 (where a 'best fit' line is drawn by using linear regression or least square fit technique). The intercept of the curve at L=0 yields the value of the internal quantum efficiency, η_{in}. Using equation (2.52), η_{in} is calculated as 64.5±0.4% (the expected error figure of ±0.4% is obtained by equation (2.91)) which is same for all devices with same stripe width at 20°C. This value is close to the reported value of 65% for the stripe geometry laser [40].

Again, by using equation (2.52) , total losses inside the laser cavity with L>0 can be estimated. Using typical values of L=250μm, η_D=41%, R_1=R_2=30% and η_{in}=64.5%, the losses inside the 5μm wide stripe laser are estimated around 27.6±0.5/cm. This value is slightly higher than the typical reported value of 25/cm in heterostructure lasers [12]. Because the devices investigated here were highly temperature sensitive and the temperature of the active layer is always several degree higher than the heatsink temperature (see chapter-3), causing higher free carrier losses, this slight increase in loss is to be expected. The spreading of carriers and the optical field in the lateral direction is not expected to have much influence on α because it is a length dependent property of the material used (this can be justified by looking at the results of chapter-3 where loss figure for 2.5μm wide stripe lasers is nearly the same as for 5μm wide stripe lasers). The spreading of carriers and the optical field in the lateral direction is expected to affect the confinement factor in equation (2.47), which will increase the value of J_{sth} to achieve the required value of g_{th} (this effect is discussed below). The experimentally estimated value of α will be compared with the loss value obtain later in

chapter-3 using a novel temperature dependent loss measurement technique. Eventually, in chapter 3, the loss value for the 2.5μm wide stripe laser will be estimated.

2.6.4. Effect of carriers and optical mode spreading in the lateral direction

A convenient figure of merit for the effectiveness of a stripe geometry laser in using the injected carriers is to compare J_{sth} (assuming that all the current is confined under the stripe) to the threshold current density measured on similar laser material fabricated in the form of a broad area laser, J_{bth}.

By using the estimated value of α=27.6/cm, the calculated value of Γ=0.46 (by ignoring the lateral mode spreading because: (1) optical mode loss has small influence on J_{sth} when compared with the carriers spreading in the lateral direction, (2) in narrow stripe ridge waveguide laser, such as used here, only the fundamental lateral mode where most of the power lies within the central area of the ridge, is favoured (because of low losses) and due to higher losses associated with higher order modes in the lateral direction and (3) the effective mode spreading width in the lateral direction is far smaller than the effective lateral current spreading width, as it will be shown below), R_1=R_2=30% and L=250μm (UB262 and UB238 both have the same length), g_{th} is calculated as 165.6/cm. For the typical value of $J_{(nom)_o}$=4.5KA/cm^2 [5] and η_{in}=42% and 64.5% (for UB262 and UB238 respectively), J_{bth} comes to be 2790A/cm^2 and 1816A/cm^2 for UB262 and UB238 respectively (from equation (2.55)). By using equation (2.64), J_{sth} for UB262 and UB238 is calculated as 7840A/cm^2 and 4640A/cm^2. This gives the ratio between J_{sth} and J_{bth} as 2.81 and 2.55. In figure 2.23, the results of reference-36 are compared with the results obtained here. It can be seen from figure 2.23 that the values of normalized threshold current density for UB262 and UB238 are very close to the reported values for ridge waveguide lasers and are better than the predicted results of reference-4, probably due to better carrier confinement in the lateral direction as

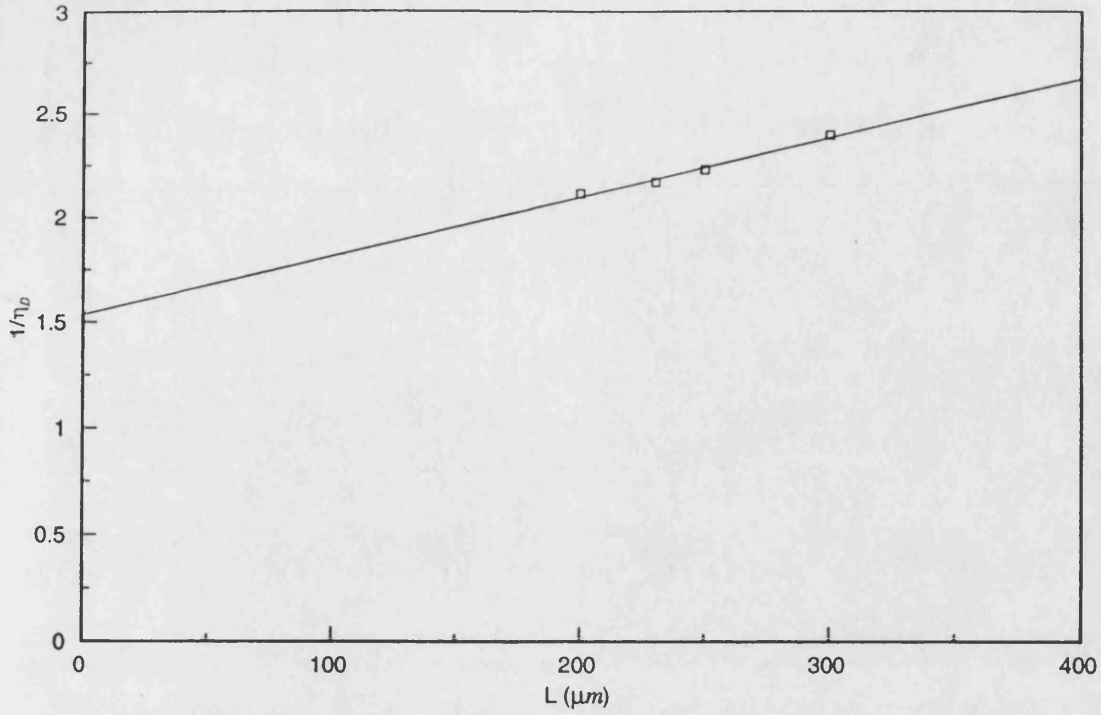

Figure 2.22. The effect of varying length on the reciprocal of external quantum efficiency.

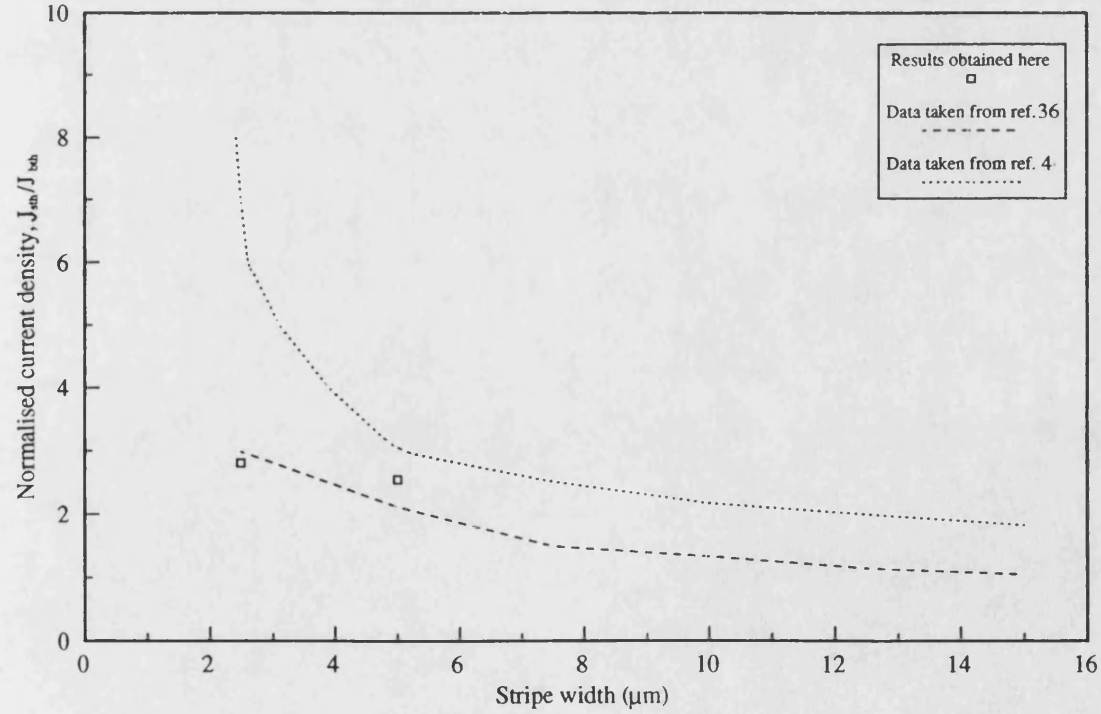

Figure 2.23. The plot of the normalised threshold current density, J_{sth}/J_{bth} against the stripe width, W.

a result of using material with a high R_x. The argument of better lateral confinement can be justified by comparing the obtained value of J_{sth} with figure 2.13. These value are marked with 'X' in figure 2.13. In both lasers (UB262 and UB238), the measured value of J_{sth} are lower than theoretical values that are plotted in figure 2.13 even though the confinement of optical radiation was poor (i.e. Γ=0.46) and J_{bth} was higher in our case (Tsang *et al* [17] has used J_{bth}=1.3KA/cm^2). This justifies ignoring the lateral mode spreading while calculating Γ for the fundamental lateral mode, as was concluded by Tsang *et al* [17].

Since J_{sth} varies with the stripe width of the laser diode and hence the influence of the current spreading and diffusion of minority carriers on J_{sth}, this changes the requirement of pumping current, which in terms of effective spreading width is given by [11];

$$I_{sth} = W_{eff} A\, mA \tag{2.93}$$

where A is defined as [11];

$$A = 0.04 d_3 L + 3.3\left\{\frac{\ln(1/R_1R_2)}{2} + \alpha L\right\}\frac{s}{k_c} \tag{2.93}$$

where s is the effective thickness of the optical distribution, k_c is the coupling constant. The typical value of (s/k_c) is 0.5μm for GaAs based lasers [11].

The effective width for carrier spreading can be calculated from the slope of a curve between I_{sth} and A. The different values of A calculated from equation (2.94) by using data of figure 2.21 are plotted against I_{sth} in figure 2.24. The slope of the curve gives W_{eff}=46μm.

In order to compare this value of W_{eff} with the theoretical value (figure 2.12), R_x has to be known. R_x can be given by re-arranging equation (2.61) as;

$$R_x = \frac{2J_t}{\beta_v J_o^2 W^2} \tag{2.95}$$

By using equation (2.95), R_x is calculated as 420.1Ω and 218.6Ω for UB262 and UB238 respectively. In figure 2.12(b), for R_x=50Ω and W=5μm, $W_{eff} \approx 70\mu m$. As R_x increases, the value of W_{eff} reduces accordingly (figure 2.12(a)). Therefore, a

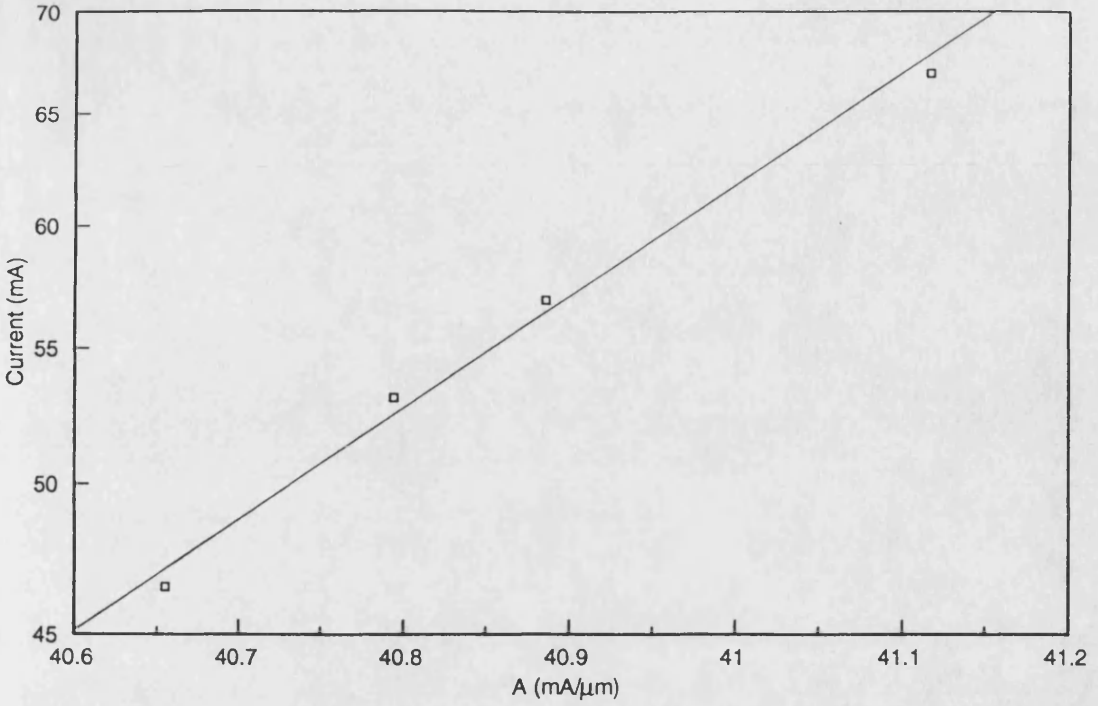

Figure 2.24. Graph used for the calculation of W_{eff}.

value of W_{eff}=46μm for 5μm wide stripe laser (UB238) is in line with theoretical results. For the same value of R_x, the effective optical mode width (including higher order modes since theoretically speaking, the guide with W=5μm can support more than one lateral mode (equation (2.78)) would be less than W_{eff} [17]. Hence the influence of optical mode loss on J_{sth} is less prominent than the spreading of carriers in the lateral direction. Therefore, ignoring the mode spreading of the fundamental mode in the lateral direction when calculating the confinement factor is justified.

2.6.5. Measurement of facet reflectivities

For many applications in optical communication systems and in OICs in particular, it is desirable to maximize the end mirror losses of semiconductor laser devices by reducing the facet reflectivities in order to suppress the internal feedback. A number of techniques to reduce the facet reflectance have been studied [41-45].

During the work reported in this thesis, the laser facet were coated with a single layer of SiO_2 A.R. coating using an ion beam sputtering film deposition technique. Deposition of the A.R. coating on the laser facet was monitored in *situ* by monitoring the thickness of the film by measuring the optical transmittance using the experimental set-up of reference-46. This method uses the quater-wave rule [47] and terminates the coating process when the minimum transmittance is achieved. The refractive index of SiO_2 varies from 1.49 to 1.59 [48,49] depending on the residual oxygen in the vacuum chamber. Furthermore, the transmittance was monitored in *situ* by using an incident plane wave, whilst for the actual laser devices, due to the small aperture size, the transmittance of the A.R. coating will differ from the plane wave transmittance. So it is important to measure the reflectivity of the coated facet after being coated. Once the facet reflectance of one facet is measured it is relatively easy to reproduce the A.R. coating on other facet under the same conditions. The reflectance of the A.R. coated facet off *situ* can be

measured by several techniques, such as;

1. by measuring and comparing the power output from both facets [4,50],
2. from the noise spectrum of A.R. coated device [51].

The former method has been adopted here because it offers simplicity of the measurement process. For this purpose, a ridge waveguide laser, UB259 was fabricated and one facet of this laser was coated with a single layer A.R. coating of SiO_2. The power outputs from the coated facet, P_1, and the uncoated facet, P_2, of this device were measured (using a small area detector along with an optical lens system) and are plotted in figure 2.25. The ratio between the power output from the coated and the uncoated facets can shown to be;

$$\frac{P_1}{P_2} = \sqrt{\frac{R_2}{R_1}\left(\frac{1-R_1}{1-R_2}\right)} \tag{2.95}$$

where R_1 and R_2 are the facet reflectances of coated and uncoated facets respectively.

The reflectance of the uncoated facet can be estimated from the Fresnel reflection formula (equation (2.49)) and for the GaAs laser it is 30%. The reflectance of coated facet can be determined experimentally by rearranging equation (2.95) as;

$$R_1 = \frac{0.49 + 0.6\left(\frac{P_1}{P_2}\right)^2 - \sqrt{0.24 + 0.588\left(\frac{P_1}{P_2}\right)^2}}{0.6\left(\frac{P_1}{P_2}\right)^2} \tag{2.96}$$

Figure 2.26 shows the relationship between R_1, calculated from equation (2.96) and device injection current. The saturated part of that curve gives the minimum value of facet reflectance as 4.48%. This value is slightly higher than the reported values of around 3% [52], measured by same method. There are probably two reasons for the discrepancy; (a) the refractive index of SiO_2 varies due to residual oxygen present in vacuum chamber even at very low pressures [53]. (b)

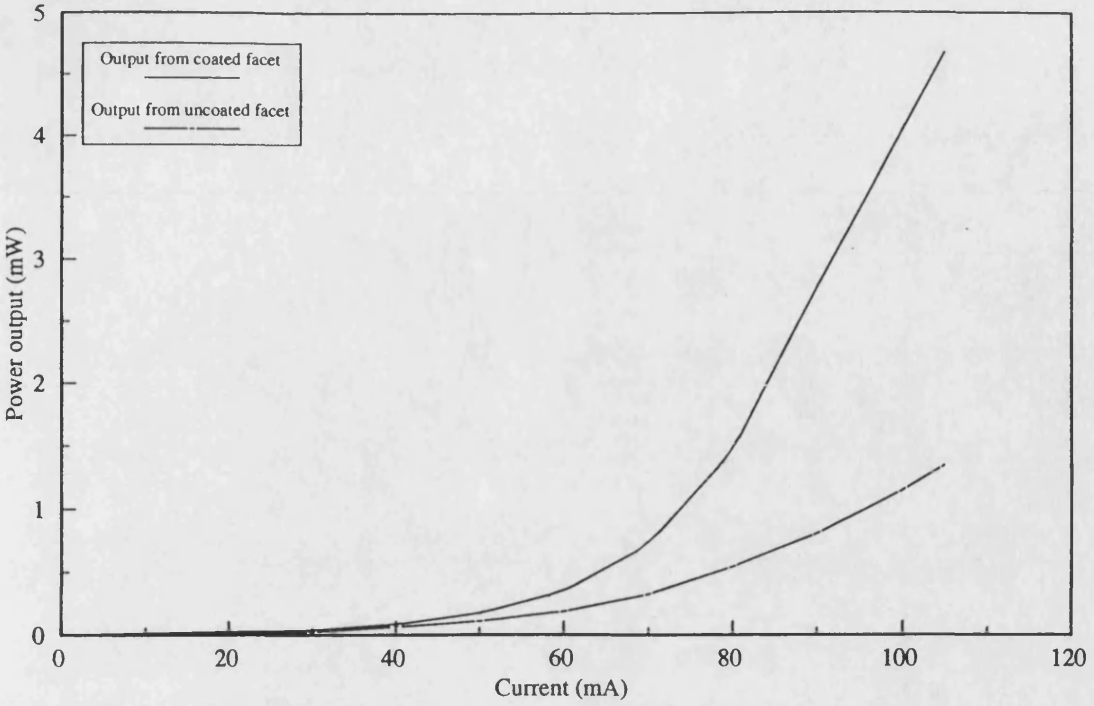

Figure 2.25. Power output from the A.R. coated facet and the uncoated facet of a single side coated device.

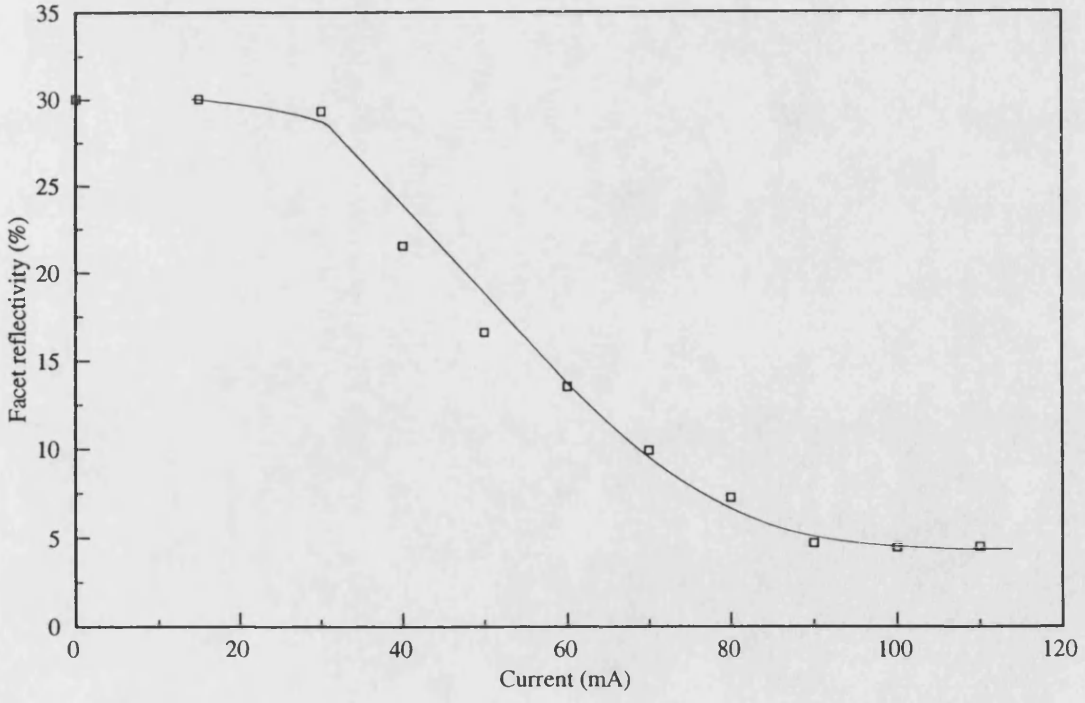

Figure 2.26. Curve used to measure the facet reflectance of A.R. coated facet.

design calculations and in *situ* measurement of the A.R. coating has been performed assuming the plane wave solution whereas due to the small effective aperture of the guide, the reflectivity for a given A.R. coating differ from plane wave reflectivity [51].

2.6.6. Effect of A.R. coating on laser characteristics

The main purpose of A.R. coating on the laser facets is to use the laser as a travelling wave optical amplifier by suppressing the internal feedback. The common way to analyse whether the device is lasing is to examine its I-L and spectral characteristics. In order to carry out this investigation, the I-L characteristic of the device UB259 was measured prior to A.R. coating. The measurement of the I-L characteristic was repeated after coating one facet of this device. The I-L characteristic of this device was then measured again with both sides A.R. coated. Results are shown in figure 2.27 along with the results of reference-52. In reference-52 the laser investigated has lower lasing threshold (prior to A.R. coating), therefore, in order to compare the results obtained here with those of reference-52, they are plotted using a normalised current scale. It can be seen from figure 2.27 that the lasing action has been successfully suppressed in both cases. When the device was coated only single side, it was found to exhibit asymmetrical I-L characteristics due to differences in the forward and reverse travelling optical densities. Whereas the output from either facet when both facets were coated was found to be nearly equal. It can be seen from figure 2.27, that the optical output power from single-side and double-side coated devices is higher in our case than that reported in reference-52 due to the higher facet reflectance in our case when compared to the facet reflectance achieved by Evankow *et al* [52].

The effect of A.R. coating on the spectral characteristics were investigated by inserting a monochrometer between the laser diode and the optical detector. At the input and output of the monochrometer, 0.25mm slits were used to increase the resolution of the monochrometer. The output from the monochrometer was plotted

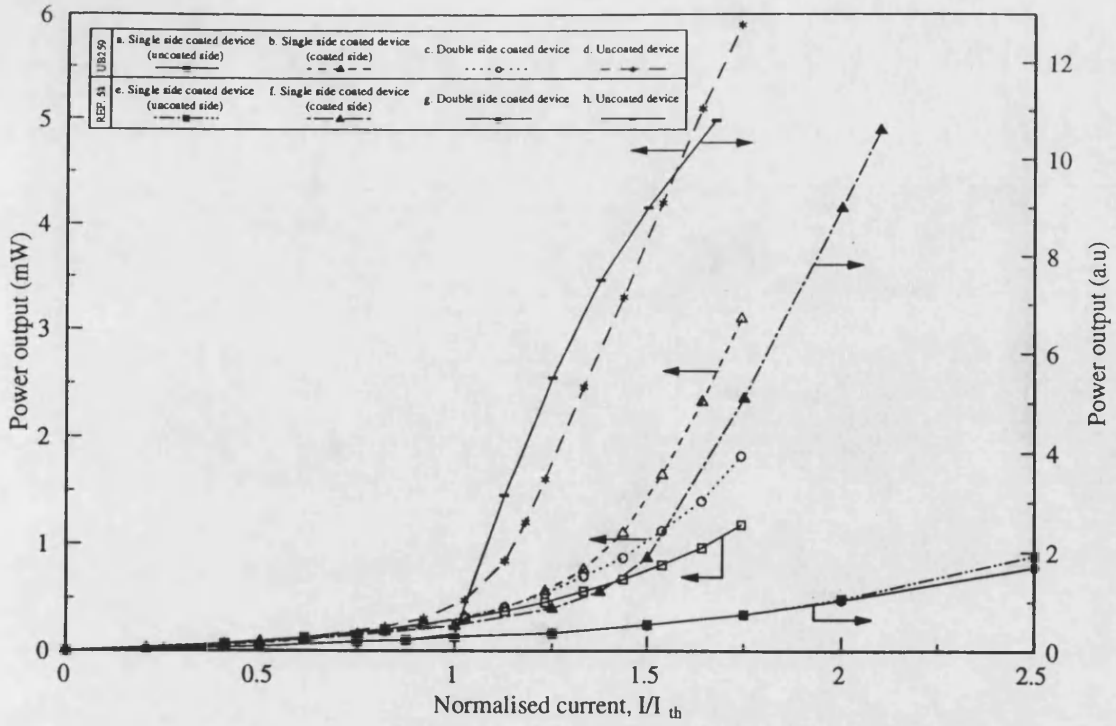

Figure 2.27. Figure showing the effect of A.R. coating on the I-L characteristic. The results of reference-58 are also plotted.

against wavelength using a sample and hold oscilloscope and an X-Y plotter. The schematic of the experimental set-up is shown in figure 2.28.

Figure 2.29 shows the spectral outputs of the laser diode at constant current with: (a) no coating on its facets, (b) one side only coated and (c) both sides coated. The spectral peaks of the uncoated, single side coated and double side coated device are 859.41nm, 856.5nm and 855.65nm respectively at room temperature. The shift of the spectral peak towards the shorter wavelength as the device behaves more like a travelling wave amplifier could be due to the following reasons;

In a Fabry-Perot laser, the carrier density, and hence the quasi-Fermi level separation becomes pinned due to the effect of strong stimulated recombination within the active region. Since it is the quasi-Fermi level separation which is largely responsible for setting the wavelength of the gain maximum, this ensures that the gain of the Fabry-Perot laser oscillates at the longer wavelengths.

For devices with A.R. coating, the effect of stimulated recombination is much weaker because the photon density is much lower and the pinning of the carrier density much lower since lasing action is being suppressed. As the carrier density within the device may be higher (indicated by the fact that the photon density is lower), the quasi-Fermi separation is wider and the wavelength of the gain maximum will shift to shorter wavelengths. Additionally, the effect of heat on the mirror facet reflectance may also be an important contribution to this in FP devices [54].

2.7. Summary

This chapter has served dual purposes. On the one hand, the basic theoretical background which is necessary for the understanding of the generation of optical radiation and its propagation in a waveguide, has been investigated. On the other hand, basic laser characteristics which are necessary to analyse the light propagation in active waveguide devices have been measured experimentally on devices

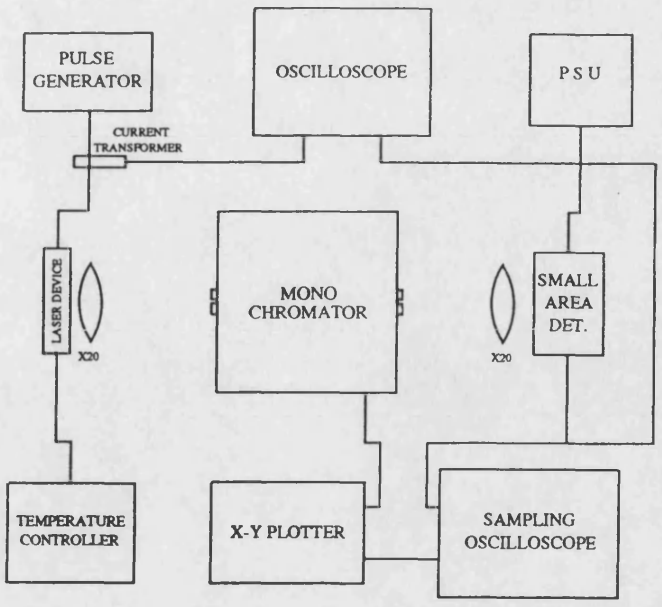

Figure 2.28. The schematic of the experimental set-up used to measure spectral characteristics.

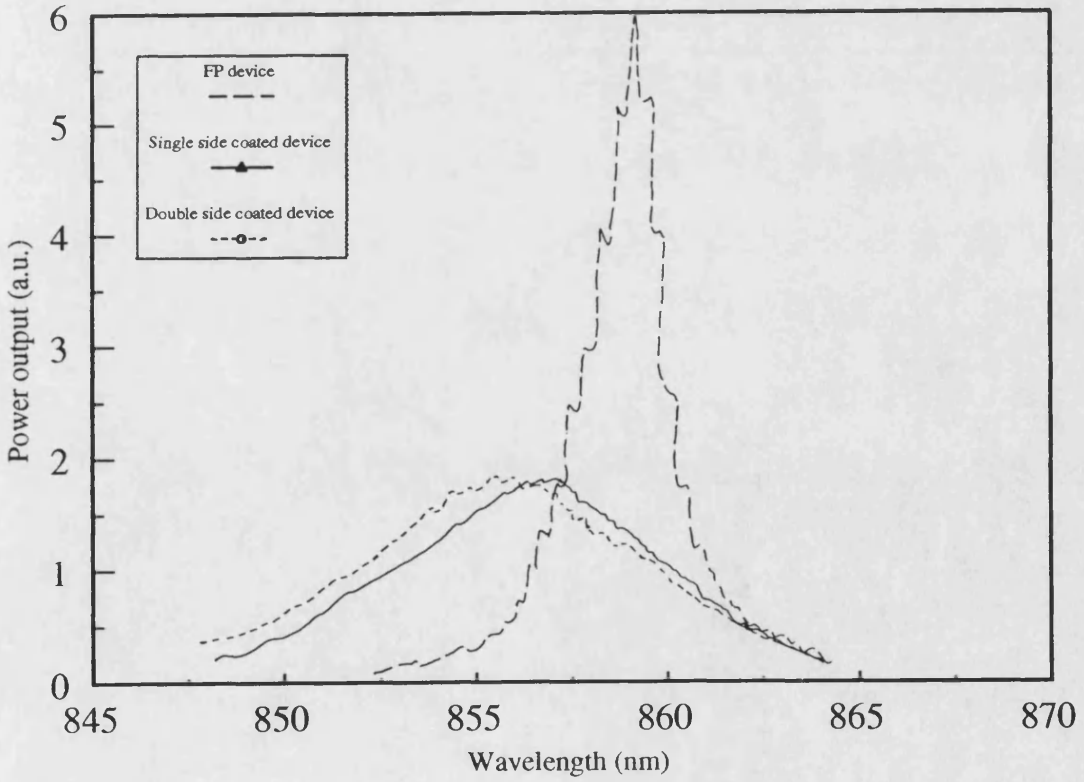

Figure 2.29. The effect of A.R. coating on the spectral output of a laser device.

produced 'in house'.

The description of the light emission process in the active medium has been carried out starting with simple two layer system using Einstien relations. The derivation of Einstein relations have given a insight into light generation process in a active medium and the role of population inversion and optical resonator have been explained on the basis of Einstein constants. The necessary condition for the lasing action in semiconductors have been derived by using Fermi-Dirac distribution and Einstein constants.

The different types of laser have been discussed in terms of practicality and performance. The analysis of the slab waveguide has shown that the symmetrical slab waveguide can always support a fundamental mode, even when the thickness of the active layer is very small, which is the case for the DH lasers. Later, 1-D slab waveguide solution was applied to the two-dimension rib waveguide structure by breaking the 2-D problem into two 1-D problems using transverse resonance method. The application of the effective index method to the rib waveguide structure was shown to be inaccurate as the waveguide approaches cutoff.

The relationship between the optical and electrical parameters of a semiconductor laser has also been established to pave the way to relate the experimental results and theory explained earlier. Experimentally, the relationship between the optical and electrical parameter was achieved by measuring the output power of laser diode against diode current. From the I-L characteristics of different laser diodes, the values of the external quantum efficiency, the internal quantum efficiency and optical radiation losses were obtained. The measured values of η_D and η_{in} found to be close to reported values. The measured value of α was found slightly higher than reported value possibly due to the higher temperature sensitivity of devices investigated here since the total losses inside a cavity depend upon free carrier losses which increase with the temperature of the active layer.

The threshold current density was found to increase as the stripe width

decreased as was expected from equation 2.64. This was found to be predominantly due to the carrier spreading in the lateral direction due to current spreading and carrier diffusion rather than because of the influence of the optical mode spreading in the lateral direction.

The facet reflectance of the A.R. coated facet of single side coated device was measured and found to be slightly higher than the reported values measured using same technique. This is because: (a) the refractive index of SiO_2 can vary with the presence of residual oxygen in the vacuum chamber, (b) the design calculations and in *situ* measurement of A.R. coating was performed using a plane wave monitoring system but the reflectivity of a given A.R. coating under lasing conditions differ from the plane wave reflectivity. Lasing was successfully suppressed by applying A.R. coating on one or both facets of a particular diode which has similar dimensions to devices to be investigated later in this thesis as active components for OIC. A shift in the spectral peak wavelength was observed as a result of A.R. coating on laser facets due to the increase in carrier concentration as a result of the absence of the optical feedback mechanism, the reduction in stimulated recombination due to the lower internal photon density and due to the reduction in mirror facet heating effect.

References

1. Bernard, M.G.A., and Duraffourg, G., 'Laser conditions in semiconductors', Phys. Status Solidi vol.1, p.699, 1961, Reprinted in Semiconductor devices: Poineering papers, Sze, S.M.(Ed.), p.880, 1991.
2. Basov, N.G., Krokhin, O.N., and Popov, M., 'Use of indirect transitions in semiconductors for the determination of states with negative absorption coefficients', Soviet Physics JETP, vol.13, p.845, 1961.
3. Agrawal, G.P., and Dutta, N.K., 'Long-wavelength semiconductor lasers', Van Nostrand Reinhold, 1986.
4. Kressel, H., and Butler, J.K., 'Semiconductor lasers and heterostructure LED's', Academic Press, 1977.
5. Casey, H.C. Jr., and Panish, M.B., 'Heterostructure lasers Part:A', Academic Press, 1978.
6. Stern, F., 'Calculated spectral of gain in excited GaAs', J. Appl. Phys., vol.47, p.5382, 1976.
7. Biard, J.R., Carr, W.N., and Reed, B.S., 'Analysis of GaAs lasers', Trans. AIME, vol.230, p.286, 1964.
8. Goodwin, A.R., Peters, J.R., Thompson, G.H.B., and Whiteaway, J.E.A., 'Threshold temperature characteristics of double heterostructure $Ga_{1-X}Al_XAs$ lasers', J. Appl. Phys., vol.46, p.3126, 1975.
9. Casey, H.C. Jr., 'Room-temperature threshold-current dependence of GaAs-$Al_xGa_{1-x}As$ double-heterostructure lasers on X and active-layer thickness' J. Appl. Phys., vol.49, p.3684, 1978.
10. Blood, P., 'Heterostructures in semiconductor lasers' in 'Physics and technology of heterojunction devices', Morgan, D.V., and Williams, R.H. (Eds.), p.231, Peter Peregrinus Ltd., 1991.
11. Thompson, G.H.B., 'Physics of semiconductor devices', John Wiley & sons, 1980.
12. Mroziewicz, B., Bugajski, M., and Nakwaski, W., 'Physics of semiconductor lasers', North-Holand and PWN-Polish Scientific Publishers, 1991.
13. Pinkas, E., Miller, B.I., Hayashi, I., and Foy, P.W., 'Additional data on the effect of doping on the lasing characteristics of GaAs-$Al_xGa_{1-x}As$ double heterostructure lasers', IEEE J. of Quantum Electron., QE-9, p.281, 1973.
14. Thompson, G.H.B., 'The analysis of optical scattering in double-heterostructure and five-layers heterostructure (GaAl)As/GaAs injection lasers', IEEE J. of Quantum Electron., QE-11, p.481, 1975.
15. Dyment, J.C., D'Asaro, L.A., Norht, J.C., Miller, B.I., and Ripper, J.E., 'Proton-bombardment formation of stripe-geometry heterostructure laser for 300K CW operation', Proc. IEEE, vol.60, p.726, 1972.
16. Kressel, H., and Eltenburg, M., 'Low threshold double heterojunction AlGaAs/GaAs laser diodes: theory and experiment', J. Appl. Phys., vol.47, p. 3533, 1976.

17. Tsang, W.T., 'The effects of lateral current spreading, carrier outdiffusion, and optical mode losses on the threshold current density of GaAs-$Al_xGa_{1-x}As$ stripe-geometry Dh lasers', J. Appl. Phys., vol.49, p. 1031, 1978.
18. Henry, C.H., Logan, R.A., and Merritt, F.R., 'The effect of surface recombination on current in GaAs-$Al_xGa_{1-x}As$ heterojunctions', J. Appl. Phys., vol.49, p. 3530, 1978.
19. Marcuse, D., 'Theory of dielectric waveguides', Academic Press, 1974.
20. Tamir, T., 'Guided-wave optoelectronics', Springer-Verlag, 1990.
21. Kogelnik, H., 'Theory of optical waveguides' in 'Integrated optics', Tamir, T.(Ed), Springer-Verlag, 1975.
22. Kogelnik, H., and Ramaswamy, V., 'Scaling rules of thin-film optical waveguides', Appl. Optics, vol.13, p.1857, 1973.
23. Marcatili, E.A.J., 'Dielectric rectangular waveguide and directional coupler for integrated optics' B.S.T.J. vol.48, p.2071, 1969.
24. Rahman, B.M.A., and Davies, J.B., 'Vector-H finite element solution of GaAs/GaAlAs rib waveguides', IEE Proc-J, vol.132, p.349, 1985.
25. Matsuhara, M., 'Analysis of TEM modes in dielectric waveguides by a variational method', J. Opt. Soc. Am., vol.63, p.1514, 1973.
26. Robertson, M.J., Ritchie, S., and Dayan, P., 'Semiconductor waveguides: analysis of optical propagation in single rib structures and directional couplers', IEE Proc-J, vol.132, p.336, 1985.
27. Knox, R.M., and Toulios, P.P., 'Integrated circuits for the millimetre through optical frequency range' in Proceedings of MRI symposium on submillimeter waves, Fox, J.(Ed), p.497, Polytechnic Press, 1970.
28. Kendall, P.C., Adams, M.J., Ritchie, S., and Robertson, M.J., 'Theory for calculating approximate values for the propagation constants of an optical rib waveguide by weighing the refractive indices', IEE Proc-A, vol.134, p.669, 1987.
29. Kendall, P.C., McIlroy, P.W.A., and Stern, M.S., 'Spectral index method for rib waveguide analysis', Electron. Lett., vol.25, p.107, 1989.
30. Kim, C.M., Jung, B.G., and Lee, C.W., 'Analysis of dielectric rectangular waveguide by modified effective index method', Electron. Lett., vol.22, p.296, 1986.
31. Ramaswamy, V., 'Stripe loaded film waveguide', B.S.T.J., vol.53, p.697, 1974.
32. Buus, J., 'The effective index method and its application to semiconductor lasers' IEEE J. of Quantum Electron., QE-18, p.1083, 1982.
33. Dunlop, J., and Smith, D.G., 'Telecommunications Engineering', second edition, Van Nostrand Reinhold (International), 1989.
34. Uchida, N., 'Optical waveguide load with high refractive-index stripe film', Appl. Optics, vol.15, p.182, 1976.

35. Taylor, J.A., 'An introduction to error analysis, The study of uncertainties in physical measurements', Chapter-8, University Science Books, 1982.

36. Kawaguchi, H., and Hawakami, T., 'Transverse-mode control in an injection laser by a stripe loaded waveguide', IEEE J. of Quantum Electron., QE-13, p.556, 1977.

37. Amann, M.C., 'New stripe-geometry laser with simplified fabrication process' Electron. Lett., vol.15, p.441, 1979.

38. Hakki, B.W., and Paoli, T.L., 'Gain spectra in GaAs double heterostructure injection lasers', J. Appl. Phys., vol.46, p.1299, 1975.

39. Andrekson, Olsson, N.A., Tanbun-Ek, T., Logan, R.A.,Coblentz, D., and Temkin, H., 'Novel technique for determining internal loss of individual semiconductor lasers', Electron. Lett., vol.28, p. 171, 1992.

40. Tsang, W.T., 'Lateral-current confinement in a GaAs planar stripe-geometry and channel substrate buried DH laser using reverse bias *p-n* junctions', J. Appl. Phys., vol.49, p.2629, 1978.

41. Mukai, T., Yamamoto, Y., and Kimura, T., 'S/N and error rate performance in AlGaAs semiconductor laser preamplifier and linear repeater systems, IEEE J. of Quantum Electron., vol. QE-18, p.1560, 1982.

42. Zah, C. E., Osinki, J. S., Caneau, C., Menocal, S. G., Reith, L. A., Salzman, J., Shokoohi, F. K., and Lee, T. P., 'Fabrication and performance of 1.5 μm GaInAsP travelling-wave laser amplifiers with angled facets', Electron. Letters, vol.23, p.990, 1987.

43. Farries, M. C., Buus, J., and Robbins, D. J., 'Analyses of antireflection coatings on angled facet semiconductor laser amplifiers', Electron. Letters, vol.26, p.381, 1990.

44. Cha, I., Kitamura, M., and Mito, I., '1.5 μm band travelling-wave semiconductor optical amplifiers with window facet structure', Electron. Letters, vol.25, p.242, 1989.

45. Cha, I., Kitamura, M., Honmou, M., and Mito, I., '1.5 μm band travelling-wave semiconductor optical amplifiers with window facet structure', Electron. Letters, vol.25, p.1241, 1989.

46. Milner, A. C., 'Monitoring the reflectivity of one facet of a laser diode during the deposition of an antireflection coating', B.Sc. thesis, university of Bath, 1989.

47. Ritter, E., 'Optical coatings and thin-film techniques' in Laser handbook, Arecchi, F. T., and Schulz-Dubois, E. O., (Eds), North-Holland Publishing Company, 1972.

48. Lissberger, P. H., 'Optical applications of dielectric thin films', Rep. Prog. Physics, Vol.33, p.197, 1970.

49. Secrist, D. R., 'Deposition of silica films by glow discharge technique', J. of the Electroche. Soc., vol.113, p.914, 1966.

50. Higuchi, H., Namizaki, H., Oomura, E., Hirano, R., Sakakibara, Y., Susaki, W., and Fujikawa, K., 'Internal loss of InGaAsP/InP buried crescent ($\lambda = 1.3\mu m$ laser', Appl. Phys. Letters, vol.41, p.320, 1982.

51. Kaminow, I. P., Eisenstein, G., and Stulz, L. W., 'Measurement of the modal reflectivity of an antireflection coating on a superluminescent diode', IEEE J. of Quantum Electron., vol. QE-19, p.493, 1983.

52. Evankow, J.D. Jr., Olsson, N.A., and K, R.T., 'Performance of packaged near-travelling-wave semiconductor laser amplifier with multilongitudinal mode input', J. of Lightwave Tech., vol.7, p.163, 1989.

53. Holland, L., 'Vacuum deposition of thin films', Chapman and Hall, 1956.

54. Pilkulun, M., Rupprecht, H., and Blum, S., 'Effect of temperature on the stimulated emission from GaAs *p-n* junctions', Solid-State Electron., vol.7, p.905, 1964.

Chapter-3

Temperature dependence properties of OIC components

3.1. Introduction

When energy in the form of a constant amplitude pulse is applied to a laser diode, it is converted into radiant energy emissions and heat energy. The amount of heat energy defines the laser operating temperature and it depends upon its construction, material and mode of operation (CW or pulse). The main task of this chapter is to investigate the temperature dependent properties of OIC components (lasing sources and amplifiers). The temperature dependent properties of the active waveguide optical detector are dealt with in the next chapter. Experimental work reported in this chapter has been performed using four different devices and these were UB238 (5 μm wide stripe), UB262, UB259 and UB258. The structural details of these devices are given in chapter 1.

The investigation of the effect of temperature on OICs begins by considering the effect of temperature variation on the principal OIC parameters in section 3.2. This section also considers the ways of reducing temperature sensitivity of laser devices. In section 3.3, power dissipation at the heterojunction in the semiconductor laser is discussed. The temperature dependence of the threshold current is investigated in section 3.4 and a new non-destructive loss measurement technique is developed in section 3.5. The effect of temperature on the spectral characteristics are examined in section 3.6. In section 3.7, the transient temperature responses are

measured using I-L and spectral characteristics and the thermal rise time for different devices is estimated. In section 3.8 requirements for CW operation of a laser device are outlined. This chapter ends with summary of main points in section 3.9.

3.2. Effect of temperature on OIC properties

Normally, the laser diode is mounted on a suitable heatsink to dissipate the heat energy to avoid overheating. Even if the laser diode is mounted on a heatsink, the active layer temperature can rise significantly above the heat sink temperature because of the thermal resistance of the various layers of the device. This not only reduces the efficiency of device, but also can have drastic effects on its operating characteristics such as;

1. the threshold current of the device increases from its typical value.
2. power output per facet decreases significantly.
3. peak wavelength shifts toward higher wavelengths.
4. spectral line width broadening takes place.
5. excessive heat generation leads to thermal runaway, that could destroy laser diode or degrade the laser diode life time.
6. it puts limitation on the maximum CW operating power.

When this laser diode is integrated with other active components in an OIC, the above effects not only put severe limitations on the optimum performance of the laser diode itself but also on the response of the other components, such as the active waveguide optical detector and active waveguide optical amplifier. For example, active waveguide amplifier is tuned to one wavelength and any sudden change in input radiation wavelength (due to change in the source laser temperature) will change the amplification of the wanted signal and this will distort output signals. If the tuned wavelength of the amplifier is changed with temperature but the wavelength of input signals stays constant then the amplification process will

be less affected because the amplifier usually has a broad gain spectrum. Furthermore, the rise in temperature of the laser source would physically increase the temperature of the active waveguide optical amplifier as in monolithic integration scheme both are integrated on a same substrate. The response of the active waveguide optical detector may vary in a similar fashion as the response of the amplifier but it is the response of the lasing source which has drastic effects on the performance of an OIC. Therefore, it is necessary to avoid overheating of all OIC components but especially the integrated source. Overheating can be avoided by;

(a). using a cooling chamber,

(b). using junction down mounting techniques,

(c). using a Peltier cooling pump,

One or more methods can be used to avoid overheating.

Since the work reported in this chapter is a part of the main work on the light propagation characteristics of butt-coupled monolithical OIC components, the junction down mounting is not desirable because it is then very difficult to get independent electrical contacts to the various stripe electrodes of the structure. During the research, a hybrid approach has been used quite frequently to achieve a better understanding of the behaviour of the input radiation into an active waveguide, which needs an open optical bench. Therefore, a closed cooling chamber would have been impractical.

Therefore, during this work, temperature stabilization was achieved by using Peltier cooling pumps along with a three channel temperature controller (based on the temperature controller circuit of reference-1) to maintain the desired temperature without affecting the output power while the devices under investigation run under pulse mode to further reduce the affects of excess heat generation [2].

3.3. Power dissipation of laser diode p-n junction

When a laser source is driven with injection current, the generation of heat

occurs in several layers, including the active region. There are a number of different heat generation mechanisms and these are considered below. The increase in the power dissipation in and around the active region can cause the junction temperature of the active layer to increase by several degrees above the heatsink temperature. Although the heating effects cannot be avoided, they can be minimized by careful design and by the use of an appropriate device model. This requires detailed study of heat sources and rate of heat generation inside a laser diode, which could lead to the estimation of the active layer temperature.

3.3.1. Origin of heat sources

In order to find the origin of the heat sources, one has to consider the total input power, P_{in}, to the laser diode. This is given by;

$$P_{in} = VI \tag{3.1}$$

where V and I are the total input voltage and total input current and are defined as;

$$V = V_{th} + \Delta V_L \tag{3.2}$$

and

$$I = I_{th} + I_L \tag{3.3}$$

where V_{th} is the voltage at threshold. I_{th} is the threshold current. ΔV_L and I_L are the voltage and current which contributes to the laser emission. V_{th} is defined as;

$$V_{th} = E_g + \Delta V \tag{3.4}$$

where E_g is the voltage across the junction and ΔV is the voltage drop other than the junction voltage drop. E_g is nearly equal to energy of emitted radiation, which is about 1.45eV for GaAs.

The relationship between V and I is shown graphically for UB238 and UB262 in figure 3.1. The inset of figure 3.1 shows the I-L characteristics of two lasers. From this figure, values of I, I_{th}, I_L, V, V_{th}, V_L and ΔV can be obtained. The linear

part of figure 3.1 can be used to calculate the series resistance of the laser and is defined as [3];

$$R_s = \frac{dV}{dI} \tag{3.5}$$

R_s for UB238 and UB262 is calculated as 5.25Ω and 5.5Ω respectively from figure 3.1. The higher value of R_s represent the higher current densities per unit area which contributes to the overall voltage drop across the laser diode.

The total input power, P_{in}, can also be written as [4];

$$P_{in} = IV_L + \eta_D I_L E_g + \eta_{in} I_{th} E_g + (1-\eta_D) I_L E_g + (1-\eta_{in}) I_{th} E_g \tag{3.6}$$

where η_{in} and η_D are the internal and the external quantum efficiencies respectively.

First three terms of equation (3.6) represent the Joule heat or ohmic heat, the optical output power, P_L, and the spontaneous radiation which is emitted in all directions. The Joule heat is consumed in the bulk of the laser diode. The spontaneous emission power emitted uniformly in all directions about the active layer, is also consumed in the bulk of the material. Thus the first three terms do not contribute significantly to the temperature rise of the active layer of a laser diode.

The last two terms of equation (3.6) are the main sources of heat in the active region of the lasing source. The fourth term may be interpreted as the lasing output contributed as heat energy via free carrier absorption. The last term is the power contributed by the nonradiative recombination in the active region. These two sources of heat are located in the active region and its close vicinity. Therefore, the total input power to a laser can be defined as;

$$P_{in} = P_{act} + IV_L + P_L + \eta_{in} I_{th} E_g \tag{3.7}$$

where

$$P_{act} = (1-\eta_D) I_L E_g + (1-\eta_{in}) I_{th} E_g \tag{3.8}$$

or

$$P_{act} = (1-\eta_D) I_L E_g + I_{th} E_g - \eta_{in} I_{th} E_g \tag{3.9}$$

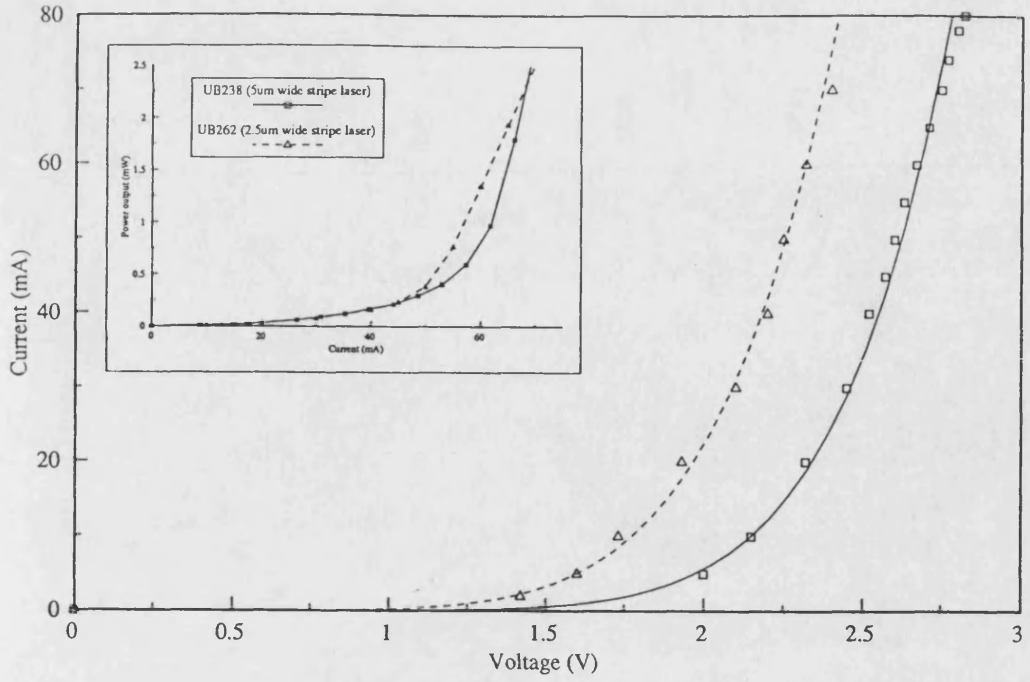

Figure 3.1. V-I curve of two LD's as a function of stripe width. Inset is showing the I-L characteristics of both laser diodes.

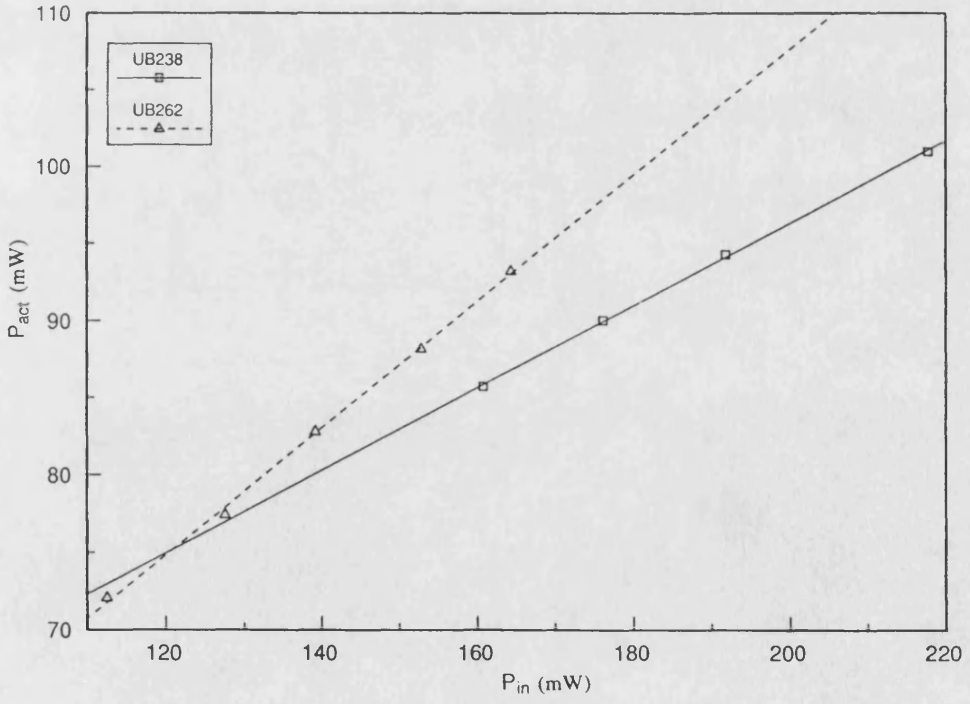

Figure 3.2. Relationship between input power and the rate of heat generation in the active layer.

where $\eta_{int} I_{th} E_g$ term is the spontaneous emission radiation emitted in all directions. This term may be neglected to calculate P_{act} as;

$$P_{act} = (1 - \eta_D) I_L E_g + I_{th} E_g \tag{3.10}$$

The values of the input power and the rate of heat generation in the active region, P_{act} are calculated from figure 3.1 and are plotted in figure 3.2 against the total input power for UB238 and UB262. From figure 3.2, the ratio between P_{in} and P_{act} for UB238 and UB262 is calculated as 53% and 58%. The higher ratio shows the higher rate of heat generation in the active layer which is probably due to the higher value of R_s (due to smaller area as result of the narrow stripe width) and the spreading of carriers and electromagnetic fields outside the stripe as a result of weak guiding in the lateral direction. In both cases, these values are close to the results of reference-4 which shows a ratio of about 50%.

3.3.2. Active layer temperature

The rate of heat generation in the active region in terms of the GaAs junction temperature is defined as;

$$P_{act} = \frac{\Delta T_j}{R_{th}} \tag{3.11}$$

where ΔT_j is the saturation temperature rise of active layer at the fixed heat sink temperature. R_{th} is the thermal resistance of laser diode and for each individual layer it is given by the relation;

$$R_{th} = \frac{d_i}{\sigma_i A_i} \tag{3.12}$$

where d_i, A_i and σ_i are the thickness, area and the thermal conductivity of the ith layer, respectively. The thermal conductivity, σ_i, for GaAs/$Al_xGa_{1-x}As$ based compounds can be calculated from the equation [5];

$$\sigma_i = \frac{1}{2.27 + 28.83x - 30x^2} \tag{3.13}$$

where x represents the Al content.

The material which was used during the present work has a layer composition between the heatsink and the active layer as shown in the inset of figure 3.3. Also, figure 3.3 shows the contribution of each layer along with the total thermal resistance as a function of stripe width. The thermal resistance of this material was calculated to be 140.72°C/W and 281.44°C/W for 5μm laser (UB238) and 2.5μm laser (UB262) respectively. The rise in GaAs active layer temperature (above the heatsink temperature) for both lasers against the rate of heat generation, P_{act} is plotted in figure 3.4. The higher rise in junction temperature is due to the higher thermal resistance because of its smaller stripe width. This implies that the rise in temperature in an OIC can be avoided by increasing the thermal conductivity of the chip and this can be achieved by p-side down mounting [6] and by using wide stripe-widths to reduce the photon and carrier density.

3.4. Temperature dependence of threshold current

The excessive temperature sensitivity of the threshold current density is attributed to the carrier confinement, the free carrier absorption, nonradiative recombination and internal quantum efficiency. Although each of these parameters has a complex temperature variation, the complexity of these factors prevents the formulation of a single equation holding for all devices and temperature ranges. Pakove [7] has suggested an empirical expression for the homojunction GaAs laser which can also be applied to for the heterojunction laser i.e.;

$$I_{th} = I_{th}(20^{o}C)\exp\left(\frac{T}{T_o}\right) \tag{3.14}$$

where T_o is a characteristic temperature parameter of the laser diode which is a measure of the relative temperature insensitivity of that device. Usually it is found to be between 80°C to 200°C for GaAs DH lasers [8]. T_o for GaAs QW lasers is reported to be as high as 437°C [9]. A lower value of T_o implies that the threshold current increases more rapidly with increasing temperature.

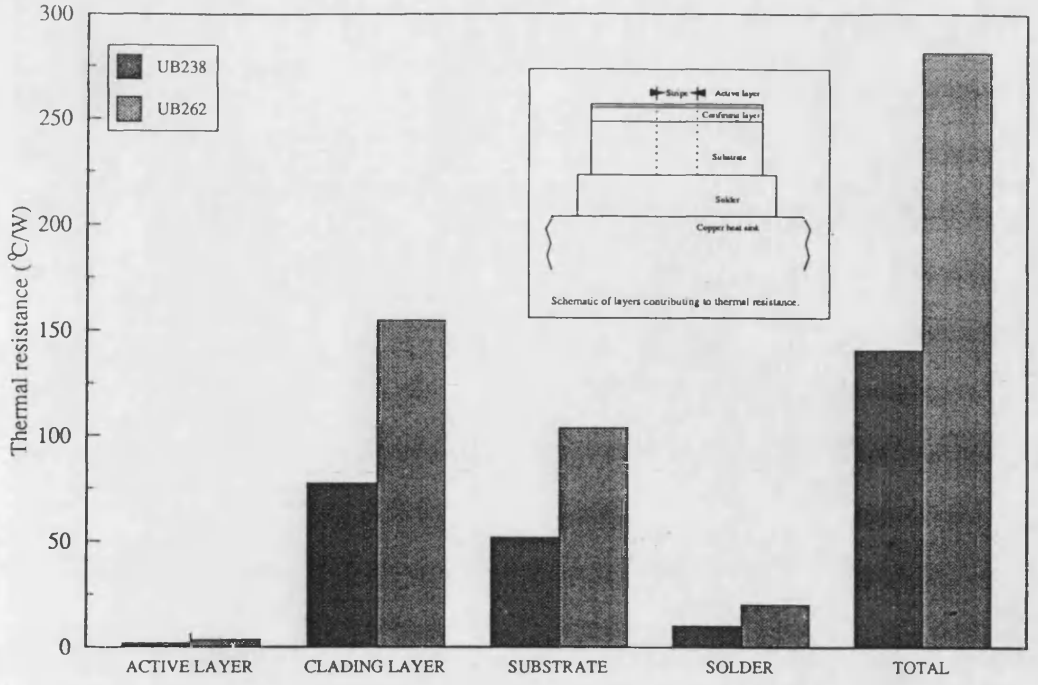

Figure 3.3. The graphical representation of the contribution of different layers to thermal resistance. Inset is showing schematically the layer structure contributing to R_{th}.

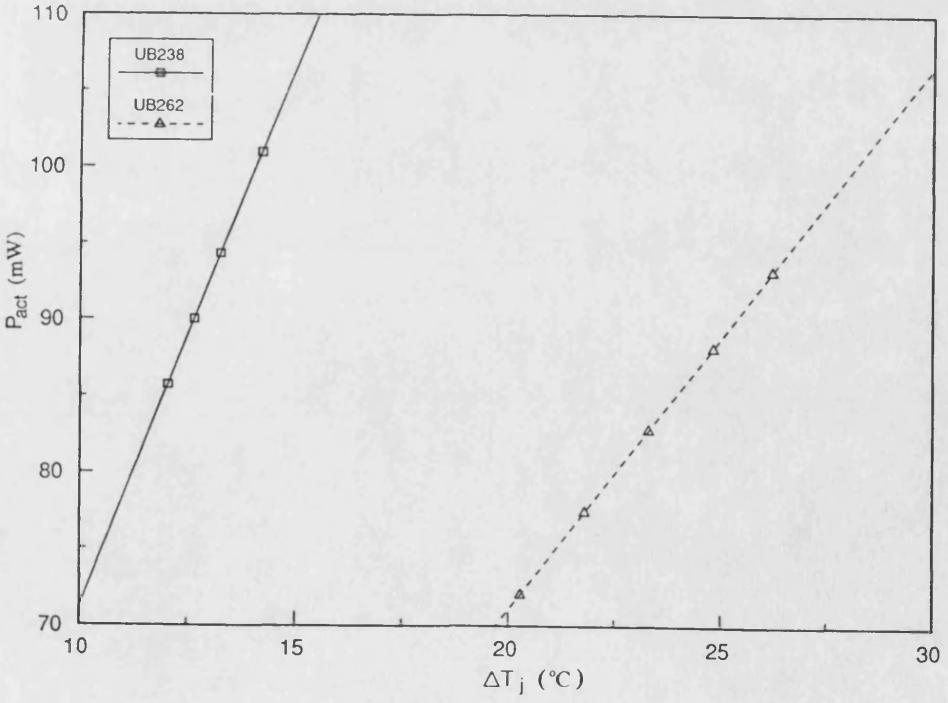

Figure 3.4. Rise in the active layer temperature above the heatsink temperature.

In order to calculate the characteristic temperature of laser sources (UB238 and UB262), the I-L characteristics were measured (using the method described in chapter-2) at different heatsink temperatures while the laser was operated with 200ns current pulses to minimise internal heating of the device. The change in the threshold current is plotted against heatsink temperature in figure 3.5. In figure 3.6, $I_{th}/I_{th}(20^{o}C)$ plotted against heatsink temperature using the data of figure 3.5. The slope of each curve represents the characteristic temperatures corresponding to each laser. The characteristics temperature of UB238 and UB262 are calculated as 117°C and 107°C respectively. A lower value of characteristic temperature for UB262 implies that the device UB262 is slightly more sensitive to temperature variations than UB238.

3.5. Temperature dependence of the internal quantum efficiency

The variation in the laser diode temperature effects the η_{in} of a particular diode and this can be calculated from the temperature dependent variation of the threshold current. The threshold current dependence of internal quantum efficiency can be obtained by rewriting equation (3.7) as;

$$\eta_{in} = \frac{P_{in} - (P_{act} + IV_L + P_L)}{I_{th}E_g} \tag{3.15}$$

where all the parameters are as defined previously.

The value of η_{in} decreases with the increase of I_{th}, which increases with temperature. Consequently the effect of temperature on the internal quantum efficiency is shown in figure 3.7 along with the results of reference-4. The data of figure 3.7 is calculated from figures 3.1 and 3.5 by using equations (3.1), (3.10) and (3.15). The rates of change of η_{in} with the heatsink temperature in the case of UB238 and UB262 is very close to the results presented by Suyuma *et al* [4]. The lower value of η_{in} for UB262 is due to a lower value of η_D as a direct consequence of increase in the spreading of electrical carriers and optical carriers in lateral direction due to the narrower stripe width.

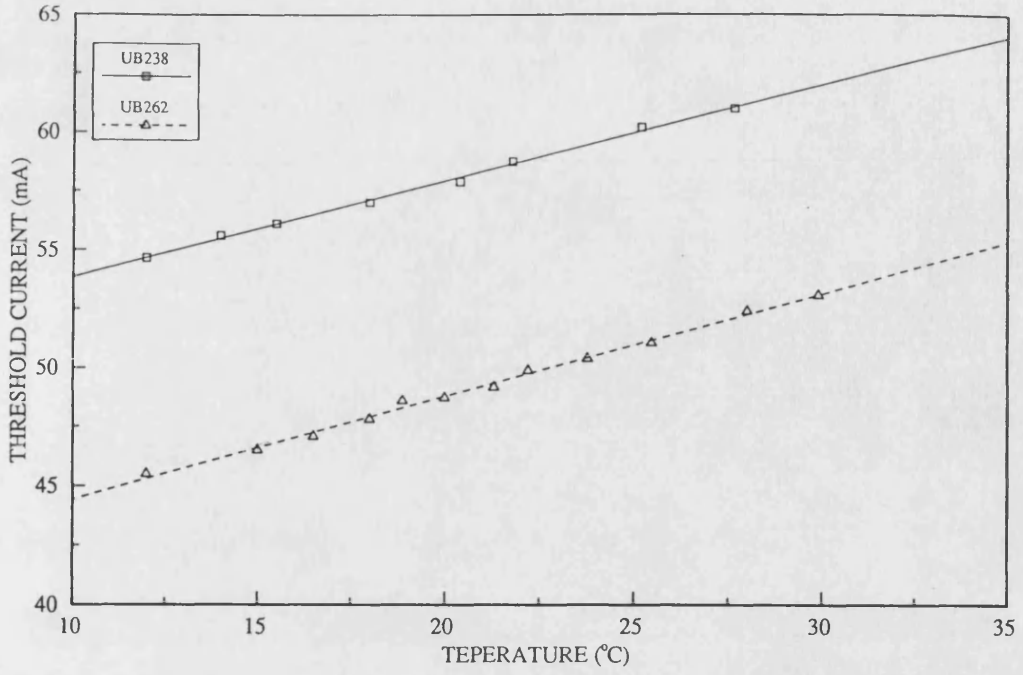

Figure 3.5. The effect of temperature rise on the threshold current of the laser diode as a function of stripe width.

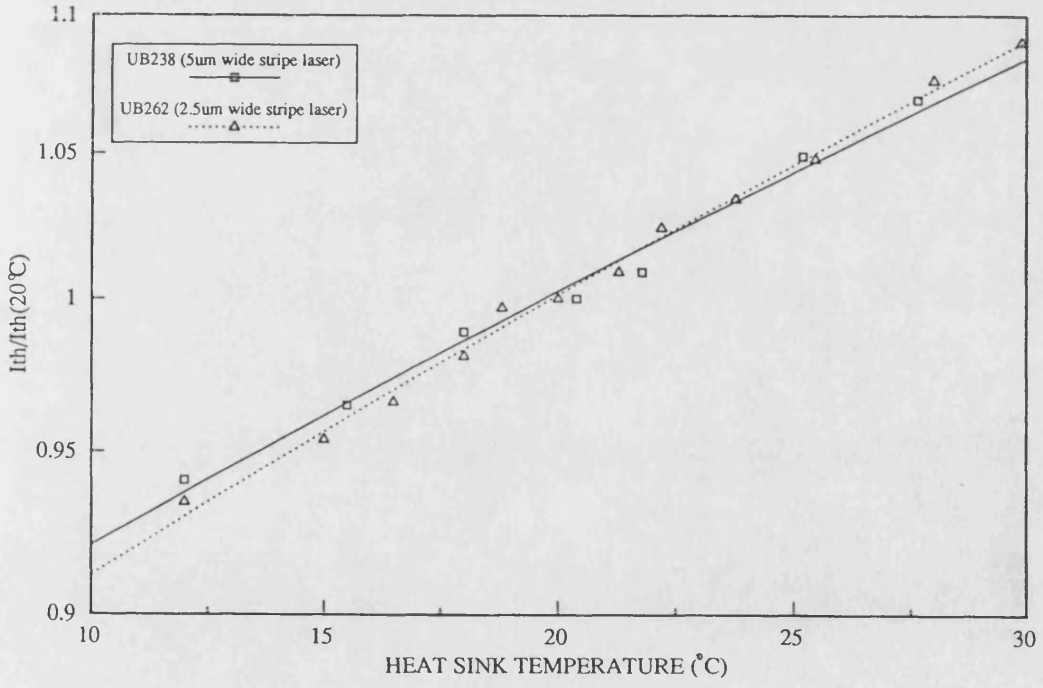

Figure 3.6. Characteristics temperature curves for 5μm wide stripe laser and 2.5μm wide stripe laser. The slope of curve gives the value of characteristic temperature for the each device.

The total losses inside the laser cavity can be calculated by making the use of the temperature dependence of η_{in} and by using equations (2.52) and (3.15) provided all the parameters in equations (2.52) and (3.15) are known. By comparing equations (2.52) and (3.15) one can write the threshold condition of equation (2.48) as;

$$\Gamma g_{th} = \frac{1}{L\eta_D} \ln \frac{1}{R} \left[\frac{P_{in} - (P_{act} + IV_L + P_L)}{I_{th} E_g} \right] \tag{3.16}$$

This equation can be used to calculate the required threshold gain and hence total internal losses of a laser diode without using the complicated and lengthy techniques [10-12].

By using equation (2.52) along with figure 3.7, the losses inside UB238 were calculated to be approximately 26.5±0.47/cm. This value is close to the loss value of chapter-2 measured using a different method. Similarly, the loss value for UB262 can be estimated from figure 3.7 at 20°C, to be approximately 28/cm. The increase in the value of α is due to the two reasons; (a) an increase in free carrier absorption losses, since UB262 has been shown to have a higher temperature sensitivity than that of UB238 and (b) optical mode spreading in the lateral direction due to narrower stripe width.

3.6. Temperature dependence of spectral characteristics

In previous sections, the temperature dependent properties of different Fabry-Perot laser devices have been investigated by using their power dissipation characteristics and the temperature dependence of the threshold current. The rise of the active layer temperature also has important consequences for the operating wavelength and this effect is used in this section to investigate the temperature dependence behaviour of not only the FP laser but also the other OIC components such as the A.R. coated optical amplifier.

For this purpose, the output spectrum of different laser devices has been

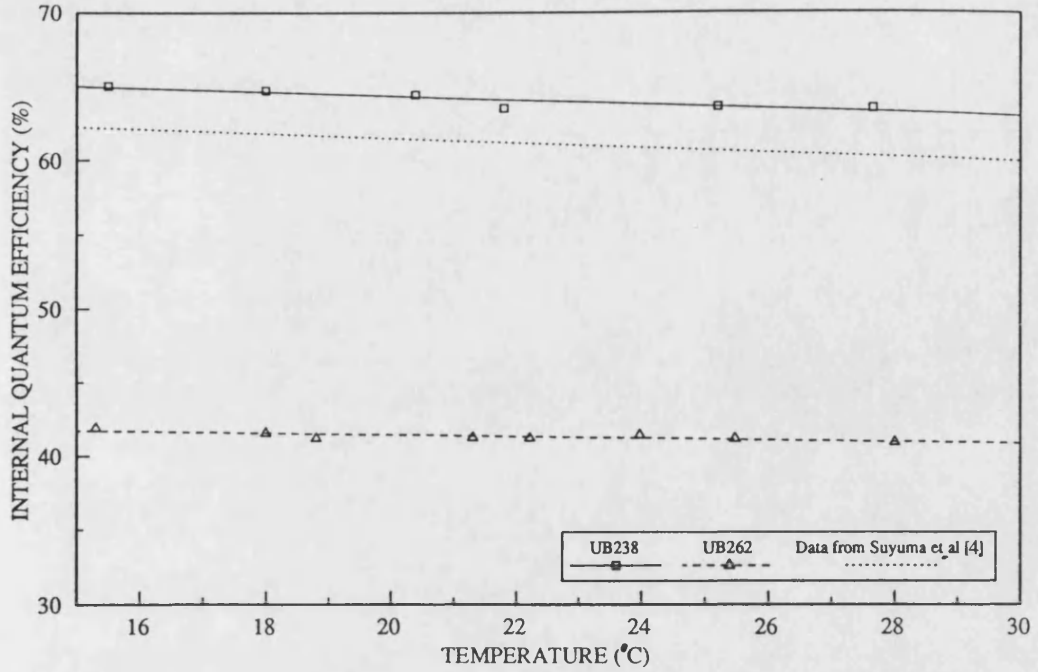

Figure 3.7. Figure showing the temperature dependence of internal quantum efficiency.

measured using a SPEX 1000 monochromator. The resolution of this monochromator was enhanced by using 0.25mm slit at the input and at the output of the monochromator. An X-Y plotter was used to plot the output from the optical detector against wavelength at different values of heatsink temperature using the experimental set-up of figure 2.28. All measurements were done at a constant drive current of 80mA to avoid wavelength shift due to changes in the injected carrier density. The value of the peak emission wavelength was measured as a function of the heatsink temperature for UB238, UB258, UB259 and UB262 and these are plotted in figure 3.8.

From figure 3.8, the rate of change of peak emission wavelength with the heatsink temperature was calculated to be 0.245±0.014nm/degree, 0.241±0.018nm/degree, 0.173±0.014nm/degree and 0.192±0.01nm/degree for laser sources UB238 and UB262 and A.R. coated devices UB259 (two side coated device) and UB258 (single side coated device) respectively. These values are in very close agreement with the reported values of 0.245nm/degree for Fabry-Perot lasers [13] and 0.19nm/degree for superluminescence diodes [14]. The lower value of $d\lambda/dT$ for A.R. coated devices is shown to be much smaller than that of uncoated devices. This shows that the A.R. coating on laser facet reduces the temperature sensitivity of a device.

The observed wavelength shift towards higher wavelength with the increase in temperature is usually attributed to: i) the increase in the cavity length, and ii) to the narrowing of the bandgap.

The increase in the cavity length is expected to be relatively small for GaAs heterojunction lasers because of a small expansion coefficient of $5.85x10^{-6}$ [15,16] for GaAs. Therefore, one can conclude that shift in the peak emission wavelength is mainly due to the band gap contraction of GaAs [13]. The peak emission wavelength is related to the bandgap of a semiconductor, E_g, by simple relation;

$$E_g = \frac{1.24}{\lambda} \tag{3.17}$$

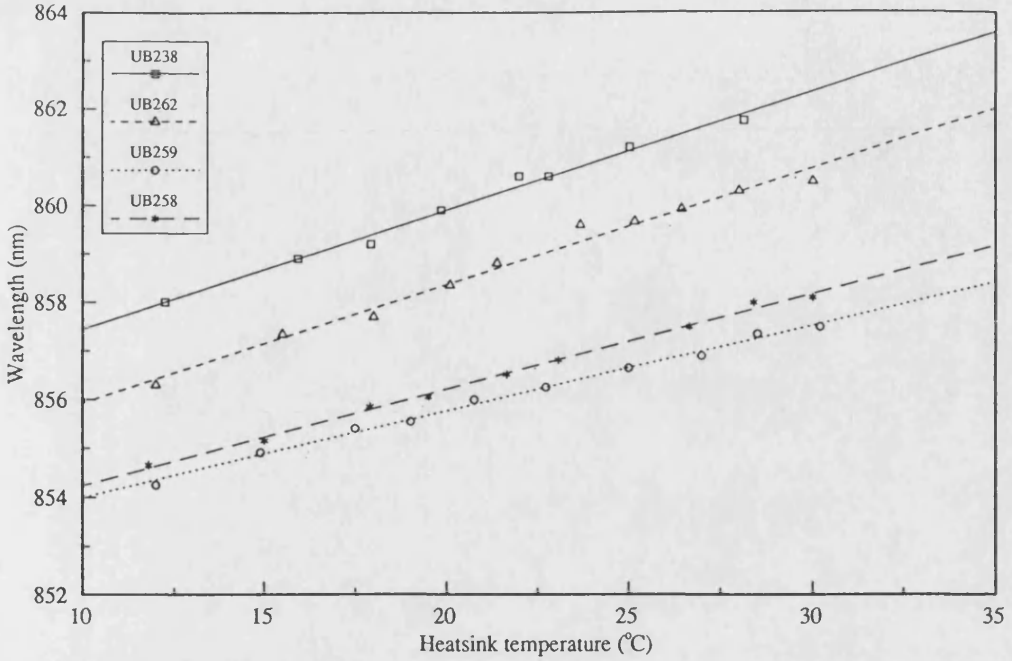

Figure 3.8. Change in the peak spectral wavelength with the heatsink temperature.

Figure 3.9 is showing the reduction in the bandgap with temperature. The effect of temperature on spectral characteristics of different devices is summarised in table 3.1 below. The values of dE_g/dT in table 3.1 for the FP devices (UB238 and UB262) are in close agreement with the reported value of 0.43meV/°C in reference-13.

TABLE 3.1. *Table showing the rate of change of peak emission wavelength with temperature for different devices.*

Device number	$\frac{d\lambda}{dT}$ (nm/°C)	$\frac{dE_g}{dT}$ (meV/°C)
UB238	0.245±0.014	0.409±0.023
UB262	0.241±0.018	0.404±0.03
UB259	0.173±0.014	0.298±0.024
UB258	0.192±0.01	0.33±0.017

3.7. Thermal rise time

The thermal rise time is a property of a laser device which defines the heat capacity of that device. When a laser source is driven with a current pulse, I, where $I>I_{th}$, the temperature of laser chip will increase and hence the wavelength will change transiently before finally reaching a steady state wavelength. The thermal rise time of a particular laser can be evaluated from the I-L characteristics of a laser diode and also from the output spectrum of a laser diode. Here both properties have been used to estimate the thermal rise time by analysing the transient temperature response of different devices.

3.7.1. Transient temperature variations

The transient temperature variation (TTV) of a particular FP laser device can be obtained from I-L characteristics of that device [17]. But for other active OIC

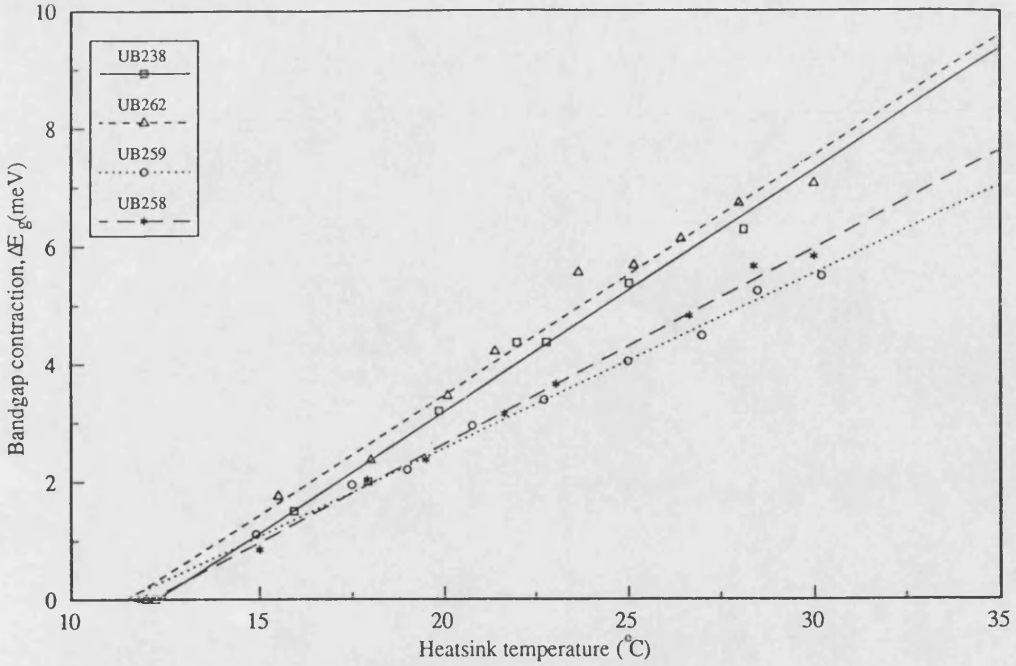

Figure 3.9. The effect of temperature on GaAs laser diode bandgap.

components such as the optical amplifier, there is no reported method available. The main purpose of this section to develop a method which could be used to calculate the transient temperature response of all active OIC components.

3.7.1.1. TTV evaluated from I-L characteristics

Suppose a laser diode is driven with a constant amplitude pulse and the optical output power is detected by a detector. Assume that the maximum output which corresponds to the lowest temperature, T, is P_L at some instant of time, t, as shown in figure 3.10(a). Also suppose after a time interval, Δt, the temperature has increased by ΔT and the optical output power has reduced by ΔP_L. The effective threshold current at this instant of time will have shifted to a higher current, $(I_{th}+\Delta I)$, as shown in figure 3.10(b) (assuming the change in η_D is insignificant [4] and it is evident from figure 3.5). The rise in threshold current at that instant of time along the pulse corresponds to a temperature rise. The rise in temperature along the current pulse can be calculated by rewriting the equation (3.14) as;

$$\Delta T = T_o \ln\left(1+\frac{\Delta I_{th}}{I_{th}(20^oC)}\right) \tag{3.18}$$

The I-L characteristics at different instants of time along the 200ns pulse have been measured for UB238 and UB262 while the heatsink temperature was kept at 20°C. The change in the threshold current along the pulse is shown in figure 3.11. A dip at initial stages can be seen. Initially, I_{th} increases slowly. After a certain time, the temperature begins to increase much faster due to the heat generated in the active region penetrating into other layers and to the heatsink. This rise in the threshold current finally begins to saturate after 40-50ns to its saturation value. This change in the threshold current at the different interval of time corresponds to an equivalent temperature rise and the rise in temperature is calculated along the pulse using equation (3.18). The calculated values of ΔT are plotted against time in figure 3.12 which shows the transient temperature variation along the pulse for UB238 and UB262.

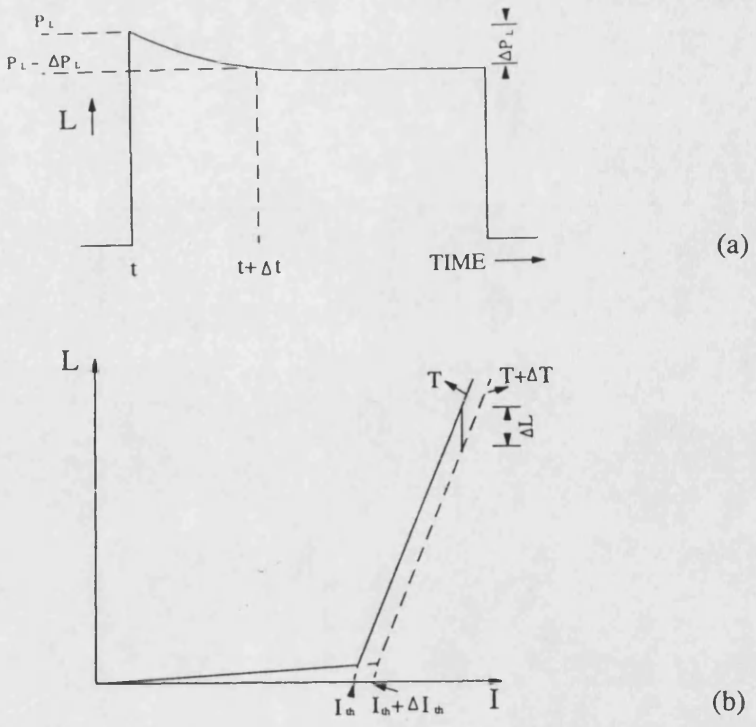

Figure 3.10. The effect of temperature rise on the laser output; (a) variation in the output along the pulse and (b) the effect of temperature different parameters.

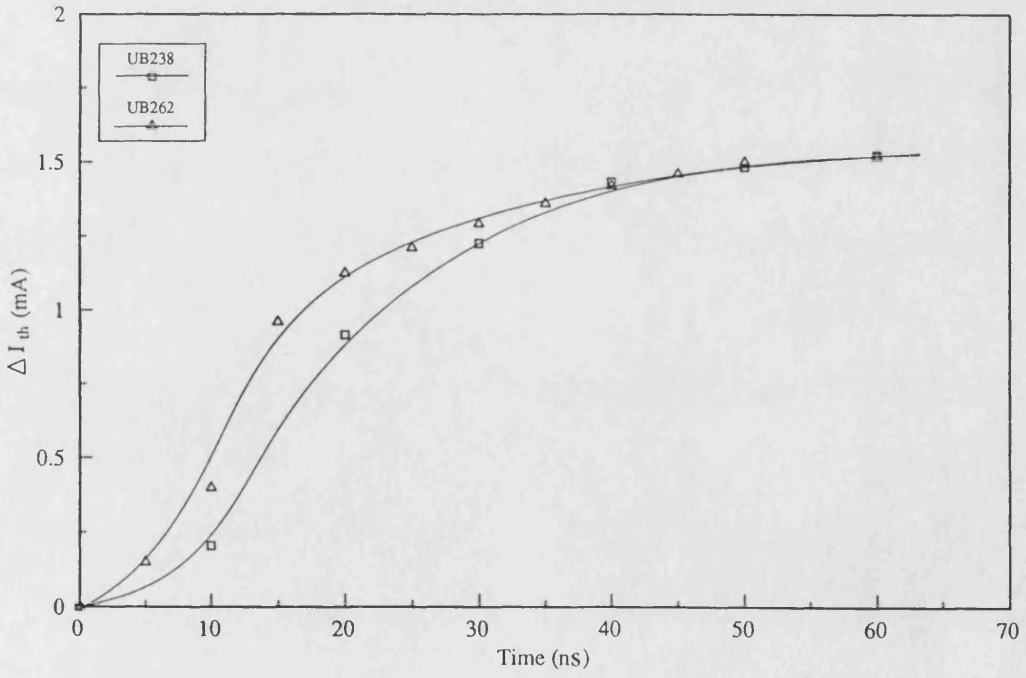

Figure 3.11. Variation in the threshold current along the pulse for UB238 and UB262.

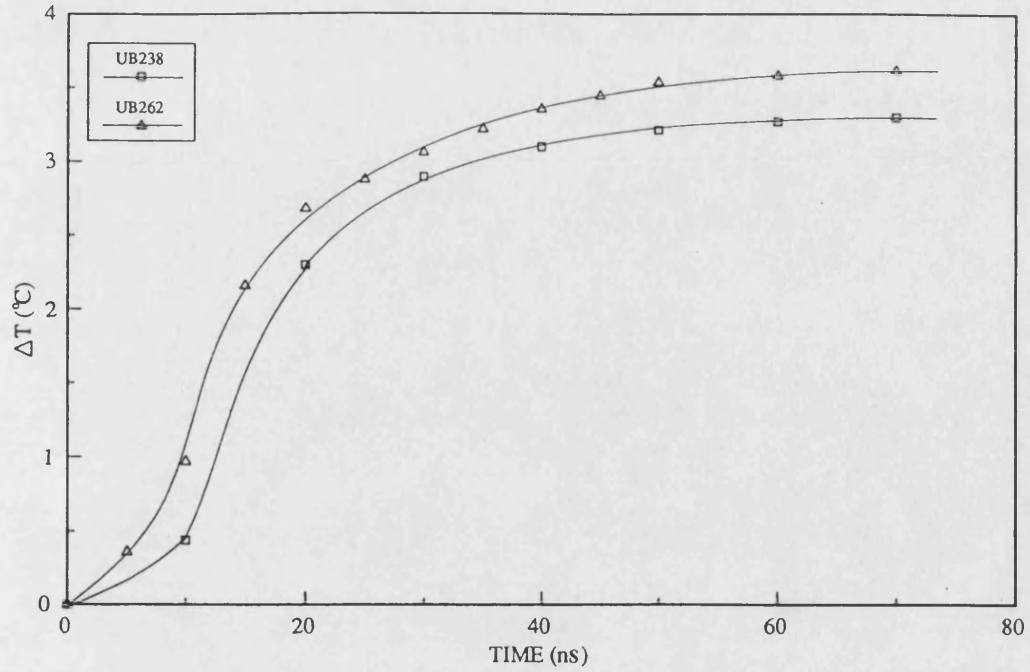

Figure 3.12. The transient temperature response of UB238 and UB262 evaluated from I-L characteristics.

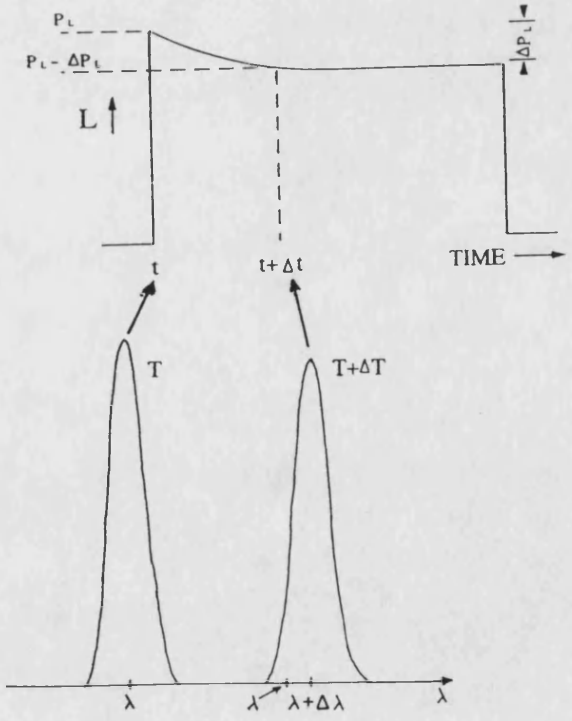

Figure 3.13. Schematic representation of the effect of temperature rise on peak emission wavelength along the pulse.

3.7.1.2. Evaluation of TTV from the spectral characteristics

The transient temperature variation was analysed in section 3.7.1.1. using the I-L characteristic for FP lasers as a function of stripe width. The transient temperature variation of the laser can also be evaluated by analysing the change in the spectrum of the laser device along the 200ns current pulse since the temperature increases along the pulse and the peak emission wavelength shifts towards higher wavelengths as shematically shown in figure 3.13. It is also possible to draw the transient temperature response of non-lasing devices (such as A.R. Coated devices) using the output spectral characteristics.

The effect of temperature on the spectrum of the device output was measured using the experimental set-up of figure 2.28 at a heatsink temperature of 20°C for the 200ns pulse for UB238, UB262, UB259 and UB258 by sampling the output from the monocromator along the pulse. Figure 3.14 shows the variation of the spectral peak along the 200ns pulse for these devices. The transient variation of peak wavelength is very similar to the transient variation in threshold current. These variations are calibrated to temperature rise, ΔT, by plotting the transient temperature variation for UB238 and UB262 evaluated from I-L characteristics (of section 3.7.1.1) and spectral characteristics in figure 3.14. Figure 3.15 finally gives the transient temperature variation curves for all four devices on a calibrated scale.

3.7.2. Calculation of thermal rise time

Because of the high thermal resistance of the different layers between the copper block and the active region, and also due to the heat capacity of copper block, the transient temperature response tends to vary exponentially above the heatsink temperature till reaching the steady-state with a single predominant time constant. Transient temperature rise for a copper block is defined as [18];

$$T(t) = T_r + T_m\left[1 - \exp\left(\frac{-t}{\tau}\right)\right] \tag{3.19}$$

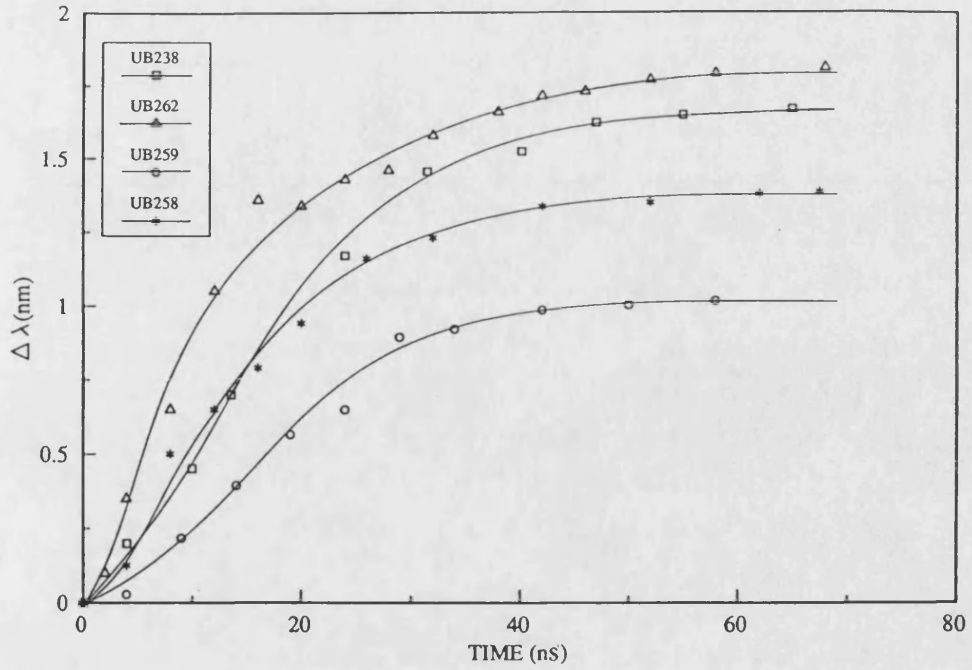

Figure 3.14. The transient temperature response of UB238, UB262, UB259 and UB258 evaluated from spectral characteristics.

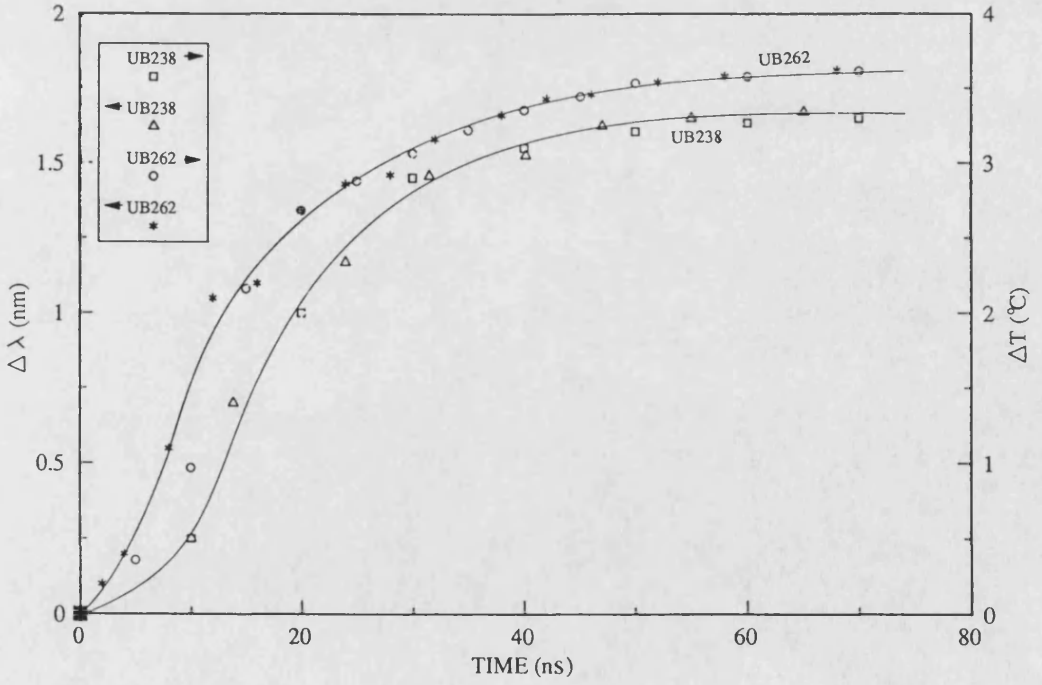

Figure 3.15. Comparison between transient temperature response evaluated from I-L and spectral characteristics.

where T_r is the reference temperature (which is 20°C in our case), T_m is steady-state value of temperature rise, t is the time along the pulse and τ is the thermal rise time .

Equation (3.19) can be re-written as;

$$t = -\tau \ln\left[1 - \frac{T(t) - T_r}{T_m}\right] \tag{3.20}$$

where $[T(t) - T_r]$ is equal to the ΔT in figure 3.15. Therefore;

$$t = -\tau \ln\left[1 - \frac{\Delta T}{T_m}\right] \tag{3.21}$$

In figure 3.16, $\left[1 - \frac{\Delta T}{T_m}\right]$ is plotted against time along the pulse. The slope of each curve gives the thermal rise time of that particular device. Thermal rise times are calculated as 86ns, 90ns, 72ns and 77ns for UB238, UB262, UB259 and UB258 respectively. 200nS pulses, which are used throughout this chapter, are sufficiently long to achieve a steady-state output by sampling at the end of pulses being injected to the devices. The difference in thermal rise time indicates that the different devices have slightly different temperature dependent behaviour. It is interesting to note that the thermal time constant decreases with the A.R. coating.

3.8. Requirement for CW operation

Even though, during the work reported in this thesis all laser devices were run under pulse mode in order to avoid the excess heating, the active layer temperature raised significantly above the heatsink temperature. This can place limitations on the maximum CW output power not only for that particular device but also for other devices which might be integrated on same substrate. If an attempt is made to operate that device continuously then the operating current needs to be increased as I_{th} is increased with temperature. In this section, the expected temperature rise of devices operating under CW conditions are extrapolated from the transient results.

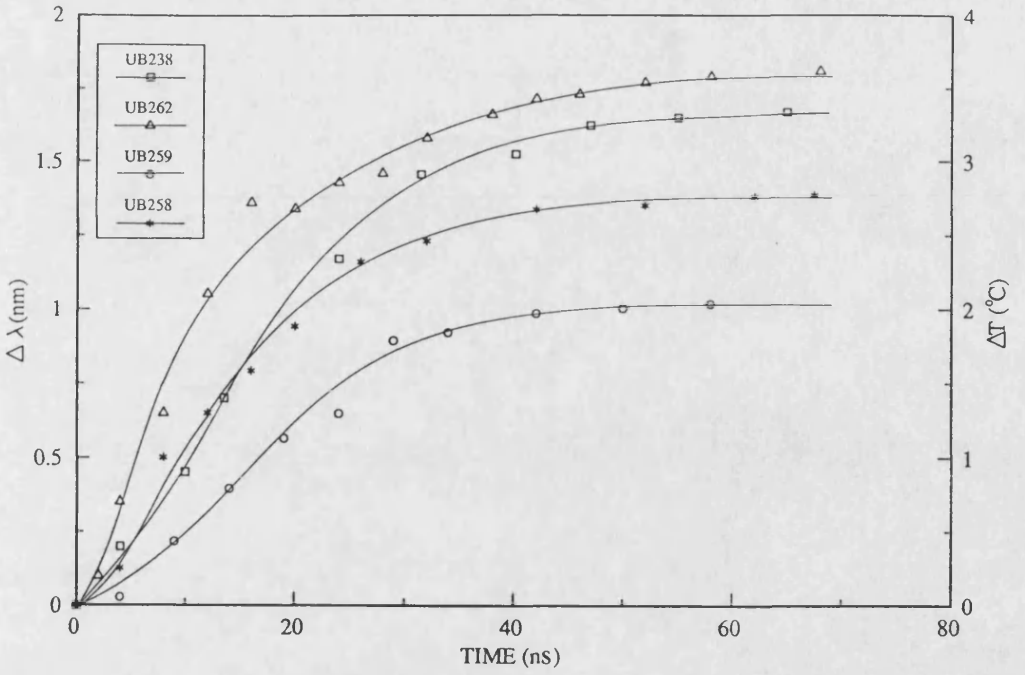

Figure 3.16. The extension of thermal step (transient temperature) response measurement to A.R. coated devices (optical amplifiers).

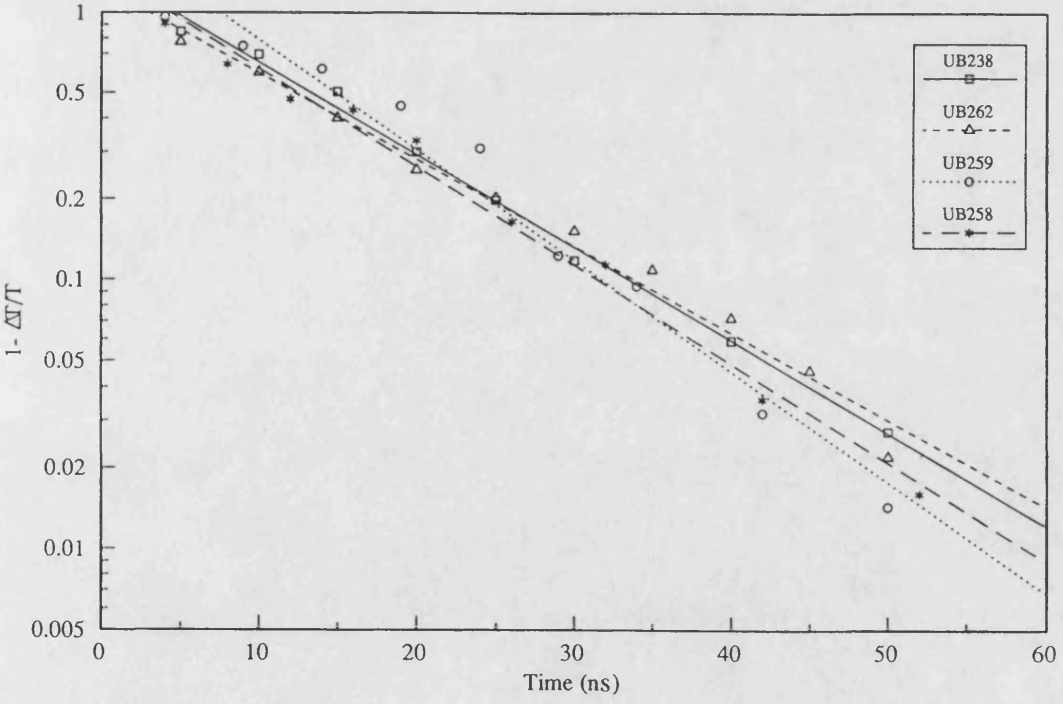

Figure 3.17. Thermal rise time calculation curve for different devices.

Whether the device is running in pulse mode or CW, three quantities are needed to be considered very carefully. These quantities are the threshold current, maximum heatsink temperature and junction temperature. For CW operation they are defined as [19];

$$I_{thc} = I_{th} \exp\left\{\frac{\Delta T_{jc} - T_r}{T_o}\right\} \tag{3.22}$$

$$T_{hc} = T_r + T_o \ln\left(\frac{I_{thc}}{I_{th}}\right) - \frac{T_o + R_{th} E_g I_{thc}}{2} \tag{3.23}$$

and

$$\Delta T_{jc} = T_r + T_o \ln\left(\frac{I_{thc}}{I_{th}}\right) \tag{3.24}$$

where I_{thc} is the threshold current in CW mode, T_{hc} is the heatsink temperature (above the ambient temperature) for CW operation, ΔT_{jc} is the rise in junction temperature for CW operation and T_a is the ambient temperature.

By looking at figure 3.4, it can be seen that UB238 and UB262 were safely operated at 15°C and 27°C above the heatsink temperature (20°C). If this value is considered as a safe value for CW operation, then I_{thc} for UB238 and UB262 comes out to be 65.84mA and 62.85mA and required heat sink temperature, T_{hc}, calculated as 243°K and 254°K for UB238 and UB262 respectively.

The calculated value of the heatsink temperature makes it a bit risky to use the device under investigation in CW mode because it is very difficult to maintain that range of low temperature by using the temperature controller which is used in this work. On the other hand, the required heatsink temperature can be increased by decreasing the threshold current (pulse or CW both), electrical series resistance and by reducing the thermal resistance. The characteristic temperature can be increased by improving the material quality (by growing defect free material), by using a quantum well structure or by increasing the Al content in the active layer. I_{th} can be reduced by controlling the spreading of carrier in lateral direction. The

electrical series resistance can be reduced to 2Ω [20] by reducing the contact resistance. The thermal resistance can be minimized by increasing the stripe width or junction down mounting.

3.9. Summary

In this chapter, the temperature dependence properties of OIC components have been investigated by using a three channel temperature controller which was developed during the work reported in this thesis.

The origin of heat sources inside a semiconductor laser diode has been discussed and the rate of heat dissipation, P_{acr} found to be around half of the input power, P_{in}. The active layer temperature above the heatsink temperature has been estimated by using the rate of power dissipation in the active layer and thermal resistance. The active layer temperature was found to be higher than that of the heatsink block which saturates along the current pulse and found to be dependent upon the stripe width.

The temperature dependence of the threshold current has been analysed and the characteristic temperature for UB238 and UB262 have been measured by using the family of I-L characteristics at different heatsink temperatures. By using the output power dissipation and temperature dependence the threshold current characteristics, a novel, non-destructive loss measurement technique has been demonstrated. The validity of this novel loss measurement technique was achieved by comparing the result obtained using this technique with that was obtained in chapter 2 (using a length dependent loss measurement technique [10]). This technique was further validated by measuring internal losses of 2.5μm wide stripe laser, UB262. The measured value for internal losses for 5μm and 2.5μm wide stripe lasers were found to be close to each other, which justify the ignorance of optical mode spreading in the lateral direction while calculating Γ. The value of α obtained in this chapter will be used later in chapter 5 to measure the unsaturated local gain of an amplifier.

The effect of temperature on the spectral characteristics were also investigated and the transient change in the peak emission wavelength with temperature has been calculated from output spectrum at different temperatures for several devices. The contraction of bandgap was felt to be the main reason for the change in the peak emission wavelength with temperature. The change in the peak emission wavelength will be used in for wavelength calibration of the active waveguide optical detector (chapters 4) and to achieve wavelength tuning of input radiation with the amplifier intrinsic wavelength (chapters 5 and 6).

The transient temperature variation of different FP devices has been evaluated from their I-L characteristics and spectral characteristics. The spectral characteristics were also used to evaluate the transient temperature variations of A.R. coated amplifiers. By comparing the transient temperature variation evaluated from I-L and spectral characteristics for FP devices, a new technique for the measurement of thermal rise time was developed and by using this technique, the thermal rise time of an A.R. coated optical amplifier was calculated. It is believed that this is the first time that the technique has been used for an optical amplifier. The maximum value of thermal rise time was achieved as 90nS and 200nS biasing pulses are expected to be long enough to achieve stable output. Therefore, through out the work reported in this thesis, 200nS pulses are used to run laser source and output is sampled at the end of the pulse to achieve steady-state output.

REFERENCES

1. Powell, V.A., 'The design and test of thermo-electric controller suitable for the control of a laser diode temperature', B.Eng. thesis, University of Bath, 1983.
2. Engeler, W. and Garfinkel, M., 'Thermal characteristics of GaAs laser junctions under high pulsed conditions', Solid-state Electronics, vol.8, p.585, 1965.
3. Casey, H.C.Jr., and Panish, M.B., 'Heterostructure lasers, Part-B, Material and operating characteristics', Academic Press, 1978.
4. Suyama, M., Ogasawara, N. and Ito, R., 'Transient temperature variation of injection lasers', Jap. J. Of Appl. Phys., vol.20, p.l395, 1981.
5. Mroziewics, B., Bugajski, M., and Nakwaski, W., 'Physics of semiconductor lasers', North-Holland and PWN - Polish Scientific Publisher, 1991.
6. Joyce, W.B. and Dixon, R.W., 'Thermal resistance of heterostructure lasers', J. Of Appl. Phys., vol.46, p.855, 1975.
7. Pankove, J. I., 'Temperature dependence of emission efficiency and lasing threshold in laser diodes', IEEE J. Of Quantum Electron., vol. QE-4, p.119, 1968.
8. Ettenberg, M., Nuese, C.J. and Kressel, H., 'The temperature dependence of threshold current for double-hetrostructure lasers', J. Appl. Phys., vol.50, p.2849, 1979.
9. Chin, R., Holonyak Jr., N. and Vojak, B.A., 'Temperature dependence of threshold current for quantum-well $Al_xGa_{1-x}As$ heterostructure laser diodes', Appl. Phys. Letters, vol.36, p.19, 1980.
10. Pinkas, E., Miller, B.I., Hayashi, I., and Foy, P.W., 'Additional data on the effect of doping on the lasing characteristics of GaAs-$Al_xGa_{1-x}As$ double heterostructure lasers', IEEE J. Of Quantum Electron., vol. QE-9, p.281, 1973.
11. Hakki, B.W., and Paoli, T.L., 'Gain spectra in GaAs double heterostructure injection lasers', J. Of Appl. Phys., vol.46, p.1299, 1975.
12. Andrekson, P.A., Olsson, N.A., Tanbun-Ek, T., Logan, D., Coblentz, D., and Temkin, H., 'Novel technique for determining internal loss of individual semiconductor lasers', Electron. Lett., vol.28, p.171, 1992.
13. Kressel, H., and Butler, J.K., 'Semiconductor lasers and heterostructure LED's', Academic Press, 1977.
14. Dyment, J.C., Cheng, Y.C., and Spring Thrope, A.J., 'Temperature dependence of spontaneous peak wavelength in GaAs and $Ga_{1-x}Al_xAs$ electroluminescent layers', J. Of Appl. Phys., vol.46, p.1739, 1975.
15. Novikova, S.I., 'Thermal Expansion', in Semiconductor and Semimetals vol:2, Ed. Willardson, R.K. and Beer, A.C., p.33, Academic Press, 1965.
16. Novikova, S.I., 'Investigation of thermal expansion of GaAs and ZnSe', in Keypapers in Physics, Gallium Arsenide, Ed. Blackmore, J.S., p.136, The American Institute of Physics, 1987.
17. Hausien, H.H., 'Pulse position modulation for optical fibre local area networks', Ph.D. thesis, University of Bath, 1991.

18. Abdelkadir, H.I., 'Electronic control of semiconductor laser for an optical fibre packet lan', Ph.D. thesis, University of Bath, 1988.
19. Hsieh, H.C., 'Maximum heat-sink temperature for CW operation of a double-heterostructure semiconductor injection laser', IEEE J. Of Quantum Electron., vol. QE-25, p.2079, 1989.
20. Yano, M., Imai, H., Hori, K.J., And Takusagawa, M., 'High temperature characteristics of stripe-geometry InGaAsP/InP double-hetrostructure lasers', IEEE J. Of Quantum Electron., vol. QE-17, p.619, 1981.

Chapter-4

Optical radiation detection properties of active waveguide optical detectors

4.1. Introduction

The optical detector is an essential component of OIC and optical fibre communication systems as it ultimately limits the overall system performance. Semiconductor *p-n* junction devices are widely used for the detection of optical radiation. As direct modulation bandwidth reaches 30 GHz [1], the need of a photodetector with high speed and high quantum efficiency, becomes more pressing. Although the speed of the Schottky-barrier and the GaAs Schottky photodetectors has reached 100 GHz [2] and 58 GHz [3] respectively, these speeds place severe limitations on the quantum efficiencies of the diodes and values as low as 5% have been recorded at these modulation rates. Furthermore, if a structure is designed for monolithic OIC circuit, then it must be a thin layer structure which must be compatible with other optical and electronic components. Bearing this idea in mind, monolithic and discrete laser-like structures are used as detectors in this chapter. This chapter serves a dual purpose. On the one hand, the theory and characteristic performance of the waveguide detector as an active component for OIC is presented. On the other hand, a reliable alignment technique for the alignment of discrete active optical components is developed to compare the results of the monolithic detector with that of the hybrid one.

As the active waveguide optical detector shares the same operating mechanism with that of conventional photodetectors, the investigation initially highlights the basic operating principle of an optical detector in section 4.2. Section 4.3 lists

the main advantages and properties of an active waveguide optical detector (AWOD) over the conventional optical detector. Section 4.4 through section 4.6, outline the basic theoretical background and discuss the main limitations of the waveguide detector. Section 4.7 provides the main core of the experimental results using monolithic and hybrid approaches. This section also provides a detailed investigation on the optical flux leakage process through active components. The main points from this chapter are summarised in section 4.8.

4.2. General operating principle of optical detector

A photodiode is capable of detecting radiation with photon energy $h\nu > E_g$, where E_g is the energy gap of the semiconductor and $h\nu$ is the energy of the incoming photons. When the junction is reverse biased (figure 4.1), the electric field develops across the *pn*-junction and creates depletion regions on either side of the junction, which prevents the majority carriers from crossing the junction. However, the field accelerates the minority carriers from both sides to the opposite sides of the junction forming the leakage current of the diode.

When a photon is incident in or near the depletion region with energy $h\nu \geq E_g$, it will excite an electron from the valance band into the conduction band , thus creating an electron-hole pair. If the incoming photon is absorbed at point '*A*', it will create a hole and free an electron. If this takes place within the diffusion length of depletion region, the electron with higher probability will reach the layer boundary and will contribute a moving charge of e to the external field. This induces a displacement current in the external circuit until the electron reaches the neutral region. If the photon is absorbed at point '*C*', a hole will contribute a charge e to the external circuit. The photon may also be absorbed at point '*B*', in this case, both the electron and hole drift to opposite sides of the depletion region. Each carrier transverses less distance than that of a full junction width. The last process is more desirable in practice since each photon absorption gives rise to a charge e and the delayed current response caused by the finite transit time across

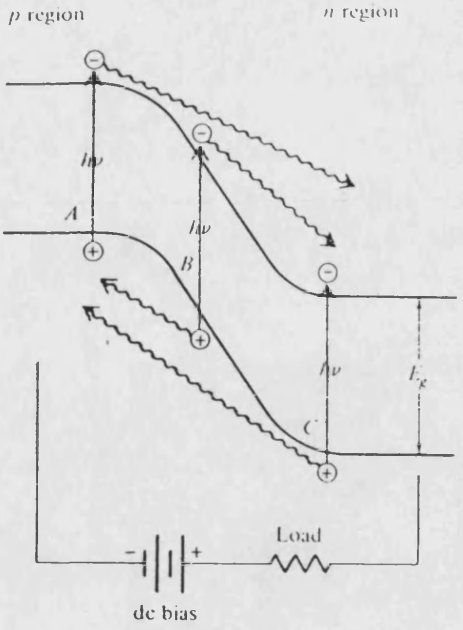

Figure 4.1. Electron-hole creation process in a photodiode.

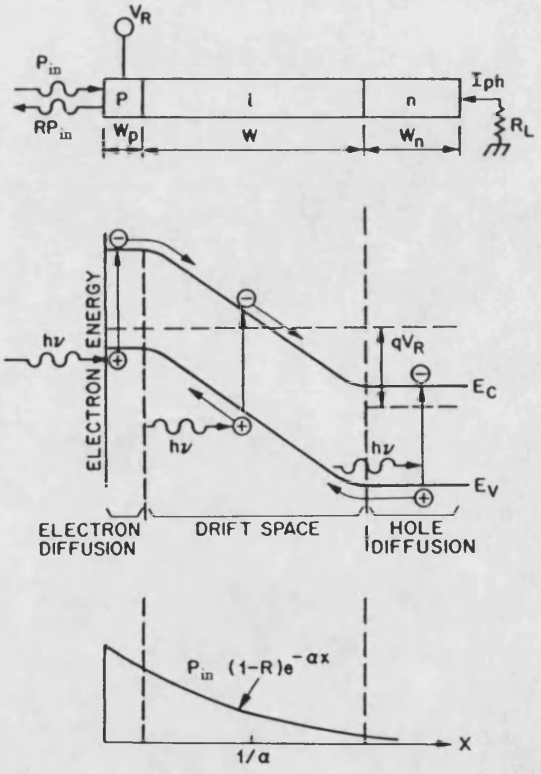

Figure 4.2. Schematic diagram showing the operation of a *pin* photodiode; (a) cross-sectional view, (b) energy band diagram under reverse bias and (c) carrier generation characteristic [4].

the depletion region is reduced. To reduce the transit time, the carriers must drift at a very high rate. This requires that the field in the drift region is very high. In order to give a near uniform field in the drift region, it is usual to grow a intrinsic layer between the *p* and *n* regions. This also prevents premature reverse breakdown of the diode.

The basic detection process in a reversed biased *pin* photodiode along with energy band diagram and carrier generation characteristics is shown in figure 4.2. For this detector, the ultimate limit for the response time is defined by the transit time of photogenerated carriers. Any attempt to minimize the transit time by minimizing the depletion layer width would result in reduction in radiation absorption, hence reducing the detector quantum efficiency. This problem is more severe in direct bandgap semiconductor like GaAs which have low absorption coefficient. There are two approaches to overcome this limitation [5];

1. Multiple reflection structure,
2. Edge-illumination structure.

Both involve making the optical path length longer than the diode depletion region in order to allow the incident light to absorb completely. The latter approach could be applied to laser structure (monolithic or discrete) by applying reverse bias voltage to use it as waveguide photodetector to detect optical radiation [6] while the incident radiation falls perpendicularly to the junction.

4.3. Advantages of the waveguide photodetector

The waveguide photodetector has several advantages over the conventional photodetector, discussed above; namely:

1. High speed and high efficiency can be achieved at zero bias [3,7,8] because the direction of incident radiation and carrier collection are normal to each other.
2. The zero bias operation not only offers circuit simplicity but also makes the dark noise negligible which help to improve signal to noise ratio [8,9].

3. It can be used as frequency multiplexer and demultiplexer by tuning it to a particular wavelength [10].

4. Finally, these detectors have a similar structure to a laser and hence they are relatively easy to integrate into complex OIC's.

4.4. Responsivity of the active waveguide optical detector

In a conventional photodetector under steady-state conditions, the total current density through the reverse biased junction is given by [11];

$$J_{tot} = J_{dr} + J_{diff} \tag{4.1}$$

where J_{dr} is the drift current density due to carriers generated inside the depletion region and J_{diff} is the diffusion current density due to carriers generated outside the depletion layer.

A semiconductor laser structure under reverse bias or zero bias conditions can act as an active waveguide optical detector (AWOD). In the AWOD, the adjacent layers consist of wider bandgap material and only contribute to the photocurrent if the low energy tail exists in the absorption profile. Moreover, in the OIC, the light source is expected to be of a same material and would have an energy close to or equal to the bandgap energy of the AWOD. Therefore the total current density in AWOD can be obtained as;

$$J_{tot} = J_{dr} = -e \int_0^L G(x)dx \tag{4.2}$$

where $G(x)$ is hole-electron pair generation rate. Referring to figure 4.2c it is given by [11];

$$G(x) = \Gamma \alpha P_{in} \exp(-\alpha x) \tag{4.3}$$

where P_{in} is the total incident photon flux, L is the length of the detector and α is the total absorption losses.

When a laser diode is used as the source of optical power, there are three contributors to the laser losses as described in section 2.3.4. But when the laser

diode is used as a photodiode, the total losses inside an active waveguide take the form [9];

$$\alpha = \Gamma\alpha_{fc} + (1-\Gamma)\alpha_{fc} + \alpha_s + \Gamma\alpha_{ib} \tag{4.4}$$

Here a term for interband absorption, α_{ib}, is included because the photodetector response depends on the band-to-band absorption, where as laser emission usually involves band-to-accepter transitions [12]. Equation (4.4) can be simplified using the arguments of section 2.3.4 to;

$$\alpha \approx \Gamma\alpha_{fc} + \Gamma\alpha_{ib} \tag{4.5}$$

The effect of free carrier losses in the active waveguide photodetector can be neglected because the active region has non or very low doping concentration and the response of a photodiode depends upon band-to-band absorption. Finally for a semiconductor waveguide detector one can write;

$$\alpha \approx \Gamma\alpha_{ib} \tag{4.6}$$

Usually the photo sensitive region is small and it is difficult to couple the optical radiation efficiently into the device. Furthermore, due to the finite facet reflectance of a semiconductor laser photodetector, a significant fraction of light will be reflected at the surface. The quantity which defines the fraction of incident photons which are absorbed and generate the photo-current is called the differential quantum efficiency and given as [13];

$$\eta = \xi(1-R)\left(1-e^{-\Gamma\alpha_{ib}L}\right) \tag{4.7}$$

where R is the facet reflectivity.

By making a simplifying assumption that the factor ξ (which represents the fraction of electron-hole pair that successfully contribute to the useful photocurrent) is equal to unity, equation (4.7) can be written as;

$$\eta = (1-R)\left(1-e^{-\Gamma\alpha_{ib}L}\right) \tag{4.8}$$

It is clear from equation (4.8) that by reducing the facet reflectance of the end facet, the quantum efficiency can be increased and this is normally achieved by applying an A.R. coating on the facet. The quantum efficiency can also be

increased by increasing the length of the device but a device length of $30\mu m$ has been used successfully [7]. Clearly, for a waveguide detector such as this device, lengths of 100-$300\mu m$ are not impractical.

The expression of equation (4.8) for the quantum efficiency does not involve photon energy and therefore, the term responsivity, $\mathcal{R}$, is often of more use when characterising the performance of a photodetector and is defined as;

$$\mathcal{R}=\frac{\eta e\lambda}{hc} \tag{4.9}$$

where c is the speed of light in air, h is the Plank's constant and λ is the wavelength of incident radiation.

4.5. High frequency response of AWOD

One of the major consideration of the active waveguide optical detector is the ability to respond to transient variations in incident radiation. In general, a time varying incident optical radiation, $P_{in}(t)$, generates a time varying current $i_{ph}(t)$ and produces a time varying voltage $v(t)$ at the load R_L. The frequency response of a photodetector will be limited by;

1. The transit time of the photogenerated carriers across the depletion region.
2. The diffusion time of carriers generated out of the depletion region to diffuse into the depletion region.
3. Charge trapping at the heterojunction.
4. Parasitic capacitance effects.

Empirically, the frequency response of a photodiode at the load is given by;

$$V_{out}(\omega)=I_{ph}(\omega).T(\omega).F(\omega).C(\omega) \tag{4.10}$$

where $V_{out}(\omega)$ is the output across R_L. $T(\omega)$, $D(\omega)$, $F(\omega)$ and $C(\omega)$ are contributions to the frequency response from the transit time, the diffusion current, the electrical circuit response and the charge trapping at heterojunction respectively. $I_{ph}(\omega)$ is the photogenerated current and given by;

$$I_{ph}(\omega)=\mathcal{R}P_{in}(\omega) \tag{4.11}$$

where $P_{in}(\omega)$ is the input power to the detector.

4.5.1. Transit time

Transit time is generally associated with the thickness of depletion region and in the active waveguide photodetector depletion layer is generally very small when compared with the conventional photodetector. This is a particular advantage of the active waveguide photodetector over the conventional one. This very thin depletion layer makes the transit time of active waveguide photodetector very short which is given by;

$$\tau_d = \frac{d_3}{v_s} \tag{4.12}$$

where τ is the transient time, d_3 is the thickness of active region and v_s is the saturation drift velocity. For GaAs the value of saturation drift velocity is $10^7 cm/s$ [14].

For the typical value of d_3=0.15μm, τ is calculated as 1.5ps. This value is very small when compared with time constant associated with electrical elements (which will be discussed below).

4.5.2. Diffusion time

In the AWOD, the depletion layer is surrounded with wider energy gap material. The diffusion time of the photogenerated carriers generated outside the depletion region can only be estimated when the thickness of depletion layer is known. It is given by considering the one side adrupted junction and a depletion region entirely inside the active layer, as [11];

$$w = \left(\frac{2\varepsilon_r \varepsilon_o (V_D - V)}{e N_D} \right)^{\frac{1}{2}} \tag{4.13}$$

where ε_r is the dielectric constant of intrinsic layer, ε_o is the free-space permitivity, N_D is the impurity concentration in intrinsic layer, V_D is the diffusion potential of the junction and V is the applied voltage. Using typical values (ε_r=10.9 [15],

V_D=1.6V and N_D=10^{17}/cm), w is calculated as 0.145μm. As this value is nearly equal to the active layer thickness of 0.15 μm, the time delay caused by diffusion current is expected to be smaller than the transit time.

4.5.3. Charge trapping

In conventional photodetectors, hole trapping at the p side of the heterojunction interface, as shown in figure 4.3 places greater speed limitations on the speed than the case of electron trapping on the n side of the heterojunction interface due to the higher effective mass of hole [16]. Under the influence of high electric fields, carriers (both electrons and holes) gain higher mobilities and may be swept over the well without being trapped. Since the AWOD is usually doped and due to the thin depletion layer, the electric field is expected to be very high (in our case around 100 *KV/cm*). Therefore, the charge trapping is expected to be less severe in the AWOD than the conventional photodetector.

4.5.4. Contribution of parasitic electrical elements

Figure 4.4a shows a normal biasing arrangement for a zero-bias detector with output signals fed to a load. If the photodiode is represented by the equivalent circuit of figure 4.4b, then figure 4.4a can be replaced by figure 4.4c. In figure 4.4, C_j and C_p are the junction and parasitic capacitance respectively. R_i, R_s and R_B are the diode incremental, series resistance and bias resistances respectively.

Figure 4.4c can represented by a simplified figure 4.4d, if one makes the simplifying assumption, which is true in most of the cases that [17];

$$R_s \ll R_L$$

and then lump the shunt components together. Usually $1/R_i$ is much smaller than $1/R_L$, therefore;

$$\frac{1}{R_i}+\frac{1}{R_L}\approx\frac{1}{R_L}\approx\frac{1}{R} \tag{4.14}$$

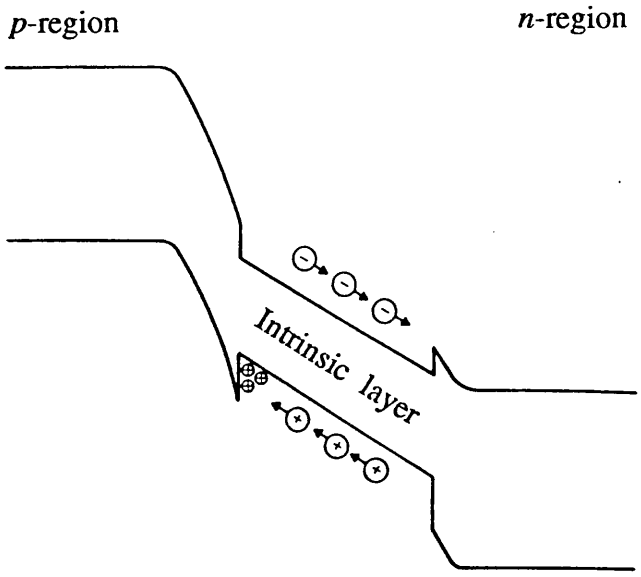

Figure 4.3. The band diagram of a detector showing charge trapping [16].

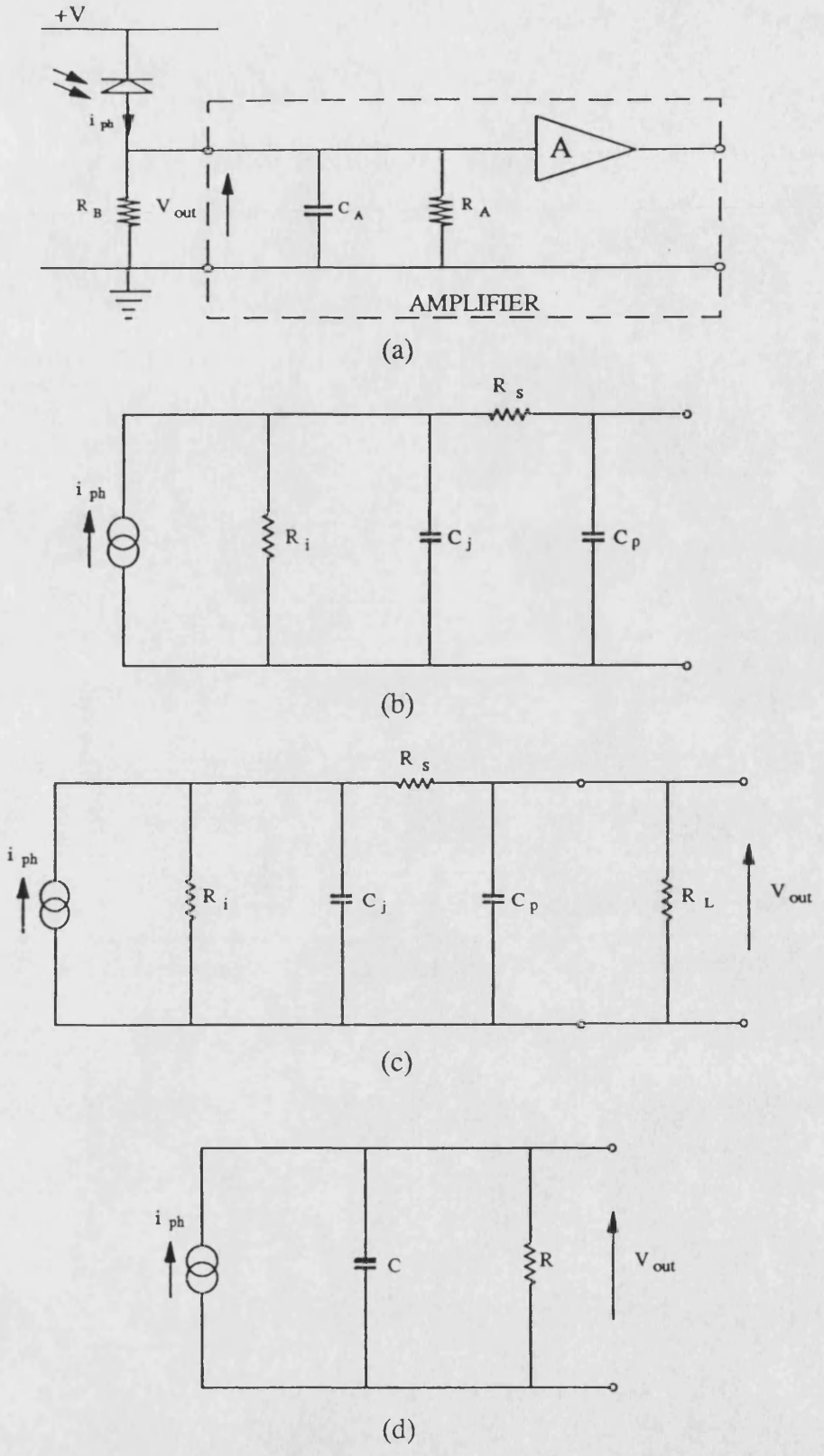

Figure 4.4. Circuit arrangement used to investigate the effect of circuit elements on the frequency response of the AWOD; (a) normal biasing circuit, (b) AWOD equivalent circuit, (c) complete circuit and (d) the equivalent circuit of (c).

here R is the total resistance of electrical circuit.

For high speed operation, it is necessary to minimize the total capacitance of device. The total capacitance of circuit can be given as;

$$C = C_j + C_p \tag{4.15a}$$

Junction capacitances of the order of $2.5pF$ are typical [9]. The typical value of C_p is of the order of 0.2 -0.5pF [18] and are expected to have less significant effect on the frequency response of AWOD. Therefore, equation (4.15a) is reduced to;

$$C \approx C_j \tag{4.15b}$$

The frequency limitation arising from the electrical parasitic element can be written as;

$$F(\omega) = \frac{R}{1 + j\omega RC} \tag{4.16}$$

Equation (4.10) can be written as;

$$V_{out}(\omega) = \mathcal{R} P_{in}(\omega) \left\{ \frac{R}{1 + j\omega RC} \right\} \tag{4.17}$$

The circuit time constant is equal to RC and equation (4.17) tells the main delay cause by the RC time constant of the external circuit. The typical value of R is usually 50Ω for the external circuit. For a good frequency response, it is essential to keep C as low as possible. The external load limited bandwidth of a active waveguide photodetector can be estimated by a simple equation [19];

$$BW = \frac{0.55}{RC} \tag{4.18}$$

4.6. Noise considerations

The contributing sources of noise in the active waveguide optical detector are essentially the same as they are in a conventional photodiode and these are inherent in every radiation detection process. The main sources of noise which must be considered are shot noise and thermal noise.

The random generation of charge carriers due to the random absorption of photons, which give the random fluctuations of photocurrent, is referred to as shot noise and can be expressed in the form of a mean square shot noise current as;

$$< i_{shot}^2 >= 2eI'B \tag{4.19}$$

where B is the bandwidth and I' is the average photodetector current.

Shot noise consists of three components as describe below;

1. Shot noise associated with signal current (I_{ph}).
2. Dark current (I_d).
3. Background Current (I_b).

Thus equation (4.17) can be re-written as;

$$< i_{shot}^2 >= 2e(I_{ph} + I_d + I_b)B \tag{4.20}$$

Because of the miniature structure of the AWOD, the effects of stray back-ground light will be negligible. Therefore, equation (4.20) is reduced to;

$$< i_{shot}^2 >= 2e(I_{ph} + I_d)B \tag{4.21}$$

The measurements of the reverse bias dark current for waveguide detectors have been performed by Alping *et al* [9]. The result of that measurements are shown in figure 4.5. The contribution of the dark current in different devices vary from 0.1nA to 1nA at 0V. However, if 50Ω load is used at the output, then the dark noise will be dominated by the thermal noise of the load resistor for a dark current up to $100\mu A$ [9]. Therefore, in most applications it is possible to neglect the dark current contribution.

In an electronic circuit any resistance gives rise to the system noise due to the random thermal motion of charge carriers and this source of noise usually called thermal or Johnson noise. In the detector circuit the noise is generated in the bias resistor, R_L, and has a mean square value of;

$$< i_{ther}^2 >= \left[\frac{4kTB}{R_L} \right] \tag{4.22}$$

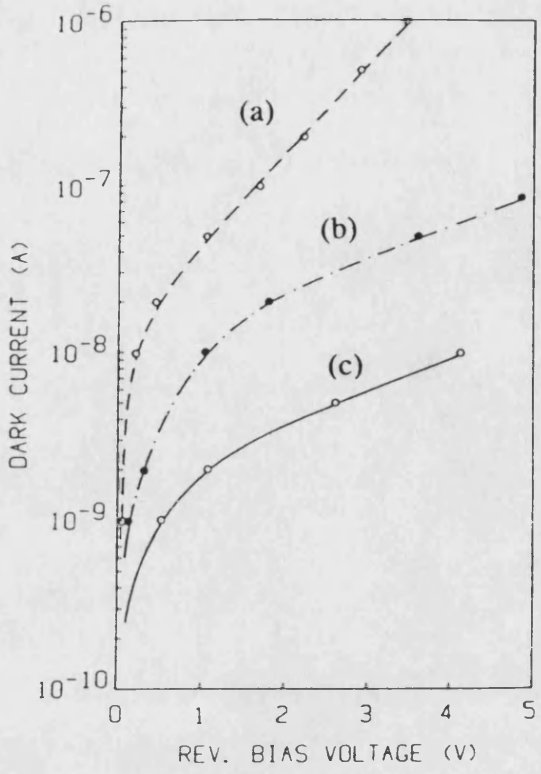

Figure 4.5. Dark current as a function of reverse bias voltage for different GaAlAs waveguide detectors; (a) channeled-substrate planar, (b) transverse junction stripe and (c) buried heterostructure/buried optical guide [9].

The term which describes the contribution of total noise in output current is called signal to noise ratio *(SNR)* is given by;

$$SNR = \frac{I_{ph}^2}{i_{shot}^2 + i_{ther}^2} \tag{4.23}$$

4.7. Experimental results

In this section, the different characteristics of an AWOD are investigated experimentally using monolithic and hybrid configurations. Also in this section, leakage of optical flux in OIC components is justified and the sources of leakage are originated.

4.7.1. Monolithic approach

A four segment laser device, UB136 (figure 1.4), was used to investigate the optical radiation detection properties of a monolithic integrated AWOD. The electrical resistance between segments A and B and between C and D was relatively low (i.e. $4.35K\Omega$). But the resistance between opposite stripes (i.e. between segments A and D and B and C) was around $2.79M\Omega$. Any of the segments of this device could be used as a detector and during the investigation of the monolithic AWOD, all four segments were used as the AWOD while the opposite segment was used as the optical source.

4.7.1.1. Responsivity of the monolithic integrated AWOD

Figure 4.6 shows the experimental set-up used to investigate monolithic AWOD response. The investigation began using UB136A as the source. The output of UB136A was measured at the front facet for different values of pumping currents. The response of the monolithically integrated GaAs AWOD was measured in the photoconductive mode at zero bias condition using the circuit of figure 4.7. The optical radiation at the back facet of UB136 was also detected and it was assumed that this must represent the leakage of optical flux through the AlGaAs layers above and below the active layer of the detector. Optical flux leakage will

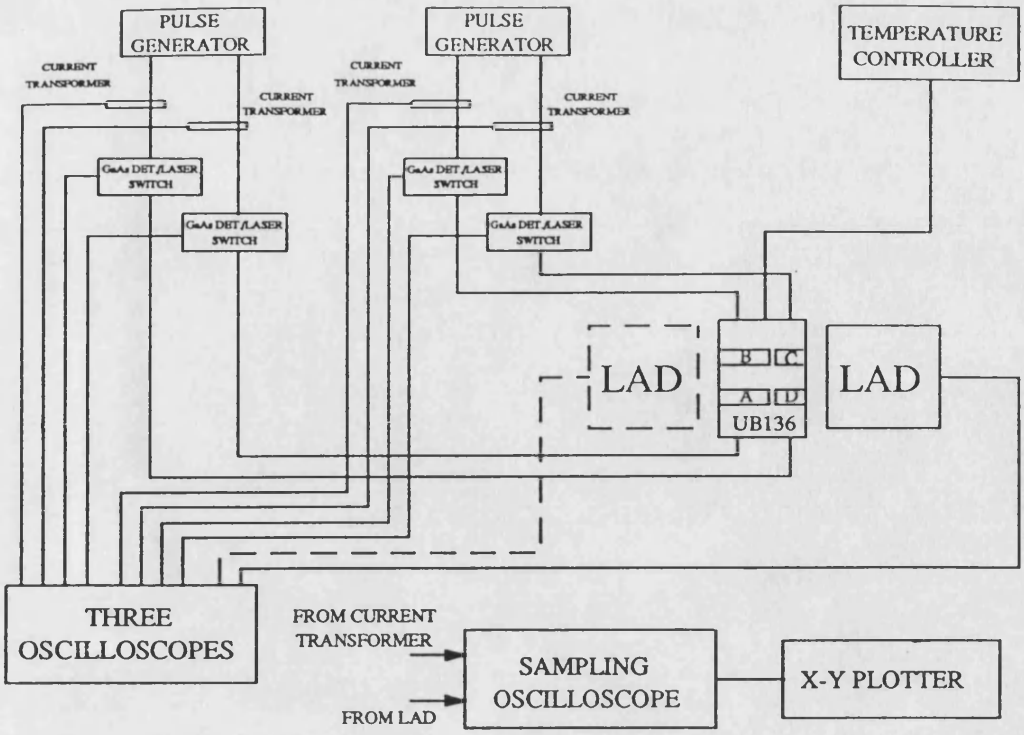

Figure 4.6. The schematic representation of the experimental set-up for the characterisation of the monolithic AWOD.

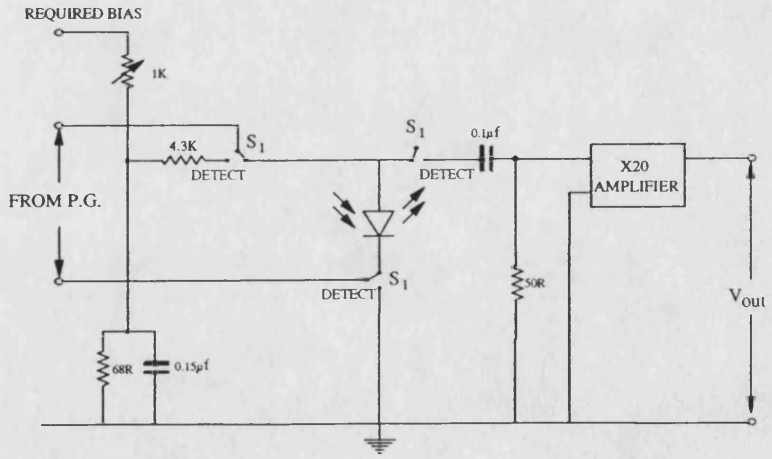

Figure 4.7. GaAs AWOD output measuring circuit.

be discussed more fully in section 4.7.3. The response of UB136C and UB136D both acting as the GaAs integrated AWOD's in parallel was also subjected to optical radiation from UB136A which acted as the optical source. Figure 4.8 shows the I-L characteristics of UB136A measured using a calibrated large area Si detector (LAD) at the front facet (curve 'b') and the monolithically integrated AWOD at the etched facet (curve 'a'). Figure 4.8 also shows the effective input power to the GaAs detector (curve 'c') which is obtained by correcting the output of UB136A measured to take into account light which is not coupled into active layer of the detector by subtracting the light leaking from the AWOD back facet (curve 'd'). In figure 4.8, at the lower values of source drive current corresponding to relatively low optical input powers, the response of the GaAs AWOD is higher than that of Si LAD, but at the higher values of optical input to detectors, LAD response is higher than the GaAs AWOD. The same experimental procedure was repeated for UB136D as the source and UB136A or UB136B as the AWOD. Figure 4.9 shows I-L characteristics of UB136D measured by using LAD and the GaAs AWOD. The response of UB136A or UB136B and UB136C or UB136D as AWODs is plotted in figure 4.10 along with the results of reference-20 and 21 (curve a, b, c and d respectively). Curves 'a' and 'b' both show a higher response at the lower value of input power. Similar effect can be seen in the results of reference-21 (curve d). In figure 4.10, the response of UB136C or UB136D (curve a) also becomes saturated at the higher values of input power. This saturation effect is less prominent in the case of UB136A or UB136B while used as AWOD (curve b).

There are a number of reasons for this saturation. One possible reason is that as the optical source current is increased the optical output power increases and the spectrum shifts to shorter wavelength. However, the responsivity of the photodetector decreases at shorter wavelengths. A second possible reason is that at high photon densities, the rate of production of carriers is such that the local electric field in the vicinity of the carriers fall. This is common in conventional photodetectors,

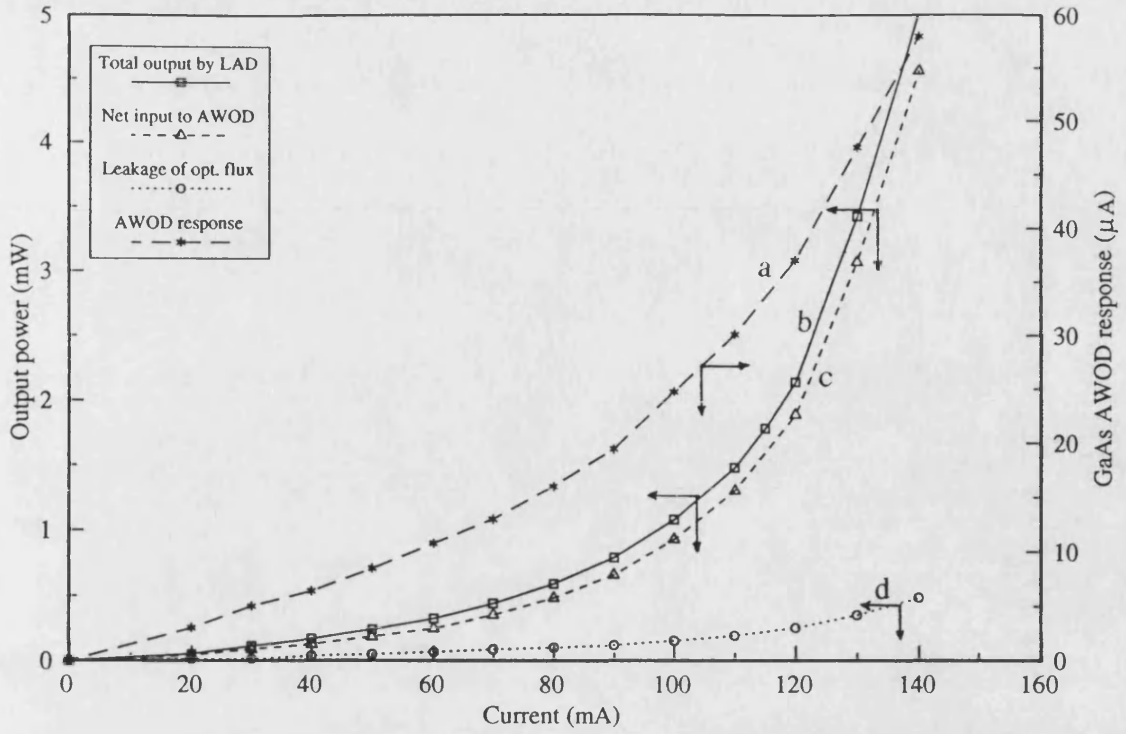

Figure 4.8. The I-L characteristics of UB136A using the LAD and UB136C or UB136D as the monolithic AWOD.

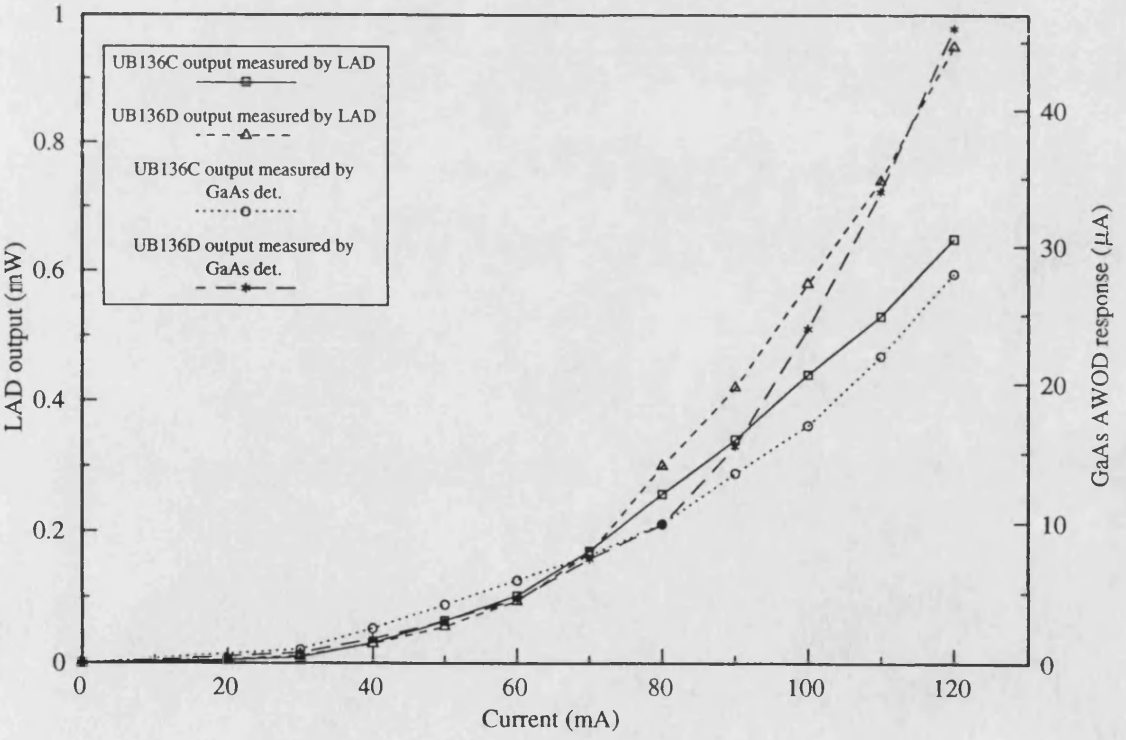

Figure 4.9. The I-L characteristics of UB136C and UB136D using the LAD and UB136A or UB136B as the monolithic AWOD.

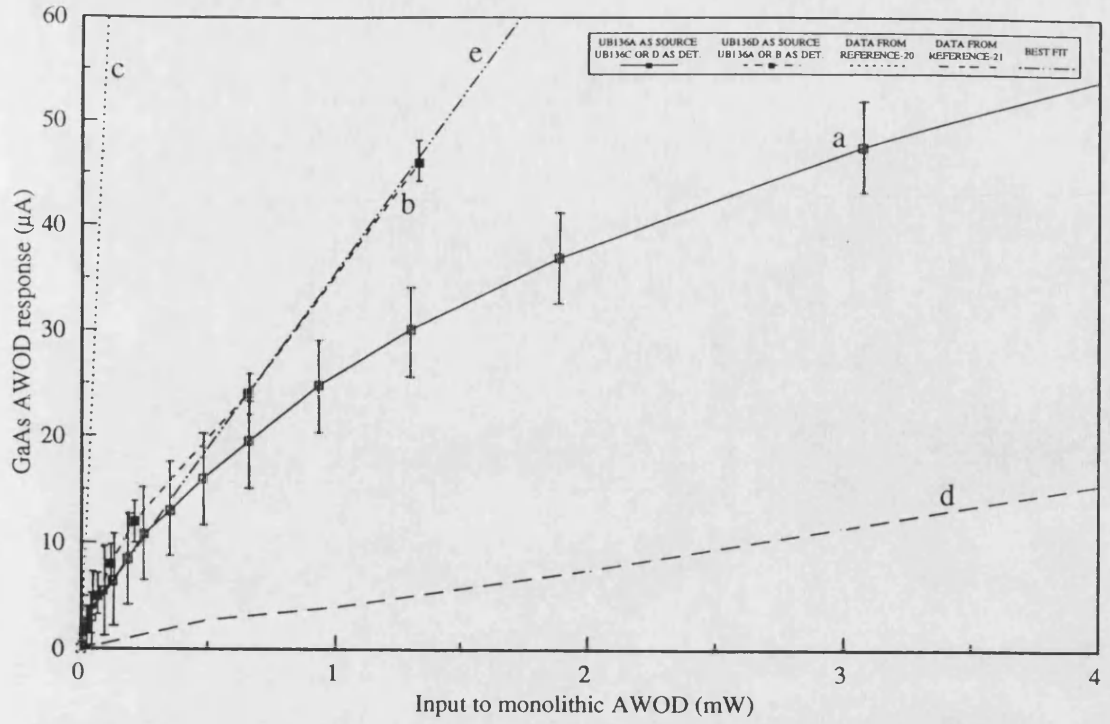

Figure 4.10. The response of different monolithic AWODs.

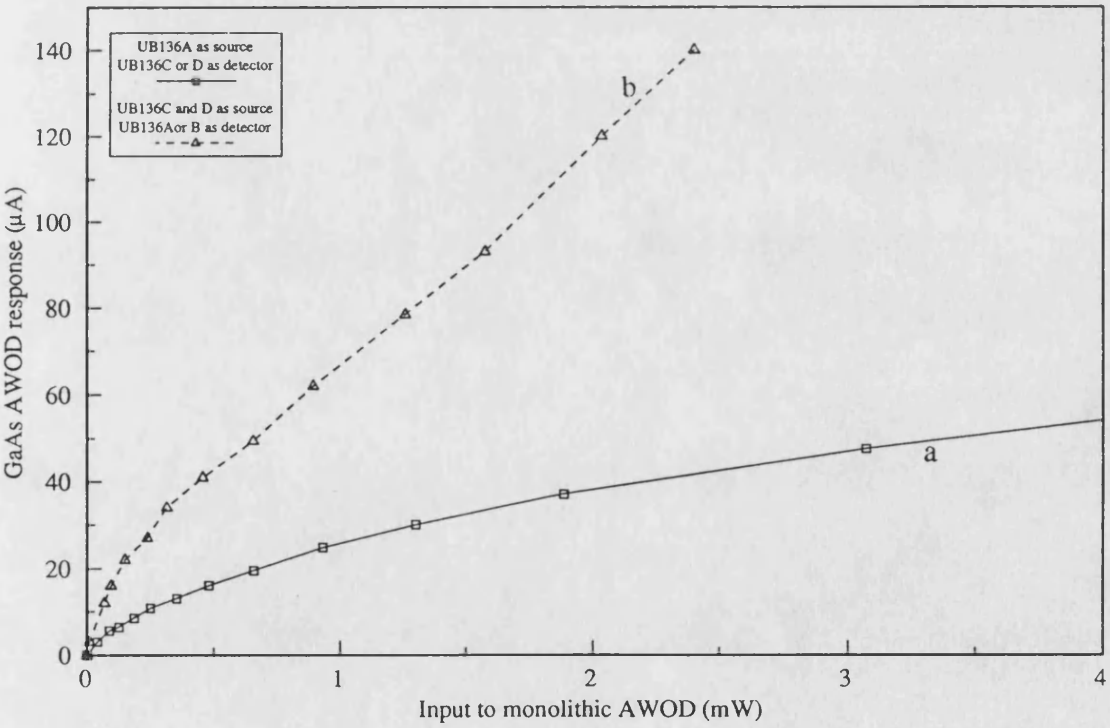

Figure 4.11. Comparison between saturation effect in different monolithic integrated AWODs.

and because of the very small cross-sectional area of the waveguide detector (0.15 to 5μm) and the excellent coupling efficiency might be a similar problem for the AWOD.

The saturation of output of the GaAs detector could also be due to the non-vertical geometry of the etched facets. Saturation effects have not been seen when segment A or segment B were used as detector and when they were subjected to a input from segment C or segment D. It was thought that probably outputs from laser segments C or D were not high enough to cause the saturation of UB136A or UB136B when they were used as AWOD. To check this, a higher optical input to segment A or B was obtained by pumping both UB136C and UB136D simultaneously. The response of the monolithic integrated GaAs AWOD (segment A or B) versus input to UB136A or UB136B along with the response of UB136C or UB136D as monolithic integrated GaAs AWOD is shown in figure 4.11. In figure 4.11, a higher response of UB136A when used as an AWOD was obtained at the lower value of input power to the AWOD. But at the higher values of input to AWOD, curve 'a' in figure 4.11 clearly shows the output saturations whereas curve 'b' does not saturate. If the saturation effect is entirely due to the small detection area, then saturation would have been seen in curve 'b' in figure 4.11 as well. From this evidence it was felt that some of the facets were not vertical and this was reducing the effective input power coupled into that detector.

From figure 4.10, an average responsivity figure (by fitting a best-fit, by using least square curve fitting technique (curve 'e')) for the monolithic AWOD is obtained as 36±2mA/W. Whereas the curves taken from references 20 and 21 give the responsivity to be 615mA/W and 5mA/W, respectively. In both cases a single stripe tandem geometry device was used. The responsivity value of 615mA/W looks rather high when one considers the angle of beam divergence inside the etched gap and it is probably due to electrical connection through the *p*-type cladding layer between two stripes which caused direct leakage of current from the laser segment to the detector segment. The responsivity value of 5mA/W, which is taken

from reference-21 is very low because the gap between two stripes was 20μm and a coupling efficiency of only 1% was achieved. In our case a reduction in etched gap has increased the coupling efficiency and hence the response of the AWOD has increased as well. Therefore, the responsivity figure of 36mA/W looks quite reasonable.

4.7.2. Hybrid approach

In the last sub-section, the active waveguide was successfully used as a monolithic AWOD. However, the saturation of the AWOD output and poor coupling efficiency has prevented the main characteristics of this detector, such as the response of the detector, wavelength dependent response and high frequency response from being measured with the available equipment. In order to have a better understanding of the main light detection properties of the AWOD, a hybrid approach, where device configuration can be optimised, is used in the following section.

4.7.2.1. Alignment of different optical components

The hybrid OIC is an alternative to the monolithic OIC, where several optical components are fabricated on different substrates and then joined together. The major advantage of the hybrid approach is that the performance of each component can be optimised according to the particular application. However, hybrid integration suffers severely from poor coupling of the light from one component to another. Normally, an optical lens system and a tapered fibre are used to couple the light, but the butt-coupling technique has also been proposed [22].

In the butt-coupling technique, the two components have to be very close to each other otherwise the technique suffers from beam divergence. If two components are placed very close to each other, temperature effects which cause the expansion of material cannot be ignored. This could cause damage to facets of device being investigated. Additionally, it becomes very difficult to isolate the laser

source from reflection from the detector.

The tapered fibre technique also suffers from relatively high coupling losses of optical radiation. But this technique has a reasonably large working distance and offers safety to the optical components from accidental facet damage.

In both techniques, the alignment of different components is difficult, time consuming and may not be reliable. In this section a novel, reliable and easy alignment technique for the alignment of active components is demonstrated by making the use of the optical radiation detection property of a laser diode. Devices UB238 and UB262 are used as the source laser and the AWOD respectively. In order to achieve the maximum coupling efficiency, optical lenses were used to couple the light from the source laser to AWOD as shown in figure 4.12 although a tapered fibre could have been used. The maximum coupling efficiency between the input from the source laser to the AWOD can be achieved when the diameter of the focussed light beam is at a minimum. The minimum spot size of the input light beam through the lens is determined by the diffraction limit of input signal and given by;

$$D_{\min} = 1.22\lambda_o/2.NA \tag{4.24}$$

where λ_o is the wavelength of input radiation and NA is the numerical aperture.

Although an x40 with a large numerical aperture of the lens would have given a smaller spot size it would have placed a large limitation on the working distance which is desirable in the most of applications. Therefore, a x20 lens with NA=0.45 was used which could give the minimum spot size of $1.165\mu m$ at λ_o=$860nm$.

Referring to figure 4.12, first the AWOD (UB262) being investigated was aligned with the camera through lens-3 by using it as a light source and then it was pulled down to provide the optical path to the input beam from the source laser such that the source laser could be aligned with the camera. After aligning the source laser with the camera through the optical system, the AWOD was brought back to its original position in such a way that it was obstructing the

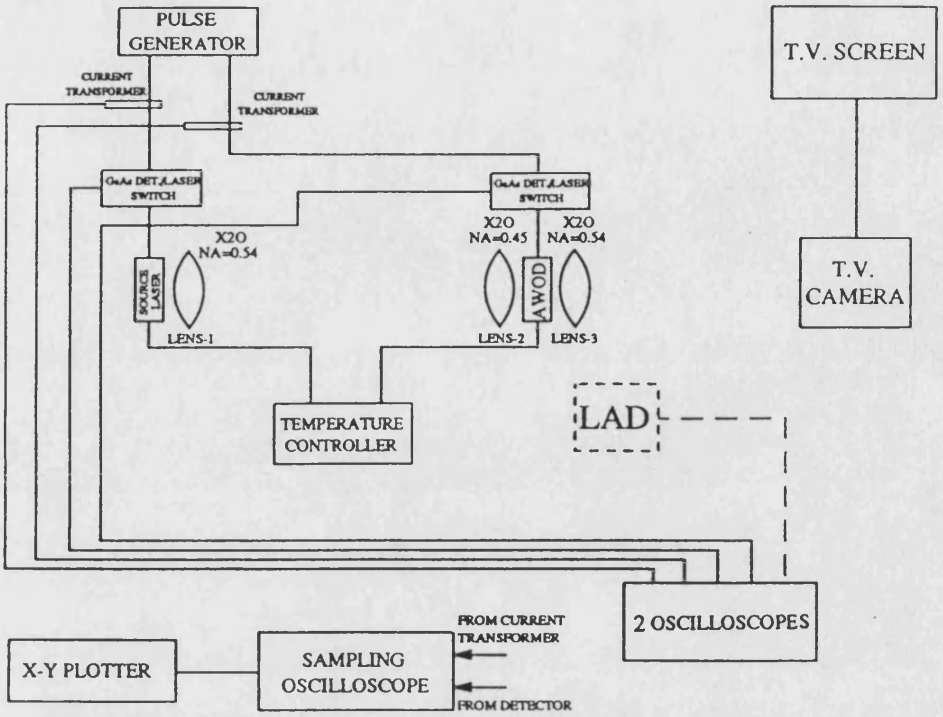

Figure 4.12. The schematic representation of the experimental set-up for the characterisation of the hybrid integrated AWOD.

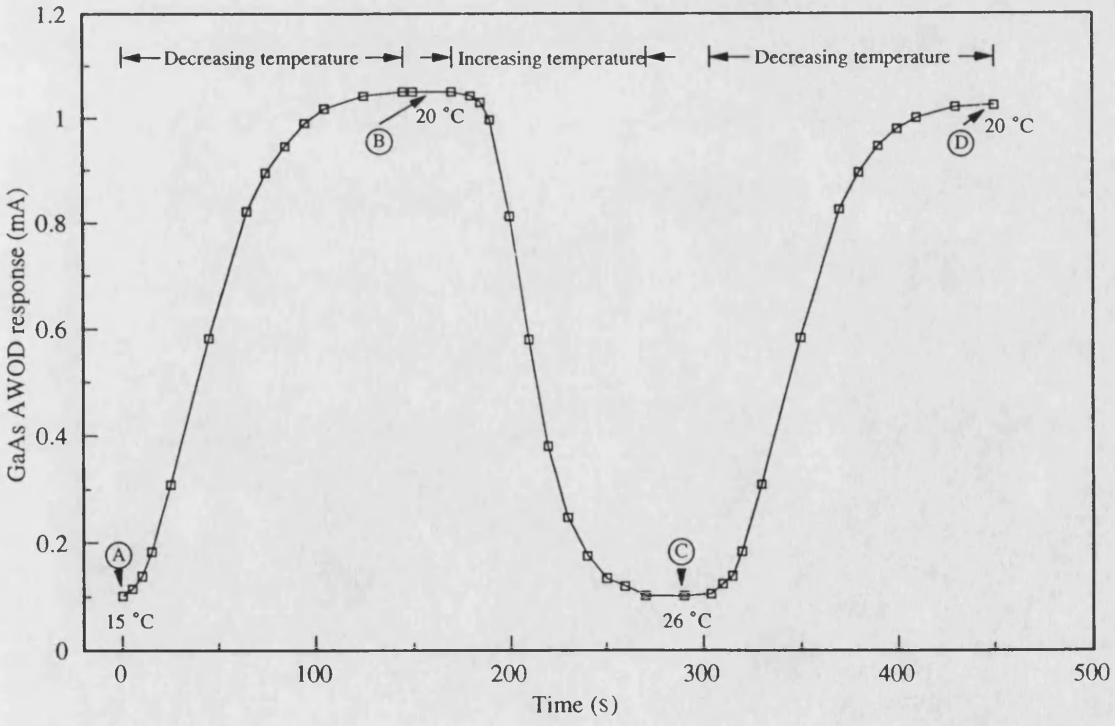

Figure 4.13. The temperature dependence of the alignment of optical components.

optical path of the source laser. At that point, switch S_1 in figure 4.7 was changed over to *detect* the optical radiation falling on the AWOD surface. By manipulating the position of the source laser, via lens-1 and lens-2 and observing the near field beam profile of the source laser on the camera, a slight response of the AWOD was observed which was maximized by repositioning of input beam on to the AWOD input facet. This maximum output of the GaAs AWOD represents the maximum alignment between two components. This was checked by using the source laser as the AWOD and UB262 as a source laser. The response of UB238 as the AWOD was found to be maximum at a point where the response of UB262 as the AWOD was found maximum described earlier. After achieving optimum alignment, it was easy to keep this alignment even though this alignment was found very sensitive to the input beam focussing point, because any change in position of any of the lens or the laser source was causing the focussing point to shift from maximum alignment position. But it was always easy to check the alignment by looking at the output of the AWOD.

4.7.2.1.1. Temperature dependence of alignment

The alignment technique explained above, was found to be very sensitive to temperature variations because any change in temperature changes the length of the AWOD and hence a shift in position of the AWOD facet. Figure 4.13 shows the effect of this temperature change on the coupling efficiency. This curve was measured in following manner. First, the system was aligned at the source laser and AWOD at an ambient temperature of 20°C. After achieving the best possible alignment between the source laser and the AWOD, the temperature of the AWOD was reduced to 15°C. At this point the degree of alignment was found to be at a minimum and point *A* in figure 4.13 represents this alignment. The temperature of the AWOD was again increased to 20°C and point *B* represents the output of the AWOD at that instance of time. The temperature of the AWOD was further increased to 26°C and the response of the AWOD was again measured to be at its

lowest (point *C*). To check the effect of temperature variation on the alignment, the temperature of the AWOD was brought back to the original value of 20°C and nearly the same output from the AWOD was achieved as at point *B* and this is represented by point *D* in figure 4.13.

The temperature dependence of the alignment can be explained by considering the temperature dependence of the cavity length which affects the position of the facet relative to the lens. At point *A*, due to decrease in the source temperature, the effective length of the laser cavity was decreased and the incoming light beam was focused in front of the input facet of the AWOD. At point *C* it was focused beyond the input facet of UB262 due to a increase in effective cavity length. Whereas at point *B* and point *D*, the system was aligned and the input beam was focused at the input facet of the AWOD.

4.7.2.2. Response of the hybrid integrated AWOD

The response of the hybrid integrated AWOD has been measured using the experimental set-up of figure 4.12. For this experiment a LAD was used instead of the infrared camera at the back facet of the AWOD. The total input to the AWOD was measured by plotting the I-L characteristic of the source laser at lens-2 using the large area detector and this was considered as total input to the AWOD. Then the AWOD was aligned with the source laser and I-L characteristic was again measured at the back facet of the AWOD and this was considered as the leakage of optical flux. The I-L characteristic of UB238 was also measured using UB262 as the AWOD. The results are shown in figure 4.14. The net input to the AWOD is also shown in figure 4.14 which was obtained by correcting the total input to take account of optical flux which does not couple into the active layer of the AWOD but propagates through the transparent AlGaAs cladding layers.

The same experimental procedure was repeated using a 5μm wide stripe laser instead of UB262 as the AWOD. Figure 4.15 shows the hybrid integrated AWOD response as a function of the stripe width. This was achieved by plotting the net

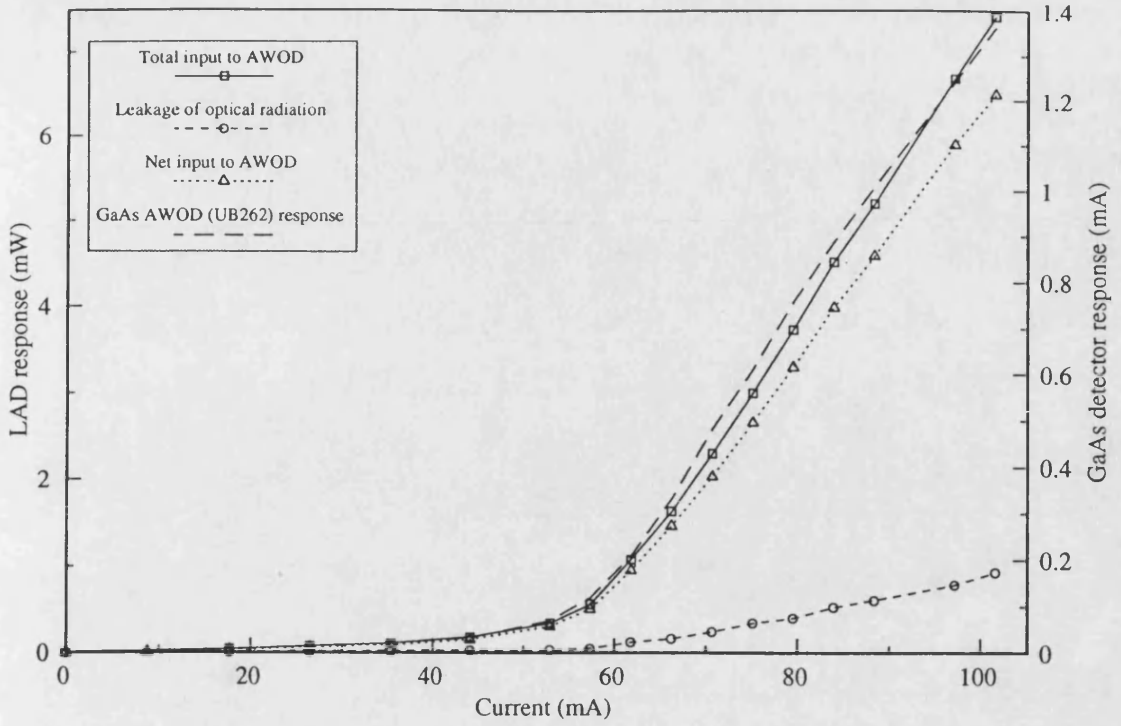

Figure 4.14. The I-L characteristics of UB238 measured by the LAD and the GaAs AWOD.

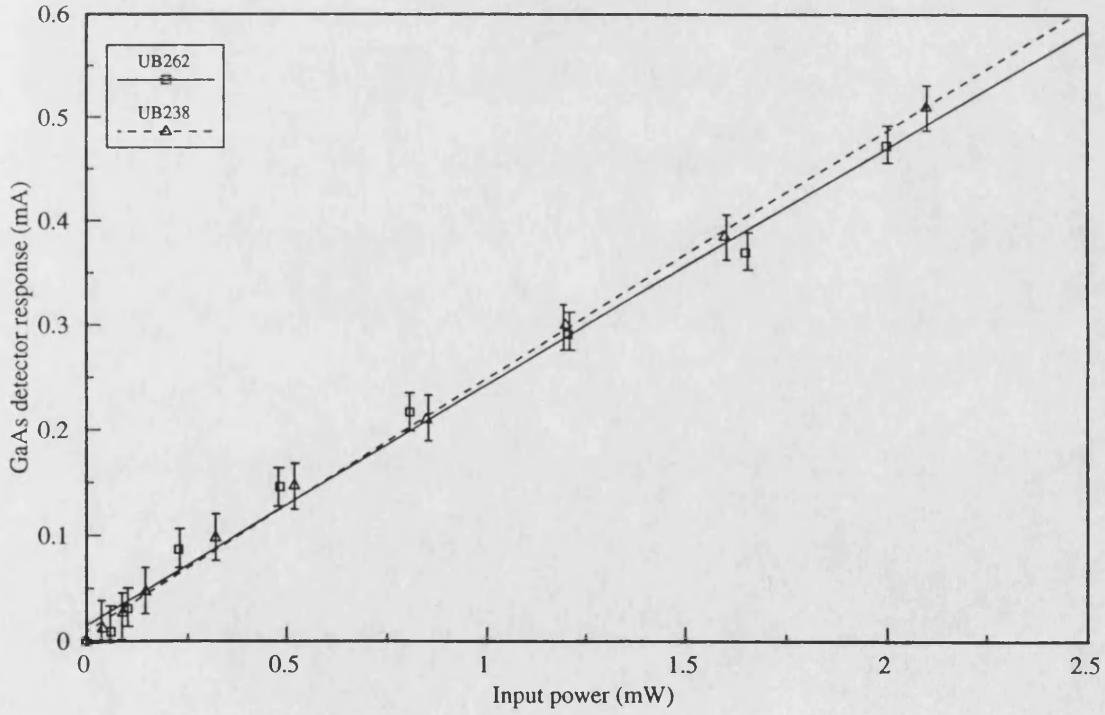

Figure 4.15. The response of the GaAs AWOD as a function of the stripe width.

input to the AWOD versus the response of the AWOD. It can be seen from figure 4.15 that changes in the stripe width does not have much effect on the response of the GaAs hybrid integrated AWOD. This is to be expected because the minimum achievable spot size achieved by lens-2 is around 1.165μm (equation (4.25)). This is much smaller than the stripe width of 2.5μm or 5μm. From figure 4.15, the responsivity of the GaAs AWOD was calculated as 0.23±0.02A/W. This value agrees with reported values in references-9 and 23. Using equation (4.9), the quantum efficiency is calculated as 33.9±2.8%.

Generally, the responsivity of a detector can be improved by increasing the thickness of the intrinsic layer. In order to look at the effect of intrinsic layer thickness on the response of the GaAs AWOD, a 250μm long laser device UB231 was fabricated. This device has a specially thick 0.5μm active layer. Figure 4.16 shows the response of the GaAs AWOD as a function of the active layer thickness. The increase in the responsivity of the GaAs AWOD for an increase in the active layer thickness is in agreement with theoretical and experimental predictions [17]. Figure 4.16 gives a responsivity value of 0.35±0.02A/W which corresponds to 49.7±3% quantum efficiency. Ideally for this hybrid case the optimum active layer thickness should be equal to the minimum spot size.

The responsivity of the GaAs AWOD is shown to increase from 0.23A/W to 0.35A/W, a 50% increase in responsivity of the AWOD with the thick active layer for an increase in the active layer thickness of 333%. This is because the input beam approximates to a Gaussian distribution where most of the power concentrated in the centre of beam.

4.7.2.3. Effect of biasing on the AWOD responsivity

The effect of biasing on the performance of the AWOD was investigated by applying a negative biasing voltage to the AWOD using the circuit of figure 4.7. The biasing voltage was controlled by the variable resistor and was monitored using a DVM. The I-L characteristics of UB238 were measured at different levels

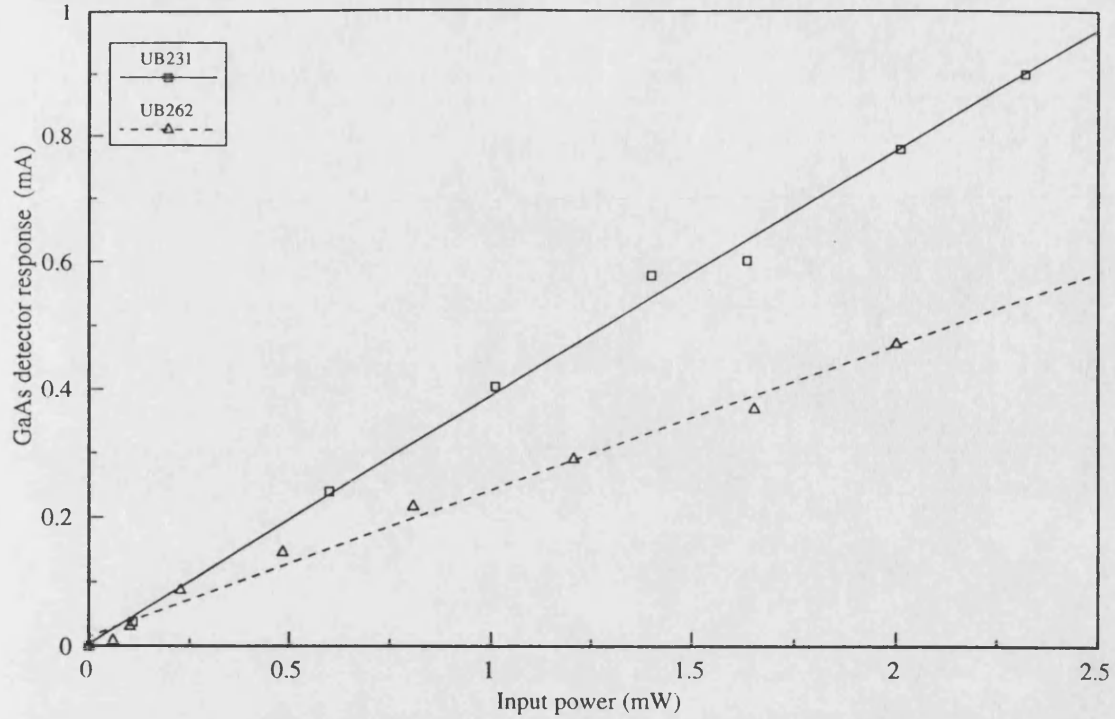

Figure 4.16. The response of the GaAs AWOD as a function of the active layer thickness.

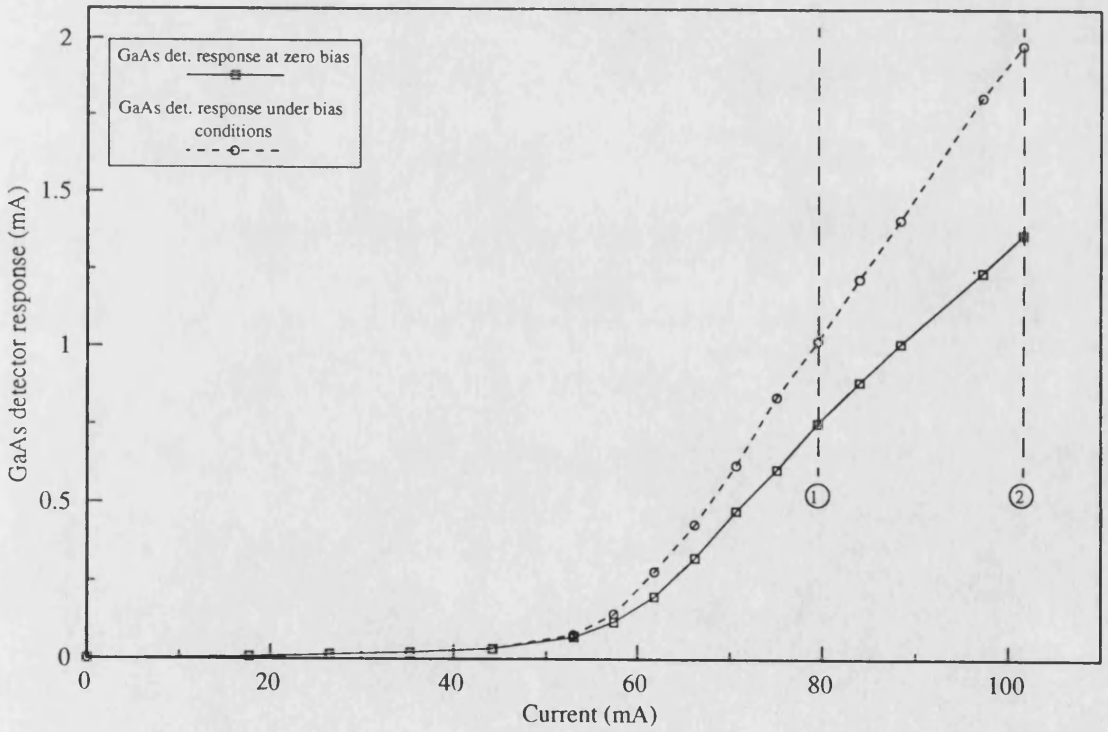

Figure 4.17. The I-L characteristics of UB238 measured using the GaAs AWOD under reverse bias and zero bias conditions.

of reverse bias. After a certain level of bias, the responsivity of the AWOD was found to be unchanged as expected. Figure 4.17 shows typical I-L characteristics at zero bias and at a biasing voltage which gave maximum response of AWOD. The saturation of the output of the AWOD can be seen at zero bias in figure 4.17 at the higher values of optical input power, as before for the monolithically integrated structure. Saturation can also be seen in figure 4.14, but it seems more dominated in figure 4.17 due to enlarged scale. Saturation effects occurred due to optical pumping of the active layer (section 4.7.3). This can be explained as following: Photons from the source laser are absorbed in the active layer of the AWOD and generate electron-hole pairs. Generated electrons and holes decay to the bottom of the conduction band and to the top of the valence band. If the intraband relaxation time is much larger than the interband relaxation time, as is usually the case for a optically pumped lasers, a population may build-up, which is further increased by the charge trapping at the potential barrier (which is meant to confine the carrier within the active layer) as shown in figure 4.3. But the band-to-acceptor transitions do not overcome the total losses inside the active medium. When an external electric field is applied, the trapped holes surmount the potential well easily and interband relaxation overcomes the intraband band relaxation time due to the increase in the mobility of minority carriers [13]. As the reverse bias voltage increases, the height of depletion barrier increases, band-to-acceptor transitions cannot take place any more and thus the absorption coefficient increases with increasing negative bias voltage [12].

The responsivity of the GaAs AWOD has also been calculated at different levels of reverse bias using the zero bias response of AWOD (at a point where it is not saturated) as the reference. Figure 4.18 shows the responsivity of the GaAs AWOD plotted against bias voltage. The responsivity of the GaAs AWOD reaches 90% of its maximum value at around -0.8V of bias voltage. This corresponds to the height of the well and it agrees well with a reported value of -0.82V in

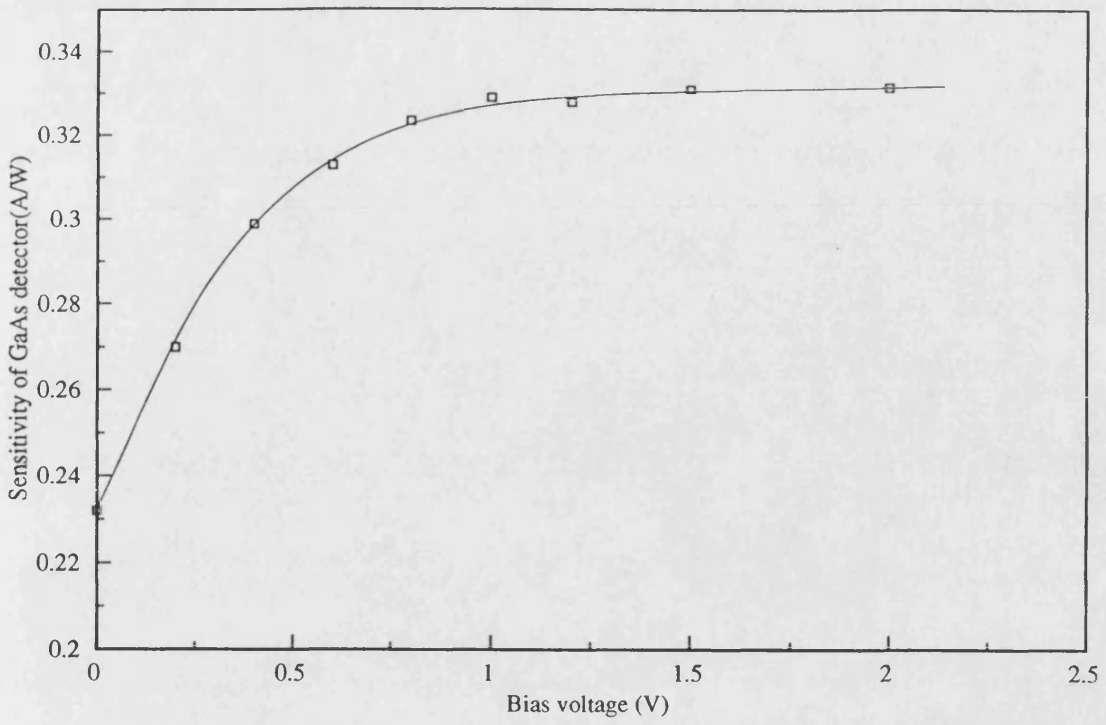

Figure 4.18.The dependence of the GaAs AWOD on the level of reverse biasing.

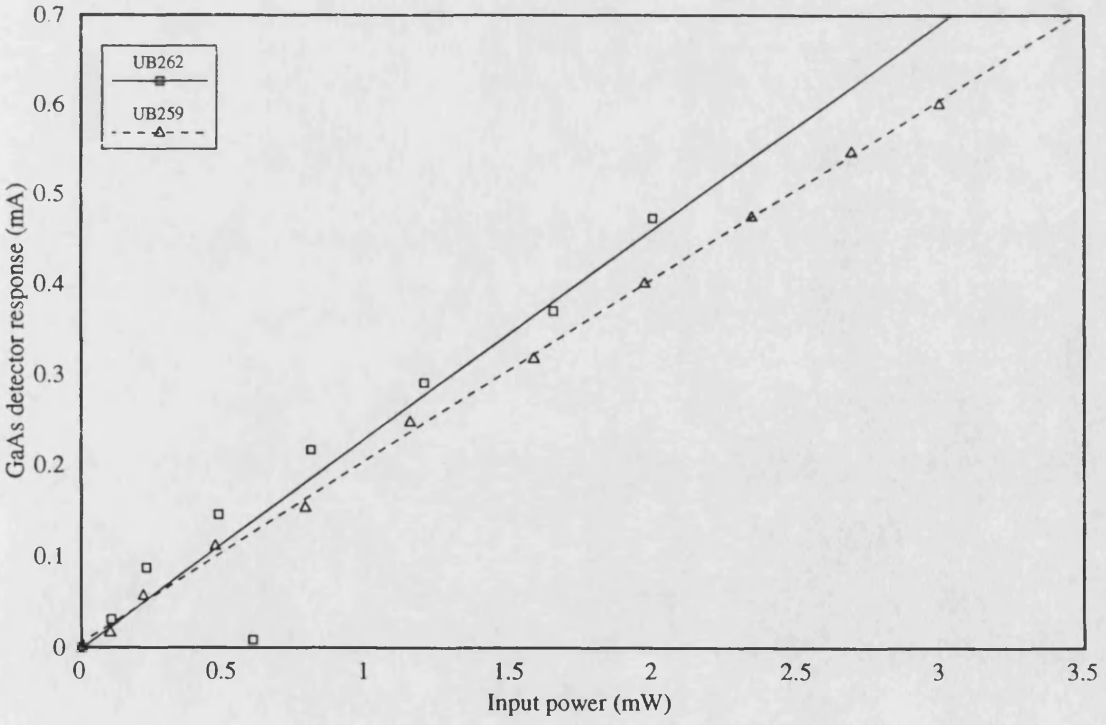

Figure 4.19. The response of the AWOD as a function of facet reflectances.

reference-24. It also supports the argument that charge trapping helps in building up the population inversion as there was no saturation effect observed above bias voltage of -0.8V even at very high level of optical input power to the AWOD.

4.7.2.4. Dependence of the AWOD responsivity on facet reflectivity

In previous sections, FP laser devices were used as the AWOD. In some cases it is desirable to reduce the facet reflectivity to avoid lasing oscillation and when to device is used as the active waveguide amplifier (chapter-5). In this section the effect of A.R. coating on the AWOD facet is investigated. UB259 was used as the AWOD. The experimental procedure of section 4.7.2.2 was repeated to measure the response of the A.R. coated AWOD. Figure 4.19 shows a graph of the response of the GaAs A.R. coated AWOD (UB259) versus the net input optical power. Figure 4.19 gives a responsivity figure of 0.20±0.01A/W. This is less than the FP AWOD because the A.R. coating reduces the amount of multiple reflection between the source laser and the AWOD, hence reducing the amount of the effective optical input power. The reduction in the amount of multiple backreflection also reduces the error figure.

4.7.2.5. Wavelength calibration of the AWOD

Since α_{ib} is strongly dependent on the wavelength [4], for a given semiconductor active layer composition, the wavelength range for which appreciable photocurrent can be generated is limited. An AWOD would be able to detect the radiation which satisfy the condition;

$$\lambda \leq \lambda_o \tag{4.25}$$

where λ is the wavelength of incoming input radiation and λ_o is the intrinsic wavelength of the AWOD.

Although the detecting wavelength of the GaAs waveguide detector has been extended successfully beyond the long wavelength cutoff point using proton-implanted technique [25], in OIC structures, where all components are fabricated on a

single substrate, the AWOD would be subjected to a radiation of the same bandgap energy. So in the AWOD the cutoff frequency limitation is very critical in contrast with commercially used detectors. For example, if $\lambda << \lambda_o$, the absorption coefficient will be very high. The absorption of incoming radiation will take place entirely near the input facet and the minority carrier generated by absorbed photons can interact with the majority carriers before diffusing to the depletion layer. This event does not contribute to photocurrent and optical signal is wasted. If $\lambda >> \lambda_o$, then the detector will be effectively transparent to the incoming radiation. Furthermore, if the wavelength is close to the intrinsic wavelength of the AWOD, the contribution of photocurrent from diffusion components will be negligible because cladding layers are made of higher energy gap material.

The wavelength response of the GaAs detector around 850nm has not been reported in the literature and this task is carried out in this section for the range of wavelengths reported in this thesis (858-862nm).

During the wavelength calibration of the GaAs AWOD, FP and A.R. coated devices (UB262 and UB259) were used. The experimental set-up of figure 4.12 was used, but a beam splitter was inserted between the two devices and a LAD was used to monitor the input to the AWOD, as shown in figure 4.20.

The input to the AWOD was measured against the GaAs FP AWOD response at different temperatures of the source laser while the temperature of the FP AWOD was maintained at 20°C. The source laser temperature was varied between 17°C and 25°C and the response of the AWOD was measured by varying the source laser current at the different source laser heatsink temperatures. The results are presented in figure 4.21 as a function of the source laser temperature. The same experimental procedure was repeated using the A.R. coated device and the response of the A.R. coated AWOD against optical input is plotted in figure 4.22 as a function of the source laser temperature. By comparing figures 4.21 and 4.22 with figure 3.8, a range of different wavelengths of the input radiation was achieved. Also, by making the use of equation (4.9) and the measured responsivity

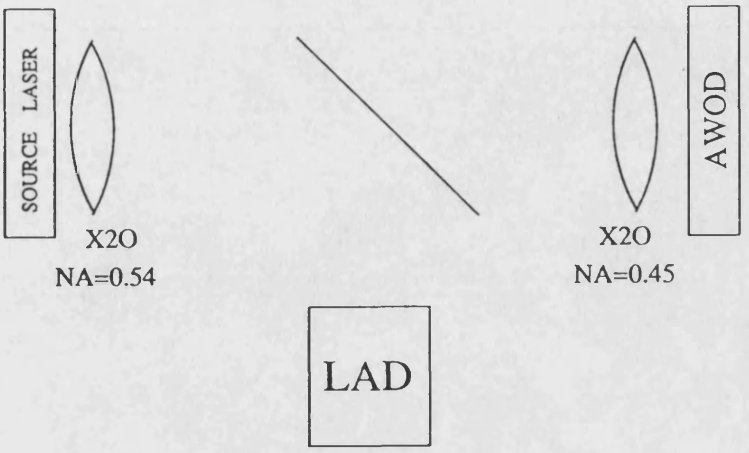

Figure 4.20. Schematic diagram showing arrangement used to measure the input to the GaAs detector.

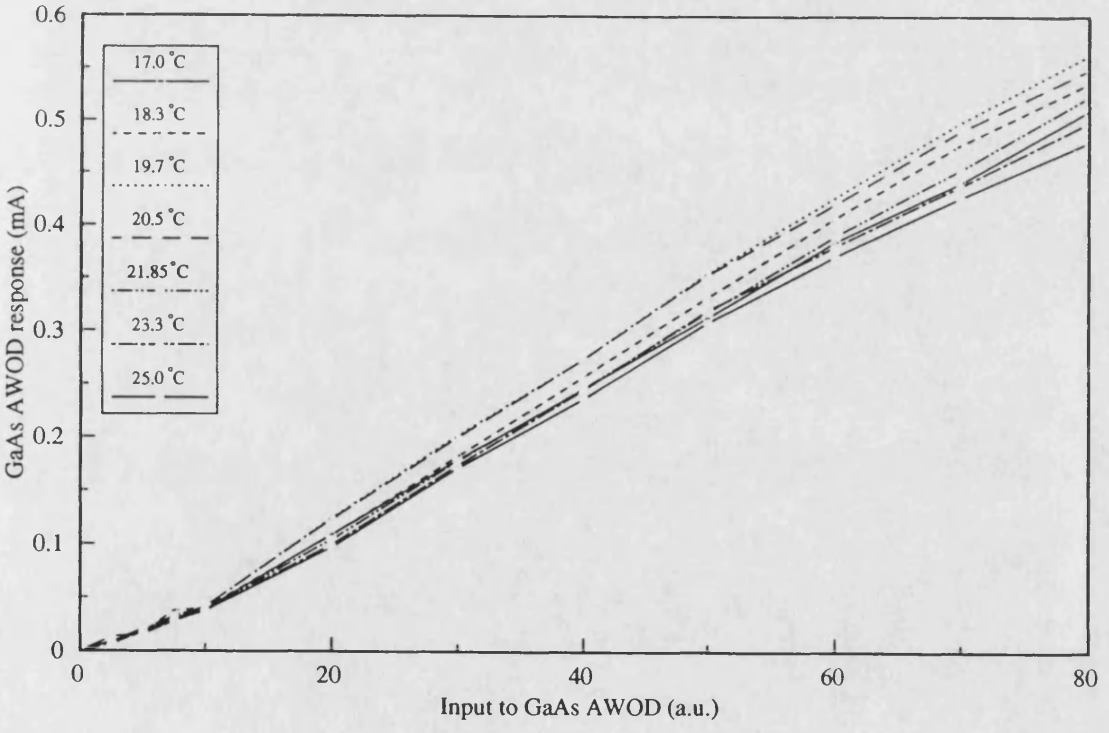

Figure 4.21. The response of FP AWOD as a function of the source laser temperature.

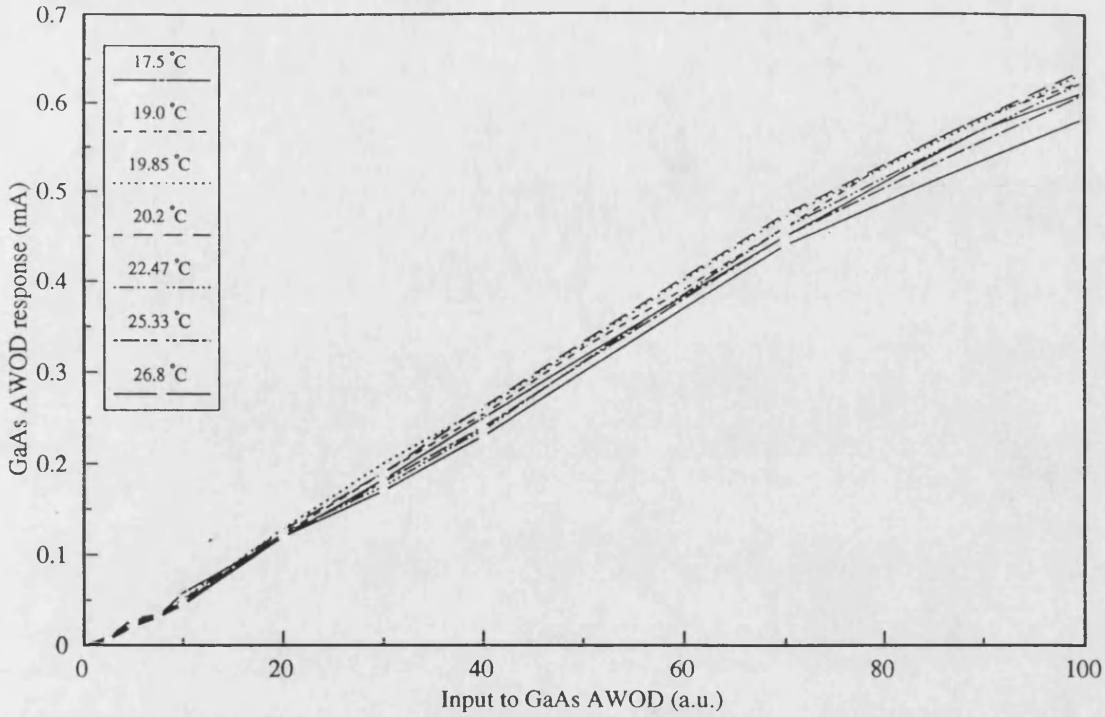

Figure 4.22. The response of A.R. coated AWOD as a function of the source laser temperature.

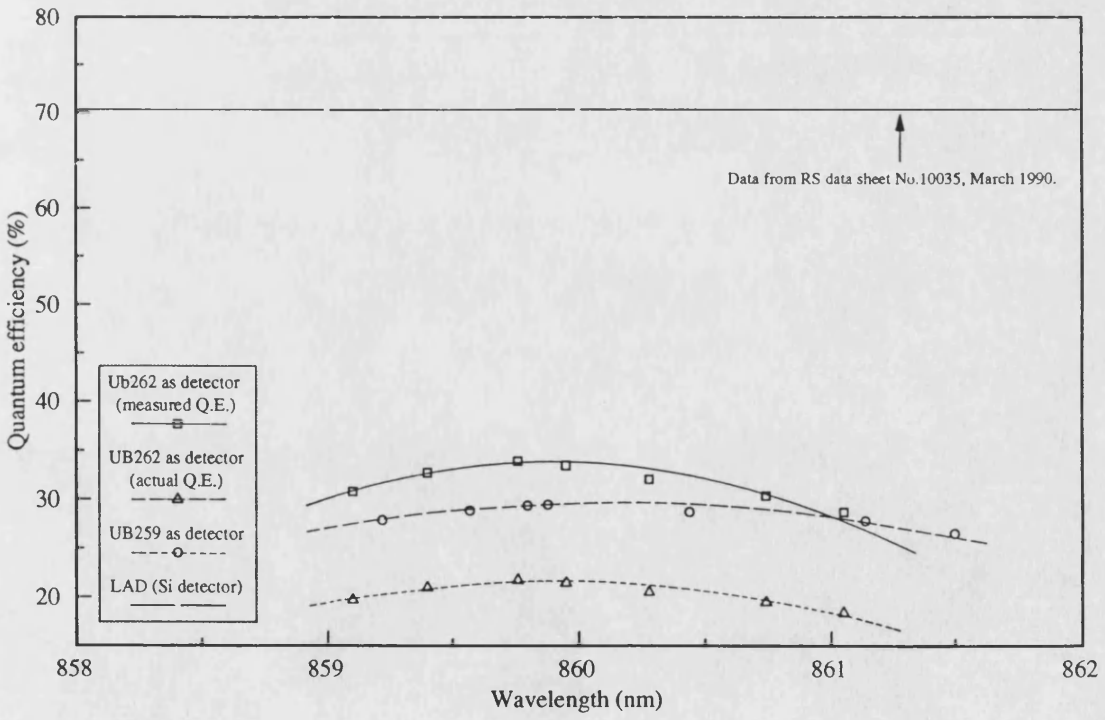

Figure 4.23. The wavelength calibration of the GaAs AWOD.

value of AWOD in section 4.7.2.2. and 4.7.2.4. as reference, a plot of quantum efficiency against wavelength for both devices was possible and this is shown in figure 4.23. This figure shows two curves for UB262, one represents the measured value and the other corresponds to actual value (value corrected to take account of multiple feedback effects). The quantum efficiency of Si detector is also given in figure 4.23 over a corresponding wavelength range. The response of the GaAs AWOD is found to be highly dependent on the wavelength of the input radiation in general, but it can be seen from figure 4.23 that the response of the FP AWOD is more wavelength dependent than that of A.R. coated AWOD. This is in line with the prediction of chapter-3.

The investigation of the wavelength dependence properties of the GaAs AWOD was further expanded to look at the temperature sensitivity of the AWOD by changing its temperature while the source laser temperature was kept constant at 20°C. In particular, the experiment aimed to look at the variation in the wavelength where sensitivity was maximum. The Same experimental procedure was repeated for this set of tests. Figure 4.24 shows the effect of wavelength on the quantum efficiency. This time, the response of the GaAs AWOD for both device was found nearly constant.

4.7.2.6. Frequency response of the AWOD

The frequency response of a detector can be characterized by using a number of different techniques. The relative merits of these various techniques largely depend on the intended application of the detector, the range of the measurement, the accuracy of measurement and equipment available. The simplest measurement of frequency response involves excitation of the detector with short pulses of light and then measuring the detector output on a sampling oscilloscope. The rise time of the output pulse can then be used to calculate the frequency response of that detector. Here this technique has been used to measure the frequency response of the AWOD. The source laser was operated with 1nS rise time pulses from a HP

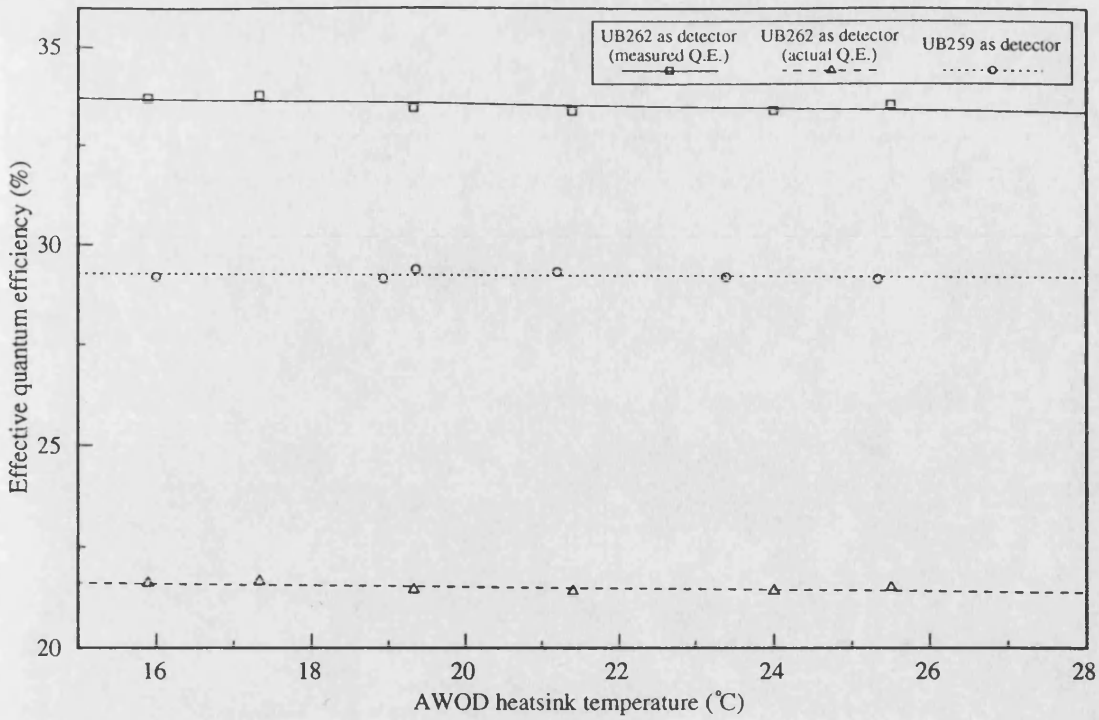

Figure 4.24. The effect of the AWOD temperature change on its efficiency as a function of the facet reflectance.

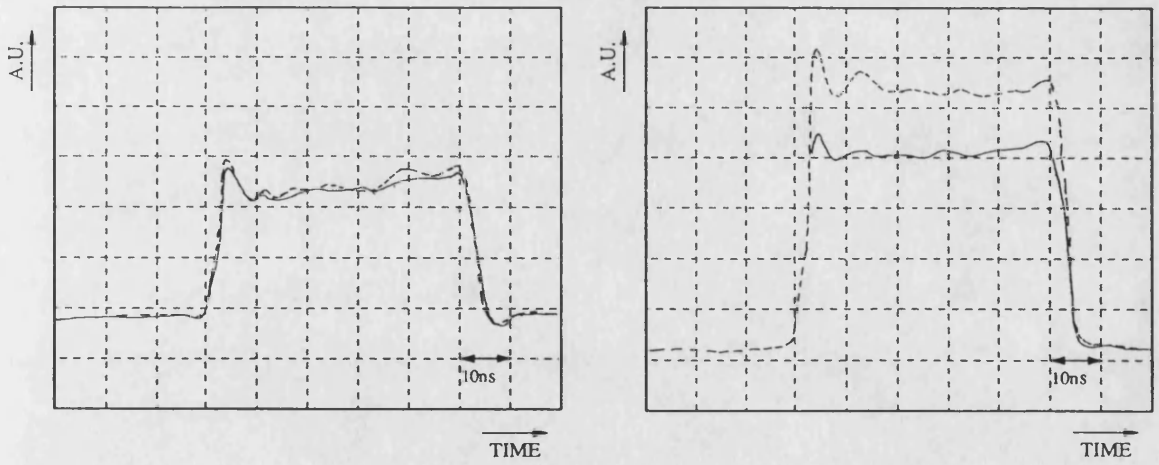

(a) (b)

Figure 4.25. The pulse response of the AWOD under bias (dotted line) and zero bias (solid line) conditions. (a) at point-1 and (b) at point-2 in figure 4.17.

pulse generator. The typical width of pulses was kept constant at 50ns. The AWOD was excited with the source laser output and the output of the AWOD was fed to a sampling oscilloscope using a 25ps Tektronix sampling head. The pulse response of the AWOD was measured under reverse-bias and zero bias conditions at point-1 and point-2 in figure 4.17. The output pulse shape was traced directly from the sampling oscilloscope CRT. Figure 4.25a is showing pulse response of the AWOD at point-1 under no bias and reverse-bias conditions. The pulse rise time under bias and no bias condition are calculated as 2.81ns. The applied voltage was expected to decrease the rise time of pulse [8], but this has not happened due to the domination of the *RC* time of the external circuit. The rise time of 2.81ns gives a approximate frequency response of 380MHz. Theoretically a frequency response of 785MHz can be achieved for typical 50Ω external circuit with C_j=14*pF*. But this value could not be achieved in practices probably due to the introduction of extra capacitance added by connecting wires. Because the laser which was under investigation was not designed for high frequency applications and the input leads were not properly screened as the same laser was going to be used as active waveguide amplifier later on. Therefore it was impossible to remove this effect and this has increased the RC time constant. Consequently, the actual frequency response of the detector is considerably wider than the above figures indicate.

Figure 4.25b shows the pulse response of the AWOD at point-2 in figure 4.17 where the saturation of the AWOD output takes place. The AWOD under bias conditions, shows a rise time of 2.74ns and at zero bias condition, the rise time of pulse has increased to 2.83ns.

In all the cases, pulse rise time is nearly same because frequency response of the AWOD is dominated by the *RC* time constant of total capacitance (junction capacitance and lead capacitance) and resistance of detecting circuit.

4.7.3. Optical flux leakage in active waveguide components

The presence of optical flux leakage was indicated in sections 4.7.1 and 4.7.2.2 for both monolithic and hybrid integrated AWOD and at that time it was assumed that the leakage of optical radiation could be through the transparent cladding layers. In this section this assumption is justified and the origin of sources of optical radiation leakage are investigated.

4.7.3.1. Justification of optical radiation leakage in an AWOD

In the following set of experiments, monolithic integrated devices were used for two reasons:

1. When segments A and B are pumped together, a very intense output can be achieved which will spread inside the etched gap due to the so called divergence process and all the layers of segments C and D are expected to be illuminated.

2. The position of the input beam to segments C and D can be manipulated by means of the bistable switching process found in twin stripe lasers by simply changing the drive current to laser A and laser B [26].

The experimental set-up of figure 4.26 was used. The LAD was mounted on an X-Y motor drive base which was able to scan in the horizontal (lateral) and vertical (transverse) directions. The speed of scanning and direction of movement was controlled by a control circuit. A 0.1mm (approximately) slit was used in front of the LAD to increase the resolution of the detected near field pattern. At the same time, a camera with a natural density filter to reduce the intensity of the light beam was used at the front facet of UB136 to examine the near field beam pattern on the T.V. screen from the front facet.

The existence of cross-coupled modes which cause bistable switching, similar to that was observed in reference-26, was observed from the front facet of UB136 when segments A and B were pumped together. This cross-coupled mode causes the optical filament produced by pumping lasers A and B together to move with

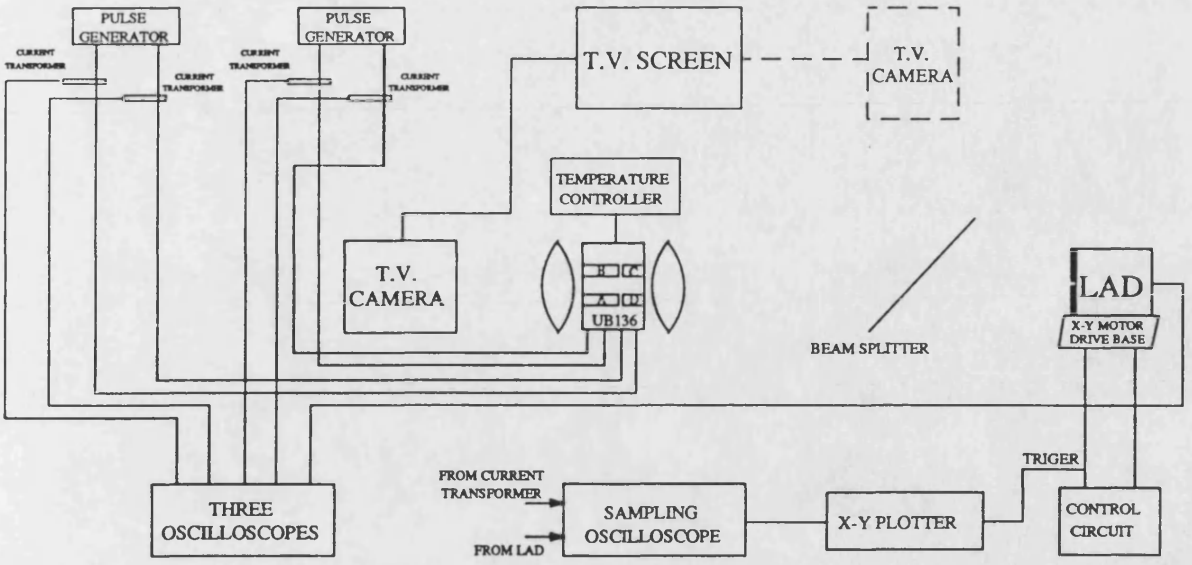

Figure 4.26. The schematic of the experimental set-up for the investigation of optical flux leakage in monolithic integrated active waveguide.

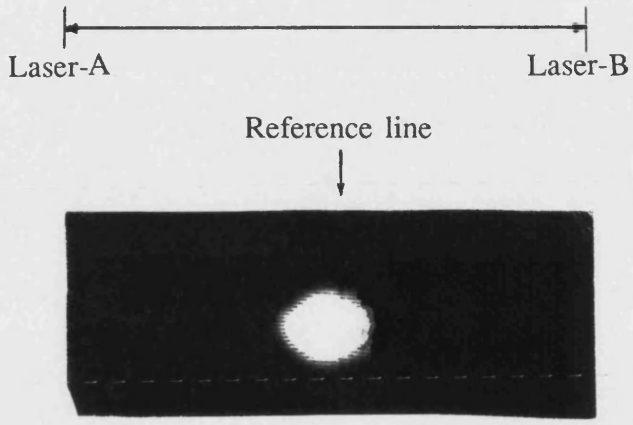

State-1

I_A=109mA

I_B=102mA

(a)

State-2

I_A=115mA

I_B=102mA

(b)

State-3

I_A=115mA

I_B=105mA

(c)

Figure 4.27. Figure showing the cross-coupling of the lateral mode in a four stripe laser. Photograph taken from the front facet of UB136; (a) state-1, (b) state-2 and (c) state-3.

the change in the laser-A and the laser-B drive currents. The movement of the filament is shown in figure 4.27 taken from the front facet around a reference line on T.V. screen. In state-1, when I_A=109mA and I_B=102mA, the output spot is on the left side of reference line. In state-2, when I_A=115mA and I_B=102mA, beam spot move towards the right and in state-3, when I_A=115mA and I_B=105mA, beam spot again has come back to the original position of state-1. Therefore, state-1 and state-3 are basically the same, but it can be seen, that the output beam is more intense in state-3. The corresponding optical flux leakage from the back facet of UB136 is shown in figures 4.28 and 4.29. These near field patterns were obtained by scanning the LAD in the lateral and transverse directions respectively. In figures 4.28 and 4.29, different scales for output optical power and distance have been used because the near fields were taken at different times but under the same conditions.

In figure 4.28a, two peaks (one with a smaller peak and the other with a higher amplitude) can be seen. In state-2 (figure 4.28b), as the filament moves towards the right, the intensity of both peaks changes. In state-3 (figure 4.28c), when the filament shift to the left, the near field pattern takes the original shape (the shape similar to figure 4.28a) but this time, the amplitude of both peaks is higher. This shows the movement of the filament follows the similar pattern of figure 4.27 and this indeed is an evidence that the light is passing through segment C and D. The leakage of optical radiation is also confirmed by the results of figure 4.29.

The leakage of optical radiation was confirmed further by taking the photographs of the near field patterns from the T.V. screen by placing the camera at the back facet of UB136 for state-1, state-2 and state-3 as shown in figure 4.30. Figure 4.30 clearly show the existence of leakage flux. By examining figure 4.28 through to figure 4.30 the assumption for optical flux leakage is shown.

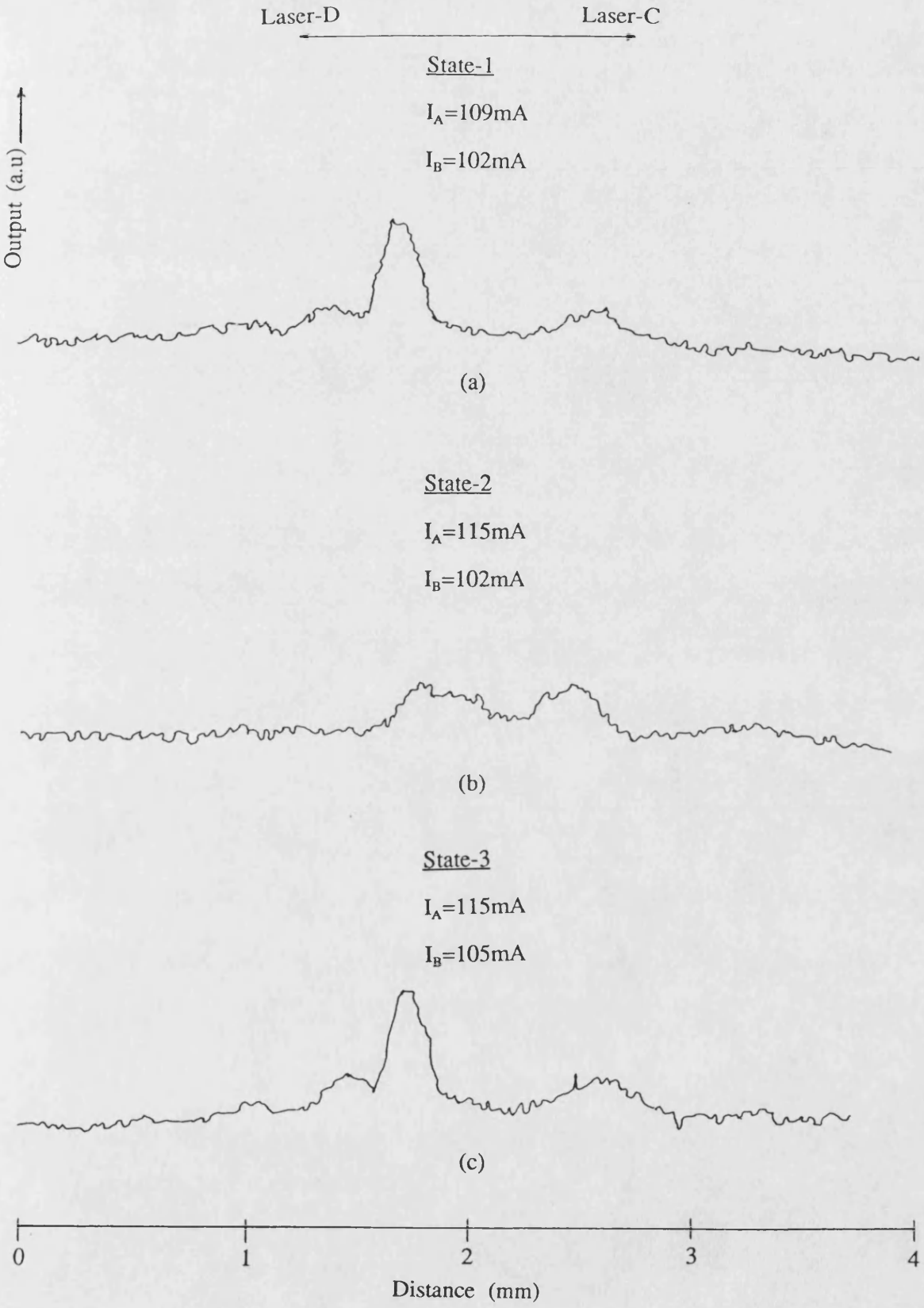

Figure 4.28. Lateral near field patterns showing optical flux leakage from the back facet of UB136; (a) state-1 and (b) state-2; (c) state-3.

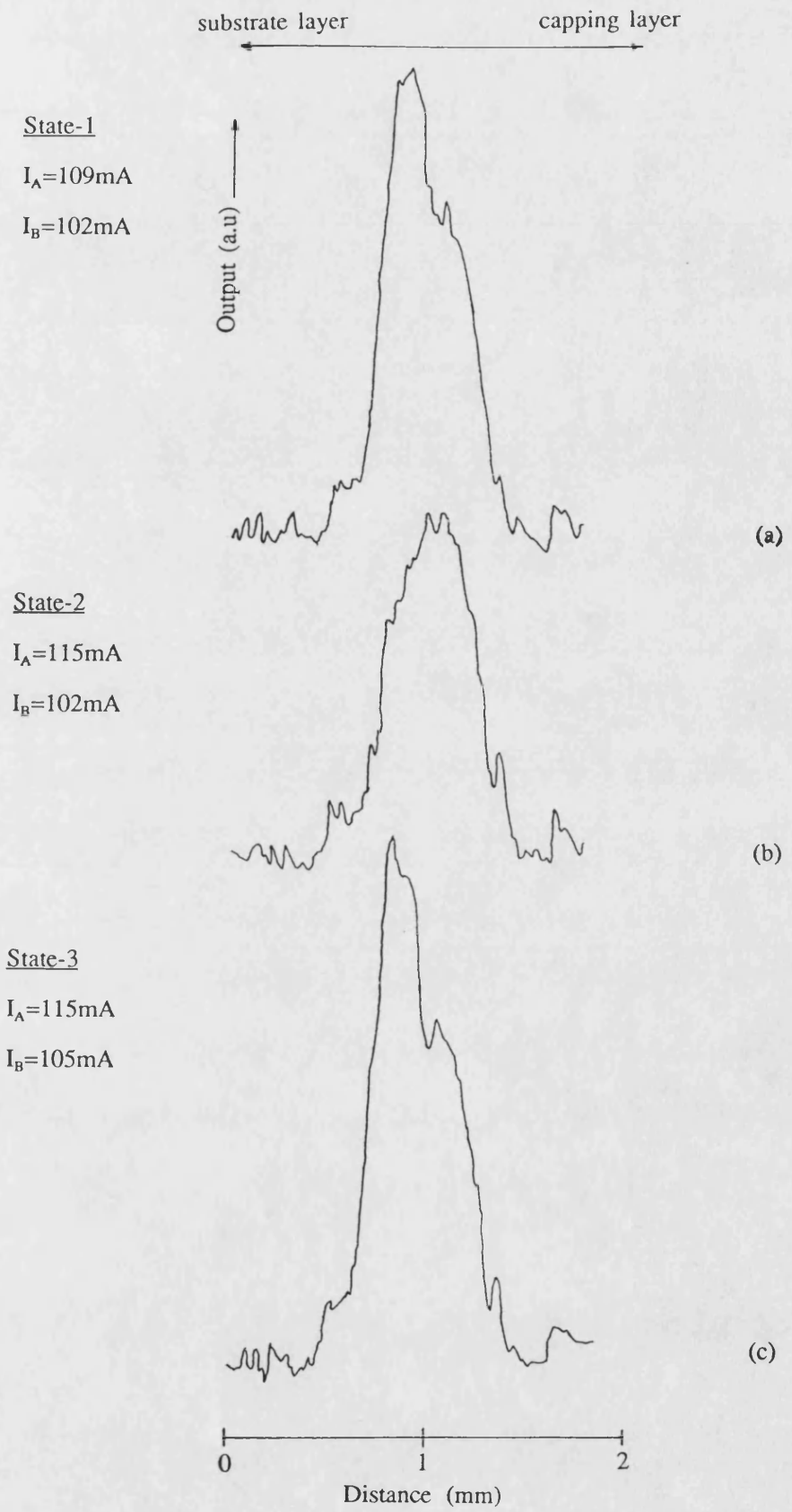

Figure 4.29. Transverse near field patterns showing optical flux leakage from the back facet of UB136; (a) state-1, (b) state-2 and (c) state-3.

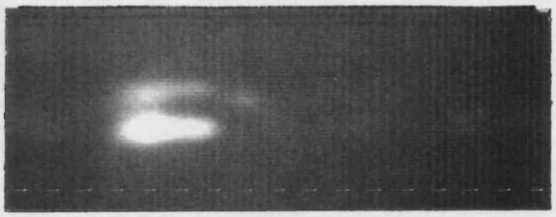

State-1

I_A=109mA

I_B=102mA

(a)

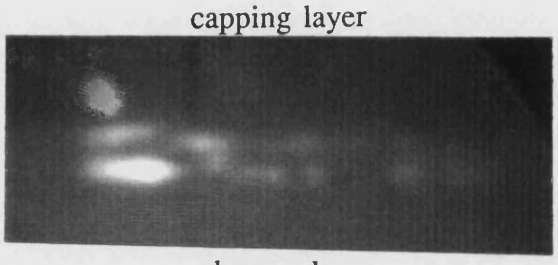

State-2

I_A=115mA

I_B=102mA

(b)

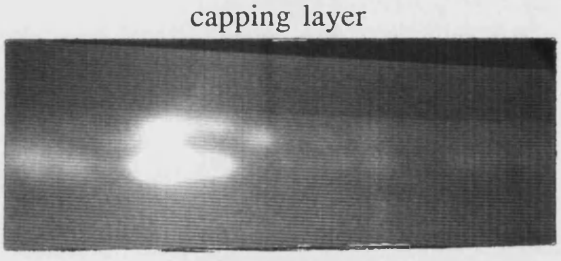

State-3

I_A=115mA

I_B=105mA

(c)

Figure 4.30. The photographic representation of near field showing the leakage of optical flux; (a) state-1, (b) state-2 and (c) state-3.

4.7.3.2. Origin of optical radiation leakage

In last section, the fact of leakage of optical radiation was shown with the help of the near field patterns. But the source of the leakage was not obtained by this method. In order to obtain the main sources of leakage, the position of laser-C and laser-D was obtained in near field pattern of figures 4.28 and 4.29 by pumping the laser-C and laser-D individually as shown in figures 4.31a and 4.31b in the lateral and transverse directions. Once the position of each respective device was found, the exact location of the sources of leakage was obtained by measuring the lateral and transverse near field profiles, whilst laser-C and laser-D were being pumped under conditions of additional optical input from laser-A and laser-B. The results are presented in figures 4.32 and 4.33 for all three states. The intensity distribution of light from the back facet was also recorded at state-2 using the CCTV. Figure 4.34a shows the near field pattern on the T.V. screen when laser-C was pumped whilst figure 4.34b shows the near field pattern on the T.V. screen when laser-D was pumped.

Figures 4.32 through to 4.34 show the existence of optical leakage around the active layer but they still do not give any clear idea about the exact location of the sources of leakage because input radiation was spread out in the etched gap between the stripes. In order to find out the exact location of sources of leakage, it was decided to use the hybrid approach because in this case each layer can be targeted easily with input radiation from the source laser by using the experimental set-up of figure 4.35. Here, UB238 and UB262 were used as the source laser and AWOD respectively. The temperature of both devices was kept constant using Peltier coolers. Also, the source laser drive current was kept constant at 100mA. After aligning the system, the active layer was targeted and a very small amount of light was passing through the active layer as shown in figure 4.36a. It can also be seen from figure 4.36a that quite intense, but dispersed, radiation was coming from the top of the AWOD and this leakage is likely to be due to reflections from different surfaces. The exact location of leakage through AWOD was pointed out

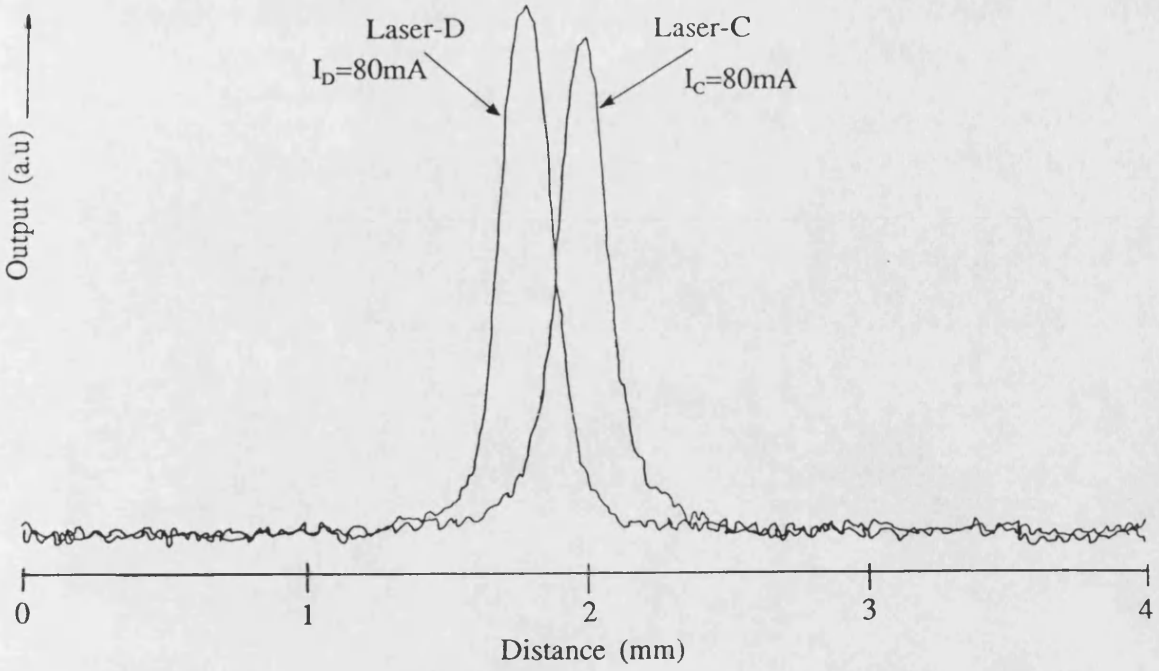

(a)

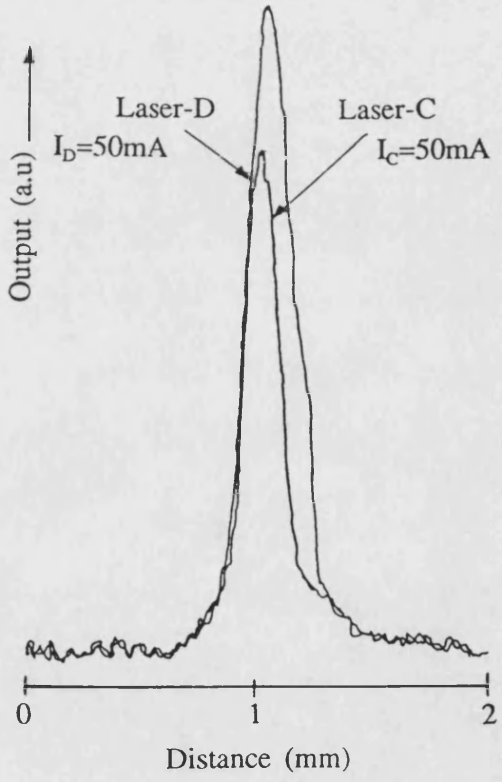

(b)

Figure 4.31. The near field patterns of laser-C and laser-D; (a) in lateral direction and (b) in transverse direction.

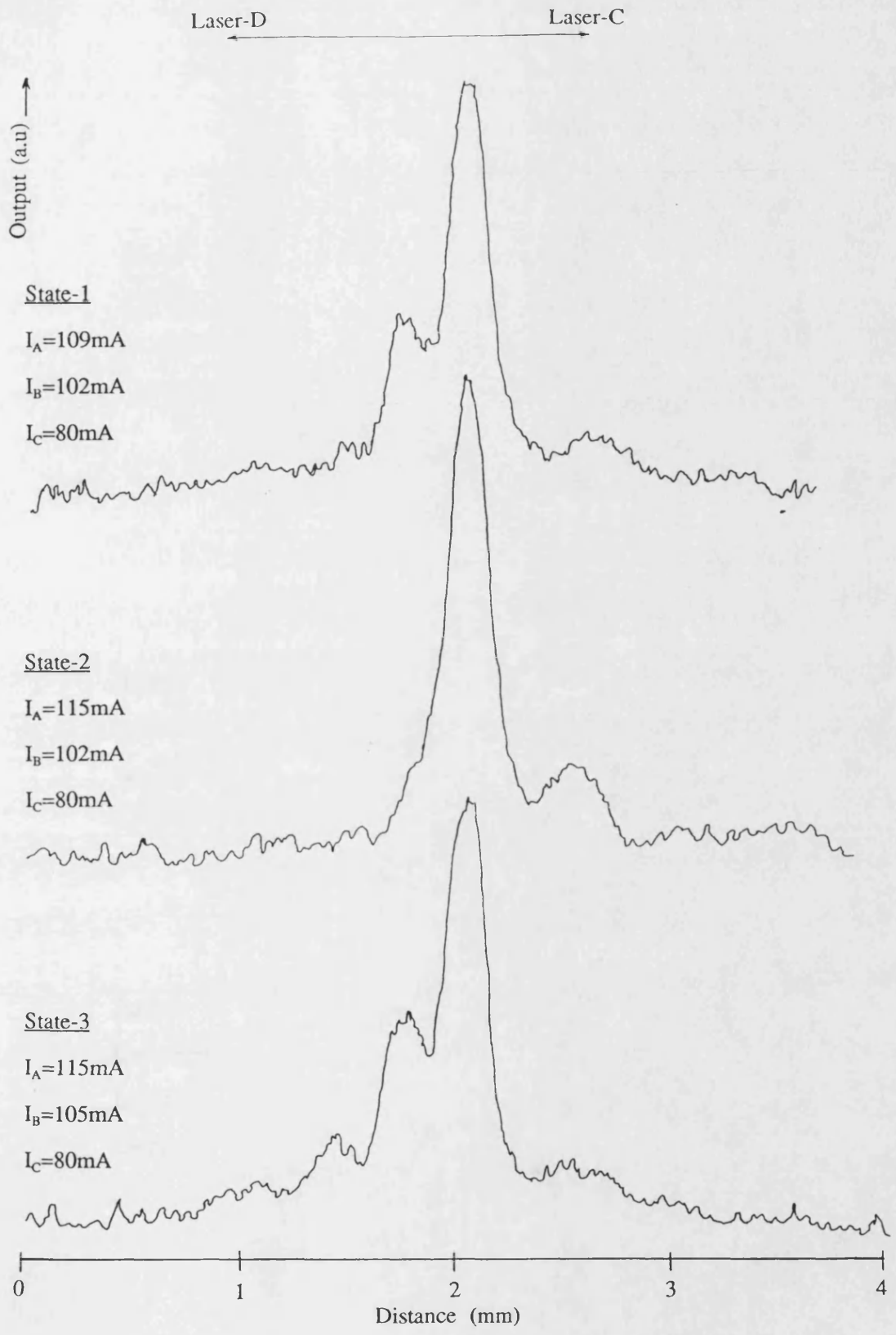

(a)

Figure 4.32 (continue).

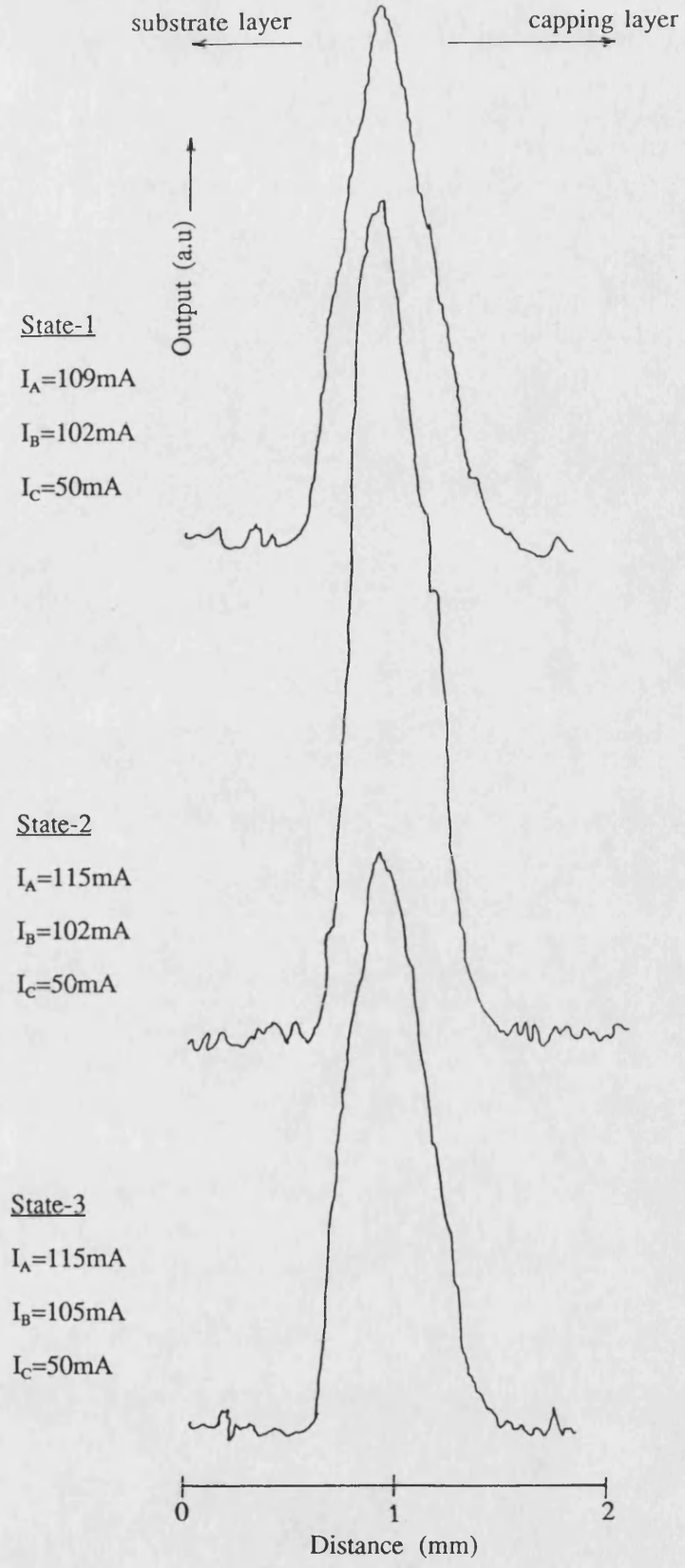

(b)

Figure 4.32. The near field pattern of laser-C subjected to an optical input; (a) lateral direction; (b) transverse direction.

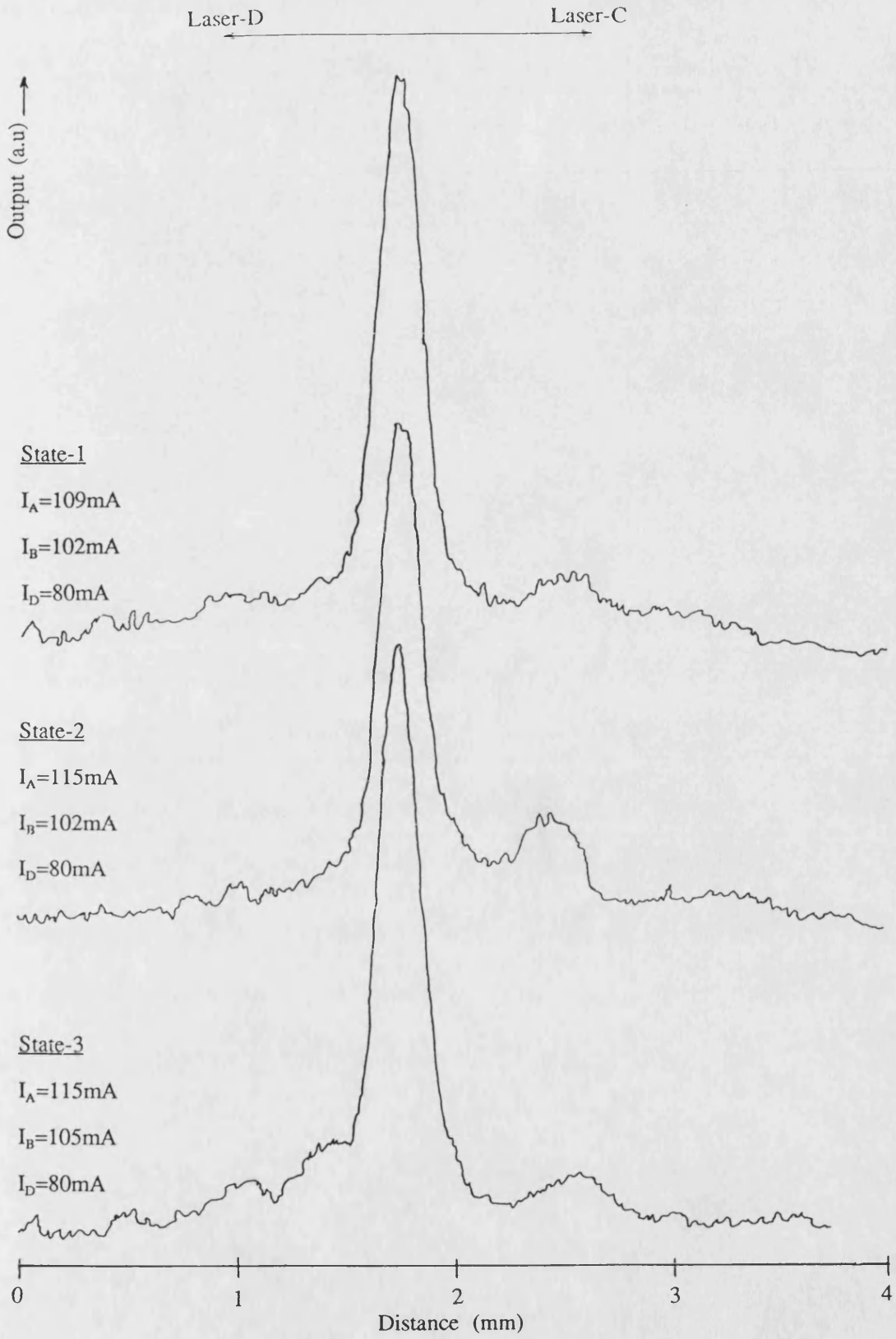

(a)

Figure 4.33 (continue).

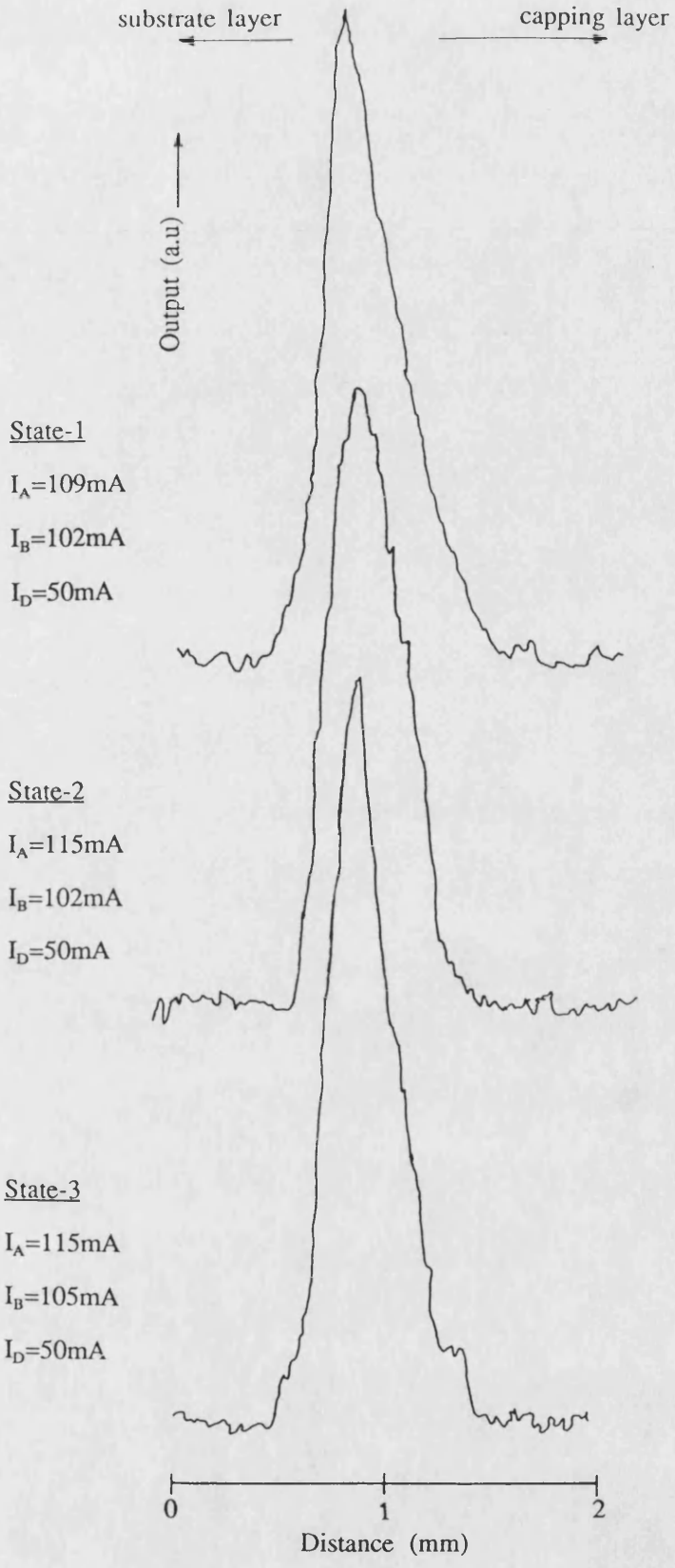

(b)

Figure 4.33. The near field pattern of laser-D subjected to an optical input; (a) lateral direction; (b) transverse direction.

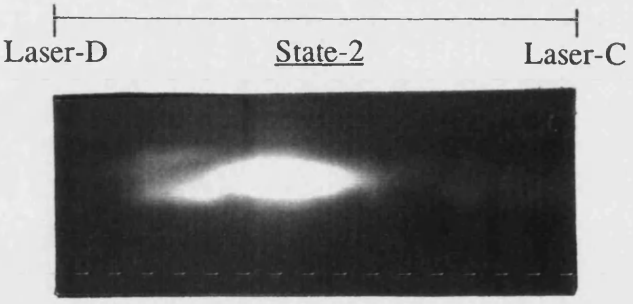

I_A=115mA

I_B=102mA

I_C=50mA

(a)

State-2

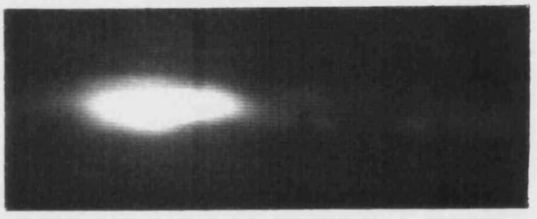

I_A=115mA

I_B=102mA

I_D=50mA

(b)

Figure 4.34. Near field pattern on the T.V. screen in the presence of optical input for state-2; (a) laser-C and (b) laser-D.

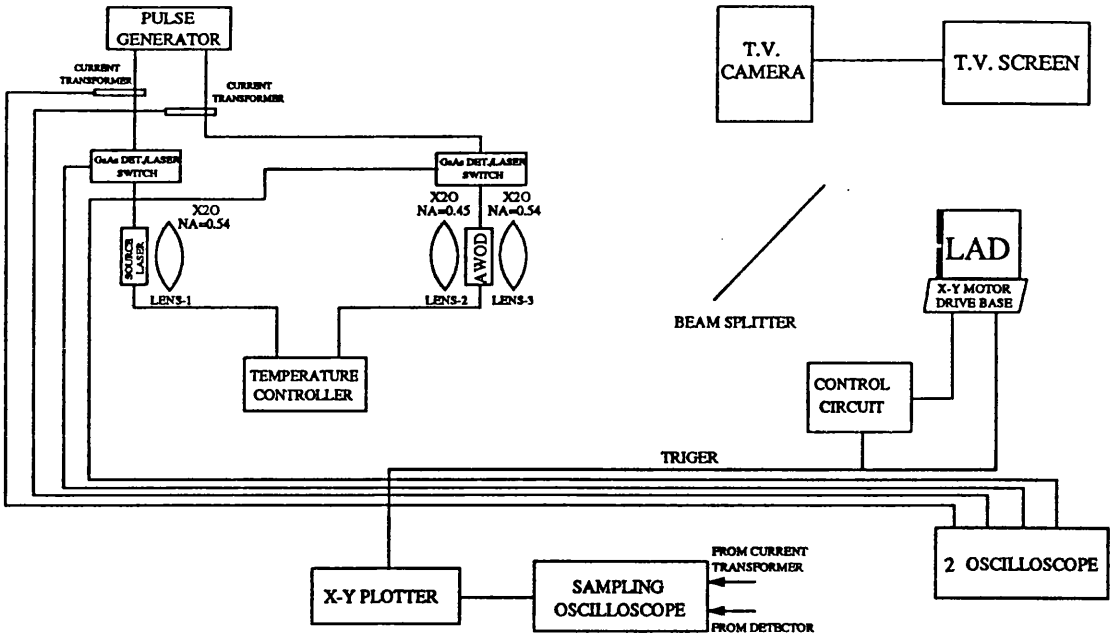

Figure 4.35. The schematic representation of the experimental set-up used to investigate leakage optical flux in hybrid integrated active waveguide.

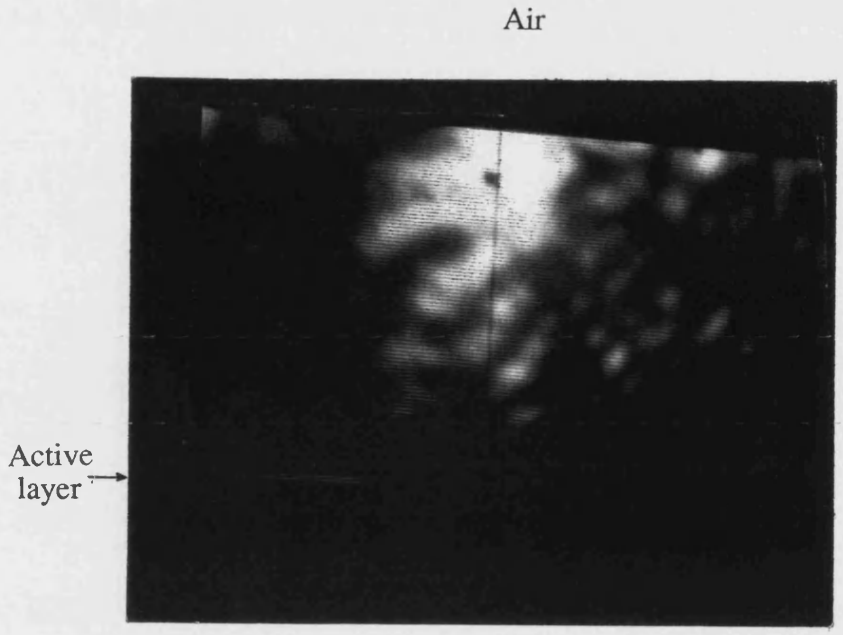

(a)

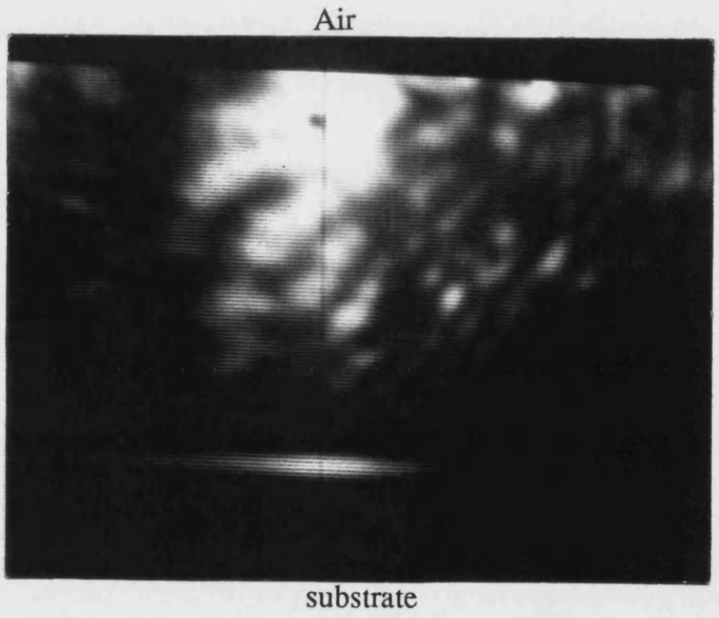

(b)

Figure 4.36 (continue).

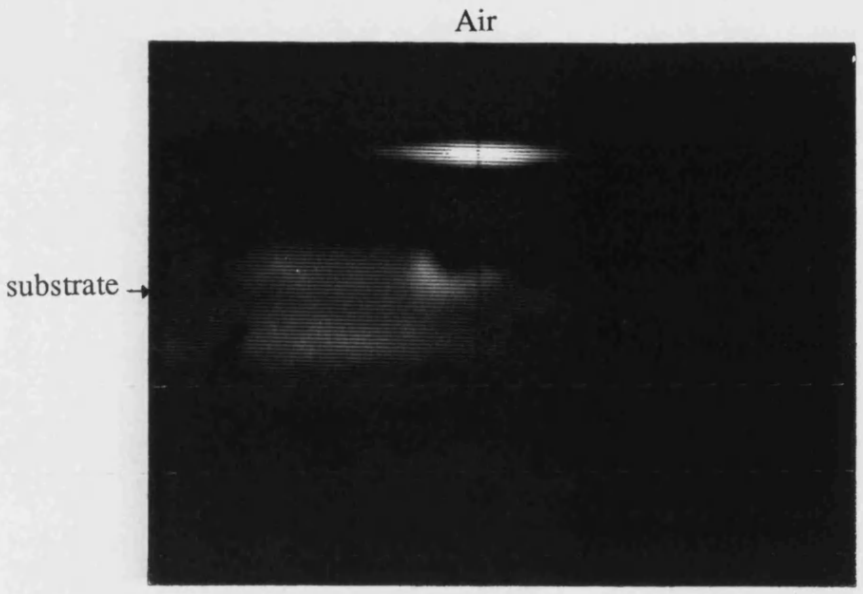

(c)

Figure 4.36. The sources of optical flux leakage in *p*-side up mounted hybrid active waveguide subjected to the optical input; (a) leakage from intrinsic layer, (b) output of from UB262 while subjected to optical input and (c) leakage from the substrate material.

by pumping the AWOD locally, while it was subjected to the input from the source laser and near field is shown in figure 4.36b. By comparing figures 4.36a and 4.36b, the leakage of the optical flux through the active layer close to area under the stripe can be seen and also, a very small amount of leakage is coming through the area under stripe. The leakage of optical radiation from the active layer does support the argument of section 4.7.2.3. and this can be explained as; when the input was coupled to the input facet of the AWOD, it was partially absorbed and partially transmitted due to low absorption coefficient. As it travels along the length, the absorption coefficient starts to increase as the intensity of the light beam reduced and at the end, either radiation was completely absorbed or most of it was absorbed. As in ridge waveguide laser, the field is weakly guided in lateral direction, a certain amount of light coupled to the area close to stripe in the lateral direction. Also in ridge waveguide, the index of the ridge is slightly higher than that of surrounding, so the amount of light coupled to area close to the area under stripe, has suffered less losses and that's why a higher amount of leakage is observed. But this source of leakage is very small as compared to the leakage from the top of the device. Under the same conditions, when the beam of light was pointed to the lower cladding layer, no leakage was observed. But as beam was moved further down towards the substrate, a more wider beam as shown in figure 4.36c was seen and this was coming through the substrate. When the beam of light was pointed to the upper cladding layer, leakage from the top of the device was increased. It was not clear that whether there was any leakage from the upper capping layer as it was very close to the air.

In order to examine the leakage from capping layer, a *p*-side down geometry laser device, UB300, was used. This device has a stripe width of 15μm and a device length of 300μm. There was no leakage observed from capping layer. In a similar manner to last case, a leakage was observed from the active layer and from the substrate as shown in figures 4.37a and 4.37b.

In conclusion it can be deduced from the above discussion and results that

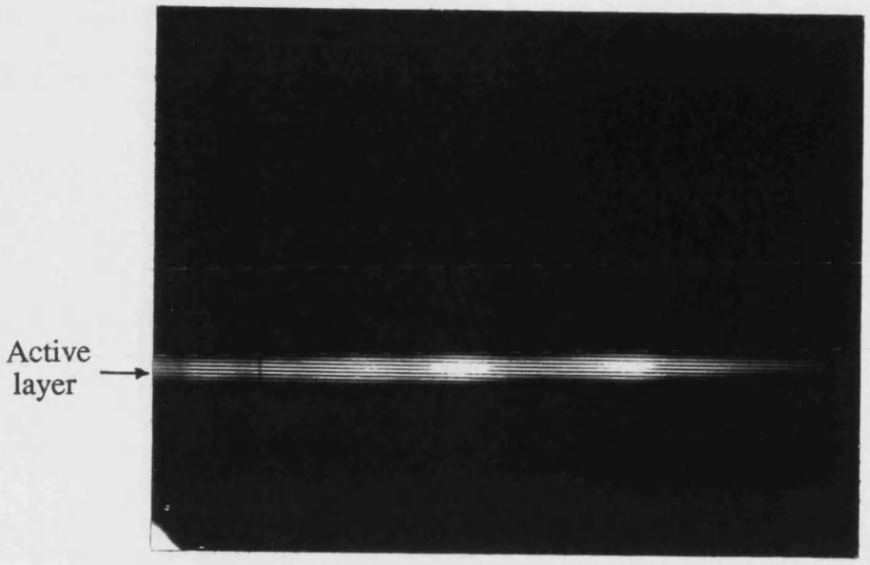

(a)

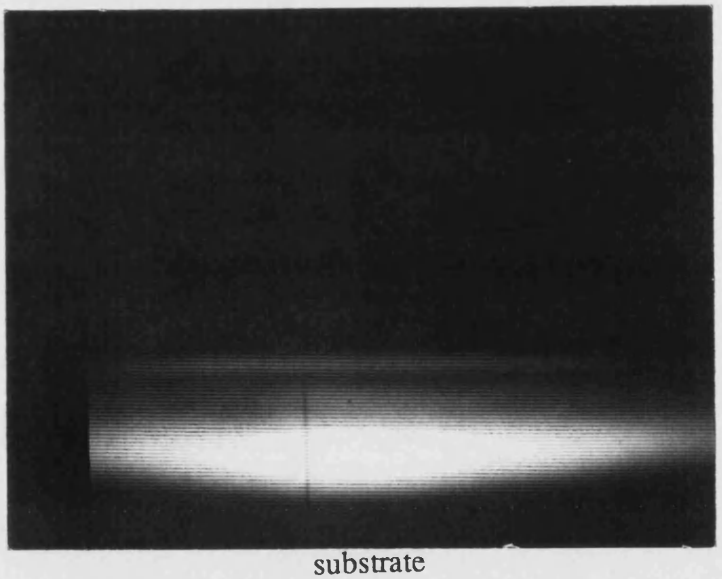

(b)

Figure 4.37. The sources of the leakage of optical flux in *p*-side down mounting (UB300) subjected to the optical input; (a) leakage from active layer and (b) leakage from active layer ad substrate material.

there could be three sources of leakage in monolithic active device and are as follows;

1. From air due to dispersion and unwanted reflections,
2. From the intrinsic layer (area under the stripe or close to the stripe),
3. From the substrate material.

However, in hybrid active devices where the input beam is focussed to the active layer, the leakage of optical radiation would be:

1. From intrinsic layer (area under the stripe or close to the stripe) and
2. From air due to unwanted reflection and dispersion phenomena.

4.7.3.3. Temperature dependence of optical radiation leakage

The effect of temperature variations on the optical flux leakage was also analysed by placing the LAD at the output facet of the AWOD, while the source laser temperature and drive current was kept constant. At the same time, the temperature of the AWOD was varied from point *C* to point *D* in figure 4.13. Figure 4.38 shows the AWOD response versus optical flux leakage. It can be seen from figure 4.38 that the leakage increases rapidly as the temperature of the AWOD is decreased. It can be deduced from figure 4.38 that there exists a maximum value of leakage which corresponds to optimum alignment and that there is a worst-case alignment where there exists a minimum value of leakage (although this maximum leakage is probably due to dispersion of optical radiation). Therefore, the condition of optimum alignment cannot be achieved without encountering optical flux leakage.

4.8. Summary

The optical detection properties of the active waveguide optical detector as an active circuit element in OIC integration have been investigated. A comparison between the basic properties of conventional optical detectors and the AWOD was carried out and the AWOD was found to offer some promising advantages such as

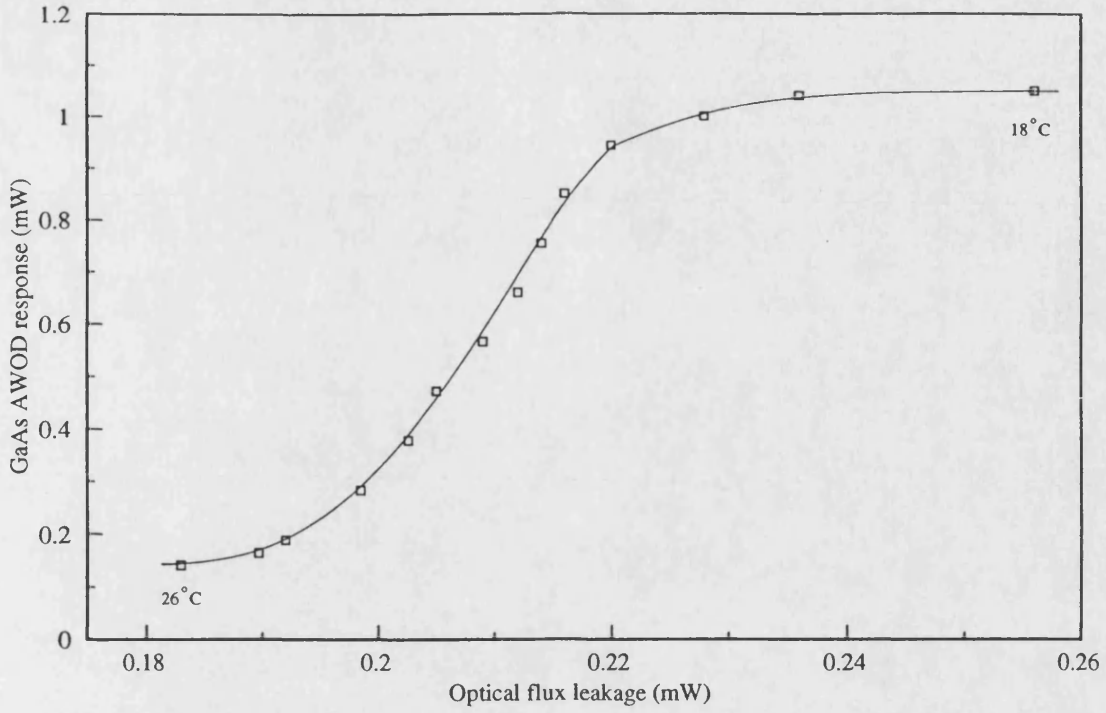

Figure 4.38.The effect temperature change on the leakage of optical flux.

multiple use (transmitter and receiver) simply by altering the bias, zero bias operation, high frequency response and low noise figure.

A non-destructive, novel alignment technique has been demonstrated for the alignment of active components in hybrid approach. This alignment technique was found highly temperature dependent due to change in cavity length with temperature variation. Optical flux leakage, observed in the monolithic approach and hybrid approach, was highest at maximum alignment. This property can be used in judging whether a component is aligned or not.

The responsivity for the hybrid AWOD was found to be in agreement with the reported values. The responsivity of the GaAs AWOD was increased successfully by increasing the thickness of the active layer to maximise coupling with the source laser. This method is ideal for the hybrid detector but would be unnecessary for a totally integrated structure.

Reduction in the responsivity of the GaAs AWOD was observed at a high levels of input power under zero bias. This problem was solved by supplying a small negative bias voltage to the AWOD in the normal way.

The responsivity of the A.R. coated and FP AWOD were compared and found to be different. Multiple reflection between the source laser and AWOD facets was concluded as a reason that caused a 56% increase in the effective input power to the FP AWOD. In all cases, the responsivity of the GaAs AWOD was found to between 0.15A/W (corrected to take account of multiple feedback between two active components) and 0.35A/W which is in agreement with reported values.

Disagreement between the calculated and measured frequency response was observed due to the introduction of extra capacitance from connecting leads. The frequency response of the existing system can be increased by improving laser design and reducing the junction capacitance. Shortening and proper screening of connecting wires is another option to increase the measured frequency response. By adopting these suggestions, the measured frequency response of the AWOD can

be increased into GHz range [19].

The leakage of optical radiation in the AWOD (monolithic and hybrid) was thoroughly investigated and existence of leakage was justified to validate the assumption made earlier in this chapter. The sources of leakage in the active wave-guide component were obtained. Monolithic and hybrid integrated devices were sharing two common sources of leakage i.e. leakage from air and from the intrinsic layer, while monolithic integration also suffers from leakage from the substrate layer. Among all sources, leakage through the top of device (from air) was more severe. These sources of noise can be reduced by increasing the length of the device.

References

1. Yuasa, T., Yamada, T., Asakawa, K., and Ishii, M., 'Performance of dry-etched short cavity GaAs/AlGaAs multiquantum-well lasers', J. Appl. Phys., vol.63, p.1321, 1988.
2. Wang, S.Y., Bloom, D.M., '100 GHz bandwidth planar GaAs Schottky photodiode', Electron. Letters, vol.19, p.554, 1983.
3. Bowers, J.E., Burrus, C.A., and Mitschke, F., 'Millimetre-waveguide-mounted InGaAs photodetectors', Electron. Letters, vol.22, p.633, 1986.
4. Melchior, H., 'Demodulation and photodetection techniques', Laser handbook, vol.1, p.725, 1972, Arecchi, F.T., and Schulz-Dubios, E.O.(Eds.).
5. Conradi, J., Kapron, F.P., and Dyment, J.C., 'Fiber-optical transmission between 0.8 and 1.4μm', IEEE Trans. on Electron Devices, vol. ED-25, p.180, 1978.
6. Merz, J.L., and Logan, R.A., 'Integrated GaAs -$Al_xGa_{1-x}As$ injection lasers and detectors with etched reflectors', Appl. Phys. Letters, vol.30, p.530, 1977.
7. Bowers, J.E., and Burrus, C.A., 'High-speed zero-bias waveguide photodetectors', Electron. Letters, vol.22, p.905, 1986.
8. Erman, M., Riglet, Ph., Jary, Ph., Martin, B.G., Menaud, M., Vinchant, J.F., and Cavailles, J.A., 'Optical circuits and integrated detectors', IEE Proc. J, vol.138, p.101, 1991.
9. Alping, A., Tell, R., and Eng, S.T., 'Photodetection properties of semiconductor laser diode detectors', J. of Lightwave Tech., vol. LT-4, p.1662, 1986.
9. Gustavsson, M., Karlsson, A., and Thylen, L., 'Travelling wave semiconductor laser amplifier detectors', J. of Lightwave Tech., vol.8, 1990.
10. Sun, M.J., Chang, W.S.C., and Wolfe, C.M., 'Frequency demultiplexing in GaAs EAP waveguide detectors', Applied Optics, Vol.17, p.3533, 1978.
11. Sze, S.M., 'Physics of semiconductor devices', John Wiley, 1981.
12. Sun, M.J., Nichols, K.H., Chang, W.S.C., Gregory, R.O., Rosenbaum, F.J., and Wolfe, C.M., 'Gallium arsenide electroabsorption avalanche photodiode waveguide detectors', Applied Optics, Vol.17, p.1568, 1978.
13. Saleh, B.E.A., and Teich, M.C., 'Fundamental of photonics', John Wiley, 1991.
14. Madelung, O.(ED.), 'Physics of group elements and III-V compounds', Landolt-Bornstein numerical data and functional relationship in science and technology, vol.17a, pp.532-533, Springer-Verlag, 1982.
15. Sasaki, A., Nishiuma, M., and Takeda, Y., 'Energy band structure and lattice chart of III-V mixed semiconductors and AlGaSb/AlGaAsSb semiconductor lasers on GAsb substrate', Jap. J. of Applied Phys., vol.19, 1695, 1980.
16. Bowers, J.E., and Burrus, C.A., 'Ultrawide-band long-wavelength p-i-n photodetectors', J. of Lightwave Tech., vol. LT-5, p.1339, 1987.
17. Gower, J., 'Optical communication systems', Prentice/Hall International, 1984.

18. Figueroa, L., Slayman, C.W., and Yen, H.W., 'High-frequency characteristics of GaAlAs injection lasers', IEEE J. Quantum Electron., vol. QE-18, p.1718, 1982.

19. Alping, A., 'Waveguide *pin* photodetectors: theoretical analyses and design criteria', IEE Proc. J, vol.136, 177, 1989.

20. Gillespie, A.K., 'Investigation into properties of a tandem double heterostructure GaAs/AlGaAs semiconductor device and use of such a device as a monolithically integrated laser and photodetector', Final year project report, Bath University, 1986.

21. Bouadma, N., Correc, P., and Brillouet, F.P., 'GaAs:GaAlAs ridge waveguide lasers and their monolithic integration using the ion beam etching process', IEEE J. Quantum Electron., vol. QE-25, p.2219, 1989.

22. Hunsperger, R.G., Yariv, A., and Lee, A., 'Parallel end-butt coupling for optical integrated circuits', Applied Optics, vol.16, p.1026, 1977.

23. Hasnain, G., Tai, K., Wang, Y.H., Wynn.,J.D., Choquette. K.D., Weir, B.E., Dutta, N.K., and Cho, A.Y., 'Monolithically integrated four-channel reciever array using diffused InGaAs JFET technology', Electron. Letters, vol.27, p.1632, 1991.

24. Baertsch, R.D., and Richardson, J.R., 'An Ag-GaAs Schottky-barrier ultraviolet detector', J. of Appl. Phys., vol.40, p.229, 1969.

25. Stoll, H., Yariv, A., Hunsperger, R.G., and Tangoman, G.L., 'Proton-implanted optical waveguide detectors in GaAs', Appl. Phys. Lett., vol.23, p.664, 1973.

26. White, I.H., Linton, R.S., and Carroll, J.E., 'Directional coupling and bistability in four contact twin-stripe injection lasers', IEE Proc. J, vol.136, 25, 1988.

Chapter-5

Amplification in active waveguide optical amplifiers

5.1. Introduction

Research on optical amplifiers has been carried out for almost three decades and has generally concentrated on the potential use of optical amplifiers in trunk optical communication systems as either a pre-amplifier, a repeater amplifier or as a booster amplifier. Its use as an essential part of an optical integrated circuit has been generally ignored until relatively recently, however, in this chapter, the use of optical amplifiers in the OIC context is considered.

The work in this chapter is aimed mainly at optical local area networks rather than trunk communication systems. Although many of the proposed optical LANs are based on point-to-point techniques, it is an attractive idea to have a continuous optical bus system, in which LAN nodes are connected simply by tapping photons from the main bus or by coupling photons from a local laser onto the main bus. This has one main drawback. Photons that are tapped-off at each node are lost and the accumulation of these tapping losses grows quickly. In a typical passive network, only 10 to 40 nodes may be added before the loss is so high that an acceptable bit error rate between farthest users cannot be achieved.

There is considerable merit and network flexibility offered by the use of the active nodes, whereby the optical splitter is accompanied by an integrated optical amplifier so that as the photons are lost due to splitting, additional photons are generated. This can be achieved by locally pumping the active waveguides so that not only the inherit losses of active waveguide are overcome but that it can provide local gain to overcome fibre losses and connector losses. In this case, the active waveguide can be termed as an active waveguide optical amplifier (AWOA).

There are several parameters required to characterise the performance of the AWOA and these are;

1. the coupling efficiency of input radiation
2. the single pass gain and the signal gain of the input signal
3. the noise power contribution
4. the input/ouput linearity in terms of total input power, P_{in}.

In this chapter these parameters are considered theoretically and investigated experimentally for monolithic integrated AWOAs and hybrid integrated devices. For the investigation of AWOAs in a hybrid configuration, the source laser and AWOA were butt-coupled through optical lens system (see figure 1.6).

The theoretical background of the optical amplifier which will later be used to evaluate the performance of an AWOA, will be outlined in section 5.2. This analysis is then utilised later in the experimental section (section 5.3). Subsection 5.3.1 deals with the monolithic approach to optical amplification and subsection 5.3.2 is devoted to the hybrid approach. In this latter subsection, the signal gain, temperature and polarisation dependence of the optical gain, 3dB frequency bandwidth, the limitation of different noise components, the 3dB noise bandwidth and noise factor are calculated by combining the available data and theory discussed in section 5.2. Also in subsection 5.3.2, the nonlinear input/output characteristics of different active waveguide devices are presented. Finally, in section 5.4, the main conclusions from this chapter are presented.

5.2. Optical amplifier

Most trunk optical communication systems in practical use are based on electro-optic or opto-electronic signal conversion for transmission, detection and regeneration using optical fibre as the transmission medium. In many applications, direct optical amplification of the optical signal (rather than modulation/demodulation and regeneration of the signal) would be advantageous. In this respect, the semiconductor optical amplifier has been studied extensively due to its potential for

use in future optical systems and for OIC integration [1,2]. In this section, the different operational characteristic of the practical optical amplifier (such as the FPA and NTWA) are considered.

5.2.1. Types of optical amplifiers

When a forward bias semiconductor laser diode is subject to external input radiation, it will act as an optical amplifier because it inherently contains the light amplification process. If the bias current is set below the oscillation threshold, the laser diode behaves as an optical amplifier to the incident light. When it is biased above the oscillation threshold, it acts as a nonlinear injection optical amplifier and is sometimes referred to as an injection-locked amplifier. This type of optical amplifier is not considered in this work.

Optical amplifiers can be further divided into two main types: Fabry-Perot amplifiers (FPAs) and travelling wave amplifiers (TWAs). The difference between the two types of semiconductor laser amplifier is that the Fabry-Parot structure has partially reflecting input/output ports whilst the travelling wave amplifier has non-reflecting input/output ports (i.e. matched in effective 'impedance' to the source and load 'impedance').

The FPA is a resonant type of amplifier and the two cleaved facets of the semiconductor laser amplifier have considerable reflectivity which act as partially reflective end mirrors as shown in figure 5.1(a). Such an amplifier has a very high Q factor and this makes it very sensitive to changes in temperature, bias current, signal polarization and signal frequency fluctuations and it also puts limitations on the modulation bandwidth. These problems can be avoided by reducing the facet reflectivity of both facets to suppress the feedback of the radiation. This reduces the Q of the amplifier but it also reduces the gain. The result is a travelling wave amplifier (TWA), which is shown schematically in figure 5.1(b). There are a number of techniques to reduce the facet reflectance including the application of anti-reflection (A.R) coating on the facets [3], tilted waveguide structures [4], facet

coated tilted waveguide structures [5] and A.R. coated window structures [6].

In the limiting case, an ideal TWA has zero facet reflectivity. In practice, however, it is difficult to achieve this over a wide range of operating conditions and even with the best available techniques, there is always some residual facet reflectivity in semiconductor TWAs (practically, facet reflectance as low as $3x10^{-5}$ have been achieved [7], but more typically, the residual facet reflectance is 10^{-3} to 10^{-4}). In this case, the amplifier lies between the FPA and the TWA and is referred to as a near travelling wave amplifier (NTWA) [8]. NTWAs are currently of interest due to their high saturation powers and wide operating bandwidth. The NTWA is also less sensitive to temperature, bias current polarization and source wavelength fluctuations than the FPA and its properties lie between those of the FPA and the TWA.

The main disadvantage of the NTWA and TWA is an increased spontaneous noise component because of the higher level of pumping that is needed to achieve the same level of optical gain as an equivalent FPA and additional sensitivity to the effects of external reflection (from other components) than the FPA.

5.2.2. Working principle

When a small current is applied to a laser amplifier (FPA or TWA), any input radiation injected into one end of the amplifier will be strongly absorbed if the wavelength of the radiation is shorter than the wavelength corresponding to the absorption edge of the active material. As the current is increased, the amplifier will first become transparent to the incoming radiation. This point is marked as the threshold of amplification in figure 5.2. Above this level of pumping, the amplifier has net optical gain and any further increase in applied current will increase the optical gain. A consequence of pumping the amplifier is the emission of spontaneous emission. The amplification of locally generated spontaneous emission (ASE) will also take place along with the signals.

If the amplifier is a FP type amplifier, the internally generated optical field

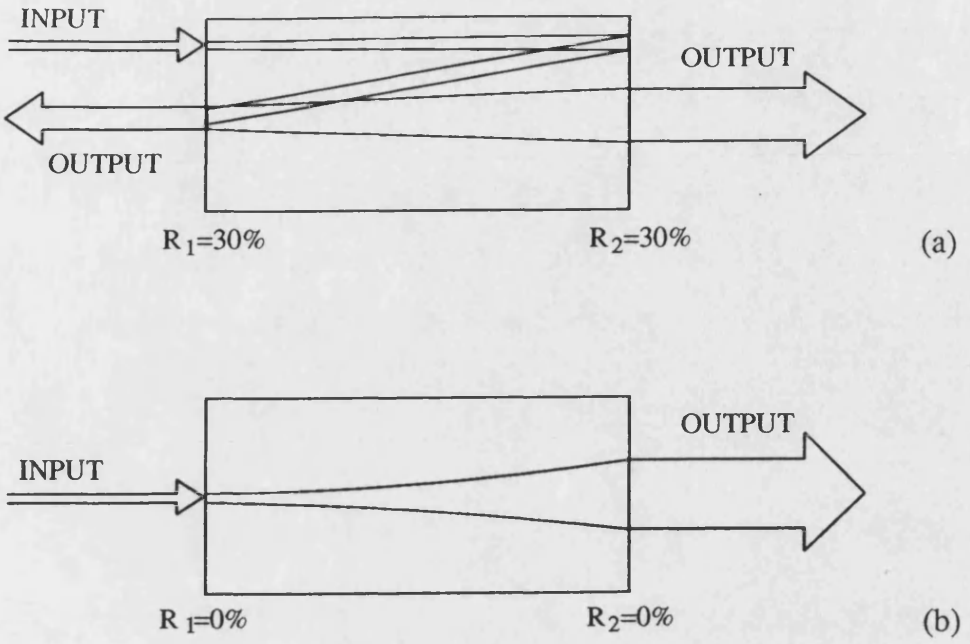

Figure 5.1. The types of the optical amplifier (a) Fabry-Perot amplifier and (b) travelling-wave amplifier.

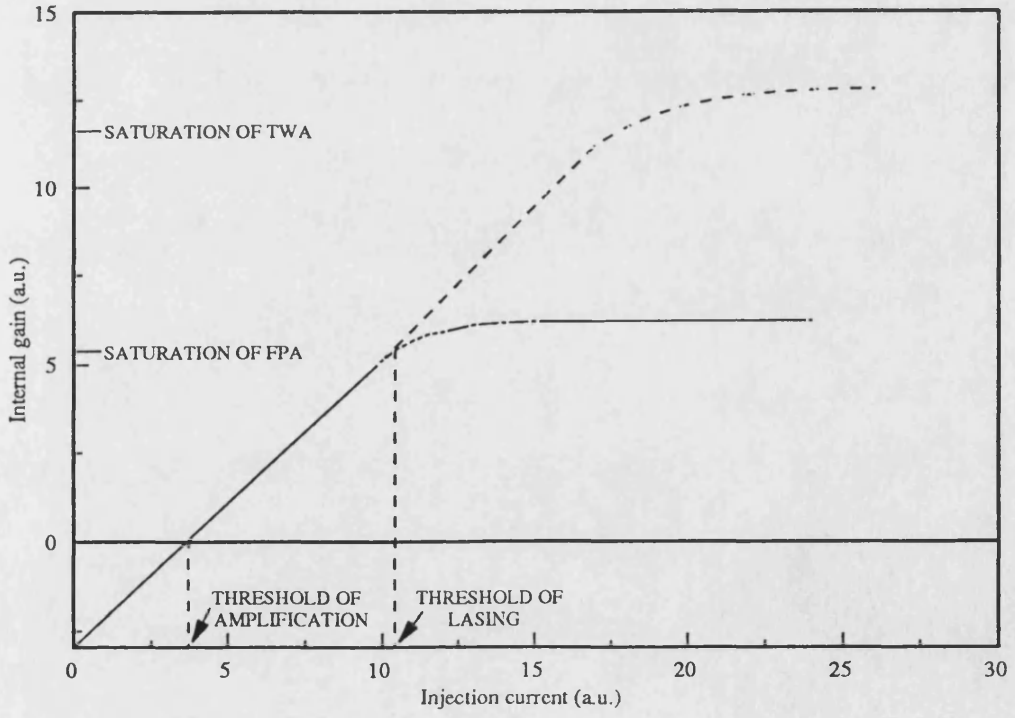

Figure 5.2. The conceptional representation of gain saturation process in an amplifier.

will resonate back and forth between two partially reflecting facets and the gain will begin to saturate at the lasing threshold. This point is marked with the threshold of lasing in figure 5.2. Beyond this point any increase in injected current no longer results in an appreciable change in the optical gain and the amplifier operates in its nonlinear mode.

If, by some means, the internal feedback mechanism is suppressed, as in the case of the NTWA and TWA, the gain saturation effect is also suppressed, till a further saturation point is reached, which is intrinsic to the system. This point is marked as a saturation of the gain of the TWA shown in figure 5.2.

The characteristics of FP and TW amplifier are summarised in table 5.1 below.

Table 5.1. Table showing characteristics of FP and TW amplifiers [1].

Characteristics	Amplifier type	
	FP	*TW*
Amplifier gain	20-30 dB	20-40 dB
Limitation	Gain saturation due to ASE and oscillating field	Gain saturation due to ASE and residual facet reflectivity
Frequency bandwidth	8-43GHz	20 THz
Saturation output level	-7 to -12dBm	5 to 10 dBm
Applications Pre-amplifier Repeater amplifier Booster amplifier Postamplifier	 Yes (with filter) Yes (with filter)	 Yes Yes Yes Yes

5.2.3. Linear amplifier characteristics

In this section, the linear amplifier characteristics such as: the signal gain, saturation and noise performance are considered in terms of the material and structural parameters.

5.2.3.1. Material and structure parameters

The internal gain of an amplifier is limited by gain saturation. The spontaneous emission coefficient, β_s and population inversion factor, n_{sp} are two basic parameters for determining the saturation and noise characteristics of an amplifier. The spontaneous emission parameter β_s, which is also called the saturation parameter, is defined as [9,10];

$$\beta_s = \frac{A\tau_s}{V_o} \tag{5.1}$$

where A is a constant, τ_s is the spontaneous lifetime and V_o is the optical mode volume. The optical mode volume is given by;

$$V_o = \frac{LWd_3}{\Gamma} \tag{5.2}$$

here W is the effective lateral width of the waveguide.

The population inversion parameter n_{sp}, represents the available carrier density degradation from the injected value resulting from the stimulated recombination of carriers. For an ideal gain medium, where no stimulated absorption takes place, n_{sp} is equal to 1. For a linear amplifier with a finite facet reflection coefficient, it is defined as [3];

$$n_{sp} = \frac{N_e}{N_e - N_o} = 1 + A\Gamma N_o \tau_p \tag{5.3}$$

where Γ is the mode confinement factor, N_e is the injected carrier density, N_o is the carrier density at transparency and τ_p is photon lifetime.

The amplification of incident optical radiation takes place in the active layer of an amplifier and the material gain in terms of carrier density in the active layer is defined as [3];

$$g_m = \frac{A}{C_A}(N_e - N_o) \tag{5.4}$$

here C_A is the optical velocity in the amplifying medium.

The material gain coefficient can be obtained by measuring the peak-trough ratio, υ of the passband ripple of an amplifier subjected to input radiation of different wavelengths [11,12]. This method is based on the loss/gain measurement technique of Hakki and Paoli [13]. The dependence of the passband ripple on facet reflectivity and wavelength and its effect on the internal gain of an amplifying medium is illustrated in figure 5.3. The peak-trough ratio leads to an expression for g_m as [10];

$$g_m = \frac{1}{\Gamma}\left[\frac{1}{L}\ln\left(\frac{1}{\sqrt{R_1R_2}}\frac{\sqrt{\upsilon}-1}{\sqrt{\upsilon}+1}\right)+\alpha\right] \tag{5.5}$$

where R_1 and R_2 are input and output facet reflectivities of the amplifier. α is the total internal radiation losses (see section 2.3.4).

The material gain plays a major role in determining the overall amplifier gain and it is related to the population inversion parameter n_{sp} through the carrier density inside an amplifying medium. The dependence of g_m on n_{sp} is shown in figure 5.4 for a carrier concentration of $10^{18}/cm^3$ [1].

5.2.3.2. Signal gain

The single pass gain, G_s in term of the material parameters can be expressed as [3];

$$G_s = \exp[(\Gamma g_m - \alpha)L] \tag{5.6}$$

The single pass gain refers to the unsaturated gain of an ideal TWA where the peak-trough ratio and facet reflectances are ideally assumed to be one and zero respectively. In practice, however, this cannot be achieved and in both the FPA or NTWA, the signal enhancement due to the multiple beam interference between the end facet leads to the overall signal gain, G which is defined as [14,15];

$$G = \frac{(1-R_1)(1-R_2)G_s}{(1-\sqrt{R_1R_2}G_s)^2 + 4\sqrt{R_1R_2}G_s\sin^2\left\{\frac{2\pi L}{C_A}(\Delta\nu)\right\}} \tag{5.7}$$

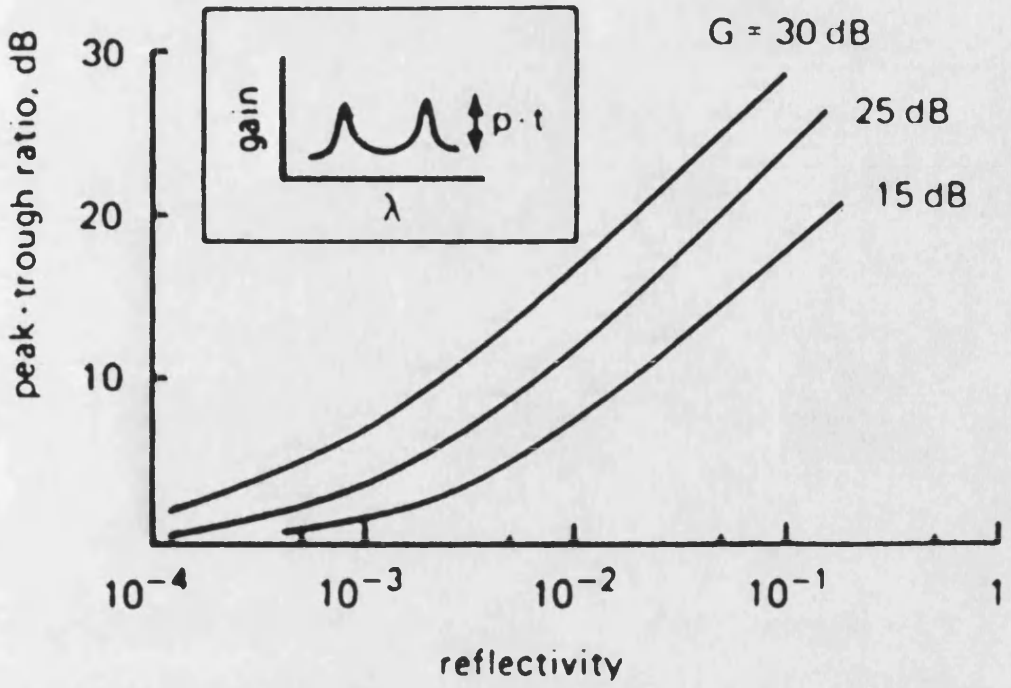

Figure 5.3. Relationship between the peak-trough ratio and facet reflectivity as a function of the signal gain [8].

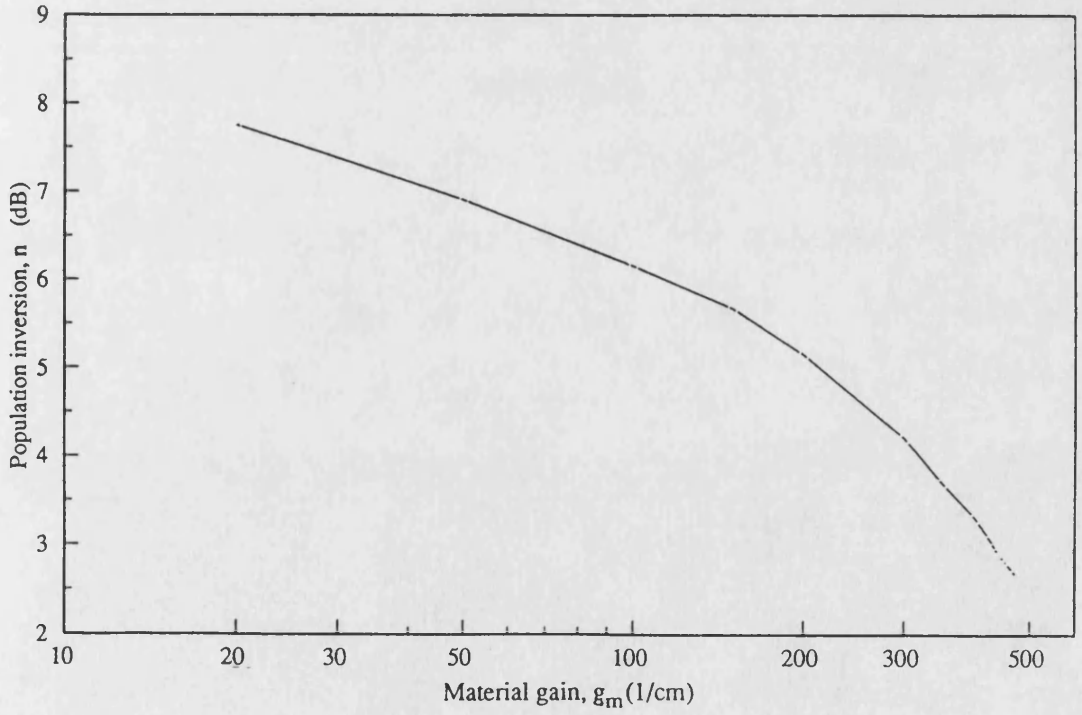

Figure 5.4. Population inversion parameter, n_{sp} versus material gain, g_m for a carrier concentration of $1X10^{18}cm^{-3}$ [1].

and

$$\Delta\nu = \nu - \nu_o \tag{5.8}$$

where ν is the incident signal optical frequency and ν_o is the resonant mode frequency of the AWOA.

The ratio υ of the output power in the resonant state $\nu = \nu_o$ to that in the non-resonant state $\nu = \nu_o + \frac{c_A}{4L}$ is given by [12];

$$\upsilon = \left(\frac{1 + \sqrt{R_1 R_2} G_s}{1 - \sqrt{R_1 R_2} G_s} \right)^2 \tag{5.9}$$

When $\sqrt{R_1 R_2} \to 0$, the amplifier approaches the TWA and $\upsilon \to 1$. When $\sqrt{R_1 R_2} \to 1$, the amplifier approaches lasing threshold limits and $\upsilon \to \infty$. At high values of υ, the amplifier acts as its own optical bandpass filter where the Fabry-Perot peak may be narrower than $\Delta\nu$ in equation (5.7). The signal gain in this case is given by the gain of the central longitudinal mode as [3];

$$G = \frac{(1 - R_1)(1 - R_2) G_s}{(1 - \sqrt{R_1 R_2} G_s)^2} \tag{5.10}$$

The relationship between the single pass gain, G_s and the cavity or internal gain, G of an optical amplifier as a function of facet reflectance is shown graphically in figure 5.5. In figure 5.5, the unsaturated value of G_s increases as the facet reflectance is reduced and in the ideal case, G_s and G are equal. But the generation and amplification of spontaneous emission prevent G_s from becoming equal to G.

Consequently, if R_1 and R_2 are known, the single pass gain G_s and the internal gain G of the amplifier can be found through equations (5.6), (5.9) and (5.7) or (5.10).

5.2.3.3. Gain saturation

In sections 5.2.3.1 and 5.2.3.2, a linear amplification process was assumed i.e. that the gain is independent of the input optical power. In the practice, as the input power increases, after a certain level of amplification, the output power and hence

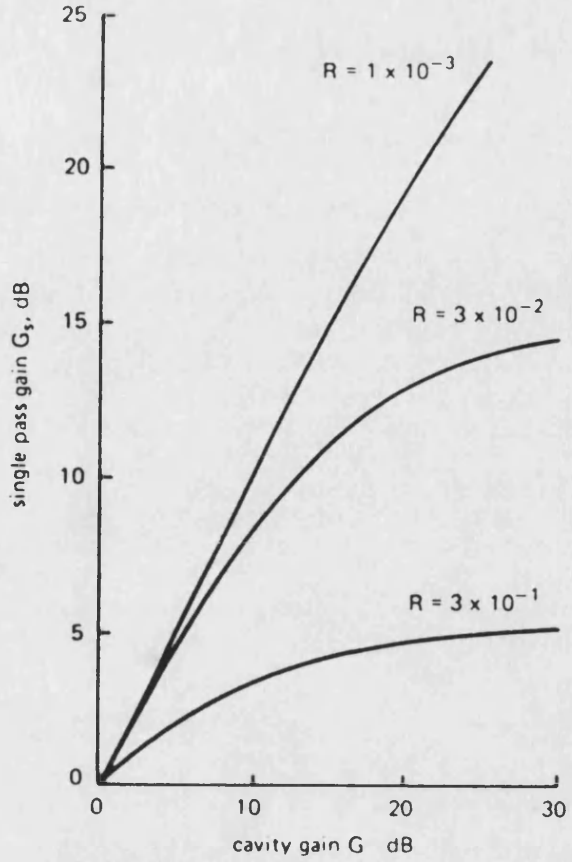

Figure 5.5. Relationship between the single pass gain and the signal gain as a function of facet reflectivities [8].

the internal gain saturates.

The internal gain of an amplifying medium depends on the carrier density. The carrier density N, hence the optical intensity S, is a function of position along the length of the amplifier, since it contains forward and reverse travelling waves, each of which depend on carrier density in forward and reverse directions [16-19]. The total intensity varies exponentially along the length and is usually maximum at output facets and is minimum near the center. For a typical GaAs device, with facet reflectivities of 30% (as in FPAs), the ratio between maximum and minimum optical density along the length is around 1.19 [20]. But in the case of devices with typical facet reflectivities of 10^{-3} (as in NTWAs), the ratio between maximum and minimum optical fluxes along the length of the device could be as high as 500 [20] due to growing waves. This radical difference in the photon density along the length would saturate the end facet first. However, saturation can take place even at very low input optical power due to the local generation and amplification of spontaneous emission (ASE). Therefore, ASE is thought to be main reason behind saturation in TWA as well in the FPA. Since the phenomena of gain saturation is intrinsic to the material and the structural system, it is easy to relate it to the material gain coefficient g_m and for a homogeneous laser medium, it can be defined empirically in terms of the saturated output power and input power can be defined as [1,21];

$$g_m = \frac{g_o}{1 + \frac{P_o}{P_{sat}}} \tag{5.11}$$

where g_o is the unsaturated local gain coefficient of the amplifying medium in the absence of the optical input. P_o is the input optical power at the input facet of an amplifier. P_{sat} is the saturation output power. The value of g_o can be evaluated as a given proportion of the material gain at lasing threshold [22]. Therefore it can be estimated from equation (2.47) near threshold before it saturates with devices with finite facet reflectance.

As the saturated output power characteristics are used in this thesis to

measure the signal gain of an amplifier, it is worthwhile to write an expression for G_s which includes the parameter of equation (5.11) as well. By comparing equations (5.6) and (5.11), one can obtain an equation which relates G_s to the saturation parameters of an amplifier as [8];

$$G_s = \exp\left[\left(\frac{\Gamma g_o}{1+\frac{P_o}{P_{sat}}} - \alpha\right)L\right] \tag{5.12}$$

This equation can be used for the measurement of the signal gain instead of equations (5.5) and (5.6).

5.2.3.4. Origins of noise in optical amplifiers

Noise is the most important factor in an optical amplifier because it determines the signal to noise ratio (SNR) at the output of an amplifier. The noise generation process in an amplifier is shown schematically in figure 5.6.

There are three types of noises in the optical amplifier;

1. Mode partition noise
2. Shot noise
3. Beat noise

When a laser source is driven by a dc current at a fixed heatsink temperature, small power fluctuations in the power of each longitudinal mode is expected because of thermal fluctuations. This can change the gain condition of an amplifying medium subjected to the optical radiation from that particular lasing source. When the source laser is driven under pulse conditions, the power of each mode in the optical pulse may vary due to the transient phenomena. The resulting mode partition noise (MPN) is caused by the random fluctuations amongst the various longitudinal modes in the amplifying medium as a result of random mode fluctuations in the lasing source and the amplifier as well. It may become one of the dominant performance limitations for laser diode systems, especially in those systems which require single mode operation. However, in multimode systems, the effect of this noise source is less significant because the fluctuations in the main

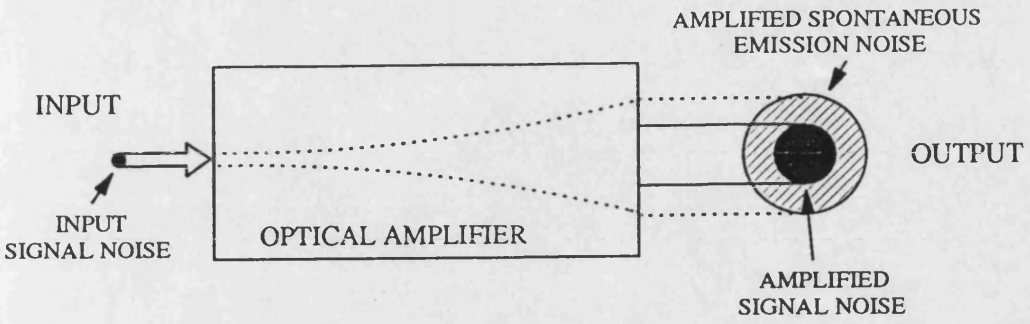

Figure 5.6. Noise generation process in an amplifier.

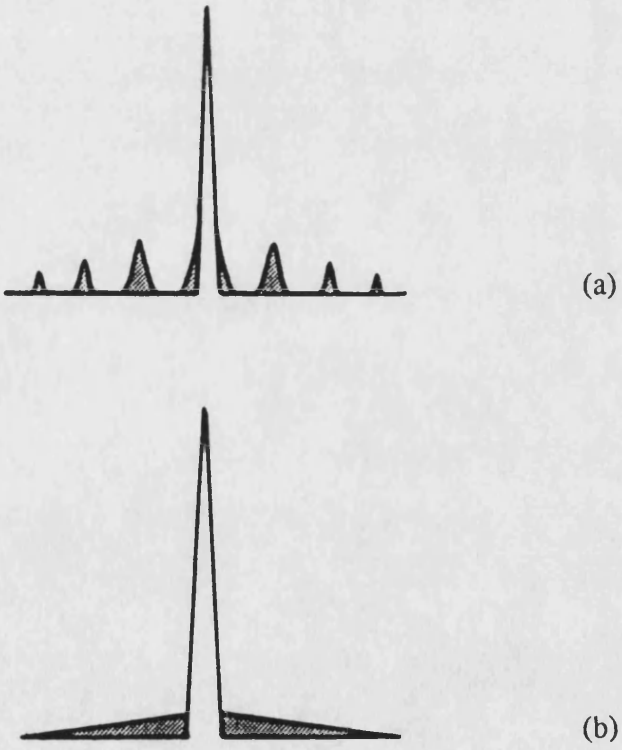

Figure 5.7. The spectral output of (a) FPA and (b) TWA.

and side modes are uncorrelated. The degree of mode fluctuation is usually defined by a universal coefficient, called k-coefficient [23], whose value decreases along the length of a pulse . Also, the penalty imposed by MPN becomes severe when a narrow band optical filter is used at the output of the amplifier [24]. During the work reported in this thesis, a multimode laser source was used under pulse conditions and the output was sampled at the end of a 200nS pulse (figure 5.8). Also no optical filtering mechanism was used. Therefore the contribution of MPN is expected to be insignificant in our study.

Shot noise is unavoidable random noise that is an inherit consequence of the quantum nature of light. It even exists in coherent optical radiation due to the particular (quantum) nature of light. It is generated by both the amplified signal and the locally generated and amplified spontaneous emission (ASE) and is referred to as signal shot noise and spontaneous shot noise respectively. The magnitude of the shot noise is directly related to the strengths of the signal and the ASE.

In a resonant type amplifier, the cavity resonance will reinforce and amplify those frequencies which satisfy the resonance condition of the FP cavity. The output emission from the amplifier consists of a central longitudinal mode at a certain wavelengths , surrounded by number of weaker components of amplified spontaneous emission created by other longitudinal modes as shown in figure 5.7(a). When the total output from that amplifier is detected by a photodetector, the various modes combine to generate beat noise. This beat noise consists of two components: (a) the signal-spontaneous beat noise generated as a result of mixing between signal and spontaneous emission components in the central longitudinal mode, (b) the spontaneous-spontaneous beat noise is generated as a result of intermixing between spontaneous emission components.

In a TWA, ASE is also generated. The spontaneous-spontaneous beat noise, which is the dominant noise source in the TWA, spreads over a wide range of

continuous spectrum, as shown in figure 5.7(b). However, in NTWA, the signal-spontaneous noise is also important when the facet reflectances are finite.

The total mean noise power at the output of an amplifier is given by [25,26];

$$P_N = \frac{h\nu n_{sp}}{\eta_T}(G_s - 1)\Delta\nu_1 m_t \tag{5.13}$$

where η_T is the total quantum efficiency, $\Delta\nu_1$ is the equivalent spontaneous shot noise bandwidth and m_t is the number of effective transverse modes. The effective number of transverse modes is equal to 2 in thin active layer devices, which corresponds to the single transverse mode operation with TE and TM mode polarization [22]. η_T is defined by the so called Henry factor as [25,26];

$$\frac{1}{\eta_T} = \frac{\Gamma g}{\Gamma g - \alpha} \tag{5.14}$$

where g is the local gain coefficient.

The inclusion of Henry's factor in equation (5.13) is justified because in an amplifying medium, the optical wave will observe two discrete processes; amplification and attenuation due to the material absorption and other mechanisms. The first process always adds the noise and second process will force it (noise) to reduce. In an ideal case, with zero facet reflectivities and zero attenuation, η_T will be equal to unity. However, in practical cases, where the achievement of zero facet reflectivities and a lossless medium is a limitation, η_T will be much lower, typically 50%.

The variance of the photon number at the amplifier output is defined as [3];

$$\sigma_{out}^2 = G < P_o > + n_{sp} m_t (G-1)\Delta\nu_1 + 2G(G-1)n_{sp}\chi < P_o > + (G-1)^2 n_{sp}^2 m_t \Delta\nu_2 \tag{5.15}$$

where $<P_o>$ is the mean input power, χ is the excess noise coefficient and $\Delta\nu_2$ is the equivalent noise bandwidth of the spontaneous emission beat noise components.

The first two terms on the right hand side of equation (5.15) represent the amplified signal and spontaneous emission shot noise and the last two terms

represent the signal-spontaneous and spontaneous-spontaneous beat noises respectively.

The excess noise factor, χ (which represents signal-spontaneous beat noise enhancement resulting from finite facet reflectances in FPA and NTWA), is defined as [3];

$$\chi = \frac{(1+R_1G_s)(1-R_2)(G_s-1)}{(1-\sqrt{R_1R_2}G_s)^2(G-1)} \tag{5.16a}$$

and in the case of $G \gg 1$ [3];

$$\chi = \frac{(1+R_1G_s)(G_s-1)}{(1-R_1)G_s} \tag{5.16b}$$

$\Delta\nu_1$ and $\Delta\nu_2$ are defined as [3,27];

$$\Delta\nu_1 = \sum_{m_l} \frac{(1+R_1G_s)(1-R_2)(G_s-1)}{(1-R_1R_2G_s^2)} \frac{C_A}{2L(G-1)} \tag{5.17}$$

$$\Delta\nu_2 = \sum_{m_l} \frac{(1+R_1G_s)^2(1-R_2)^2(G_s-1)^2(1-R_1R_2G_s^2)}{(1-R_1R_2G_s^2)^3} \frac{C_A}{2L(G-1)^2} \tag{5.18}$$

where m_l is the number of longitudinal modes.

In all types of amplifier, the spontaneous-spontaneous noise can effectively be reduced by introducing a narrow-band optical filter at the output [28], however, this can increase MPN. The signal-spontaneous beat noise is associated with the amplified signal, and consequentially this noise cannot be removed.

Following engineering practice for RF amplifiers, the noise introduced by an optical amplifier can be represented by a noise figure, F. The noise figure for the optical amplifier is defined as the signal-to-noise degradation before and after amplification, such that;

$$F = \frac{\left(\frac{S}{N}\right)_{ilp}}{\left(\frac{S}{N}\right)_{olp}} \tag{5.19}$$

Assuming that the input signal to the amplifier is shot noise limited, and considering two dominant beat noise sources, the noise figure, F can be written as [29];

$$F = 2n_{sp}\chi + \frac{n_{sp}^2 m_t \Delta\nu_2}{< P_o >} \tag{5.20}$$

The first term on the right hand side of equation (5.20) represents the signal-spontaneous beat noise and the second term represents the spontaneous-spontaneous beat noise components. The noise contribution from the spontaneous-spontaneous beat noise can be reduced by reducing $\Delta\nu_2$ by using a narrow band optical filter at the output (as mentioned above) or by increasing $<P_o>$ by increasing the input power to the amplifier.

Generally, at the higher values of internal gain of the amplifier, the beat noise components dominate the shot noise components [30,31]. Among the beat noise components, the spontaneous-spontaneous beat noise is dominated by the signal-spontaneous beat noise. Therefore, under the condition that $G \gg 1$ (as in our case), the spontaneous-spontaneous beat noise components in equation (5.20) can be ignored and the noise figure of an amplifier can be approximated to [28,29];

$$F = 2n_{sp}\chi \tag{5.21}$$

Equation (5.21) will be used later in the experimental section to evaluate the noise power contribution in the different amplifiers being investigated.

5.3. Experimental results

In this section, the theory described earlier is utilised. This section is divided into two parts. In the first part, monolithic approach is considered and in the second part, hybrid approach, where different optical components are butt-coupled through an optical lens system, is used.

5.3.1. Monolithic AWOA

In chapter-4, monolithic device UB136 was successfully used as an AWOD.

The AWOD can be turned into an AWOA if it is locally biased to overcome the inherent losses in the active layer. For this purpose, the experimental arrangement of figure 4.6 was used. In this case, device UB136A was used as the source and UB136D was used as the AWOA. UB136D was locally pumped while it was subject to input radiation from UB136A. In order to investigate the effect of local carrier injection, segment-D was pre-biased with longer pulses than segment-A biasing pulses. The typical value of pulse length was 200nS for segment-A and 300nS for segment-D, as shown schematically in figure 5.8. The biasing current for segment-A was varied from 0 to 160mA and the leakage of the optical flux through segment-D (with no biasing) was measured. Then segment-D was pre-biased at 20mA and segment-A's biasing current was varied from 0mA to 160mA. The optical output at the back facet of segment-D was measured using the large area detector (LAD). This procedure was repeated for 30mA, 40mA, 50mA, 6mA, 70mA and 80mA of pre-biasing. The output detected by the LAD at the different levels of pre-biasing was then corrected to take account of the leakage flux and this was plotted against the laser-A drive current in figure 5.9.

It is clear from figure 5.9 that the AWOA suffers from internal losses due to the absorption of input radiation because neither of the segments was lasing (including segment-A which was used as the source) as a result of the non-vertical etched facet geometry. This effect can be seen more clearly in figure 5.10 where the output of segment-D is plotted against the total input intensity measured at the front facet of UB136A.

A similar experimental procedure was repeated for the other segment combinations using the same device, but due to excess net losses in the active layer, results similar to figures 5.9 and 5.10 were obtained and they are not presented here.

5.3.2. Hybrid AWOA

In this section, different characteristics of AWOA are investigated thoroughly

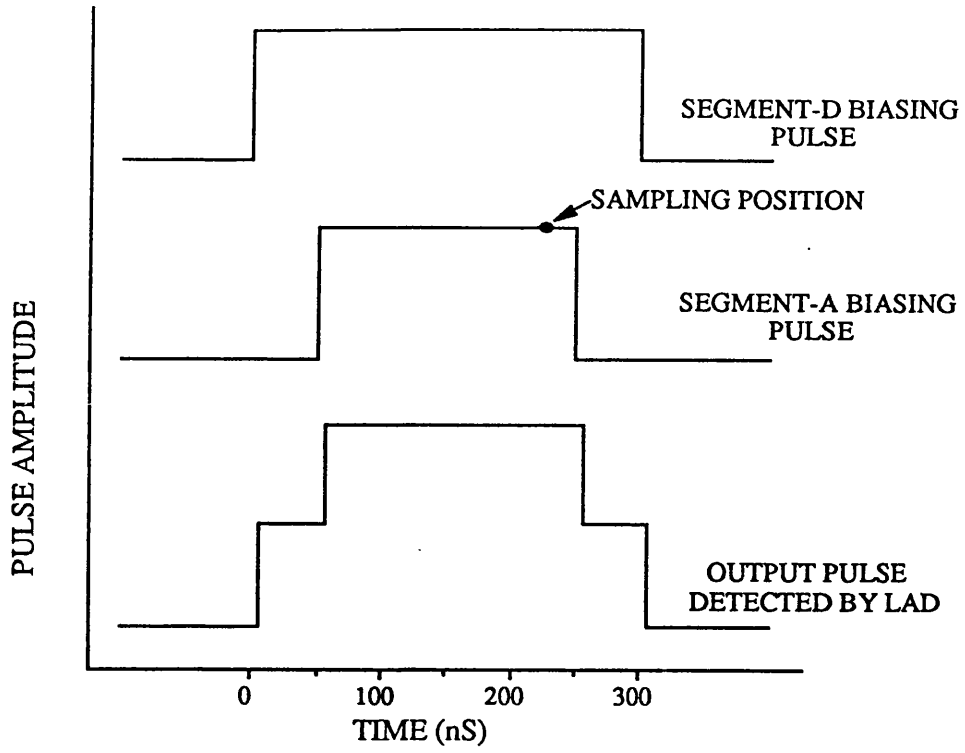

Figure 5.8. The schematic illustration of the source laser and the AWOA biasing scheme.

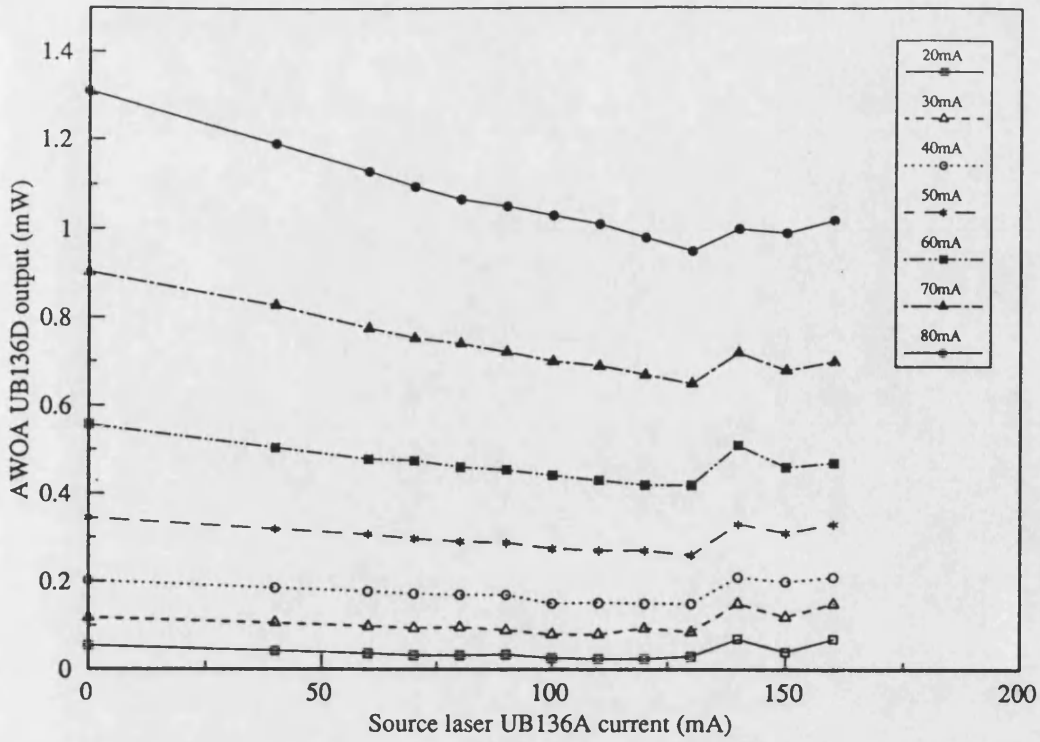

Figure 5.9. AWOA UB136D output power versus the source laser UB136A current as a function of AWOA prebiasing.

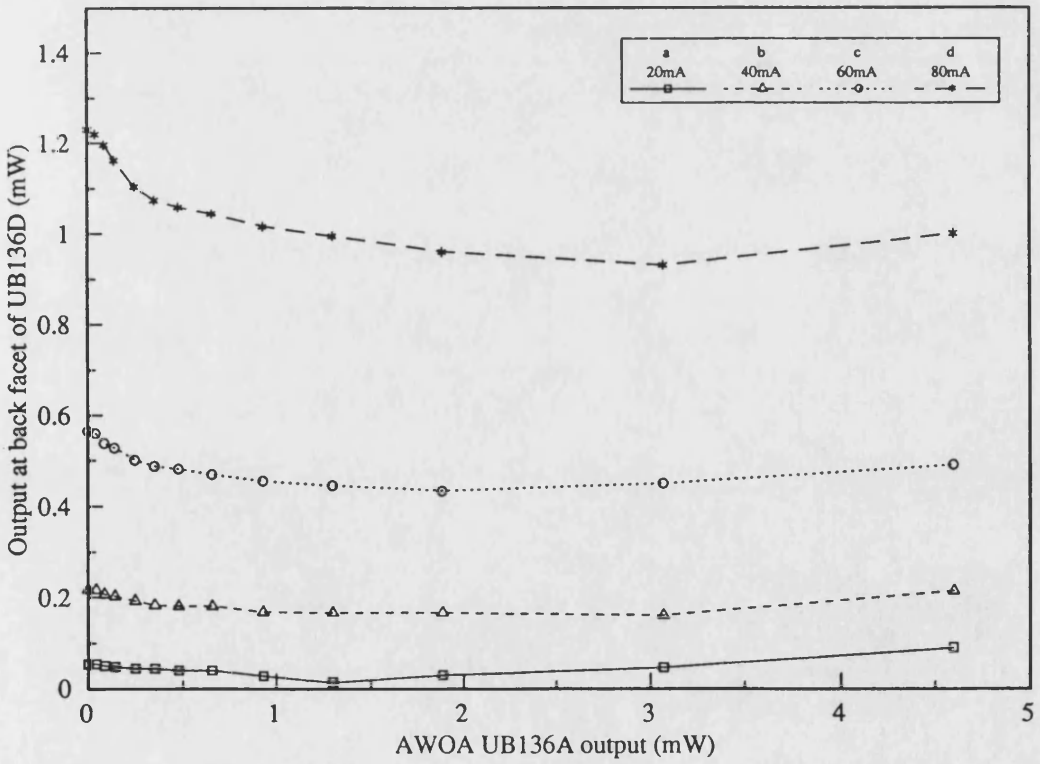

Figure 5.10. The saturation of monolithic AWOA in loss regime due to spontaneous recombination.

using the butt-coupling scheme of figure 1.6 so the results obtained in this section can applied directly to monolithic integrated devices. Throughout this section UB238 is used as the source laser and UB258, UB259 and UB262 are used as AWOAs.

5.3.2.1. Light amplification in the hybrid AWOA

For the case of the hybrid integrated AWOA, the source laser and the AWOA were butt-coupled through optical lenses as shown in figure 4.12. Here a fast detector was used at the output instead of the LAD as in section 5.3.1. A portable monochrometer was also used at the output to observe the frequency tuning using a infrared camera. Figure 5.11 shows the schematic of the experimental set-up used for the characterization of the AWOA. The source laser and the AWOA laser were aligned using the novel alignment technique developed in chapter-4 based on the use of the active waveguide as active waveguide optical detector.

5.3.2.1.1. Output power characteristic of AWOA

In the hybrid case, the structural and material parameters could be optimised for each particular application. The experimental procedure which was used for the monolithic approach in section 5.3.1, was also used for the hybrid measurements as well. Device number UB262 was pumped just below threshold level, and the input light from the source laser UB238, pumped well above its threshold, was coupled into the AWOA (UB262). The temperature of both devices was varied slowly but continuously and independently to tune the optical frequency of the incoming radiation with the cavity resonance frequency of the AWOA. The tuning of the optical input was observed by an infrared T.V. camera equipped at the exit slit of the monochrometer. At the same time, alignment between the two devices was tightly controlled by monitoring the output power of the AWOD (under zero bias conditions). Also the output of the AWOA was watched closely for any

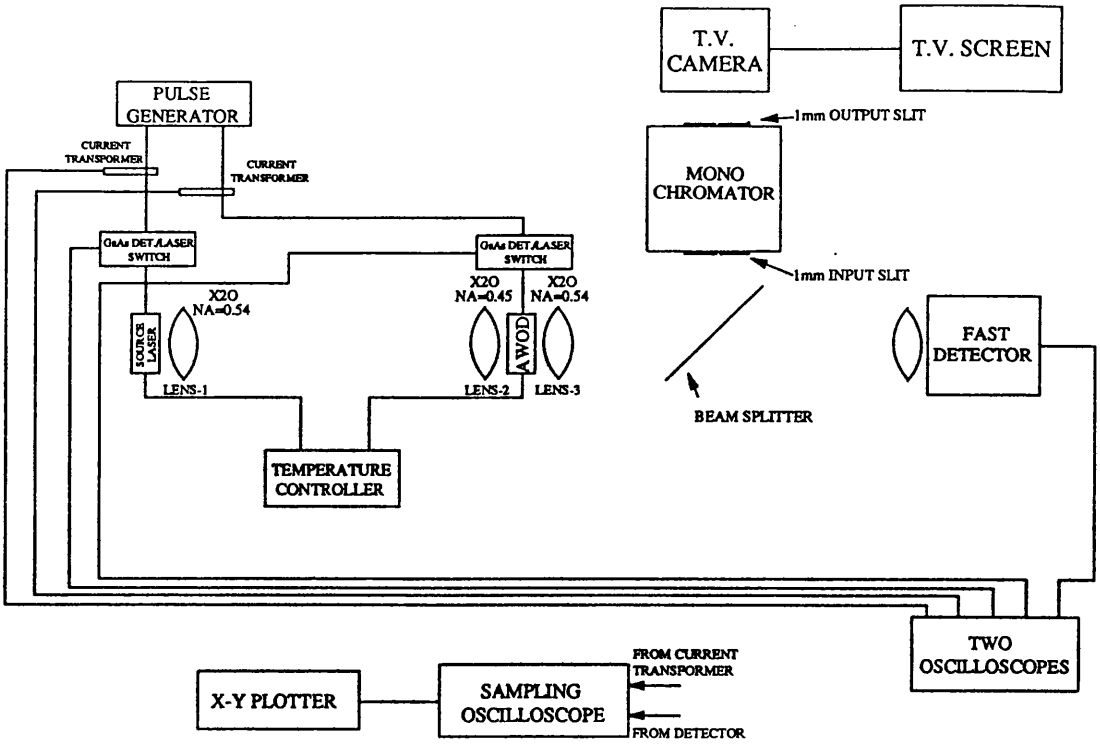

Figure 5.11. The schematic of experimental set-up used to evaluate the performance of AWOA in hybrid approach.

change in output which could be attributed to the amplification process. Once a slight amplification was observed, the source laser temperature was fixed and the gain was maximised by varying the temperature of UB262. The power output of the AWOA was measured as a function of AWOA pre-biasing current by varying the source laser drive current from 0mA to 140mA. The source laser drive current was limited to 140mA because beyond this level the output of the source laser was saturating. Prior to plotting the results, the output of the AWOA was corrected to take into account optical leakage effects as described in section 5.3.1.

A similar experimental procedure was repeated for devices UB259 and UB258. It is worth mentioning here that UB258 played a dual role due to differences in the two facet reflectances and was investigated twice. First, the A.R. coated facet was used as the input facet and then the uncoated facet was used as the input facet. So for future reference, the device configuration with R_1=4.48% and R_2=30% is referred to as UB258A. Whereas, the device configuration of R_1=30% and R_2=4.48% is referred to as UB258B, where R_1 and R_2 are input and output facet reflectivities respectively. Results for all four devices are presented in figures 5.12-5.15

5.3.2.1.2. Signal gain in AWOA

For the measurement of the signal gain in a device, the material gain, g_m has to be known. g_m can be obtained using either equation (5.5) or (5.11). Usually, the internal gain of an amplifier is calculated through equation (5.5) which involves the measurement of peak-trough ratio at the output of the amplifier. This method requires the use of a single wavelength source to achieve reliable results. However, when the source laser is a multi-wavelength source, the amplifier can support and amplify several longitudinal modes as it has a broader output spectrum (since its threshold is suppressed by operating it below threshold (as in FPA) or by applying A.R. coating (as in TWA)). In this case each amplified mode shows different Fabry-Perot resonances. If one wants to measure the signal gain, it is important to

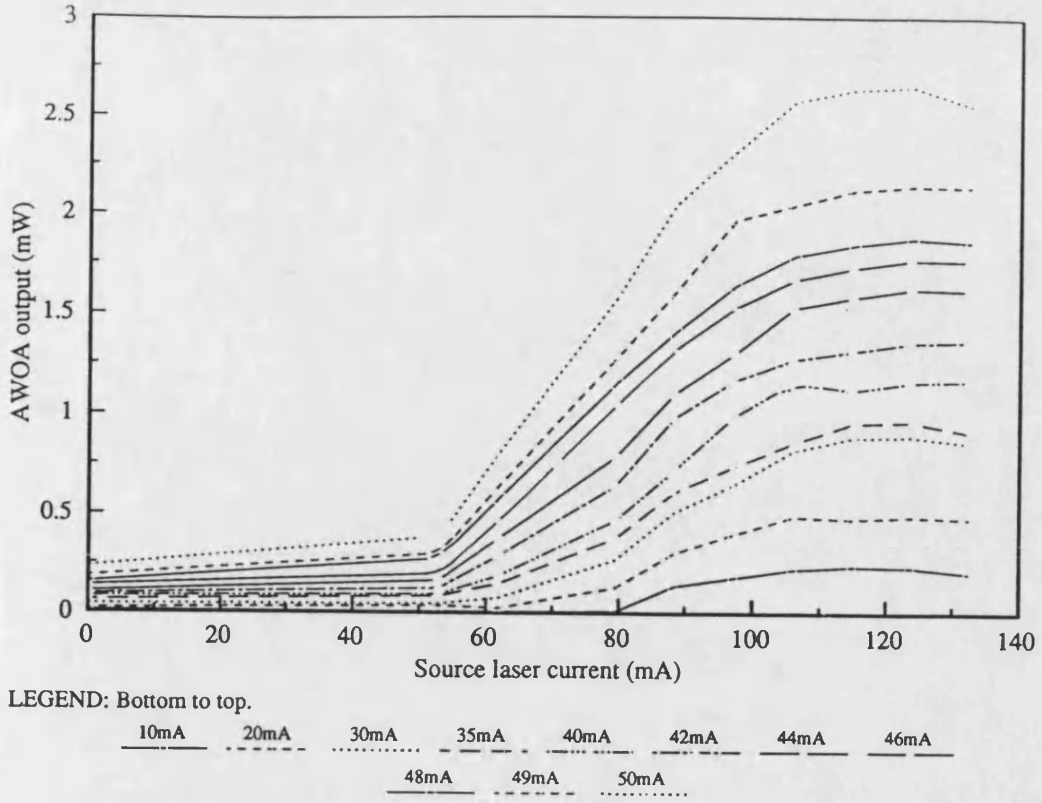

Figure 5.12. AWOA UB262 output power versus the source laser UB238 current as a function of AWOA bias current.

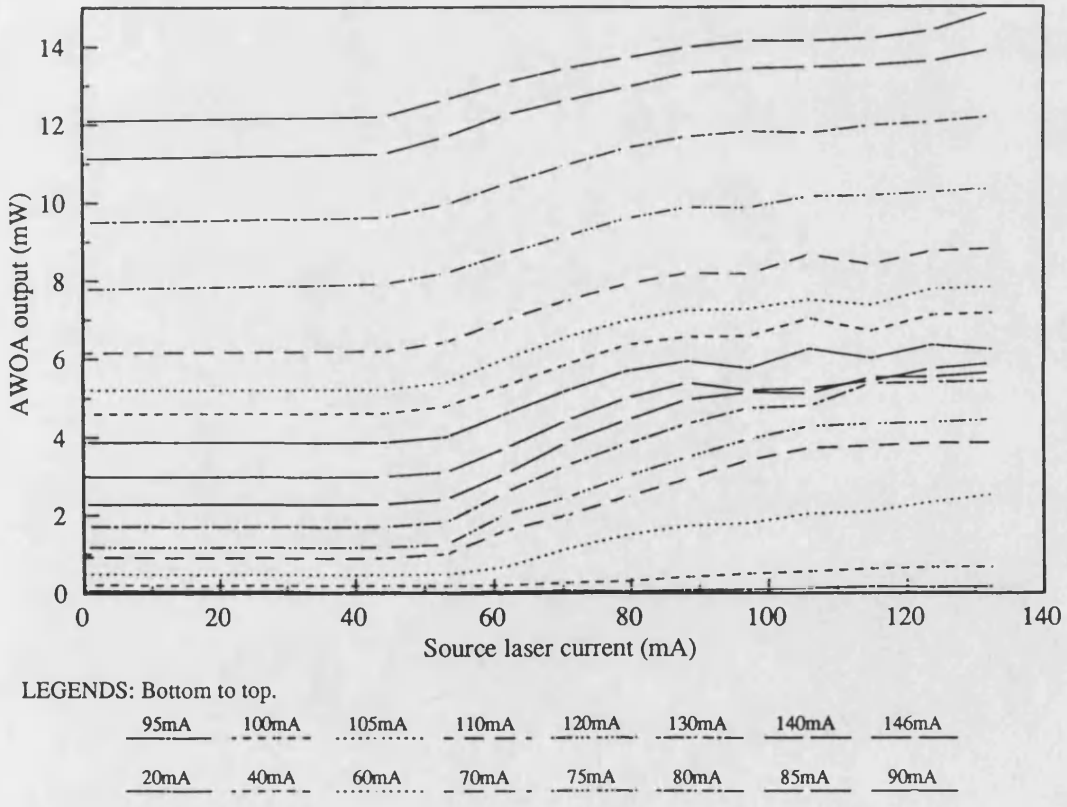

Figure 5.13. AWOA UB259 output power versus the source laser UB238 current as a function of AWOA bias current.

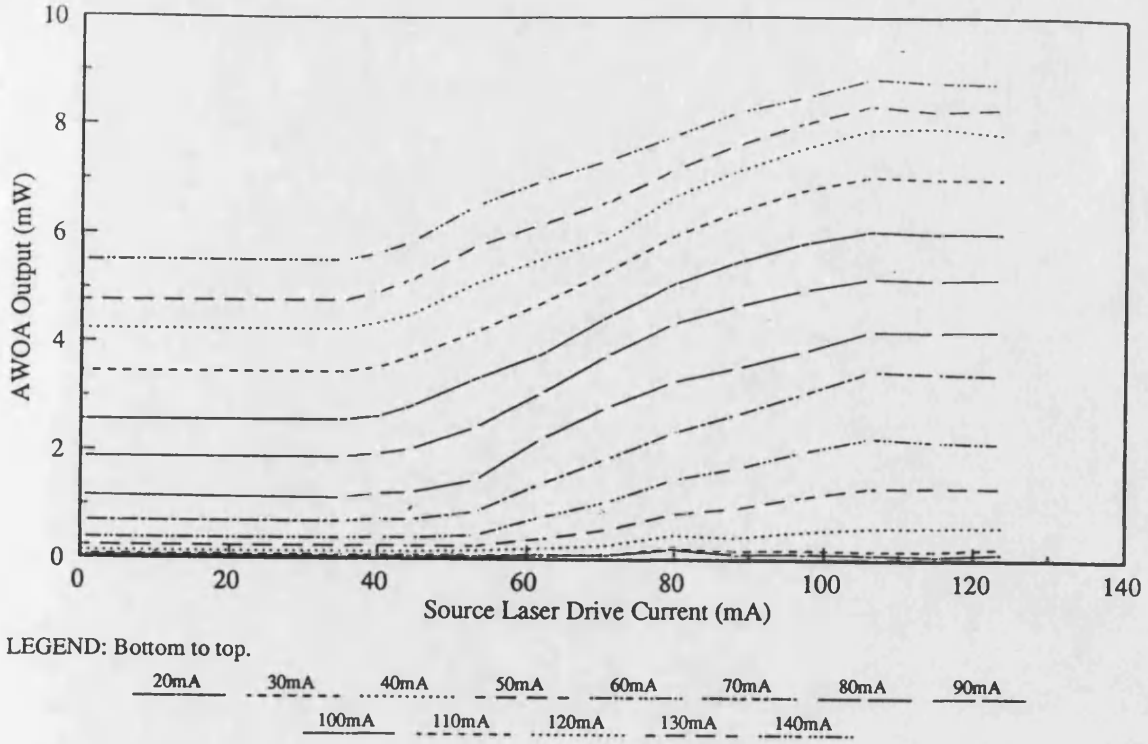

Figure 5.14. AWOA UB258A output power versus the source laser UB238 current as a function of AWOA bias current.

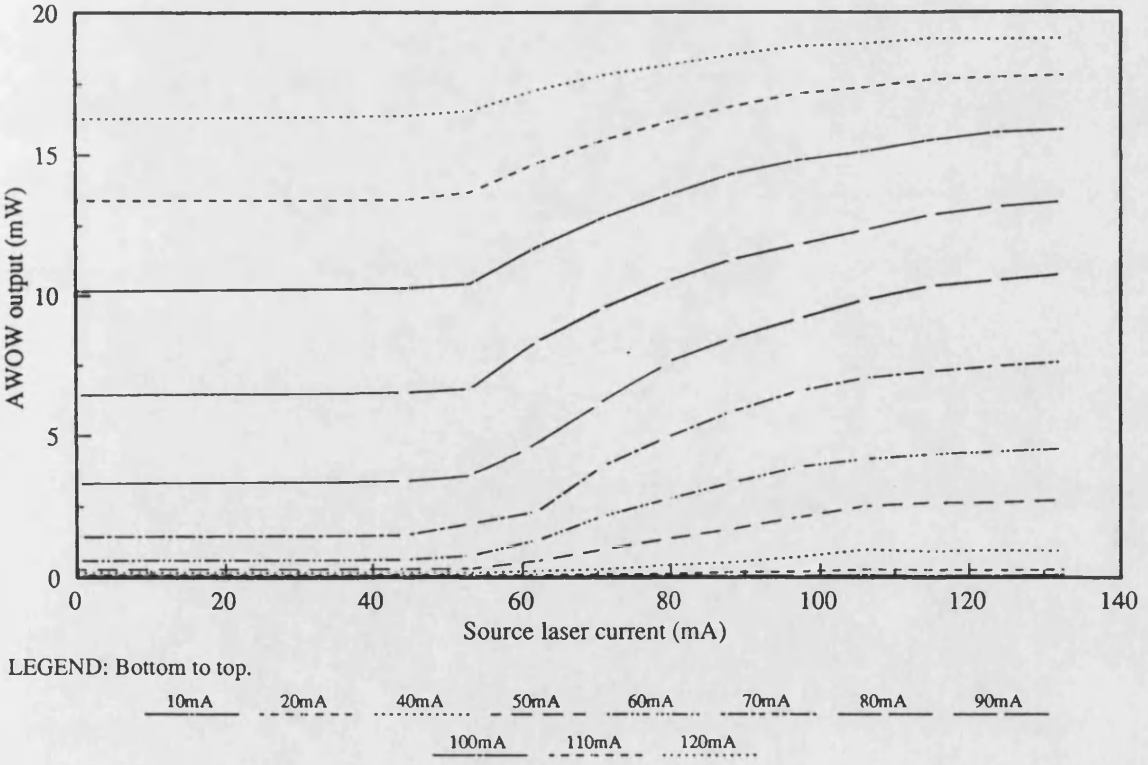

Figure 5.15. AWOA UB258B output power versus the source laser UB238 current as a function of AWOA bias current.

evaluate the gain of each resonating mode separately. But the gain of each mode cannot be evaluated separately by measuring the peak-trough ratio of each mode due to the superimposition of several resonance frequencies on the central longitudinal mode resonance frequency [32]. Because a multi-wavelength source laser was used in this work, this method could not be used. Alternatively, the saturated output characteristics were used to calculate the optical gain using equations (5.11) and (5.12) as the exact value of the input power was known. To best of the author's knowledge, this is the first time the method has been used.

In order to use this method for gain measurement, the precise value of P_o and P_{sat} were required. The exact value of P_o was calculated by deriving a simple expression for the effective coupling efficiency and P_{sat} was estimated by exploiting gain saturation induced nonlinear properties of the amplifier. These two parameters will be discussed below.

5.3.2.1.2a. Coupling efficiency of input radiation

In chapter-4, the total input power coupled into the active waveguide was measured by using it as an AWOD. However, in the optical amplifier with finite facet reflectivities, as in our case, the cavity resonance will reinforce and amplify those frequencies which satisfy the resonance conditions of the cavity. Since the input optical radiation had multi-wavelength radiation components, only a fraction of the input radiation which satisfies the cavity resonance will take place in the amplifying process. In order to calculate the signal gain, the effective input power coupled into the active layer has to be known and this can be found via the effective coupling efficiency of the input radiation. The coupling efficiency, C of the input radiation coupled to the active layer can be defined as [33];

$$C=\frac{(1-R_1)d_3}{D_{min}} \tag{5.22}$$

where R_1 is the input facet reflectivity, d_3 is the thickness of the active layer and D_{min} is the diameter of the minimum achievable spot size of the input beam.

By combining equations (4.24) and (5.22), a relation for C as a function of the input radiation wavelength, can be written as;

$$C=\frac{2(1-R_1)d_3}{1.22\lambda_o}N.A. \tag{5.23}$$

The effective input power coupled to the active layer can then be written as;

$$\begin{aligned} P_o &= C.P_{in} \\ &= \frac{2(1-R_1)d_3(N.A.)}{1.22\lambda_o}.P_{in} \end{aligned} \tag{5.24}$$

where P_{in} is the total input power detected by the active waveguide while used as an AWOD.

The effect of facet reflectance on the responsivity of the AWOD was discussed in last chapter and it was included in sensitivity calibration of the AWOD. Therefore, the effect of reflectance can be neglected here and equation (5.24) reduced to;

$$P_o=\frac{2d_3(N.A.)}{1.22\lambda_o}.P_{in} \tag{5.25}$$

By inserting typical values of d_3=0.15μm, NA=0.45 and λ=860nm, equation (5.25) can further be reduced as;

$$P_o=0.1286P_{in} \tag{5.26}$$

5.3.2.1.2b. Saturation intensity

It can be seen from figure 5.12 through figure 5.15 that the output of the AWOA becomes saturated at higher levels of the optical input power. This is because of the gain dependence of the carrier density. At these higher input powers, the stimulated recombination process reduces the carrier concentration and causes the reduction in the optical gain. The gain saturation induced nonlinearities leads to distortion of the input pulse in the form of pulse compression or pulse

broadening [34,35] because the leading edge saturates the amplifier and the trailing edge suffers a gain reduction due to the saturation of the amplifier.

In the low input power regime, where the pulse power is considerably less than the amplifier saturation power, very narrow pulses have been amplified without much distortion [34]. In the high input power regime, the gain saturation of an amplifier causes the broadening or narrowing of input pulses, depending on the operating conditions [34-36].

The level of the input power which causes the saturation of the optical amplifier was calculated by making the use of the unwanted mechanism of gain saturation induced nonlinearity in the amplifier. This was achieved by plotting the near-fields of the AWOA. This work was started with UB262 (FP amplifier) as the AWOA in the experimental set-up of figure 4.35. The AWOA was tuned to the input signal and maximum gain was achieved. At that point the AWOA current was kept just below the lasing threshold. The near-field optical intensity was measured at the different levels of optical input power by varying the source laser current. While measuring the near-field patterns, the optical gain of the input signals was kept to a maximum value by varying the AWOA temperature as the increase in the source laser drive current changed the peak emission wavelength of the input signals. The same experimental procedure was then repeated for the other devices and the FWHM of the near-field was plotted against the source laser current for all devices, as shown in figures 5.16-5.19. In all cases, a minimum pulse width was achieved and that particular level of the source laser pumping for each device was considered as the saturation limit of that particular amplifier. The output power of the AWOA at that point was taken as P_{sat} and the level of the optical input power at that point measured by using the AWOA as an AWOD, was used in equation (5.26) to calculate P_o.

5.3.2.1.2c. Signal gain

Once the exact value of P_o and P_{sat} had been obtained, the material gain was

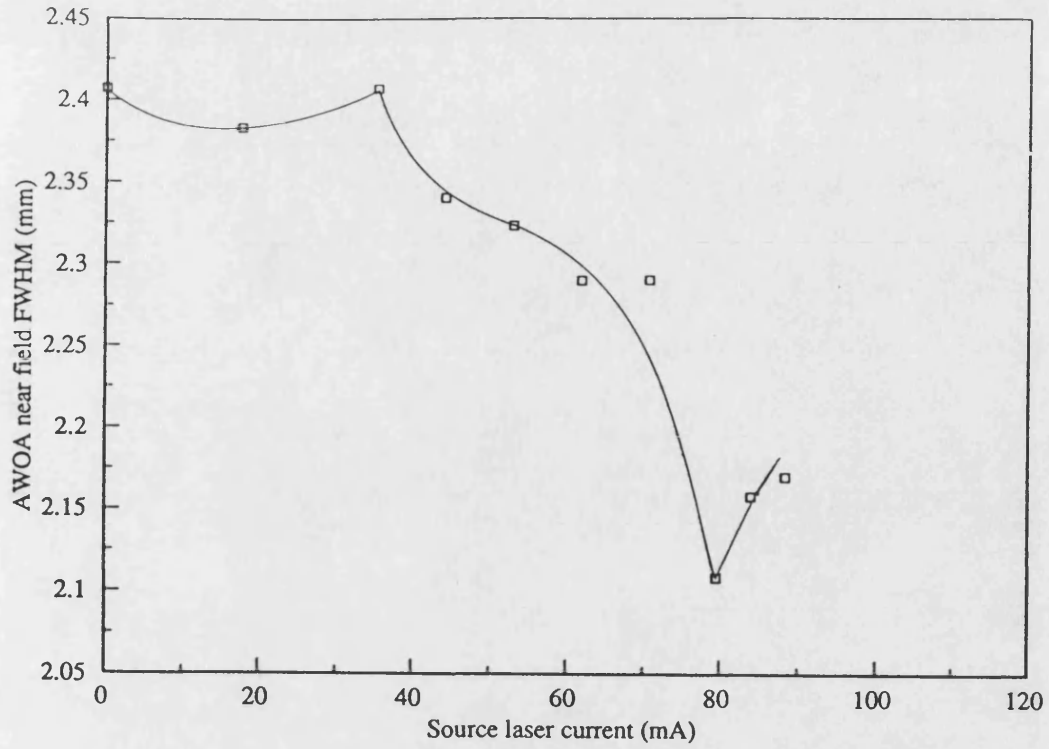

Figure 5.16. The near field pattern of AWOA UB262 versus the source laser current showing saturation phenomena in active medium as a result of saturation induced nonlinearity.

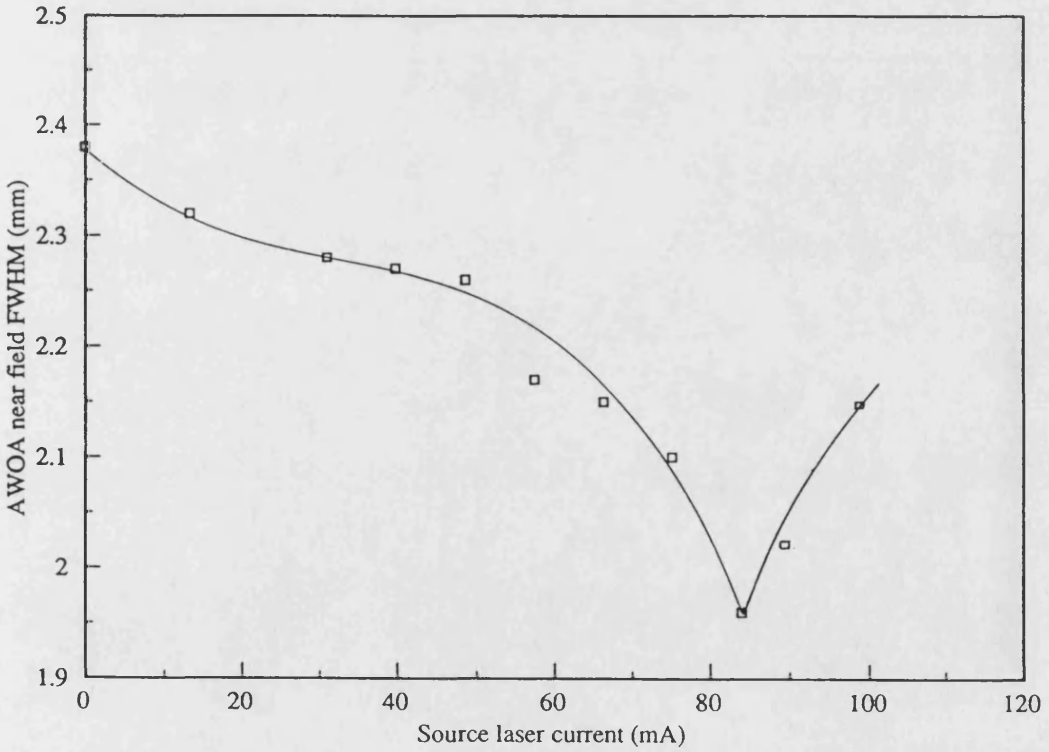

Figure 5.17. The near field pattern of AWOA UB259 versus the source laser current showing saturation phenomena in active medium as a result of saturation induced nonlinearity.

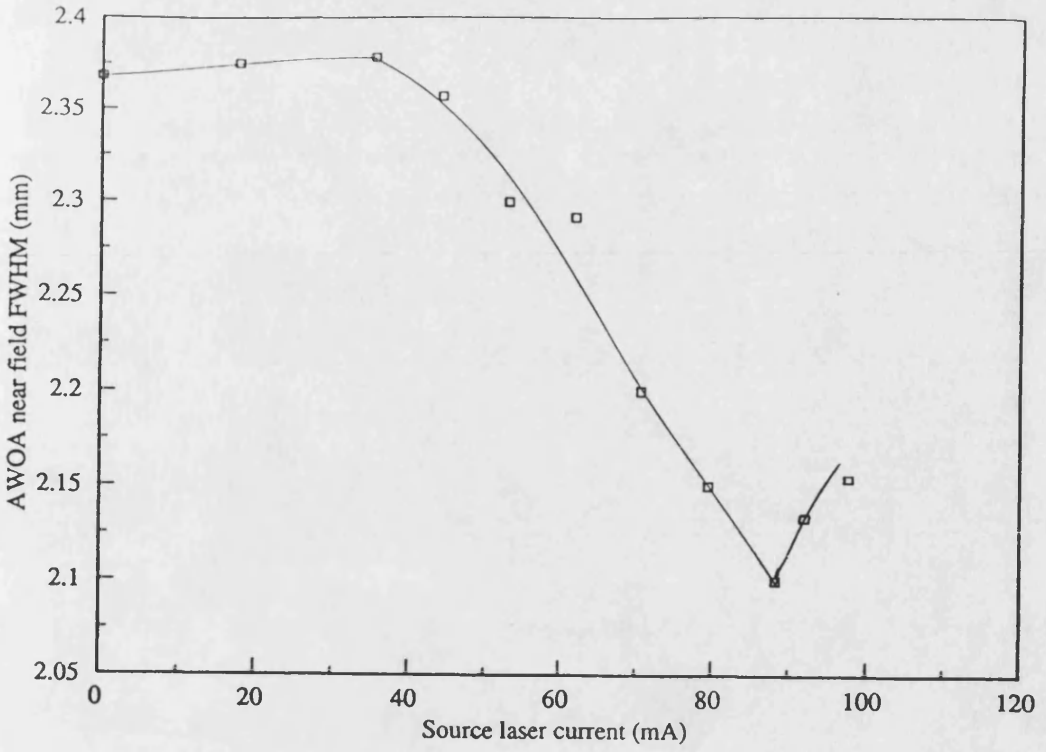

Figure 5.18. The near field pattern of AWOA UB258A versus the source laser current showing saturation phenomena in active medium as a result of saturation induced nonlinearity.

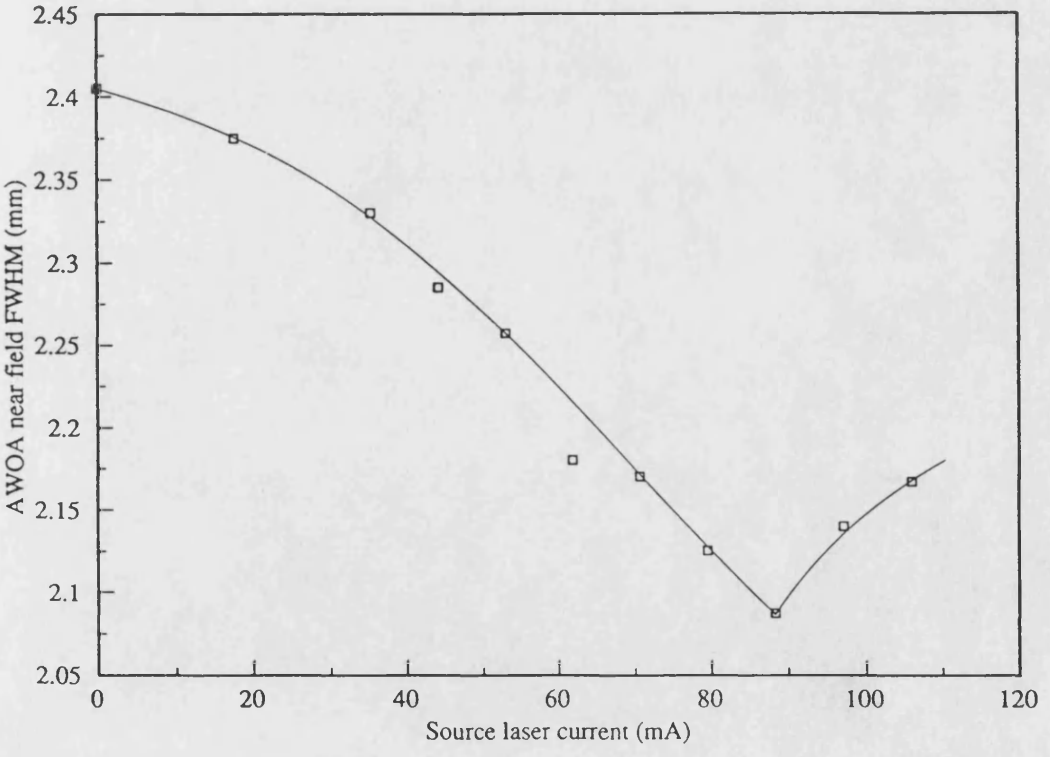

Figure 5.19. The near field pattern of AWOA UB258B versus the source laser current showing saturation phenomena in active medium as a result of saturation induced nonlinearity.

calculated using equation (5.11) for different devices. The single pass gain, G_s was then calculated from equation (5.12). The material gain, g_m is plotted against the single pass gain, G_s in figure 5.20 as a function of mirror facet reflectances. The signal gain for each device has been calculated from equation (5.10) and plotted against amplifier pumping level for different devices in figure 5.21.

The gain characteristics for the uncoated device and the A.R. coated devices show different behaviour. In UB262 (a FP device), the signal gain increases together with the local pumping of the AWOA at levels below the lasing threshold and above the lasing threshold, the signal gain slowly decreases due to the gain saturation resulting from photon-carrier interactions inside the active medium. In the A.R. coated devices, the reduction in facet reflectance gives rise to the signal gain in UB258A, UB258B and UB259 because the lasing threshold has been suppressed by reducing the feedback between two facets. The effect of facet reflectance can further be explained by plotting the single pass gain against signal gain or cavity gain as a function of facet reflectivities as shown in figure 5.22. As the facet reflectance reduces, the single pass gain increases accordingly and it brings the device characteristic more closer to the ideal case where the single pass gain would be equal to the signal gain (subjected to the limiting factor of ASE). But experimentally this has not been achieved due to small residual facet reflectivities and in the presence of finite facet reflectivities, signal waves have a longer optical path length due to multiple feedback. In general, the results of figure 5.22 are in line with the published results of reference-8 (figure 5.5).

5.3.2.2. Temperature dependence of the gain

The dependence of the peak emission wavelength on temperature was used to obtain the tuning of the resonance frequency of the AWOA in section 5.3.2.1.1 and in this section, the temperature dependence properties of the AWOA are analysed. For this purpose, the experimental set-up of figure 5.11 was used and UB262 was used as the AWOA at the start of the experiment. The AWOA was

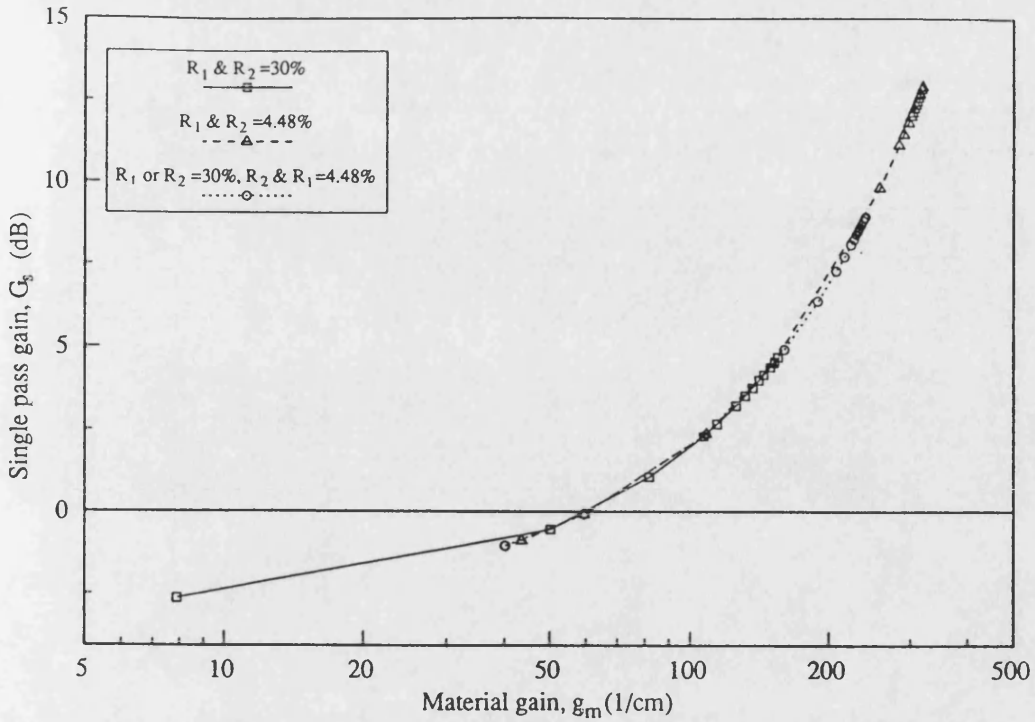

Figure 5.20. Figure showing material gain does not change with structure change.

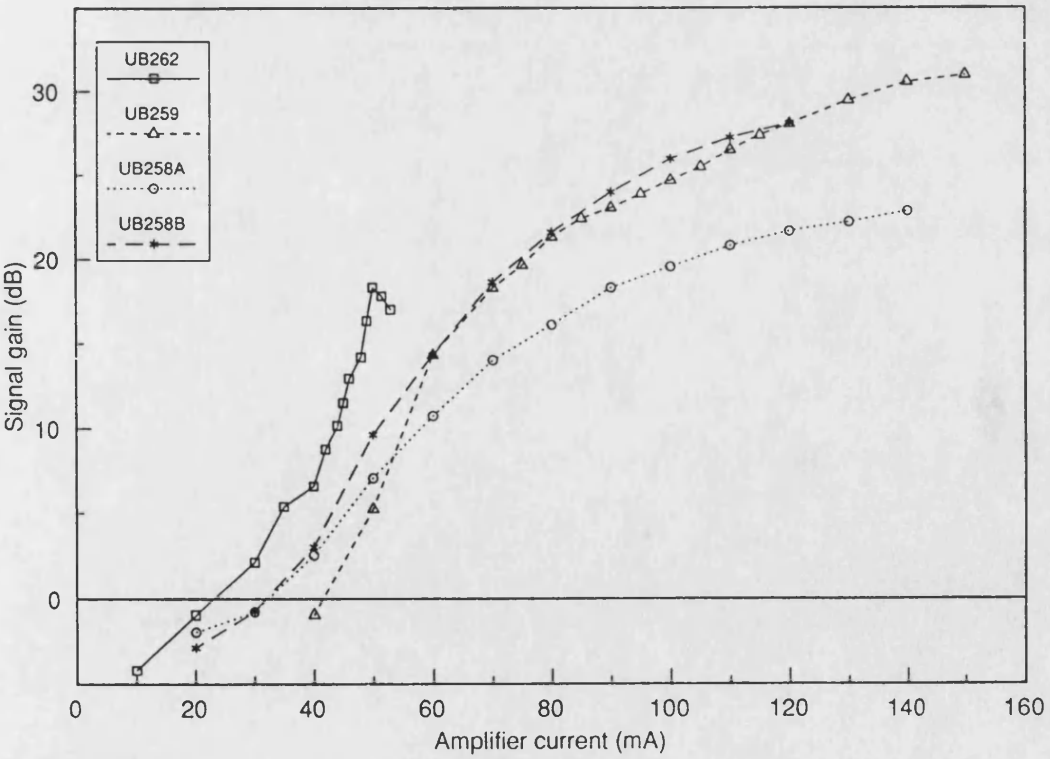

Figure 5.21. The signal gain of different devices.

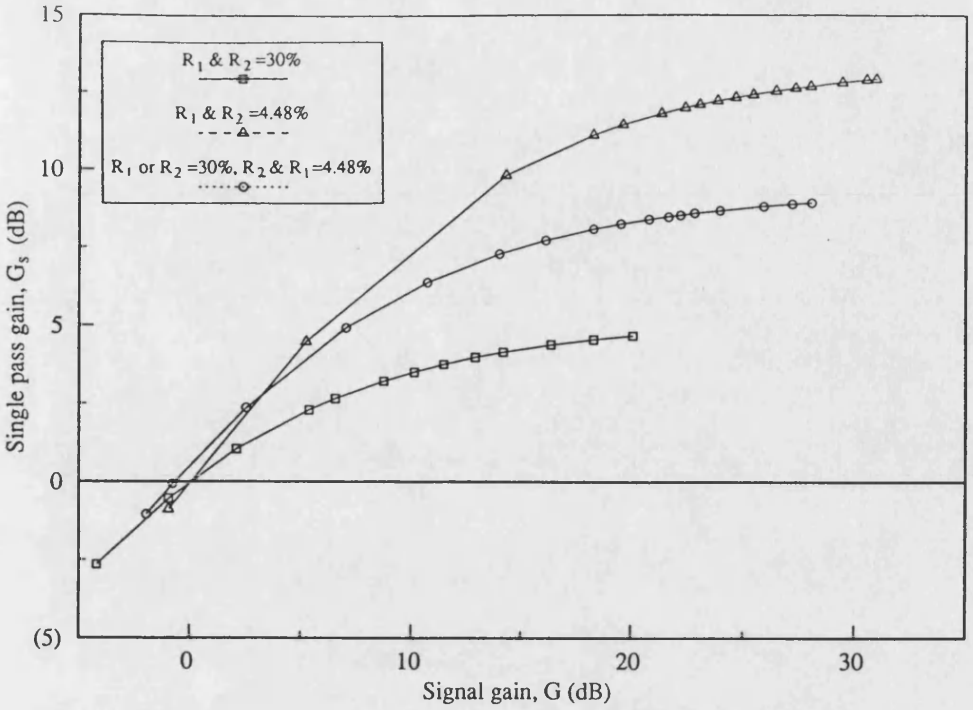

Figure 5.22. Graph showing relationship between cavity gain and single pass gain.

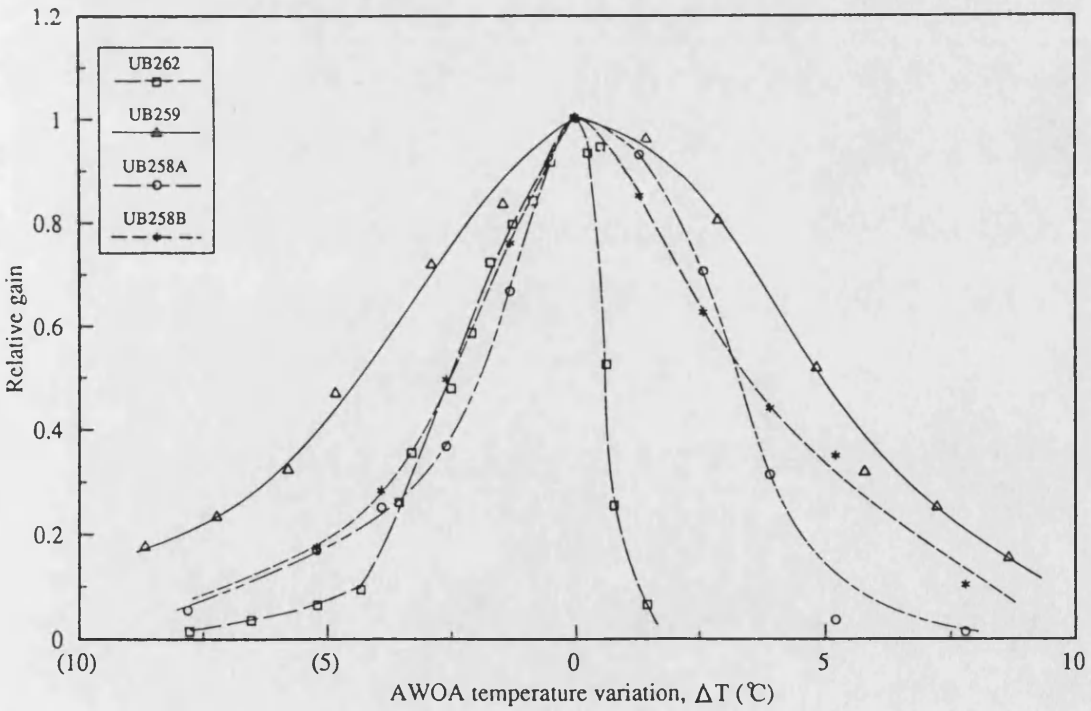

Figure 5.23. The gain dependence of temperature or wavelength for different devices.

tuned to maximum gain using the procedure of section 5.3.2.1.1. Maximum gain was achieved at a temperature of 20°C for the source laser and 18.7°C for the AWOA respectively. At maximum gain, the temperature of the AWOA was considered as optimum temperature (i.e. 18.7°C for UB262). Then the temperature of AWOA was varied around 18.7°C and the output of the AWOA was measured against the source laser current as a function of AWOA temperature for a constant level of pre-biasing. The optical signal gain was calculated at the each value of temperature using the procedure described in section 5.3.2.1.1. The same experimental procedure was then repeated for the other devices. The results of measurement of the relative optical gain against the AWOA temperature variation, ΔT are presented in figure 5.23.

It can be seen from figure 5.23 that the optical gain for all the devices depends upon temperature. In the case of the double-side facet coated device, UB259, the optical gain decreases by approximately 3dB if the temperature is increased or decreased from its optimum value (20°C in the case of UB259) by 5°C due to a shift in the AWOA resonance frequency with the variation of the AWOA temperature. This value is in agreement with the reported value of 5°C in reference-8. In the FP type AWOA (UB262), the change in optical gain is more prominent because the FP type devices are highly temperature sensitive as compare to the NTW type devices (see table 3.1). Due to the higher temperature sensitiveness of the FP type AWOA, the temperature must be controlled to within [EQUATION]^{o}C to maintain the maximum optical gain.

The dependence of the optical gain for the single side A.R. coated devices (UB258A and UB258B) lies between that of the FP and NTW type AWOAs (as the rate of the change of peak emission wavelength in these devices lies between uncoated devices and double side coated devices (table 3.1)). Table 5.2 summarises the effect of temperature variation on the optical gain for the different devices.

Table 5.2. The effect of temperature variation on the relative gain at the source laser temperature of 20(°C).

Device number	Optimum temperature (°C)	Temperature at $-3dB$ relative gain (°C)	Temperature at $+3dB$ relative gain (°C)	FWHM at $\pm 3dB$ relative gain (°C)
UB262	18.7	2.0	0.5	2.5
UB259	20.0	4.6	5.0	9.6
UB258A	20.65	2.5	3.0	5.5
UB258B	19.35	2.6	3.3	5.9

It can also be seen from figure 5.23 and table 5.2 that the temperature dependence of the gain of all devices except UB262 (FP AWOA) is approximately symmetrical around the optimum temperature of a particular device. UB262 shows asymmetrical temperature dependence behaviour. This can be explained as follows: At lower temperatures, the signal frequency does not match the resonance frequency of the AWOA amplifier. As the AWOA temperature increases, the peak emission wavelength of the AWOA is pushed towards longer wavelength, until maximum gain value is reached. The carrier density in the active region decreases as the result of high optical gain. This leads to an increase in refractive index of medium causing the AWOA resonance wavelength shift towards higher wavelength. This effect combines with the shift in wavelength with temperature of the AWOA (as the temperature of the AWOA continue to increase) and causes the cavity resonance wavelength to move sharply towards longer wavelength. A similar type of asymmetric effect has been observed by Nakai *et al* [37] in the FP amplifier by varying the wavelength of input signals. The asymmetric wavelength response of the amplifier has also been used to obtain the detuning characteristic of the optical amplifier to look at the bistability in laser devices [38]. Asymmetrical tuning has not been seen in A.R. coated devices due to broader output spectrum which reduces temperature sensitivity of these devices.

5.3.2.3. Frequency bandwidth

The signal gain G of an amplifier, with finite facet reflectances, depends upon the frequency of the incident signal ν and the cavity resonance frequency ν_o. The effect of frequency mismatch between the input signal frequency and the amplifier resonance frequency has been demonstrated in figure 5.23. It can be seen from figure 5.23, that 3dB bandwidth of the gain versus temperature curve increases with the application of A.R. coating on the mirror facets. But this does not help to calculate the frequency bandwidth (which can be represented in terms of wavelength as the spectral width or linewidth).

The 3dB frequency (FWHM) bandwidth of the output power of central longitudinal mode can be obtained from equation (5.7) by determining the frequencies at which the gain of the system falls to half of its maximum value. This occur at frequency $\Delta\nu_{1/2}$ and defined as [14];

$$4\sqrt{R_1R_2}G_s\sin^2\left\{\frac{2\pi L}{C}(\Delta\nu)\right\} = (1-\sqrt{R_1R_2}G_s)^2 \tag{5.27}$$

yielding a ±3dB spectral width

$$\mathbf{B} = 2.\Delta\nu_{1/2} = \frac{C}{\pi L}\sin^{-1}\frac{1-\sqrt{R_1R_2}G_s}{2(\sqrt{R_1R_2}G_s)^{\frac{1}{2}}} \tag{5.28}$$

In figure 5.24, the ±3dB frequency bandwidth calculated from equation (5.28) is plotted against the signal gain for different devices. The FWHM frequency response of the Fabry-Perot device (UB262) is calculated as 5.95 GHz at 20dB signal gain. This value is higher than the reported value of 4 GHz for the FP amplifier [3] because in reference-3, the author has used a 300μm long device, which probably has increased the Q value of the amplifying cavity. In the single-side coated device (UB258A and UB258B), the ±3dB frequency width is calculated as 20 GHz again at 20dB signal gain. This is 3.36 times larger than the FP device (UB262). Mukai *et al* [3] have reported an improvement of 1.8 times with

the facet reflectivities of 6% and 30%. The improvement in our result is probably due to the lower facet reflectivity achieved in our case. The ±3dB spectral width is further increased in the double-side coated device (UB259) to 49 GHz at 20dB signal gain, which is 8.23 times larger than that of UB262 and 2.45 times larger than UB258 (A or B). This increase in ±3dB frequency bandwidth is due to the reduction in the Q-factor of the device.

The summary of results plotted in figure 5.24 along with root gain bandwidth product, $\sqrt{G}\,\mathbf{B}$ at the different level of the optical gain is given in table 5.3. It is clear from figure 5.24 and table 5.3 that ±3dB frequency bandwidth increases with a reduction in the signal gain and at 5dB signal gain, 3dB bandwidths of 590, 240 and 70.5 are achieved for UB259, UB258 and UB262 respectively.

Table 5.3. Summary of results plotted in figure 5.25.

Device number	UB262		UB258 (A or B)		UB259	
Signal gain (dB)	**B** (GHz)	$\sqrt{G}\,\mathbf{B}$ (GHz)	**B** (GHz)	$\sqrt{G}\,\mathbf{B}$ (GHz)	**B** (GHz)	$\sqrt{G}\,\mathbf{B}$ (GHz)
5	70.5	157.64	240	536.66	590	1319.3
10	31	98.03	103	325.71	250	790.57
15	13.1	50.74	43	166.54	104	402.79
20	5.95	48.88	20	89.44	49	219.13
25	2.7	13.5	8.3	41.5	21	105

5.3.2.4. Gain dependence of the polarization

The gain of an amplifier is strongly dependent on the polarization of input signals because the single pass gain for the TE and TM modes are different in the active medium. For the TWA or NTWA this effect is due to the difference in confinement factor for TE and TM modes, but for a FP amplifier (also to some extent the NTW device) the facet reflectances are different for TE and TM modes. In a typical laser geometry, the output radiation is normally polarized parallel to junction plane and above the lasing threshold TM mode is dominated by TE mode

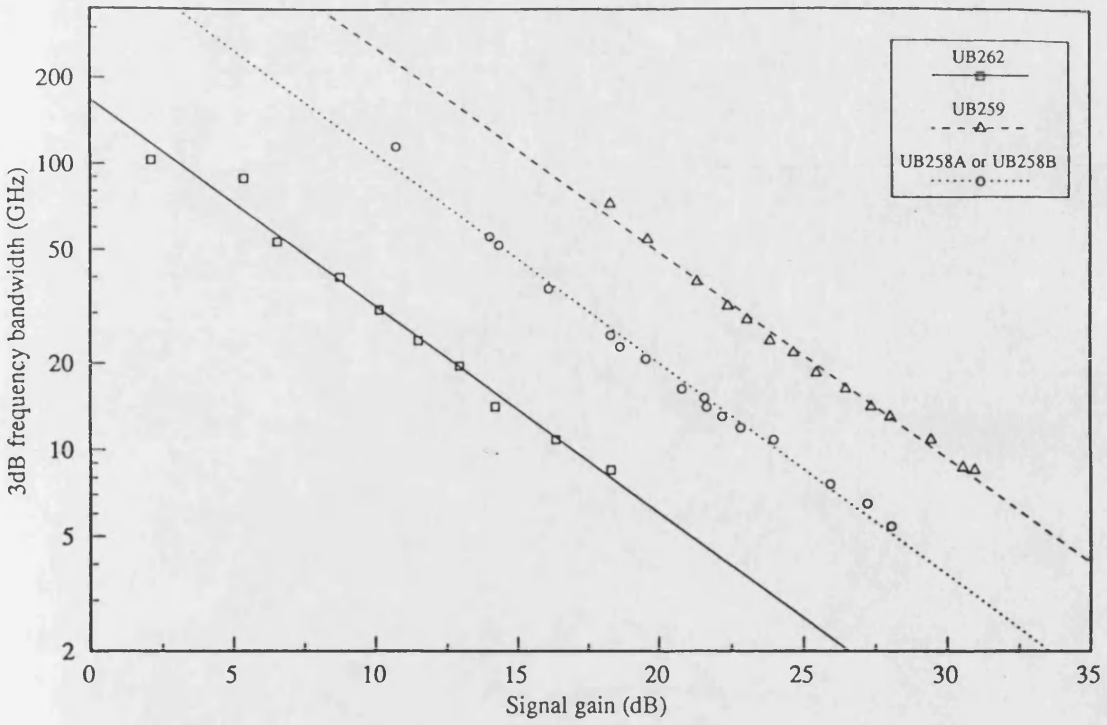

Figure 5.24. The 3dB bandwidth of central longitudinal mode for different devices.

due to higher reflectivity. In section 5.3.2.1.1, the gain of the TE polarization was measured and the gain dependence of the polarization of the AWOA was investigated by mounting the source laser in transverse direction rather than in lateral direction. This arrangement was used to excite the TM polarization instead of the TE polarization. In this case, the AWOA is subjected to input light which is predominantly polarized perpendicular to the junction plane.

The gain measurement process which was adopted for TE polarization was repeated for this case of orthogonal mounting. Figure 5.25 to figure 5.28, shows the light output of the AWOAs against the transversely mounted source laser drive current. Figure 5.29 through figure 5.32 gives comparisons between the TE and TM modal gains under same conditions for UB262, UB259, UB258A and UB258B respectively. Although all these devices show the polarisation dependence of the gain, the effect is highest in the FP AWOA (UB262) because UB262 is a resonant type AWOA and TE modes are favoured inside resonant cavity because of the difference in the facet reflectance for the TE and TM modes. The polarization dependence of gain is reduced in the A.R. coated devices but because of the finite facet reflectances and mainly due to difference in the confinement factor of both polarizations there is some residual polarisation dependence. In all cases, the difference between TE and TM mode increases further with the increase in AWOA current probably due to the difference in the rate of change of TE and TM mode spectra with increasing current.

The polarisation sensitivity of the gain due to the facet reflectance can be eliminated by applying multilayer coatings to the laser facet [39]. Several approaches have been proposed to eliminate the difference between the difference in the TE and TM mode confinement factors, such as; introduction of a thick active layer [40,41,42], orthogonally aligned two-amplifier configuration [43], separate confinement geometry [28] and the introduction of strained layers into the MQW active region of a MQW amplifier [44]. The last three approaches could not be used in OIC construction in this thesis, because of 'in-house' fabrication

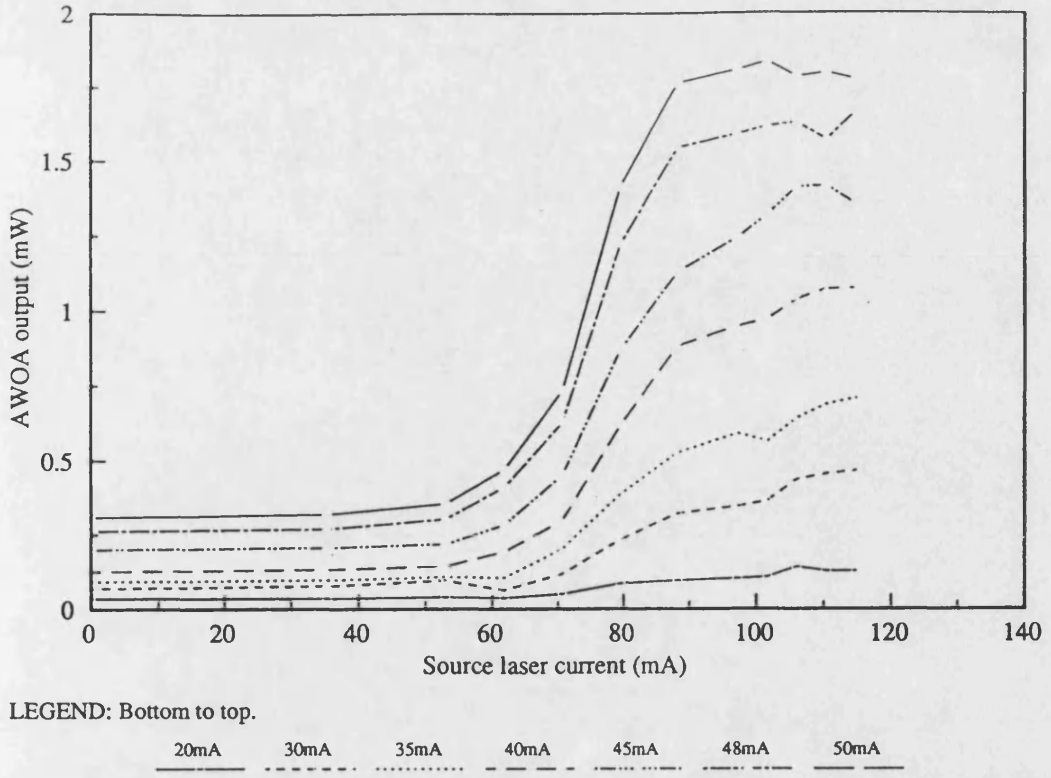

Figure 5.25. AWOA UB262 output power versus the source laser current as a function of the AWOA prebiasing (TM polarization).

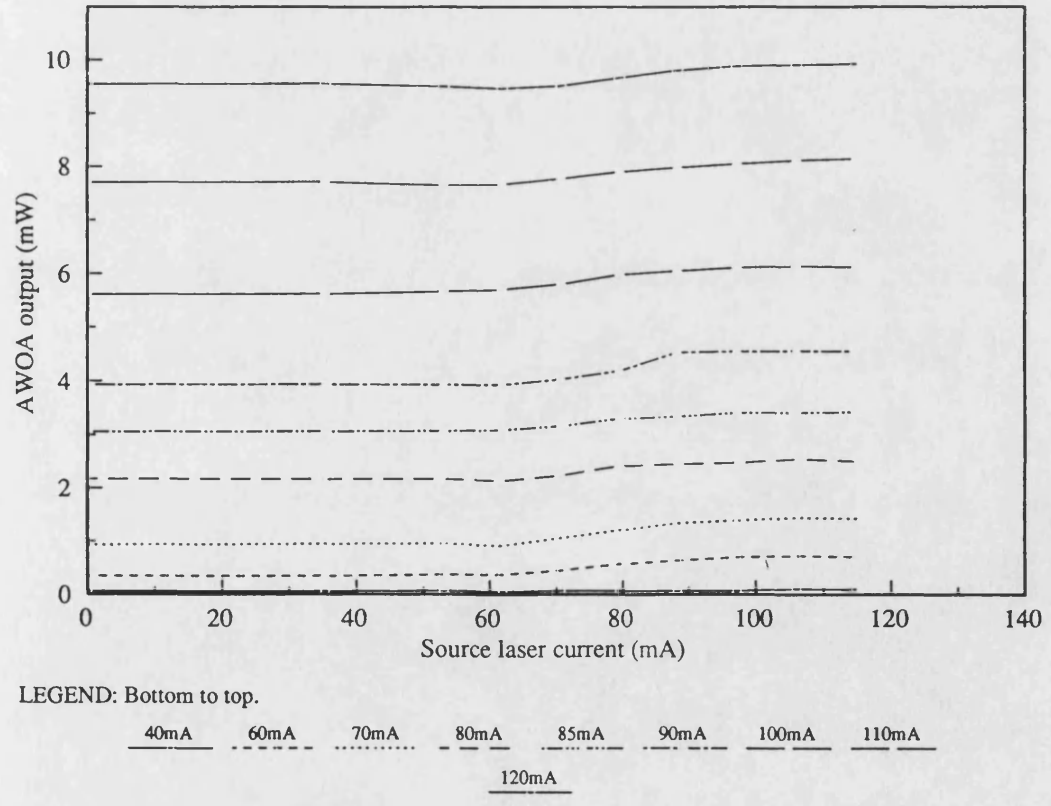

Figure 5.26. AWOA UB259 output power versus the source laser current as a function of the AWOA prebiasing (TM polarization).

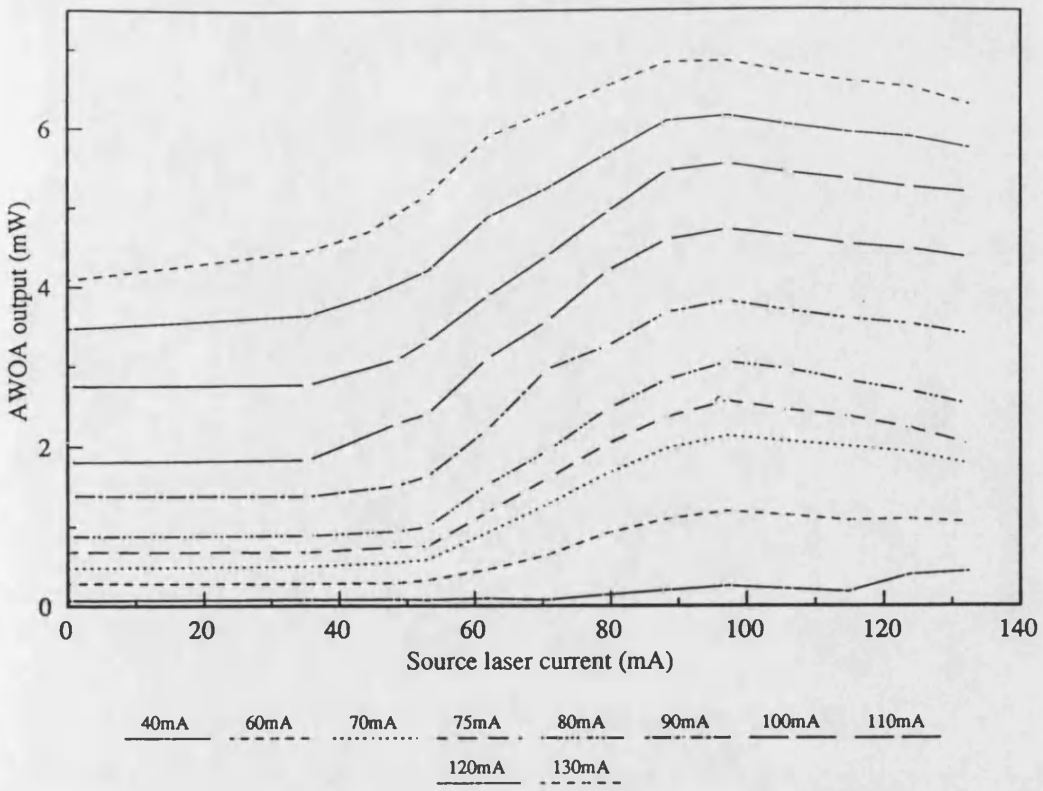

Figure 5.27. AWOA UB258A output power versus the source laser current as a function of the AWOA prebiasing (TM polarization).

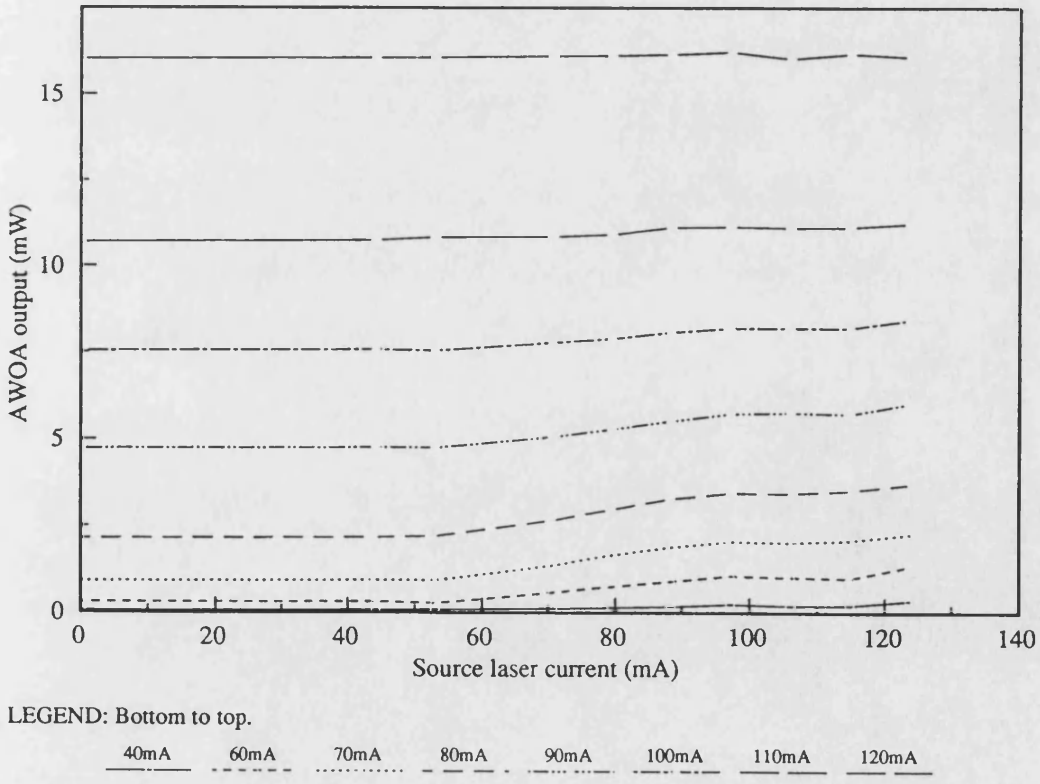

Figure 5.28. AWOA UB258B output power versus the source laser current as a function of the AWOA prebiasing (TM polarization).

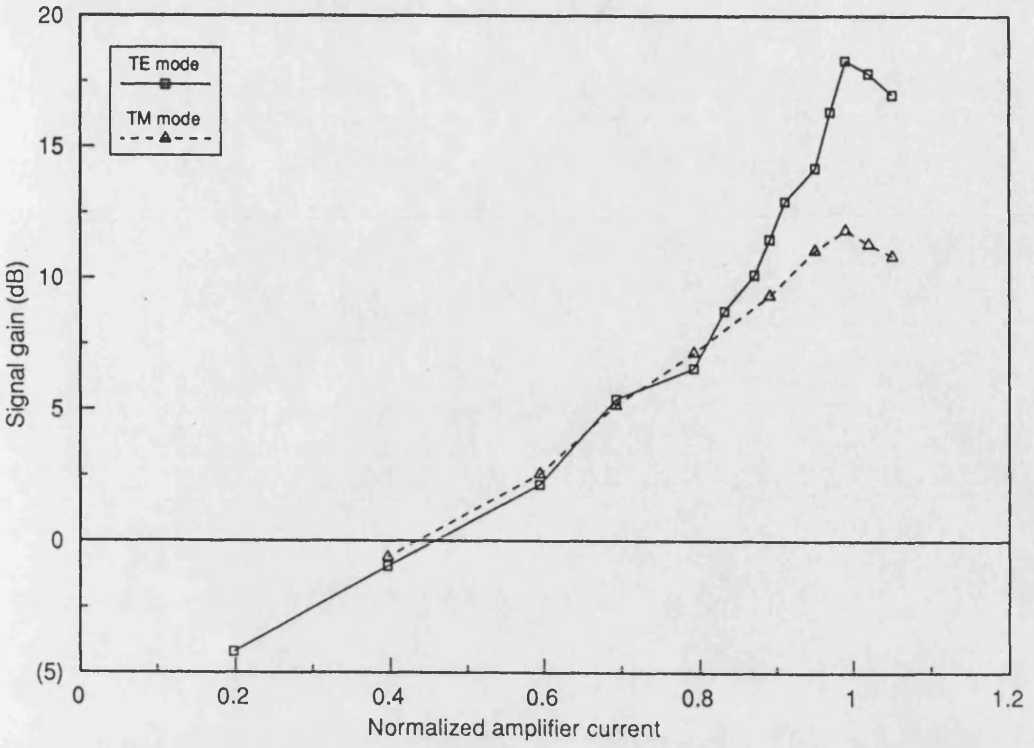

Figure 5.29. Comparison between TE and TM mode amplification in AWOA UB262.

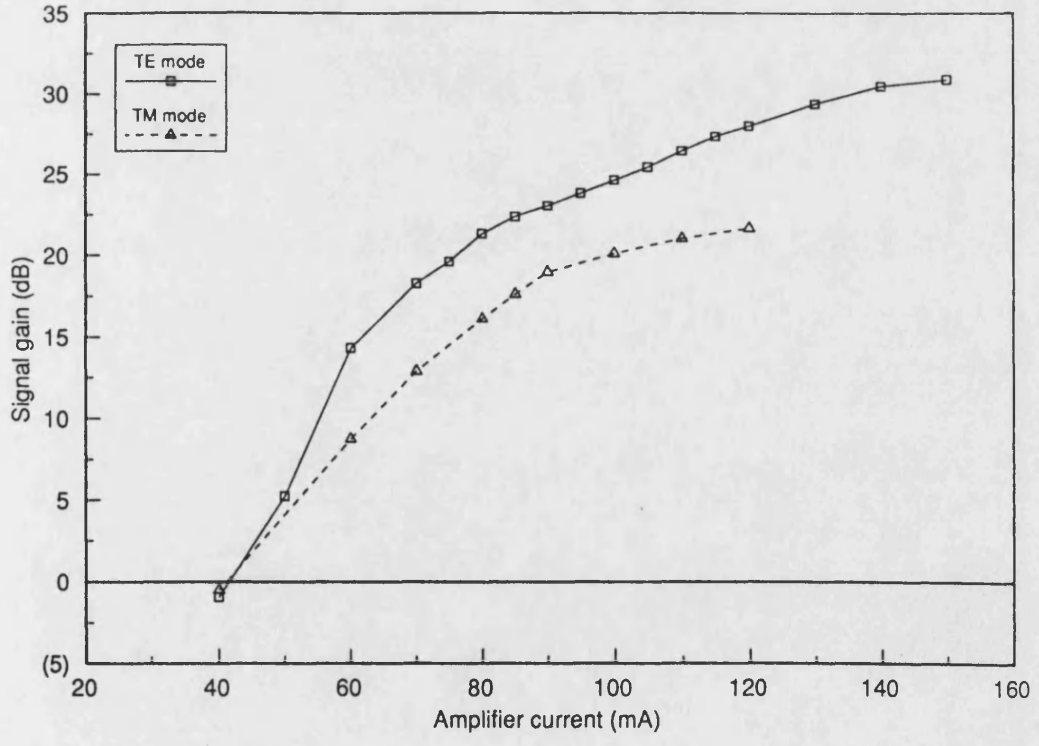

Figure 5.30. Comparison between TE and TM mode amplification in AWOA UB259.

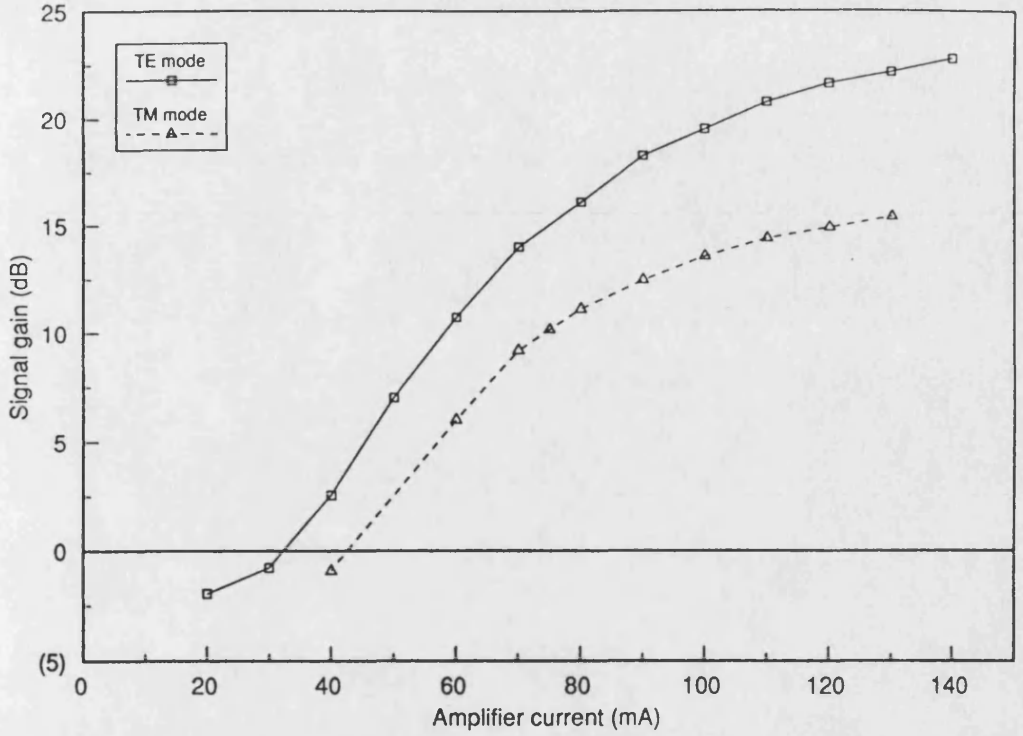

Figure 5.31. Comparison between TE and TM mode amplification in AWOA UB258A.

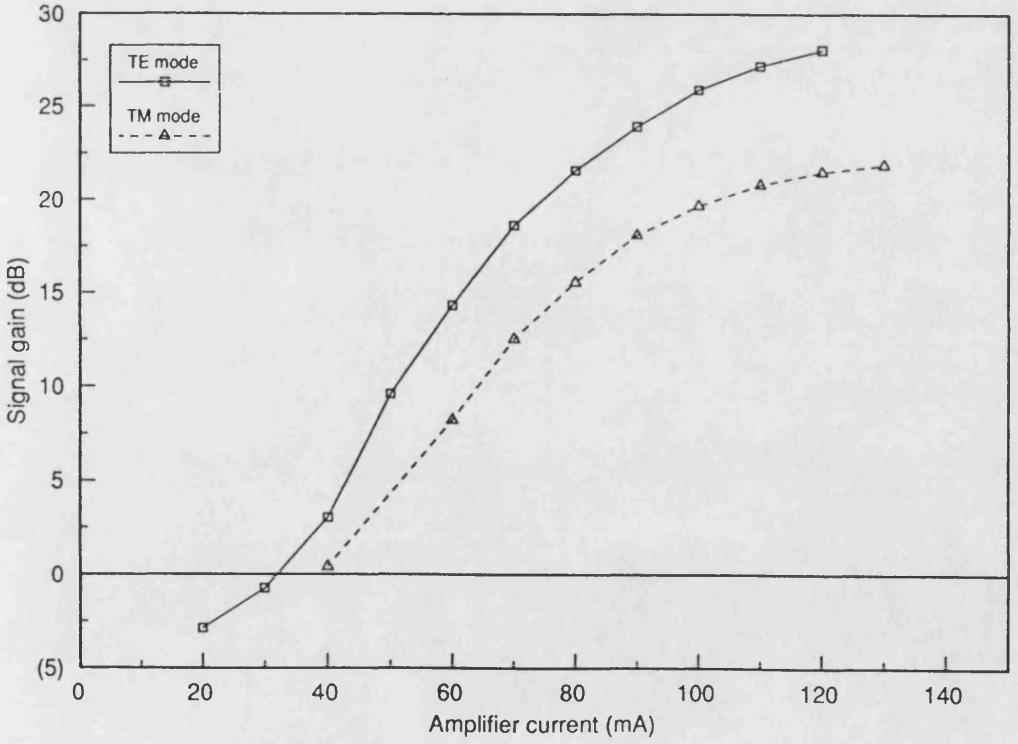

Figure 5.32. Comparison between TE and TM mode amplification in AWOA UB258B.

difficulties. A combination of thick active layer and polarization insensitive multi-layer coating could meet the simple design requirements. But such a structural design would degrade the saturation and noise performance because it cannot operate at large material gain coefficients [1]. Also, the thermal effects cannot be ignored because the thick active layer would be operated at higher levels of current. Thermal effects can be minimized by increasing the Al content in the active layer, but this then shifts the peak emission wavelength towards lower wavelength.

From the above discussion, it can be deduced that in OICs construction, where relatively simple design is an essential requirement, the differences between Γ_{TE} and Γ_{TM} is expected to play major role in polarization dependence characteristics rather than facet reflectivity [8] as facet reflectivities as low as $3X10^{-5}$ can be achieved [7].

5.3.2.5. Noise contribution

The noise performance of a semiconductor optical amplifier is one of the key parameters affecting its performance. In equation (5.15), the noise variance depends upon the contribution of the individual noise sources and the contribution of each noise source depends upon the equivalent noise bandwidths of the spontaneous emission shot noise and the beat noise between spontaneous emission components, $\Delta\nu_1$ and $\Delta\nu_2$ and also the input power. The optical input to the AWOA have already been measured by using an AWOA as an AWOD. In order to calculate the contribution of each noise source in equation (5.15), the equivalent noise bandwidths $\Delta\nu_1$ and $\Delta\nu_2$ had to be calculated and they were calculated for the central longitudinal mode using equations (5.18) and (5.19). The calculated values of the equivalent noise bandwidths, $\Delta\nu_1$ and $\Delta\nu_2$ of the central longitudinal mode are plotted in figures 5.33-5.36 for UB262, UB259, UB258A and UB258B respectively. In all cases (figures 5.33-5.36), $\Delta\nu_1$ and $\Delta\nu_2$ decrease with an increase in the signal gain within the range of 10-350GHz.

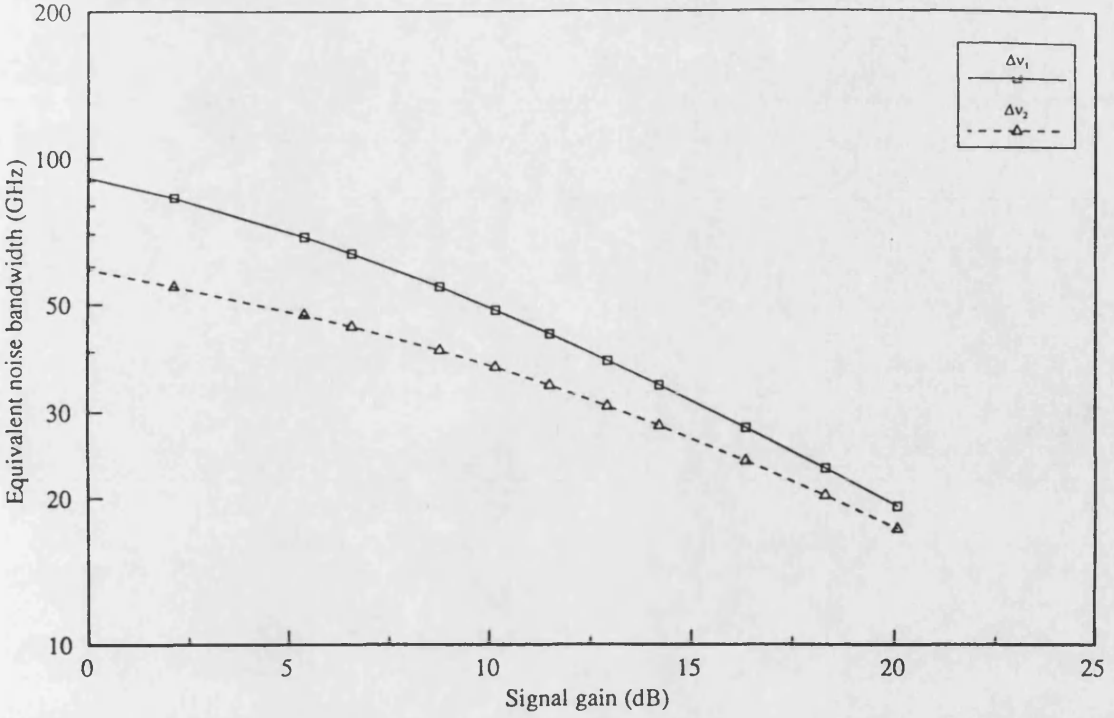

Figure 5.33. Equivalent noise bandwidths $\Delta\nu_1$ and $\Delta\nu_2$ for UB262.

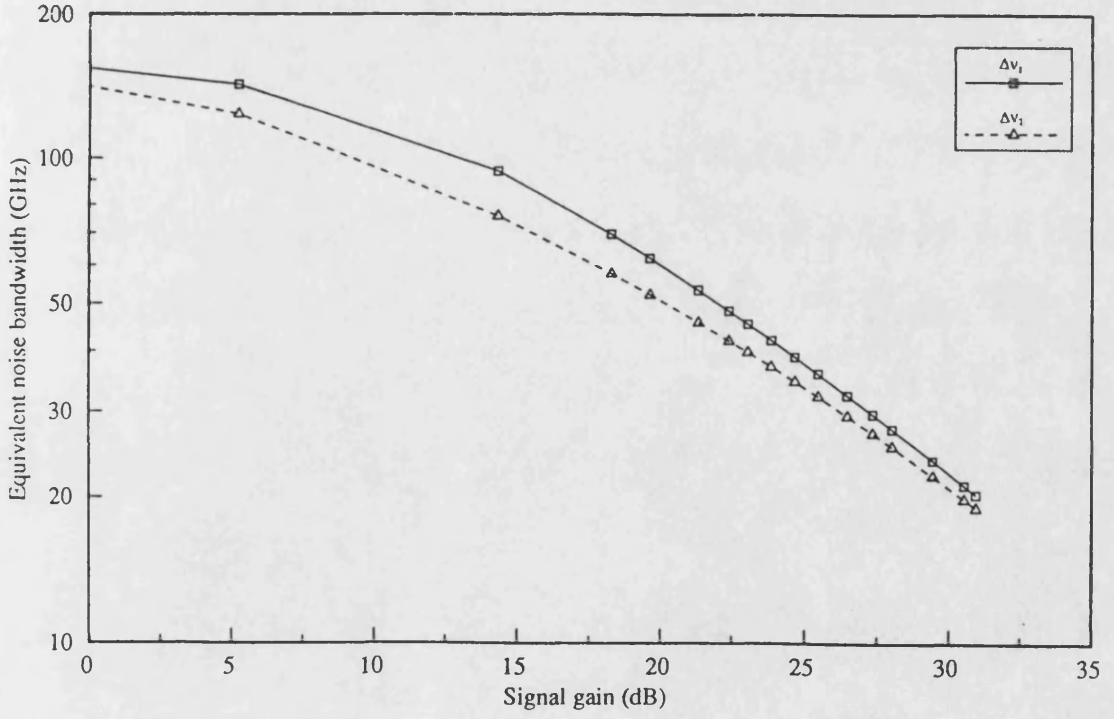

Figure 5.34. Equivalent noise bandwidths $\Delta\nu_1$ and $\Delta\nu_2$ for UB259.

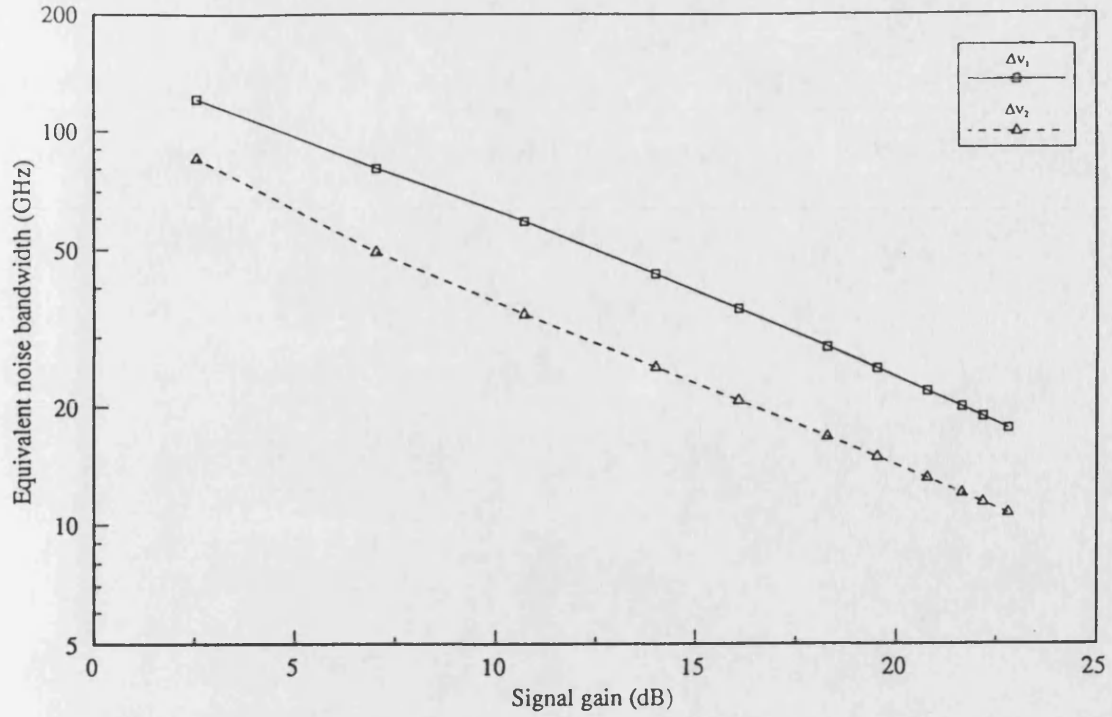

Figure 5.35. Equivalent noise bandwidths $\Delta\nu_1$ and $\Delta\nu_2$ for UB258A.

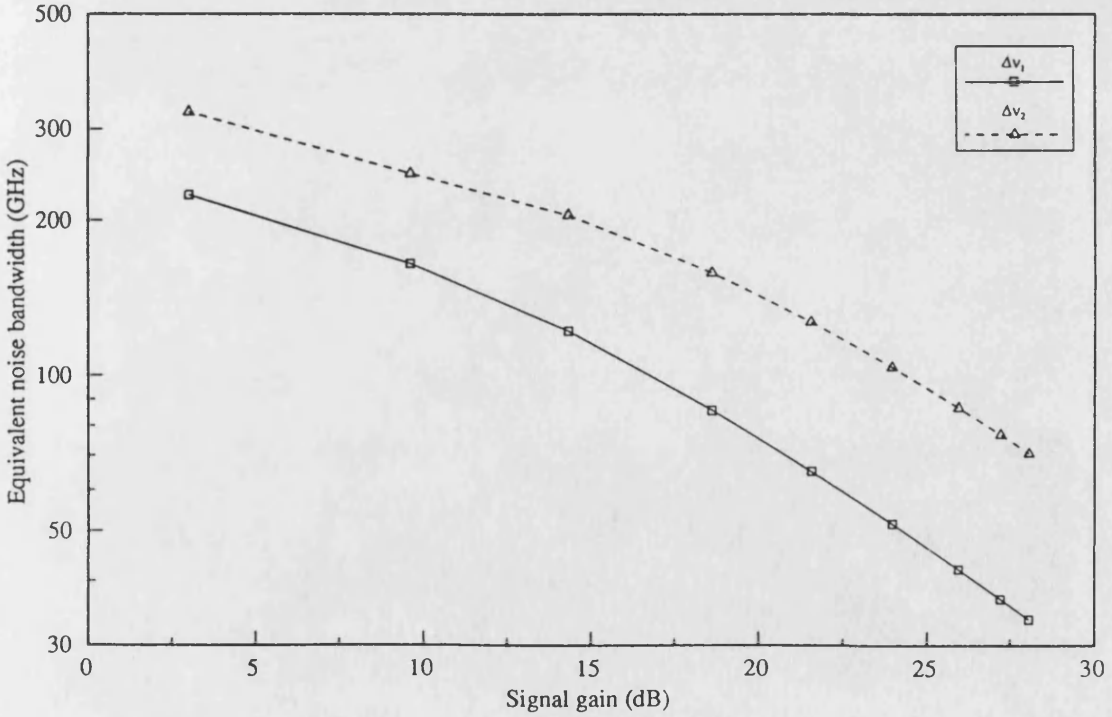

Figure 5.36. Equivalent noise bandwidths $\Delta\nu_1$ and $\Delta\nu_2$ for UB258B.

The results of figures 5.33 through 5.36 represent the equivalent noise bandwidth for the central longitudinal mode. As a multi-wavelength source was used through out this research and AWOAs were operated below threshold level, therefore, the equivalent noise bandwidth will be higher for several longitudinal modes (in the range of 20GHz to 10THz [3], as the number of longitudinal modes experience gain will be higher in equations (5.17) and (5.18) because the multi-wavelength laser source was used during the investigation). For the measurement of the total value of $\Delta\nu_1$ and $\Delta\nu_2$, the total number of longitudinal mode and the gain of each mode has to be known. The gain of each mode cannot be measured accurately due to the superimposition of closely spaced longitudinal modes. However, $\Delta\nu_1$ and $\Delta\nu_2$ can be reduced to an equivalent of 3dB frequency bandwidth using a narrow band optical filter as to select the central longitudinal mode for all devices from which its gain can be measured.

In figures 5.33 through 5.35, $\Delta\nu_1$ is wider than $\Delta\nu_2$. This is in line with the results of reference-3. But for the case of UB258B (figure 5.36), $\Delta\nu_2$ is wider than $\Delta\nu_1$ probably due to the higher value of locally generated and amplified spontaneous emission at the output facet due to the low output facet reflectivity. As the bias current to UB258B increases, then the difference between $\Delta\nu_1$ and $\Delta\nu_2$ becomes larger. This evidence supports the argument that the higher value of $\Delta\nu_2$ is due to the lower output facet reflectivity because as bias current increases, the ASE increases and so too does $\Delta\nu_2$.

The dominant noise components depend upon the particular application and the system gain. Generally beat noise components dominate the shot noise components [1,12,29]. The contribution of the beat noise components was investigated by calculating the relative noise power of each component (the relative noise power is defined as the noise power generated with 1Ω resistance per unit bandwidth (figure 5.23)). Figure 5.37 shows the contribution of the signal-spontaneous beat noise components and the spontaneous-spontaneous beat noise components in terms of the relative noise power for all devices. In figure 5.37, the signal-spontaneous beat

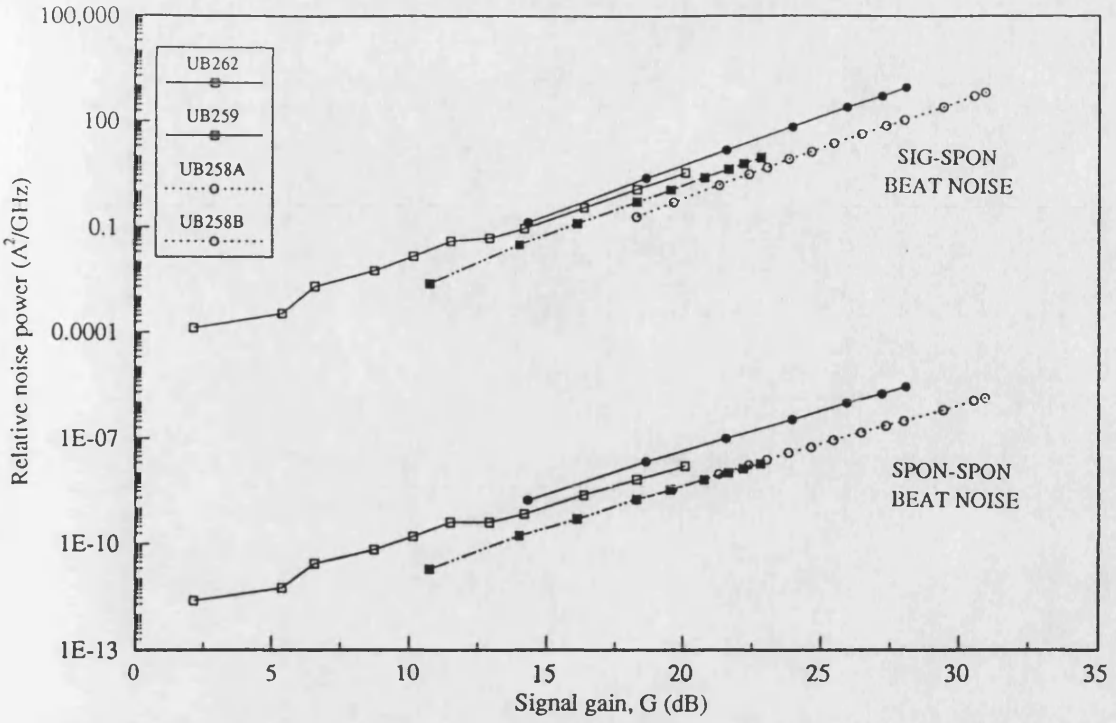

Figure 5.37. The contributions of beat noises to total noise power in terms of relative noise power.

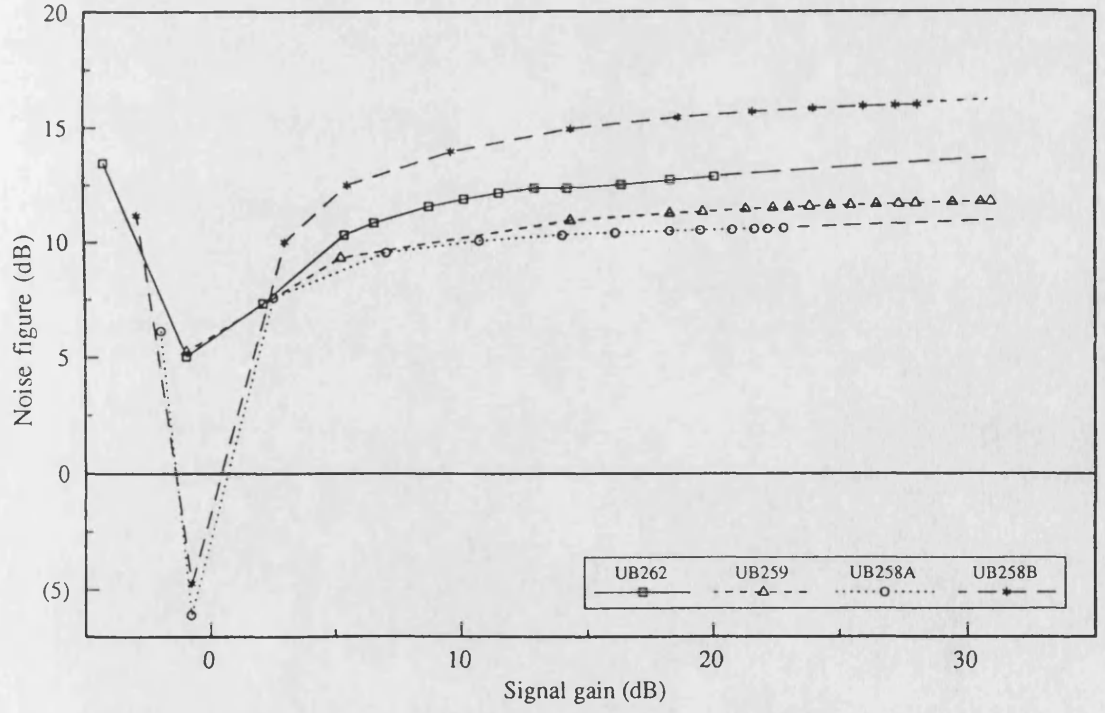

Figure 5.38. Noise figure, F vs the signal gain, G as a function of facet reflectivities.

noise components dominate the spontaneous-spontaneous beat noise components, as was assumed in section 5.2.3.4, and has been demonstrated by several authors [13, 45,46]. In all cases, the relative noise power for UB258B is higher than the other devices due to the higher value of the spontaneous emission at the output facet because of low output facet reflectivity when compared to the input facet reflectivity.

Since the signal-spontaneous beat noise components dominate the spontaneous-spontaneous beat noise components, equation (5.23) was used to evaluate the noise performance of different devices. The noise figure, F was calculated from equation (5.23) is plotted against the signal gain as a function of facet reflectivities in figure 5.38.

In figure 5.38, the devices with differing facet reflectances show maximum and minimum values of F. The device with the low input reflectance has the lowest value of noise figure, whereas the device with high input facet reflectivity exhibit highest noise figure. This is because the excess noise factor, χ strongly depends on the input facet reflectance (equation 5.16). This argument can be further supported by looking at the difference between the noise in symmetrical cavity devices, where UB262, a FP device, shows a higher contribution of the noise than that of the NTWA (UB259). Differences between the noise figures for both devices at the same signal gain is obtained by extrapolating UB262's noise curve. This gives a difference of 2.5-3.0 dB.

The above discussion reinforces the argument that the excess noise contribution, χ is the main reason behind a higher value of noise. The excess noise contribution can be suppressed by optimising the material and structural parameters such as by using asymmetrical facet configuration with lower R_1 and higher R_2. However, the introduction of this type of asymmetrical facet configuration would generate a considerable amount of backward travelling flux. This probably could worsen the dynamic behaviour of the amplifier and certainly the amplifier bandwidth (chaotic dynamics in the active waveguide is discussed in chapter-6).

5.3.2.6. Input-output characteristics of AWOA

The local carrier density within the active layer of the AWOA decreases along the length of the device with the injection of an external optical input signals due to the growth of the photon density and the increase in stimulated recombination and complex refractive index changes accordingly. This gives rise to gain saturation effects and this nonlinear coupling mechanism gives rise to nonlinear input/output characteristics. This produces harmonic distortion if the optical carrier is modulated with either data or a sine wave [47,48]. The input/output characteristics of the locally pumped active waveguide has been investigated theoretically in reference-47. The purpose of this section is to demonstrate the nonlinear relation between the input and output of the locally pumped butt-coupled AWOD experimentally.

The input/output characteristics of the AWOA were measured by adopting the procedure of reference-47 and to best of our knowledge, this is a first attempt in this regard. For this purpose, the experimental set-up of figure 5.11 was used, but instead of using the fast detector at output, the LAD was used close to the back facet of AWOA. Investigations began with device UB262. UB262 was tuned to maximum gain and after achieving maximum gain, UB262 was electrically biased to transparency for an optical input power, P_{in} of 1mW. Then the input power was varied and the AWOA bias current was kept constant at 50mA (the transparency level of 1mW of input power). Later the net optical input power to the AWOA was plotted against the AWOA output power. The same experimental procedure was then repeated by altering the temperature of the source laser by 5°C around the both side of the optimum temperature (temperature where the optical gain was maximum). This gives a peak input wavelength variation of $\pm 1.225nm$. The input/output characteristics are plotted in figure 5.39 as a function of the source laser temperature for UB262. A similar experimental procedure was repeated for the other devices and the results are presented in figures 5.40 to 5.42.

All devices show a nonlinear input/output response, as predicted in

reference-47. In UB262, the nonlinearity is the strongest of all the devices tested at high temperature of the source laser. This can be explained as follows; as the temperature of the source laser increases, the peak emission wavelength of input radiation shifts towards the longer wavelengths. As the source laser biasing current increases, the peak wavelength of input radiation moves towards shorter wavelengths until it is tuned to the AWOA cavity resonance, resulting in an increase in the population inversion parameter, n_{sp}. This depletes the cavity gain and appears as a saturation of the output of the AWOA due to the asymmetric detuning effect described in section 5.3.2.2. This can further be explained by looking at the results of UB259 (figure 5.40). The nonlinearity of the input/output characteristic increases smoothly with the increase in the source laser temperature (i.e. output of AWOA increases with the decrease in temperature at constant input power below transparency level) due to reduced temperature sensitivity and symmetrical temperature behaviour (figure 5.23, solid line) as a result of A.R. coating. This is in fact closer to the theoretical predictions. This can be described as follow; when the UB259 is subjected to multimode input radiation, several longitudinal modes experience the gain and any reduction in the gain of one mode due to the change in input peak radiation wavelength, is compensated by other closely oscillating modes due to wide wavelength response of that device. Therefore, the overall change in output response stays small and the nonlinearity in the input/output characteristic follow the theoretical predictions.

Also here the device UB258 shows dual input/output characteristics due to the difference in input and output facet reflectances. On the one hand, UB258A shows strong nonlinearity, similar to the nonlinearity found in UB262. However, in this case, the strong nonlinear behaviour is expected to be due to a increased external feedback as a result of low input facet reflectance rather than temperature sensitivity because this device (UB258A) has shown low temperature sensitivity (see figure 5.23 and table 3.1). On the other hand, in UB258B, the nonlinearity is

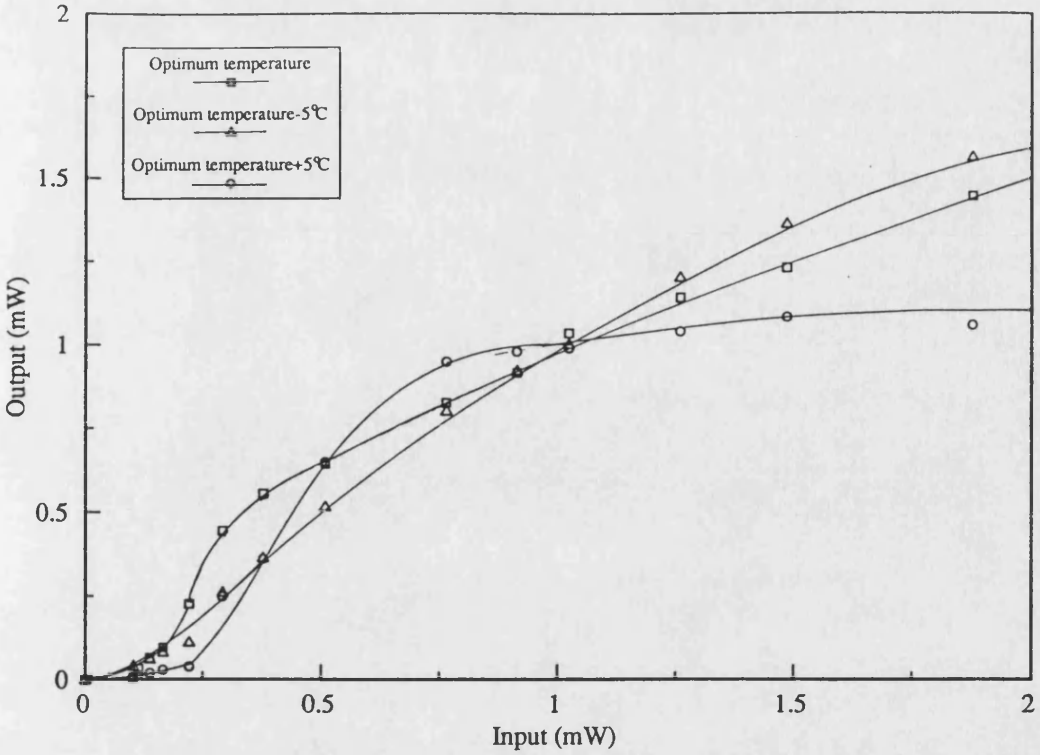

Figure 5.39. The input/output characteristics of AWOA UB262 biased to transparency of 1mW (TE polarization).

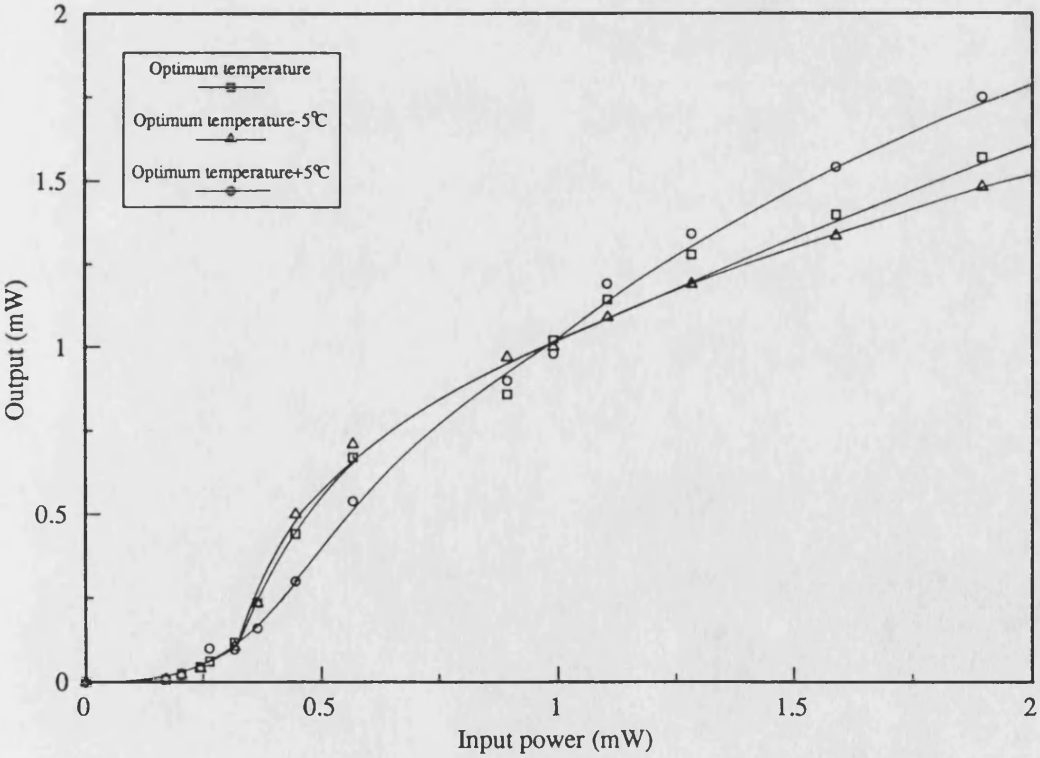

Figure 5.40. The input/output characteristics of AWOA UB259 biased to transparency of 1mW (TE polarization).

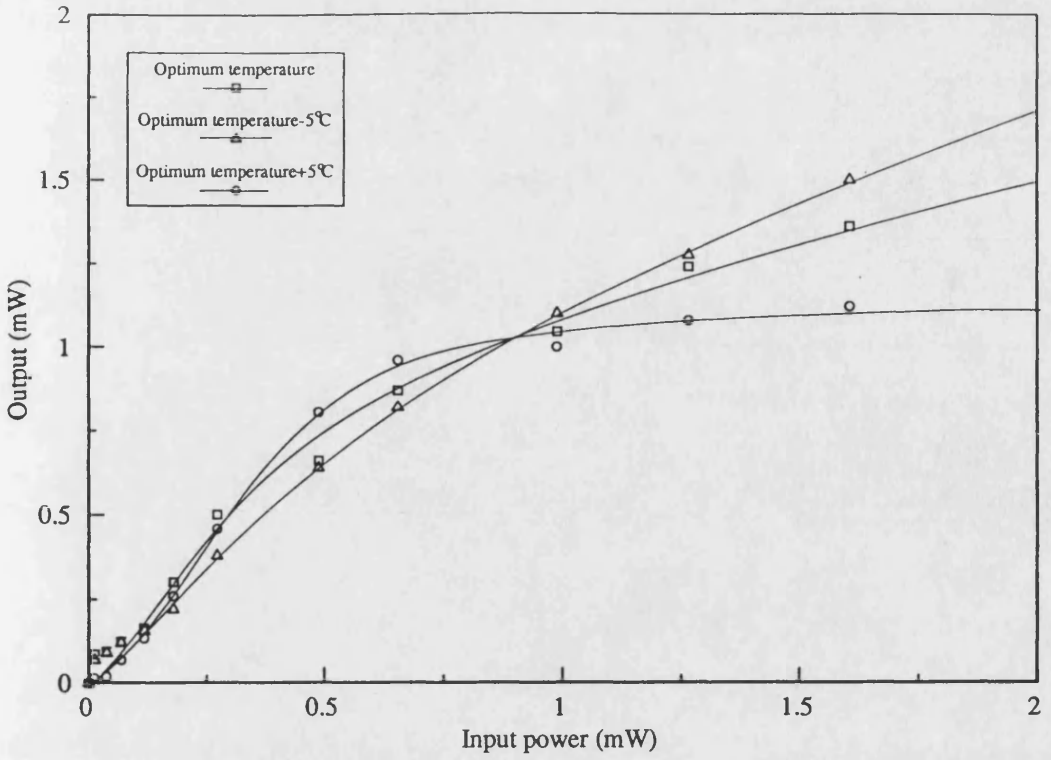

Figure 5.41. The input/output characteristics of AWOA UB258A biased to transparency of 1mW (TE polarization).

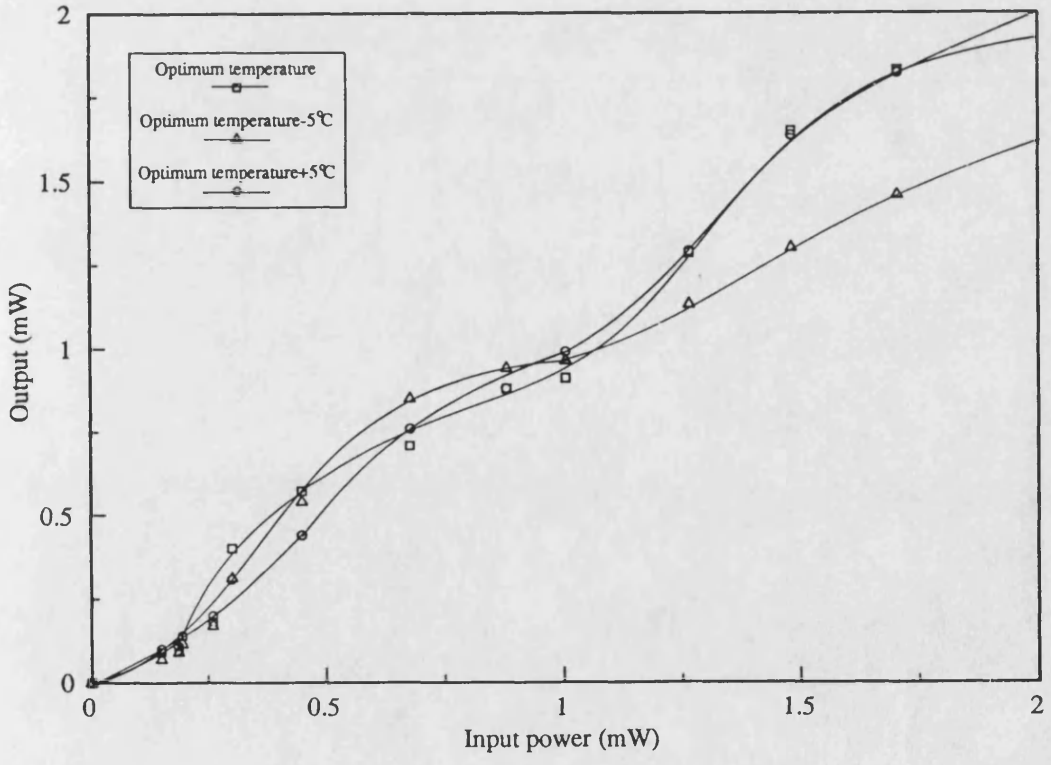

Figure 5.42. The input/output characteristics of AWOA UB258B biased to transparency of 1mW (TE polarization).

minimum probably due to a comparatively low influence of the input power on the output power (see figures 5.15 and 5.28) as a direct consequence of low facet reflectivity of the output facet.

5.4. Summary

In this chapter, the properties of AWOA have been investigated experimentally by using the existing theoretical background of external optical signal amplification in semiconductor laser amplifiers in terms of material and structural parameters.

The investigation started with the FP amplifier. The very high Q factor of FP cavity makes its very sensitive to changes in temperature, bias current, signal polarisation and signal frequency fluctuations. Also the signal gain is limited due to low optical output power saturation. It is a well established fact that the application of A.R. coating suppresses the internal feedback and the amplifier can be operated to higher optical output powers as a linear amplifier. Amplifier equations were then derived which were applicable to both the FPA and NTWA by allowing finite facet reflectances.

The signal gain of the AWOA (in hybrid configuration) was calculated by using the amplifier equation and the AWOA saturated output characteristics. For this purpose, a simple relationship for coupling of input radiation was established and a coupling efficiency of 12.86% was achieved using x20 (NA=0.45) lens. The coupling efficiency could have been increased by using x20 lens with a NA=0.54 or x40 lens, but the former lens was preferred because of the flexibility offered by having a larger working distance. The saturation limit of the optical input power which led to the saturation of the output power, was estimated by using carrier induced nonlinear phenomena in the active medium. Optical signal amplification as high as 31dB and 21dB was achieved in the NTWA and FPA respectively before significant saturation occurred. An increase in signal gain in the NTWA was the direct consequence of A.R. coated facets which has suppressed internal feedback.

The asymmetrical facet devices, UB258A and UB258B, showed differences in their amplification characteristics with a peak gain difference of around 6dB, which was attributed to differences between their input and output facets reflectances.

The signal gain in all devices was found to be temperature dependent. The temperature dependent sensitivity of the AWOA was found to reduce with a reduction in facet reflectivities. In the FPA, asymmetric detuning has been observed which could have been used to draw the detuning characteristic of the FP device. Unfortunately the source laser which was used during this work was a multi-wavelength source and for the determination of detuning characteristics, a single wavelength source would be required before this technique can be properly applied.

The 3dB frequency bandwidth (spectral linewidth) of the central longitudinal mode was calculated as a function of the signal gain for each device by considering the frequency mismatch between the 3dB corner frequency of central longitudinal and the AWOA cavity resonance. The application of A.R. coating on the mirror facet was found to increase the 3dB frequency bandwidth considerably due to the reduction in the Q value of amplifying cavity. At 20dB signal gain, FWHM frequency bandwidths were measured as 5.95, 20 and 49GHz for UB262, UB258 and UB259 respectively. These values are better than previously published values.

The polarization dependence of the optical gain was demonstrated by changing the mounting position of the source laser in such a way that the incoming radiation was likely to excite the TM modes in the AWOA. The gain of the amplifier to both polarizations was compared. It was found that the optical gain of the FP AWOA was highly sensitive to the polarization of the input signal but A.R. coated devices were much less sensitive to the state of the input signal polarization. In the A.R. coated devices, especially in UB259, the polarization dependence of the optical gain was reduced but was not totally eliminated. It was concluded that in this case the main difference in gain was due to the different confining factors for the two polarizations. The difference between Γ_{TE} and Γ_{TM} can be minimized by using a thick active layer with multilayer A.R. coatings.

The noise contribution in the AWOA was discussed and the contribution of the mode partition noise was considered to be insignificant in our case because the mode partition noise is expected to play a major role in the noise characteristic of the single wavelength system and during work presented in this thesis, a multi-wavelength source laser was used and no optical filtering process was used at the output of the AWOA. The shot noise was found to be unavoidable. Among the beat noise components, the spontaneous-spontaneous beat noise can effectively be reduced by using a narrow band optical filter at the output. However, the introduction of a narrow band optical filter at the output could introduce mode partition noise and the penalty imposed by the mode partition noise increases as the filter bandwidth gets narrower. At the higher value of the signal gain, the spontaneous-spontaneous beat noise components are dominated by the signal-spontaneous beat noise components. Since the signal-spontaneous noise cannot be removed because this noise is associated with amplified signals, it was found to play a leading role in noise performance of an AWOA (this would be the case in monolithic integrated AWOA). The realisation of fact that the signal-spontaneous is the main performance limiting noise source led to the derivation of a simple relation for the noise figure to analyse the noise performance of the different devices. UB258A (device with low input facet reflectance) was least effected by noise whereas UB258B (device with high input facet reflectance) was worse effected by noise. This was due to the higher value of the noise enhancement factor, χ associated with UB258B because the noise enhancement factor, χ strongly depends upon the input facet reflectance.

The symmetrical facet structure devices, UB262 and UB259 were shown to have the lower value of noise factor and the difference between noise contributions was found within the range of reported values. Among symmetrical facet devices, the FPA also generates a considerable amount of backward travelling flux and the NTWA is highly susceptible to the reflections from outside due to lower facet reflectivities. Therefore, the effect of back reflection along with the detuning effect

appear due to the injection of the external signal is considered in next chapter. However, in the hybrid approach, the effect of back reflection can be avoided by introducing an optical isolator between the source laser and the AWOA.

The underlying non-linear mechanism in locally pumped AWOA was analysed by measuring the input/output characteristics of the different devices. A considerable nonlinearity between the input and output of the AWOA was found. Nonlinearity was stronger in the FPA as a direct consequence of higher wavelength sensitivity of that device. UB258A was also shown to have a considerable amount of nonlinearity which was probably due to the unwanted reflection from outside because low input and high output facet reflectances. The input/output characteristics of UB258B were some how independent of input power due to high input facet and low output facet reflectivities. The result of UB259 were found to be closer to the theoretical prediction of reference-47. In all cases, the input/output characteristics were found to be influenced by the multi-wavelength input radiation. This problem can only be solved by using single wavelength source laser and this would reveal the real behaviour of underline non-linear mechanism in the AWOA.

REFERENCES

1. Mukai, T., Yamomoto, Y., and Kimura, T., 'Optical amplification by semiconductor lasers', in Semiconductor and semimetal vol.E, Ed. Tsang, W.T., p.265, Academic Press, 1985.
2. Special issue on optical amplifiers, Ed. Yamomoto, Y., and Mukai, T., Optical and Quantum Electron., vol.21, 1989.
3. Mukai, T., Yamomoto, Y., and Kimura, T., 'S/N and error rate performance in AlGaAs semiconductor laser pre-amplifier and linear repeater systems', IEEE J. Quantum Electron., vol. QE-18, p.1560, 1982.
4. Zah, C.E., Osinki, J.S., Caneau, C., Menocal, S.G., Reith, L.A., Salzman, J., Shokoohi, F.K., and Lee, T.P., 'Fabrication and performance of 1.5*mum* GaInAsP travelling-wave laser amplifiers with angled facets', Electron. Lett., vol.23, p.990, 1987.
5. Farries M.C., Buus, J., and Robbins, D.L., 'Analyses of antireflection coatings on angled facet semiconductor laser amplifiers', Electron. Lett., vol.26, p.381, 1990.
6. Cha, I., Kitamura, M., and Mito, I., '1.5 *mum* band travelling-wave semiconductor optical amplifiers with window facet structure', Electron. Lett., vol.25, p.242, 1989.
7. Olsson, N.A., 'Lightwave systems with optical amplifiers', J. of Lightwave Tech., vol.7, p.1071, 1989.
8. O'Mahony, M.J., 'Semiconductor laser optical amplifiers for use in future fibre systems', J. of Lightwave Tech., vol.6, p.531, 1988.
9. Yamamoto, Y., 'AM and FM quantum noise in semiconductor lasers- Part-I: Theoretical analysis', IEEE J. Quantum Electron., vol. QE-19., p.34, 1983.
10. Yamamoto, Y., 'AM and FM quantum noise in semiconductor lasers- Part-II: Comparison of theoretical and experimental results for AlGaAs lasers', IEEE J. Quantum Electron., vol. QE-19., p.47, 1983.
11. Kobayashi, S., and Kimura, T., 'Gain and saturation power of resonant AlGaAs laser amplifier', Electron. Lett., vol.16, p.230, 1980.
12. Yamamoto, Y., 'Characteristics of AlGaAs Fabri-Parot cavity type laser amplifiers', IEEE J. Quantum Electron., vol. QE-16, p.1047, 1980.
13. Hakki, B.W., and Paoli, T.L., 'Gain spectra in GaAs double heterostructure injection lasers, J. of Appl. Phys, vol.46, p.1299, 1975.
14. Gordon, E.I., 'Optical maser oscillators and noise', B S T J, vol.43, p.507, 1964.
15. Ross, D., 'Lasers light amplifiers and oscillators', Ch.5, Academic Press, 1969.
16. Marcuse, D., 'Computer model of an injection laser amplifier', IEEE J. Quantum Electron., vol. QE-19, p.63, 1983.

17. Perkins, M.C., Ormondroyd, R.F., and Rozzi, T.E., 'Effect of photon lifetime on absorbtive bistability in inhomogeneously pumped lasers', Electron. Lett., vol.22, p.857, 1985.

18. Perkins, M.C., Ormondroyd, R.F., and Rozzi, T.E., 'Analysis of absorbtive bistability characteristics of multisegment lasers', IEE Proc.-J, vol.133, p.283, 1986.

19. Perkins, M.C., and Ormondroyd, R.F., 'Transient analysis of optical bistability in inhomogeneously pumped lasers', IEE Proc.-J, vol.135, p.133, 1988.

20. Kaminov, I.P., and Tucker, R.S., 'Mode-controlled semiconductor lasers', in Guided-wave optoelectronics, Tamir, T. (Ed.), p.211, Springer-Verlag, 1990.

21. Yariv, A., 'Quantum electronics' 2nd edition, John Wiley & Sons, 1975.

22. Adams, M.J., Westlake, H.J., O'Mahony, M.J., 'Optical bistability in semiconductor laser amplifiers' in 'Optical nonlinearities and instabilities in semiconductors', Ed. Haug, H., Academic Press, 1988.

23. Ogawa, K., and Vodhanel, R.S., 'Measrements of mode partition noise of laser diode', IEEE J. Quantum Electron., vol. QE-18, p.1090, 1982.

24. Fyath, R.S., and O'Reilly, J.J., 'Performance of lightwave systems incorporating multilongitudinal mode laser and optically preamplified receiver combinations', IEE Proc.-J, vol.137, p.230, 1990.

25. Henry, C.H., 'Theory of spontaneous emission noise in open resonators and its application to lasers and optical amplifiers', IEEE J. of Lightwave Tech., vol. LT-4, p.288, 1986.

26. Lowery, A.J., 'Amplified spontaneous emission in semiconductor laser amplifiers: validity of the transmission-line laser model', IEE Proc.-J, vol.137, p.241, 1990.

27. Yamamoto, Y., 'Noise and error rate performance of semiconductor laser amplifiers in PCM-IM optical transmission systems', IEEE J. Quantum Electron., vol. QE-16., p.1073, 1980.

28. Saitoh, T., and Mukai, T., 'Structural design for polarization-insensitive travelling-wave semiconductor amplifiers', Optical and Quantum Electron., vol.21, p.S47, 1989.

29. Mukai, T., and Yamomoto, Y., 'Fundamentals of optical amplifiers', Optical and Quantum Electron., vol.21, p.S1, 1989.

30. Mukai, T., and Yamomoto, Y., 'Noise in an AlGaAs semiconductor laser amplifier', IEEE J. Quantum Electron., vol. QE-18, p.575, 1982.

31. Kobayashi, S., and Kimura, t., 'Semiconductor optical amplifiers', IEEE Spectrum, p.27, May 1984.

32. Takeuchi, H., and Oe, K., 'Low-loss single-mode GaAs/AlGaAs miniature optical waveguides with straight and bending structures', IEEE J. of Lightwave Tech., vol. LT-7, p.1044, 1989.

33. Bogatov, A.P., Eliseev, P.G., Okhotnikov, O.G., Rakhval'skiy, M.P., and Khayretdinov, K.A., 'Nonlinear opticsof semiconductor lasers', Ed. Basov, N.G., Nova Science Publication, Commack.

34. Marshall, I.W., Spirit, D.M., and O'Mahony, M.J., 'Picosecond pulse response of a travelling-wave semiconductor laser amplifier', Electron. Lett., vol.23, p.818, 1987.

35. Lowery, A.J., 'Explanation and modelling of pulse compression and broadening in near-travelling-wave laser amplifiers', Electron. Lett., vol.24, p.1125, 1988.

36. Lowery, A.J., 'Pulse compression mechanisms in semiconductor laser amplifiers', IEE Proc. J, vol.136, p.141, 1989.

37. Nakai, T., Ito, R., and Ogasawara, N., 'Asymmetric frequency response of semiconductor laser amplifiers', Jpn. J. of Appl. Phys., vol.21, p.L680, 1982.

38. Kobayashi, K., Nishimoto, H., and Lang, R., 'Experimental observation of asymmetric detuning characteristics in semiconductor laser injection locking', Electron. Lett., vol.18, p.54, 1982.

39. Vassallo, C., 'Polarization-independent antireflection coatings for semiconductor amplifiers', Electron. Lett., vol.24, p.61, 1988.

40. Olsson, N.A. Kazarinov, R.F., Nordland, W.A., Henry, C.H., Oberg, H.G., White, H.G., Garbinski, P.A. and Savage, A., 'Polarization-independent optical amplifier with buried facet', Electron. Lett., vol.25, p.1048, 1989.

41. Cha, I., Kitamura, M., Honmou, M., and Mito, I., '1.5μm band travelling-wave semiconductor optical amplifiers with window facet structure', Electron. Lett., vol.25, p.1241, 1989.

42. Simon, J.C., 'Polarisation characteristics of travelling-wave-type semiconductor amplifier', Electron. Lett., vol.18, p.438, 1982.

43. Groβkopf, G., Ludwig, R., Waarts, R.G., and Weber, H.G., 'Optical amplifier configurations with low polarization sensitivity', Electron. Lett., vol.23, p.1387, 1987.

44. Magari, K., Okamoto, M., Yasaka, H., Sato, K., Noguchi, Y., and Mikami, O., 'Polarization insensitive travelling wave type amplifier using strained multiple quantum well structure', IEEE Photonic Tech. Lett., vol.2, p.556, 1990.

45. Mukai, T., and Yamomoto, Y., 'Gain, frequency bandwidth, and saturation output power of AlGaAs DH laser amplifiers', IEEE J. Quantum Electron., vol. QE-17, p.1028, 1981.

46. Mukai, T., and Yamomoto, Y., 'Noise in an AlGaAs semiconductor amplifiers', IEEE J. Quantum Electron., vol. QE-18, p.564, 1982.

47. Ormondroyd, R.F., Pennington, P.N., and Perkins, M.C., 'Nonlinear static characteristics of monolithic active integrated-optic waveguides', IEE Proc. J, vol.136, p.59, 1989.

48. Pennington, P.N., and Ormondroyd, R.F., 'Large-signal modulation response of monolithic active integrated-optic waveguides', IEE Proc. J, vol.137, p.11, 1990.

Chapter-6

Chaotic dynamics of active waveguide components

6.1. Introduction

The source and amplifier devices considered in this thesis have been butt-coupled to each other. In this case, additional feedback can take place because the devices are not isolated from each other. Therefore, the effect of multiple-feedback on the different operating characteristics of different components needs to be considered very carefully.

Suppose an optical amplifier is integrated with a lasing source on a single substrate (as in UB136) and is subjected to an external input from the lasing source. The etched facet of the optical amplifier can act as an external mirror to the incoming light beam. The gap between the two etched facets can work as an external cavity. As the optical amplifier is also forward biased to overcome the losses, it is possible optical feedback can occur from the lasing source to the amplifier via the etched facet. The involvement of a number of different wavelength components creates a number of interesting phenomena, including frustrated instabilities [1,2]. These instabilities in the semiconductor laser systems can give rise to a complex but predictable behaviour called chaos which can be clearly distinguished from noise since the later is random in nature.

In this chapter, frustrated instabilities and chaos are discussed further. Frustrated instabilities are demonstrated experimentally for the first time in this chapter. During the investigation of frustrated instabilities and the chaotic dynamical behaviour of the butt-coupled active waveguide optical amplifier, UB136 is used but due to the net losses in that device, the hybrid approach was used later on. In the hybrid approach, the two laser devices were butt-coupled to each other

through an optical lens system, as before. When two laser devices are used in a hybrid configuration, the amount of back reflection and hence the influence of the external cavity can be monitored by deliberately tilting either the amplifier or the source laser. In this way the detuning of the optical amplifier can be achieved.

The investigation begins with the consideration of the rate equations corresponding to the carrier and photon densities in section 6.2 for a laser. Section 6.3 deals with the non-linear behaviour and chaos in the laser diodes. This section also discusses ways of generating self-sustained pulsations in a laser system, and particularly in integrated active waveguide amplifiers. In section 6.4, the basic theory of frustrated instabilities in semiconductor lasers is established. Section 6.5 consists of the main body of the experimental results which have been achieved using the hybrid approach. In section 6.6, the experimental results are compared with the available theory. As usual, this chapter ends with the summary of the main points in section 6.7.

6.2. Rate equations

The dynamic behaviour of lasing devices is very complex. The best available example is the phenomena of relaxation oscillation in lasers which is usually attributed to the interaction between the carrier concentration and the photon density. The dynamic behaviour is governed by two rate equations: i). for the carrier concentration and ii). for the photons concentration [3,4];

$$\frac{dN}{dt}=\frac{J}{ed_3}+D\frac{d^2N}{dx^2}-\frac{N(t)}{\tau_s}-G(N)S \tag{6.1}$$

and

$$\frac{dS}{dt}=\left[G(N)-\frac{1}{\tau_p}\right]S+\beta\frac{N(t)}{\tau_s} \tag{6.2}$$

where N is the carrier density, J is the current density, e is the electron charge, d_3 is the thickness of the active region, D is the diffusion constant, S is the photon

density, τ_s is the spontaneous lifetime, τ_p is the photon lifetime and β is the spontaneous emission factor. *G(N)* is the net rate of stimulated emission and defined as;

$$G(N) = \Gamma v_g g(N) \tag{6.3}$$

here v_g is the group velocity and g(N) is the local gain.

The first term on the left hand side of equation (6.1) describes the increase in the carrier concentration within the active region due to the injection of carriers (the rate of pumping, *P*). The second term accounts for the decrease in the carrier concentration due to carrier diffusion within the active region. The last two terms govern the rate of spontaneous recombination (both radiative and non-radiative) and the rate of stimulated recombination respectively. On the other hand, the two terms on the left hand side of equation (6.2) take into the account the increase of the photon density due to stimulated and spontaneous emissions.

Carrier diffusion can play an important role depending on the waveguide structure, but it complicates the analysis. For the case of an index-guided stripe geometry laser, where the active region dimensions are small compared to the diffusion length of the carrier, the carrier density does not vary significantly in the region of maximum optical emission. Hence this term is ignored here and equation (6.1) re-written as;

$$\frac{dN'}{dt} = P - \frac{N'(t)}{\tau_s} - G(N')S \tag{6.4}$$

where N' is an effective carrier density which takes into account the effect of diffusion.

6.3. Chaos in Semiconductor lasers

In certain cases, the steady-state solution of rate equations (6.4) and (6.2) cannot be achieved due to the inability of the gain to react quickly enough to the perturbation in the optical field of the cavity. In this case, one deals with a dynamic problem whose solution has the form of self-sustained pulsations (SSP).

SSP is a major obstacle to the application of semiconductor lasers in ultra-high frequency applications and it is undesirable in optical communication systems and in OICs. The elimination of this phenomena must be achieved. However, it is now well established that the existence of SSP may represent one form of quite general complex dynamical behaviour related to the appearance of optical chaos in semiconductor lasers. Therefore, SSP has been used in the past for the investigation of the chaotic behaviour of laser systems [5-8].

Normally, SSP is not expected in the semiconductor laser due to the fast intraband relaxation rate. But SSP can be achieved by introducing some external effects, such as;

1. modulation of the pumping currents.
2. feedback of the output by an external cavity.
3. injection of external signals.

SSPs in semiconductor lasers have already been demonstrated, both theoretically and experimentally using the first two approaches [9,10]. SSP has not been achieved yet using the last approach but has been predicted by Otsuka *et al* [11]. In all three approaches, the essential requirement is the existence of two frequencies which characterise the nonlinear dynamics of the device. One of these frequencies is the intrinsic frequency of the system ω_o and the second is the external forcing frequency ω_i. The ratio between the two frequencies is defined as the winding number [12];

$$\rho_w = \frac{\omega_o}{\omega_i} \tag{6.5}$$

If the winding number takes a rational value p/q, where p and q are integers, the output pulsation frequency can lock to harmonics or subharmonics of the modulation frequency.

The above approach assumes only one degree of freedom, but in butt-coupled devices, the feedback of optical radiation and the injection of the external signal can be achieved simultaneously and this provides two degrees of freedom. In the

case of butt-coupled active devices, equation (6.5) is invalidated because of the involvement of more than two frequencies and this results in frustrated instabilities which will be discussed in the next section.

6.4- Frustrated instabilities

Although the existence of frustrated instabilities has been reported in references 2 and 3, it has, as yet, received very little attention from researchers. There has never been any reported work (theoretical or experimental) on frustrated instabilities in semiconductor-based laser systems. It is the purpose of this section to create a basic theoretical background which could be used for further investigations.

The phenomenon of frustration instabilities appears when two stable states of a system are possible. The existence of two frequencies result in the frustration of one or the other. These instabilities originate from the interaction of the carrier and photon densities and the dependence of the medium refractive index on the carrier concentration.

As this study is concerned with the investigation of butt-coupled active waveguide components, these instabilities can be better analysed using a coupled-cavity scheme, as shown in figure 6.1 rather than the monolithically integrated approach.

In figure 6.1, the two active cavities are coupled to each other through a passive cavity. Suppose cavity-1 acts as a lasing source and cavity-2 as a waveguide amplifier. The air gap between the two cavities forms a FP cavity. The inter-cavity coupling between cavity-1 and cavity-2 provides an optical loss and there is also a phase shift while the wave transverses the gap. The fields are related by the scattering matrix as [4,13];

$$\begin{pmatrix} E_1' \\ E_2' \end{pmatrix} = \begin{pmatrix} C_{11} & C_{12} \\ C_{21} & C_{22} \end{pmatrix} \begin{pmatrix} E_1 \\ E_2 \end{pmatrix} \tag{6.6}$$

or

$$E_1' = C_{11}E_1 + C_{12}E_2 \tag{6.7}$$

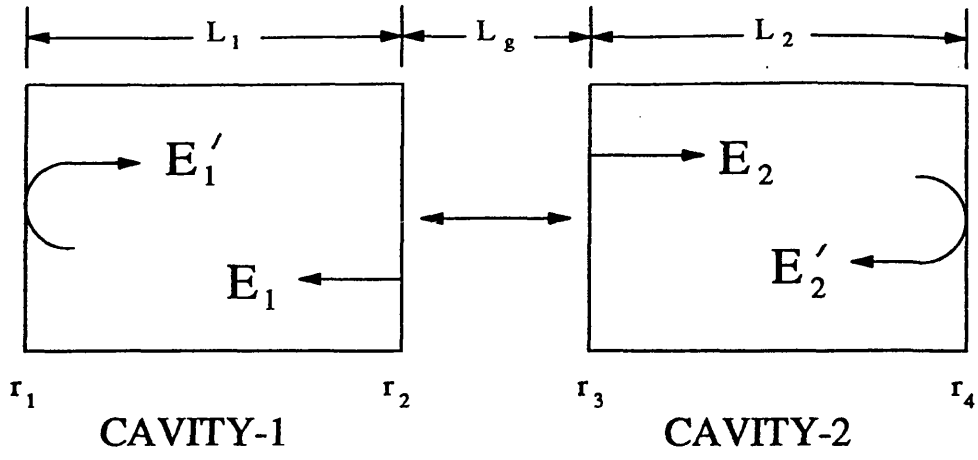

Figure 6.1. Diagram showing the coupled cavity scheme.

and

$$E_2' = C_{21}E_1 + C_{22}E_2 \tag{6.8}$$

where E_1', E_2', E_1 and E_2 are the electric field components. C_{11}, C_{12}, C_{21} and C_{22} are the complex scattering matrix elements and can be written as;

$$C_{11} = r_2 - \frac{r_3(1-r_2^2)t_g}{1-r_2r_3t_g} \tag{6.9}$$

$$C_{22} = r_3 - \frac{r_2(1-r_3^2)t_g}{1-r_2r_3t_g} \tag{6.10}$$

and

$$C_{12} = C_{21} = \frac{\sqrt{t_g(1-r_2^2)(1-r_3^2)}}{1-r_2r_3t_g} \tag{6.11}$$

where r_2 and r_3 are the amplitude reflection coefficients of the two facet forming the gap. t_g is the complex round-trip transmission coefficient and is defined as;

$$t_g = \exp(2\imath\beta_g L_g) \tag{6.12}$$

here β_g is the complex propagation constant in the gap and account for phase shift and losses in the gap. L_g is the gap length. The gap between r_2 and r_3 is physically replaced by an interface whose effective reflection coefficients are C_{12} and C_{21} from cavity-1 to cavity-2 or cavity-2 to cavity-1. The strength of mutual coupling can be defined as;

$$C = \sqrt{\frac{C_{12}C_{21}}{C_{11}C_{22}}}\left(\frac{1}{\exp i\theta}\right) \tag{6.13}$$

where θ is the external or coupling phase angle.

The same scheme can be applied to the two independent laser devices coupled to each other through optical lenses as shown in figure 6.2 by neglecting the reflection losses due to lenses, as they can be made to have very low reflection losses. In this case, coupling between the two devices and also the facet reflectance can be altered using A.R. coating on the laser or amplifier facets. By controlling the facet reflectance, the behaviour of the chaotic dynamics can be

Figure 6.2. The coupled cavity scheme applied to the two externally coupled devices.

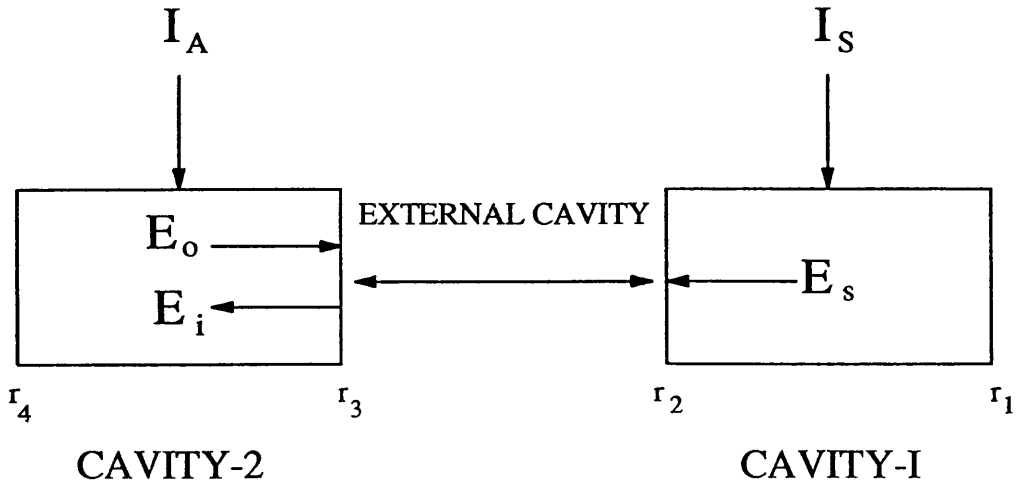

Figure 6.3. The schematic of the experimental set-up used for the investigation of monolithic integrated devices.

investigated more thoroughly and independently.

The system of figures 6.1 and 6.2 can be considered as an AWOA coupled with a lasing source through an external cavity and the AWOA is subjected to an external input and optical feedback, as shown in figure 6.3. Taking into account the fact that the reflected and external injected signal share the same gain medium, they are also subjected to the dispersion effects where phase detuning plays a major role. Therefore, the number of rate equations can be extended to include the phase detuning effects, and the system is governed by the following equations [11,14,15];

$$\frac{dN}{dt} = P - \frac{N}{\tau_s} - G(N)S \tag{6.14}$$

$$\frac{dE_o}{dt} = \left[G(N) - \frac{1}{\tau_p}\right]\frac{E_o}{2} + E_i \cos\theta \tag{6.15}$$

and

$$\frac{d\theta}{dt} = \omega_o - \omega i - \omega_o\left(\frac{E_i}{E_o}\right)\sin\theta \tag{6.16}$$

where $S \sqcup |E|^2$, ω_o is the intrinsic frequency of the gain medium, ω_i represents the injected frequencies which is the combination of external signals from the laser source and multiple-feedback frequencies. The dependence of G and ω_o on N is due to the fact that the active region refractive index changes with the variation in the carrier density as a result of interaction between N and S in the medium. The injected carrier density decreases with the injection of the external optical input while the refractive index increases accordingly. As a consequence, the gain in the medium decreases. The dependence of optical gain on the carrier density can be defined as;

$$G(N) = \frac{1}{N_{th}\tau_p} + \frac{\partial G}{\partial N}(N - N_{th}) \tag{6.17}$$

where N_{th} is the injected carrier density at threshold.

The injected carrier locking of external carrier modes and the AWOA cavity modes strongly depends on the detuning of the AWOA cavity and it is defined by the normalized detuning parameter, Δ, as [11];

$$\Delta = \left[\frac{N_{eff}}{n}\right][\omega_i - \omega_o(N_{th})]\tau_p \qquad (6.18)$$

where N_{eff} is the effective refractive index.

A stability diagram obtained by Otsuka *et al* [11] using equation (6.18) is shown in figure 6.20. This figure will be used to compare the experimental results with theory in section 6.6.

6.5. Experimental results

Chaotic dynamic behaviour in many different types of system is the subject of intense study due to its potential application in the better understanding of non-linear control systems. The additional feedback which takes place between the two butt-coupled active devices and the injection of the input signal can generate considerable amount of non-linearity in an optical system. This section is devoted to the experimental investigation of the non-linear response of the active wave-guide. At the start of this experimental investigation, the monolithic approach was attempted to characterise the non-linear dynamical response of the AWOA. But, the non-vertical etched facet geometry, the limited coupling of external signals and the net loss in all segments (since none of the segments was lasing) prevented any significant non-linear effects from being achieved.

As no evidence of non-linearity was seen in the monolithic device, the main efforts were devoted to the hybrid approach to investigate the chaotic dynamics in the AWOA. In this section, the details of the experimental work carried out for the hybrid case is provided.

6.5.1. Effect of external signals

The experimental set-up for the investigation of the chaotic dynamics in the hybrid approach is shown in figure 6.4. UB238 and UB262 were used as the source laser and the AWOA respectively. The source laser and the active waveguide optical amplifier were aligned using the alignment technique described in section 4.7.2.1 and the maximum gain was achieved by tuning the amplifier resonance frequency as outlined in section 5.3.2.1. Once the maximum gain had been achieved, the I-L characteristics were measured with: (a). no external input and (b). with external input at different levels of the source laser biasing currents. These results are presented in figure 6.5. It can be seen from figure 6.5 that the presence of the extra external facet and additional optical input from the source laser reduces the value of the lasing threshold of the FP AWOA but it also introduces a kink [16]. Further increase in the external input power increases the dip of kink. As the external input is increased further, a second kink appears. These results indicate that the coupling of the external input can introduce nonlinear effects in the laser device. The injection of the external signals also cause an increase in the effective value of the active region refractive index and this can, therefore, provide the initial detuning (equation 6.18) which is necessary to generate the chaotic dynamics.

Because the FP AWOA is very sensitive to temperature variations, the temperature dependence of instabilities in I-L characteristics were also examined by measuring the I-L characteristics of the AWOA at fixed values of the external input power (the value of the external optical input which causes the maximum non-linearity in figure 6.5 (curve 'd')). Figure 6.6 shows the effect of temperature on the non-linearity of output. As the temperature increases, the lower kink starts to shift and the upper kink starts to disappear.

Hence, the optimum temperature and the maximum instability regions due to

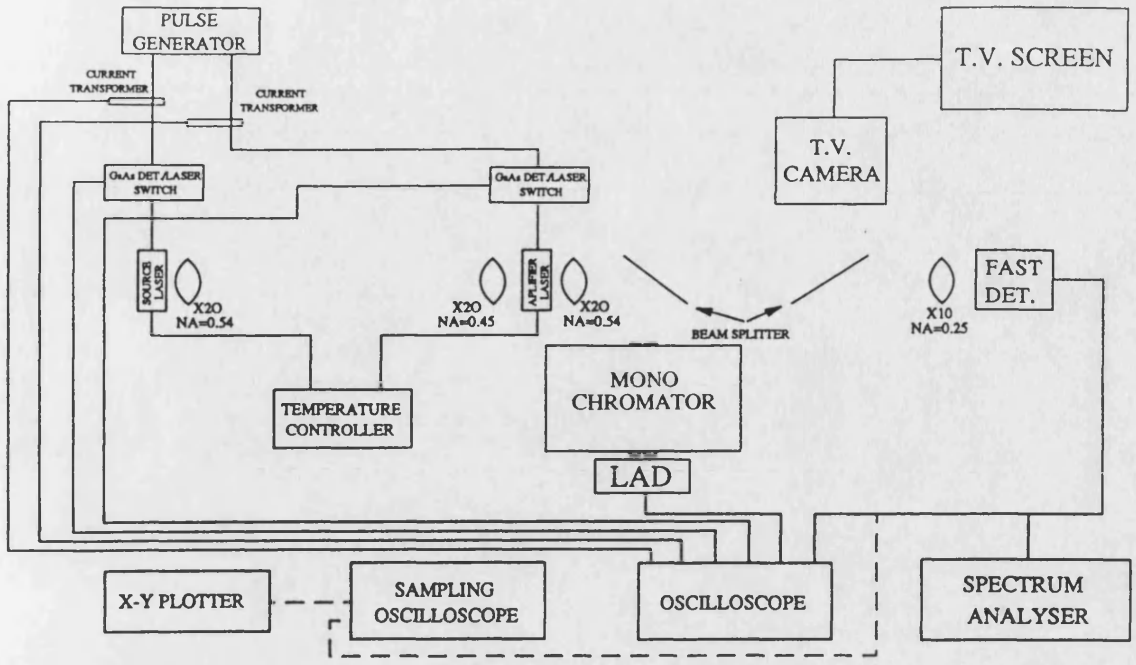

Figure 6.4. The schematical representation of the experimental set-up for the hybrid approach.

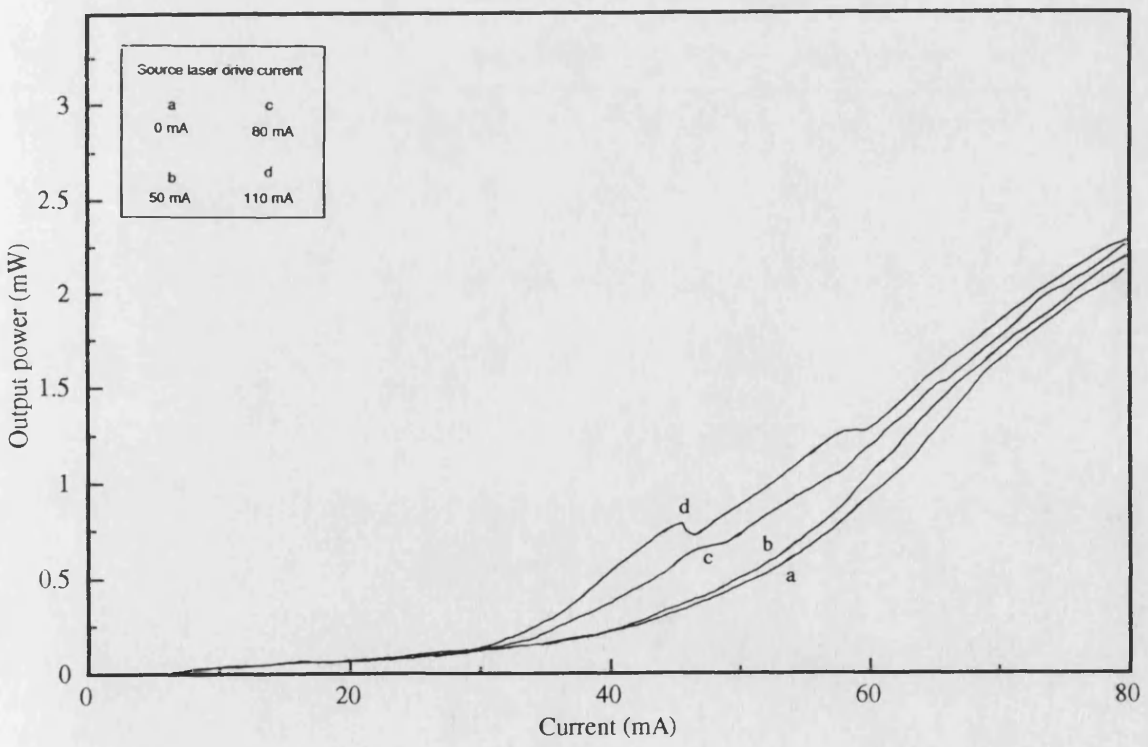

Figure 6.5. The effect of externally injected signals on the I-L characteristic of the AWOA in hybrid mode as a function of the source laser current.

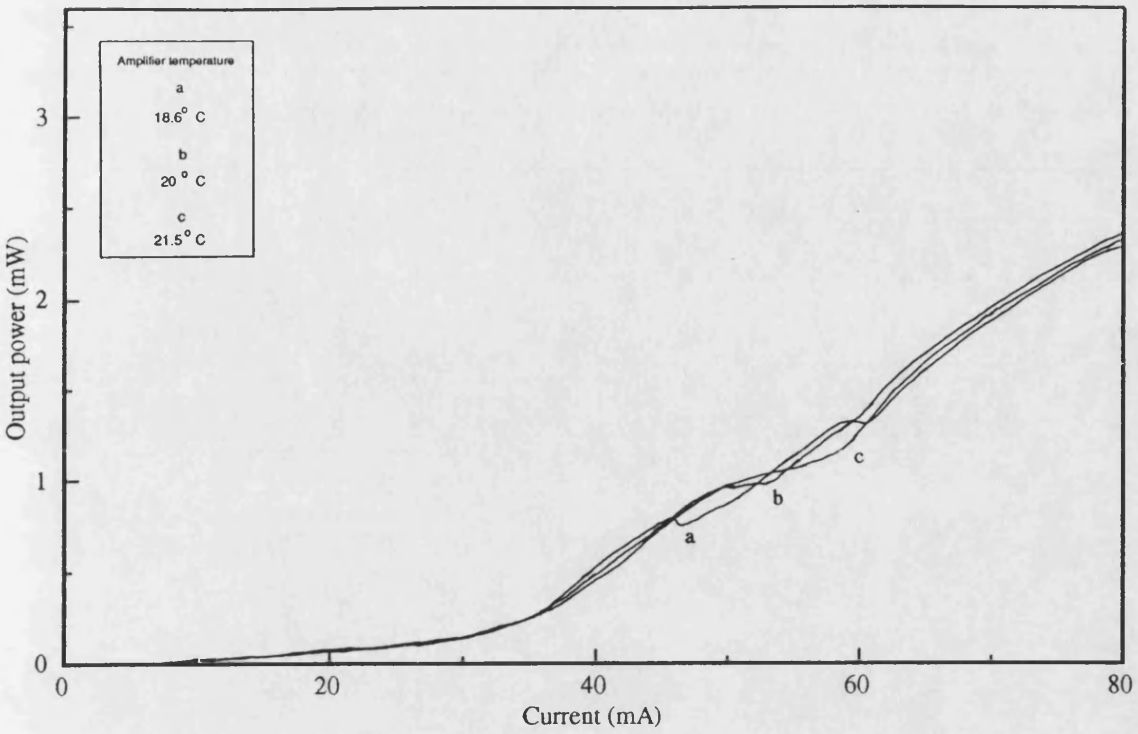

Figure 6.6. The effect of temperature rise on nonlinear I-L characteristics caused by the injection of external signals.

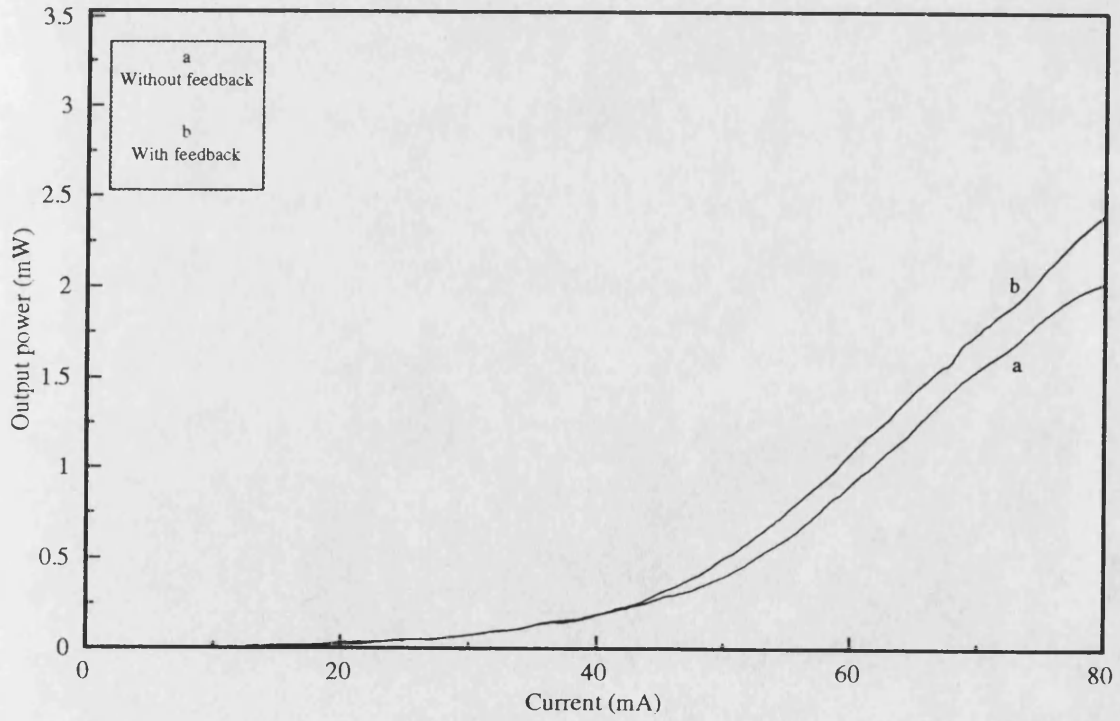

Figure 6.7. The effect of multiple-feedback on the AWOA (UB262) I-L characteristics.

external input can be identified from figures 6.5 and 6.6 and in future only that part will be considered as potentially suitable to obtaining chaotic dynamics of the device structure.

6.5.2. Effect of feedback

For the observation of feedback effects on the device characteristics, the experimental set-up of figure 6.4 was used. No bias to the source laser was applied. Maximum alignment was achieved using the source laser as a detector, as before. A manual shutter was inserted between the two laser devices. The amplifier laser (UB262) bias current was increased slowly well above the threshold value. The optical path between the two lasers was occasionally blocked. The effect of feedback was monitored by looking at the difference in the output of the detector when the optical path was blocked and when it was open. The difference between the two outputs was observed to be very small. The maximum feedback was achieved by manipulating the position of the AWOA. The I-L characteristics of the AWOA were measured in the absence and presence of optical feedback at that alignment. The results are plotted in figure 6.7. The alignment of the GaAs detector was again checked and found to be different than the previous value (when the two devices were aligned properly and the maximum alignment was achieved).

The effect of achieving maximum feedback on the maximum alignment was investigated by measuring the input to the source laser. For this purpose, a beam splitter was inserted between the source laser and the AWOA and the input to the source laser was measured using a large area detector (LAD) as shown schematically in figure 6.8. The output from the source laser, while used as an waveguide detector, and the LAD was continuously monitored. Figure 6.9 shows the output of the GaAs detector (using the source laser) against the output of LAD when both devices were properly aligned (maximum alignment) and when there was maximum feedback.

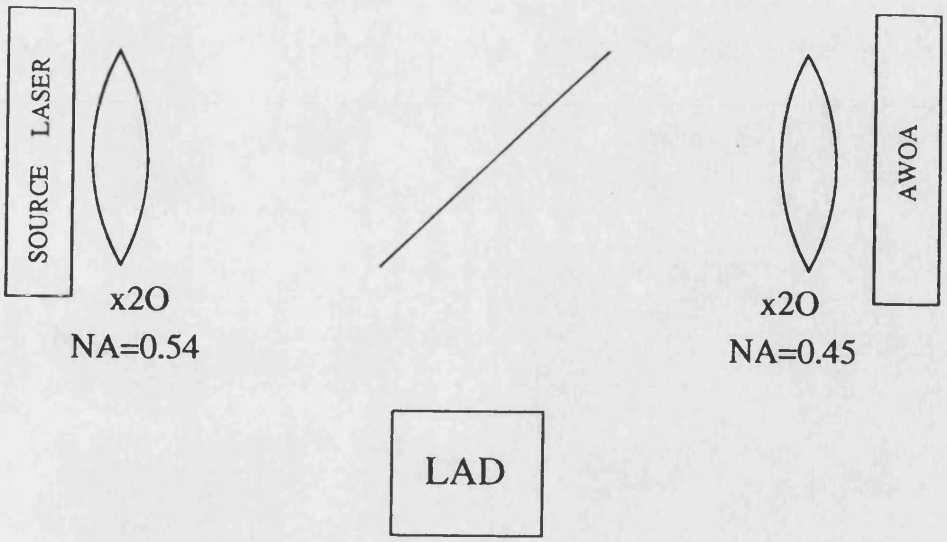

Figure 6.8. Schematic diagram showing arrangement used to measure the input optical power to the GaAs active waveguide optical detector.

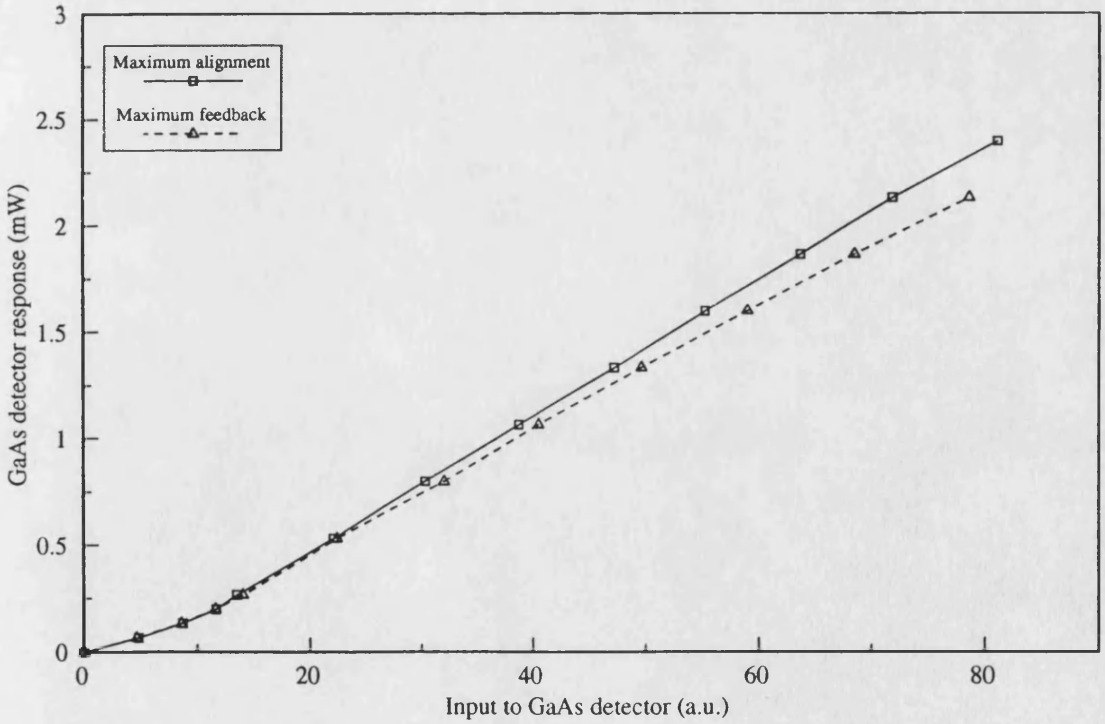

Figure 6.9. The effect of maximum feedback on alignment.

It can be seen from figure 6.9, that the output of the GaAs detector is lower when the feedback is at a maximum. Strictly speaking, the alignment should have not been changed but this happened probably due to a very slight tilt in one or both device mountings. Even though a reduction in the output of the GaAs detector has occurred at the maximum value of feedback, it does not affect the coupling efficiency significantly and the external input is still sufficient to cause instabilities. This can be seen in figure 6.10, where the I-L characteristics were measured at the maximum alignment and at the maximum feedback while the source laser biasing current was kept constant at a value where maximum non-linearity was achieved in figure 6.5.

6.5.3. Achievement of self-sustained pulsation

The experimental set-up of figure 6.4 was used here. Different laser devices (FP and A.R. coated devices) were used to achieve the self-sustained pulsation (SSP) in the active waveguide optical amplifier.

6.5.3.1. Achievement of SSP using FP amplifier

Once the alignment with maximum feedback (the alignment which gives maximum coupling of external input signal from source laser and feedback signals) had been achieved, the next step was to obtain self-sustained pulsation in order to look at the chaotic dynamics of the system. Initially, SSP were attempted by tuning the AWOA resonance frequency by changing the temperature of the AWOA at constant AWOA and source laser biasing currents. Unfortunately this technique did not work.

The source laser biasing current was then varied to obtain an initial detuning while the AWOA drive current was kept constant at the value where kink in the I-L characteristic was observed, while maintaining a constant temperature of both devices. Detuning was further increased by deliberately tilting the AWOA by changing its position. This method worked and a train of pulsations was observed,

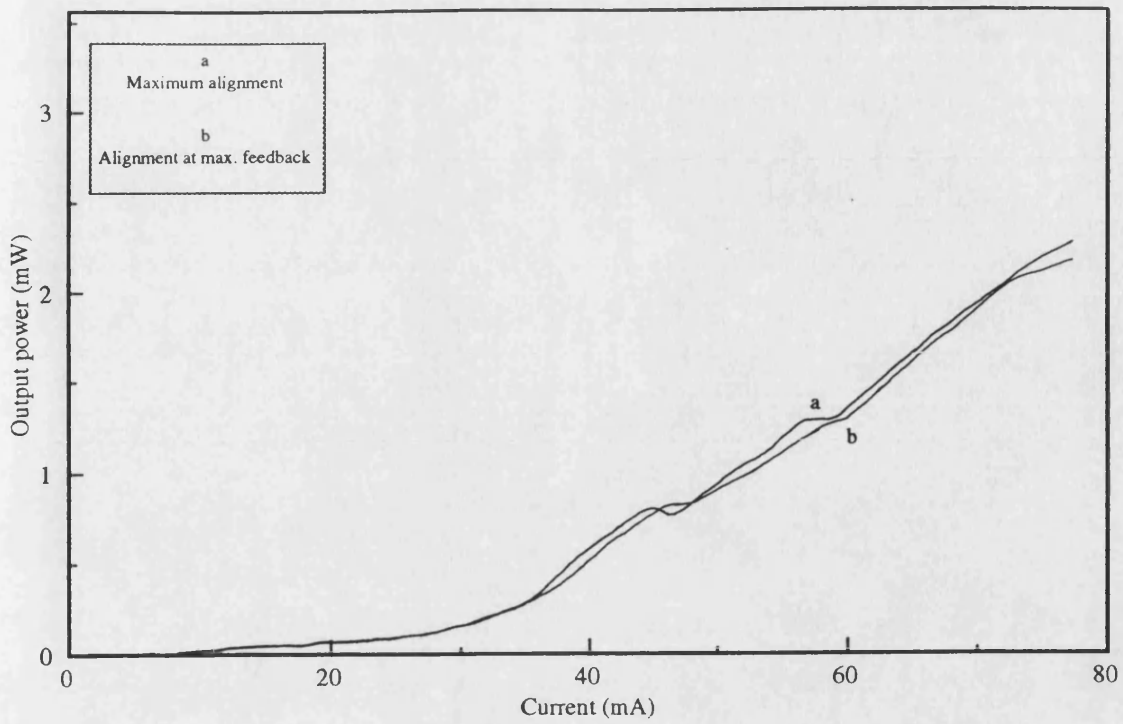

Figure 6.10. The nonlinear response of the active waveguide optical amplifier as a function of alignment.

although the amplitude of the train of SSP was small as shown in figure 6.11(a), taken from oscilloscope. At a high level of AWOA biasing current, the train of pulsations of figure 6.11(a) was broken into more frequent pulsations, which was more chaotic at the end of the signal pulse, as shown in figure 6.11(b). This train of SSP was found to be very sensitive to any change in the position of the AWOA and the source laser bias and disappeared with a slight increase in the external input after showing signs of chaos.

By continuous manipulation of the source and AWOA biasing current, the position of the AWOA and the temperature of the AWOA, a clear train of self-sustained pulsations was observed (figure 6.11(c)). This train of SSP was obtained at the higher value of external input than that of figure 6.11(a) and was not very sensitive to the external input but was still sensitive to the position of AWOA (since it was affecting the coupling of external signals and hence the feed-back signal). An increase in the external input forces these pulsation to take the shape of chaos and then to disappear. With an increase in the AWOA bias level, the train of pulsations changed its shape to more frequent pulsations of figure 6.11(d) as observed before. This train of pulsations was different to that of figure 6.11(b) however in the sense that this train of pulsations was not very sensitive to the external optical input and it had a larger amplitude.

The effect of this new position of the AWOA on the coupling efficiency was checked by measuring the output of the GaAs detector as before and the result is plotted in figure 6.12 along with the results of figure 6.9. A very small difference can be seen between the two alignments (the alignment at SSP and the alignment at maximum feedback). For future reference, this alignment is named as 'optimum alignment'.

The train of pulsation in figure 6.11(a) represents one group of SSP and the train of pulsation in figure 6.11(c) represents second group of SSP. These two types of pulsation will be referred as type-1 and type-2 pulsations.

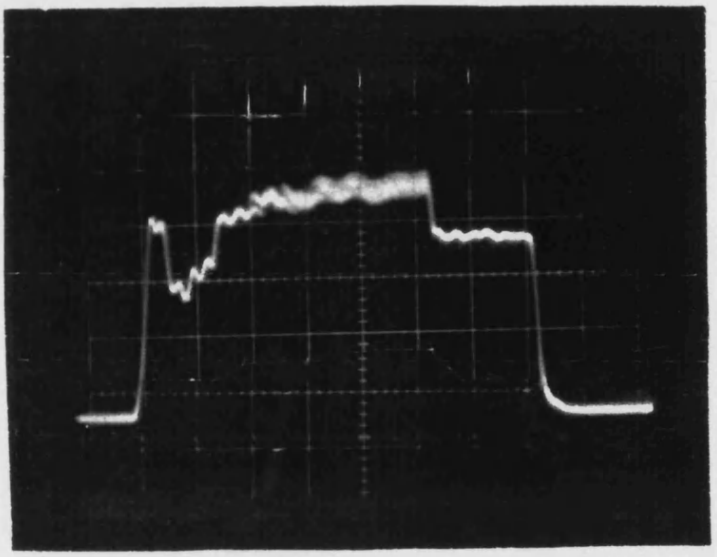

I_S=59.5 mA, I_A=65 mA

(a)

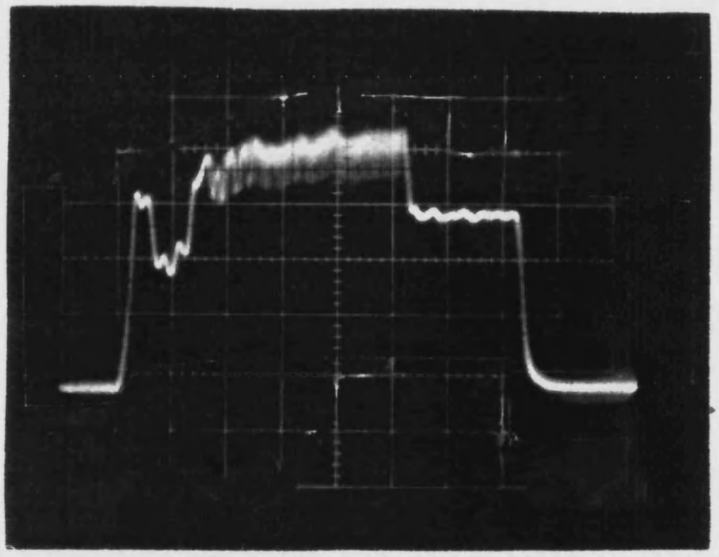

I_S=59.5 mA, I_A=110 mA

(b)

Figure 6.11 (continue).

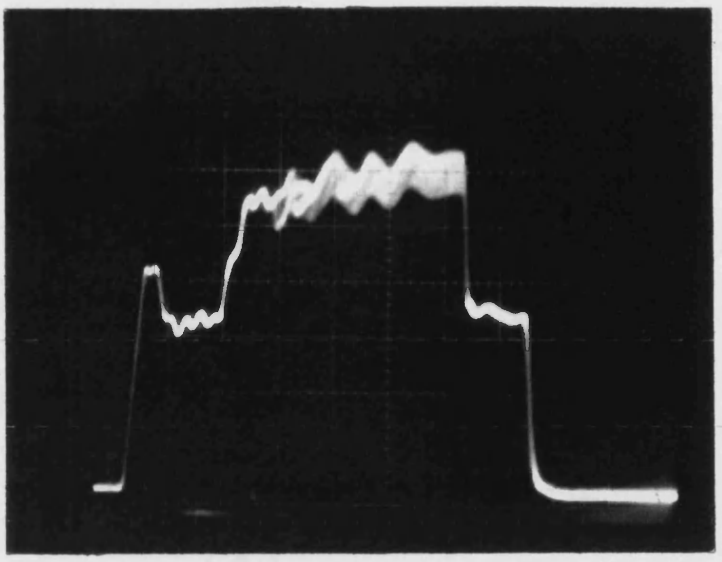

I_S=80 mA, I_A= 65 mA

(c)

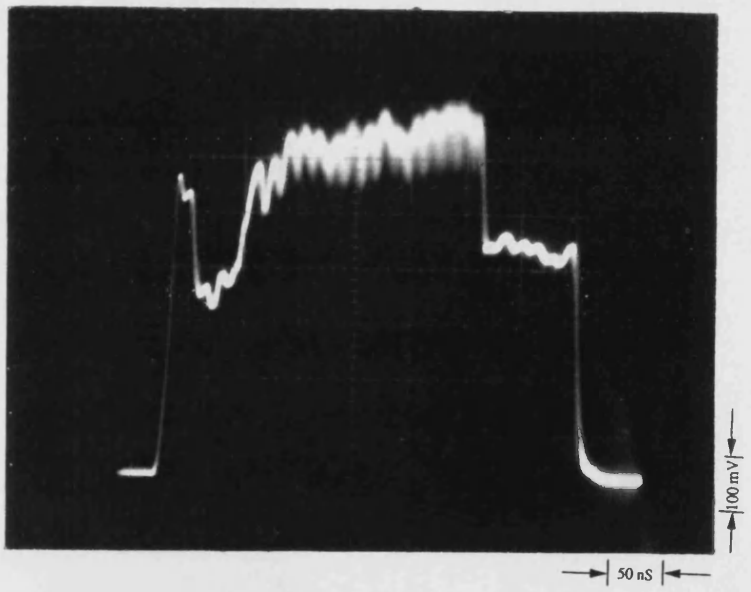

I_S=80 mA, I_A=110 mA

(d)

Figure 6.11. The observation of the type-1 and the type-2 SSP in UB262; (a) & (b) type-1 and (c) & (d) type-2 pulsations.

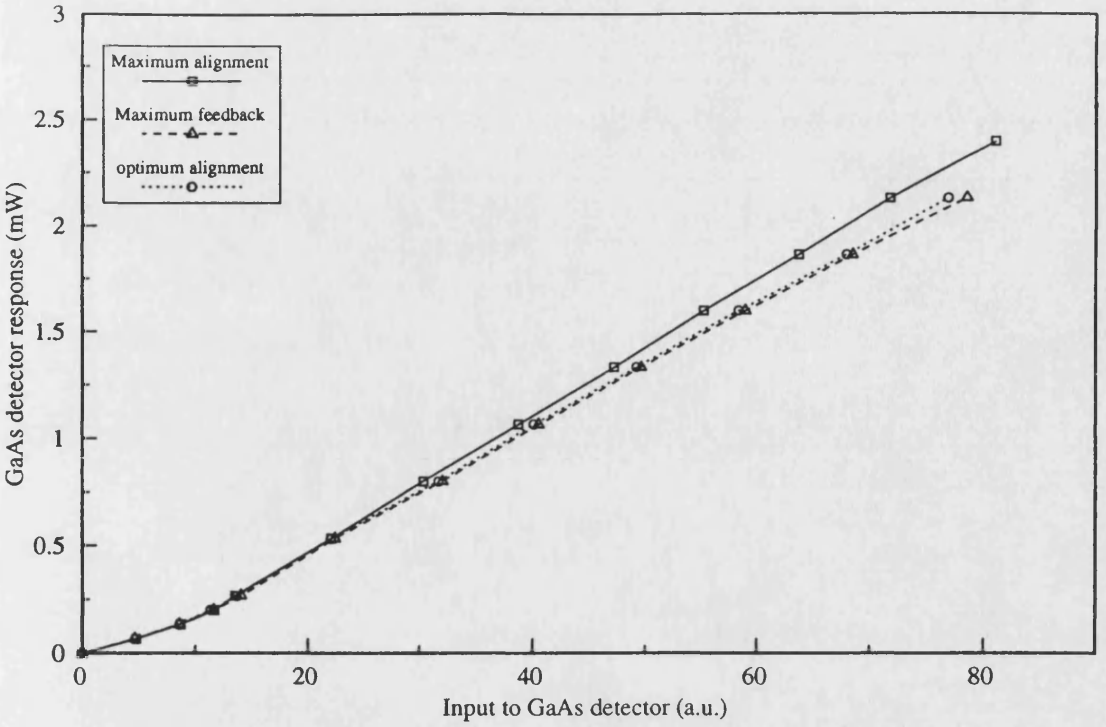

Figure 6.12. The effect of 'optimum alignment' on the coupling of input radiation.

6.5.3.2. Achievement of SSP using A.R. coated amplifiers

After achieving SSP in UB262, it was replaced by UB259 (double-side coated device). The same procedure as the last section was repeated to achieve SSP in this device. Both types of SSP were observed for this device and are shown in figures 6.13(a) and 6.13(b). The type-1 pulsation was more visible unlike in UB262 and the amplitudes of type-1 pulsation and type-2 pulsation were nearly equal due to the higher single pass gain of the device in the forward and backward directions. Here, the existence of the type-1 pulsation was more critical to the external input and the position of the AWOA than the type-2 pulsation. Both types of SSP were observed to disappear in a manner similar to UB262. In this device, the comb type pulsation was not observed but the appearance of subharmonics in figures 6.13(a) and 6.13(b) are quite clear.

Later, UB259 was replaced with UB258 (single side coated device) in such a way that the coated side was facing the source laser to act as the gain medium for the external cavity modes in order to have more influence on the feedback signal and the external optical input on the AWOA characteristics as chaos in the external cavity laser can be achieved relatively easily. Similar experimental procedure was repeated to obtain SSP in UB258 as was in previous cases. Here also, the two types of SSP were observed in a similar manner to the above and results are shown in figures 6.14(a) and 6.14(b). The type-1 pulsation was similar to that obtained for UB262, but the type-2 pulsation obtained here, was different from that obtained in UB262 and UB259 because the appearance of subharmonics is not visible in figure 6.14(b). The type-2 pulsation was more periodic, frequent and exhibited a higher amplitude. This difference can be attributed to single side coating. The type-1 SSP disappeared in a similar way as reported before. The type-2 pulsation was observed to disappear through subharmonics (which takes the shape of chaotic pulsations).

It can be seen in figures 6.11, 6.13 and 6.14 that the type-1 and the type-2 pulsations are 180° out of phase to each other. The type-1 pulsation rise very

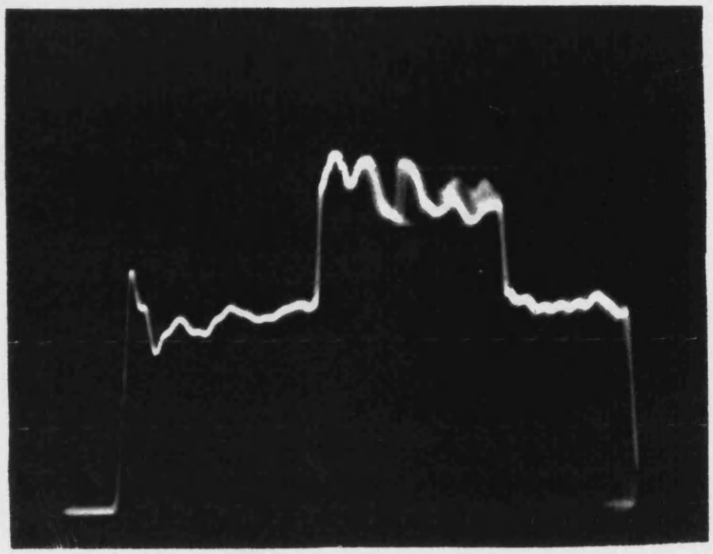

I_S=74 mA, I_A=70 mA

(a)

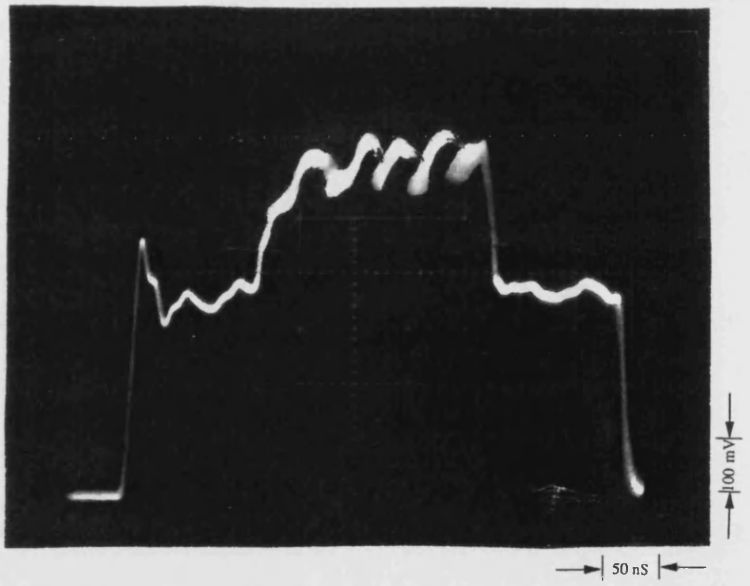

I_S=75.5 mA, I_A=72 mA

(b)

Figure 6.13. The observation of the type-1 and the type-2 SSP in UB259; (a) type-1 and (b) type-2 pulsations.

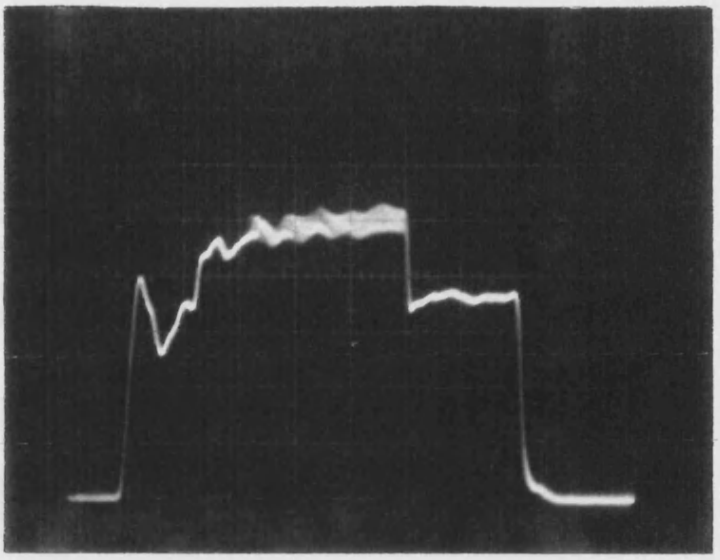

I_S=81 mA, I_A=82 mA

(a)

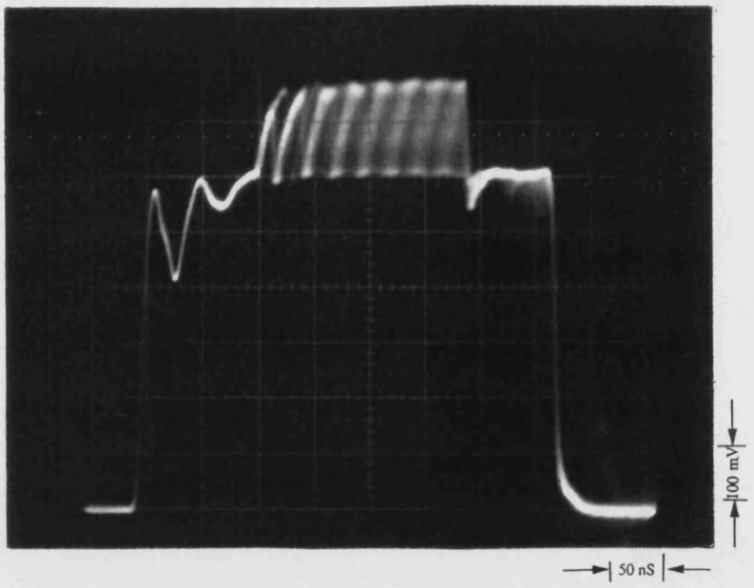

I_S=81 mA, I_A=85 mA

(b)

Figure 6.14. The observation of the type-1 and the type-2 SSP in UB258; (a) type-1 and (b) type-2 pulsations.

rapidly and decay slowly. But in the case of the type-2 pulsation, the process is reversed. The difference in pulsation process in type-1 and type-2 pulsation can be explained by analysing a single pulse out of the train of SSP as shown in figure 6.15. The inset diagram of figure 6.15 shows the main pulse. The AWOA is pre-biased and it is subjected to incoming external signals which are tuned to the resonance frequency of the amplifying medium (AWOA) and a steady-state output is achieved at constant input and AWOA biasing current (point A). The AWOA is also subjected to multiple-feedback. As the AWOA bias current changes, the resonance conditions of the AWOA also change. At a certain level, the feedback signals also satisfy the cavity resonance condition at point A in figure 6.15 (two stable solutions). At that point, the intensity of the feedback signals is small in comparison with the injected signals. As it travels along the cavity in the forward direction (z-direction), it experiences the gain along with the injected signals. This frustrates the amplification of the injected signals and reduces the photon density. As a consequence, the refractive index of the amplifying medium increases, which changes the phase relation between the intrinsic frequency of the amplifying medium, ω_o and the frequency of external injected signals, ω_1. This decreases the effectiveness of the interference between ω_o and ω_1 and increases the band edge losses. This phase mismatch is continuous as the gain of feedback signal increases and appears as the exponential decay of the pulse. At the end of the slope (point B), the pulse wavefront is at the emission end, where it is mostly transmitted to the outside world.

The flux travelling in the backward direction faces a reverse mechanism as it travels along the optical cavity. In this case, due to a rapid build-up of the carrier density (due to the reduction in the feedback signal intensity because of the emission of photons at the emission end), a rapid increase in photon density takes place (point C). The carrier density depletes due to a high optical flux density and the optical gain decreases as a result. In the mean time, the gain of feedback frequency components starts to build-up and which again frustrate the amplification of

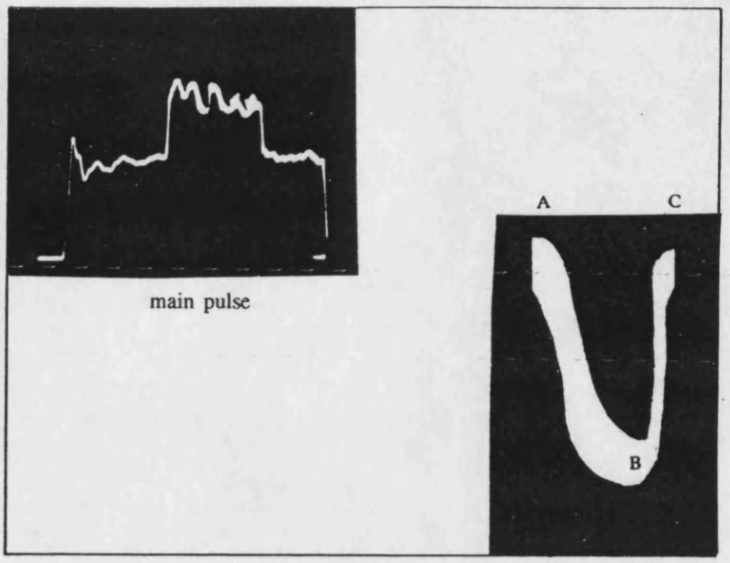

Figure 6.15. Forward and backward travelling fluxes in the AWOA butt-coupled to the external source. Inset is showing the main pulse.

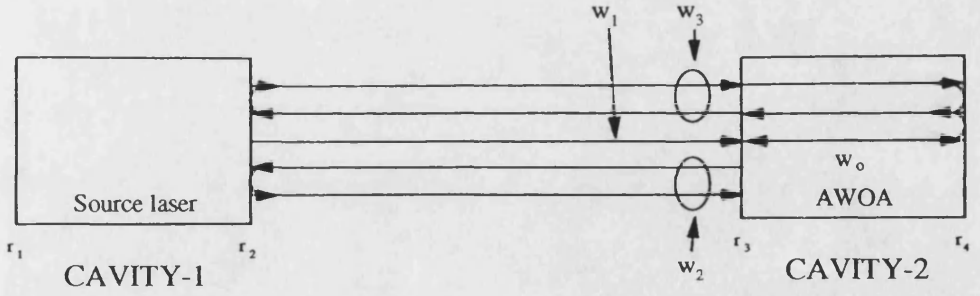

Figure 6.16. Figure showing schematically the existence of four frequencies.

externally injected signals. Once again the optical flux decays exponentially while it is travelling in the backward direction as explained above for the forward travelling flux.

6.5.4. Involvement of more than three frequencies

The above discussion suggests that the two types of SSP arise from different types of feedback mechanism. This indicates that there may be four frequencies involved, which contradicts reference-17 which assumes three frequencies are involved. However, only three frequency components are expected to interact to give rise to frustrated instabiliries at one time. This scenario is demonstrated in figure 6.16.

In figure 6.16, ω_o is the intrinsic frequency of the AWOA, ω_1 is the frequency of external signals from the source laser, ω_2 is the feedback frequency originated between r_2 and r_3 and ω_3 is the feedback frequency originating from multiple-feedback between r_2 and r_4.

At r_3, frequency components ω_2 which satisfy the cavity resonance is small (since the effect of external injected signals is higher than feedback signals, see figures 6.5 to 6.7). Therefore they experience less gain than the injected signals. As the beam of light travels along the amplifying cavity, the gain at ω_2 increases and results in the frustration of ω_1 (frequency components of externally injected signals which satisfy the resonance condition of the cavity).

At r_4, frequency component ω_3 has a relatively higher value as it has now passed through the AWOA cavity and the AWOA acts as the gain medium for these signals. In the active cavity of the AWOA, the backward travelling flux experiences a rapid build-up of carrier density, and hence photon density. However, the backward travelling flux also experiences a higher gain for the feedback frequency components. Therefore, the frustration of ω_1 would naturally be higher as the value of ω_3 is expected to be higher, depleting the carrier density in the active layer.

From the above discussion, and by comparing figure 6.15 and figures 6.11, 6.13 and 6.14, it can be deduced that the type-1 pulsation is more likely to be the result of the frequency component ω_2 and the type-2 pulsation is probably due to the frequency component ω_3. This argument can be further supported by figure 6.14, where the amplitude of the type-2 pulsations is higher than the type-1 pulsation because the single pass gain is higher in the backward direction than the forward direction in UB258 (figure 5.21) due to the higher output facet reflectance than the input facet reflectance. A similar sort of effect can be seen in figure 6.11 for UB262 which has a high output facet reflectance. However, in UB259, type-1 pulsation also has higher amplitude. This can be explained as follow: due to the low input facet reflectance, the coupling of external signals (injected and feedback) is high. Also, due to the low output facet reflectances, this device exhibits the higher single pass gain (figures 5.5 and 5.22). This leads to the higher frustration of the frequency components ω_1 travelling in the forward direction because the relatively stronger feedback frequency components ω_2 also experience a higher gain and appears as higher amplitude type-1 pulsation (figure 6.13(a)). The backward travelling flux in UB259 follows a pattern similar to the other devices (as explained before) and appears also as a higher amplitude type-2 pulsation (figure 6.13(b)).

6.5.5. Routes to chaos

The periodic waveforms observed in the domain between stable and erratic (or chaotic) behaviour is referred to as route to chaos. In section 6.5.3, two types of periodic pulsation have been demonstrated. In all devices (with the exception of figure 6.14(b)), subharmonics are shown to exist, especially in UB262 which gives the hint that the route to chaos could be through subharmonics, the only route to chaos so far observed in semiconductor lasers [10,16]. In figure 6.14(b), the existence of subharmonics is not seen but this pulsation was still leading to chaos. This indicates that there could be another route to chaos in the active waveguide optical

amplifier as Otsuka *et al* [11] has demonstrated for the case of detuned solid state amplifiers. This is the period-doubling route to chaos.

In this section, the subharmonic route to chaos and the period doubling route to chaos are demonstrated for the first time in the semiconductor optical amplifier.

6.5.5.1. Subharmonics route to chaos

The same experimental set-up of figure 6.4 was used for the investigation of the subharmonic route to chaos. UB238 was used as the source laser and UB262 was used as the active waveguide optical amplifier. The output of the fast detector was fed to a spectrum analyser and a real time oscilloscope simultaneously. Typical results obtained from the oscilloscope and spectrum analyser are presented in the left and right column of figure 6.17. The output of the monochrometer was monitored as well and occasionally presented in the left column along with the output of fast detector on the same time scale to show any unusual effect. In this case, the upper trace (in the left column) corresponds to the response of the fast detector and the bottom trace (in the left column) corresponds to the output of the monochrometer.

First of all, the type-2 pulsation was obtained because of their higher amplitude and stability than type-1 pulsations. Once the stable train of SSP was achieved at 80mA and 65mA of the source laser and the AWOA biasing currents respectively, the source laser drive current was kept constant and the amplifier drive current was reduced to 55mA (where the train of SSP completely disappeared, as shown in figure 6.17(a)). At this instance, the output of the spectrum analyser shows three clear noise peaks which correspond to the intensity of the beat noise notes between the external cavity modes separated by;

$$f_{ext} = \frac{c}{2L_{ext}} \tag{6.19}$$

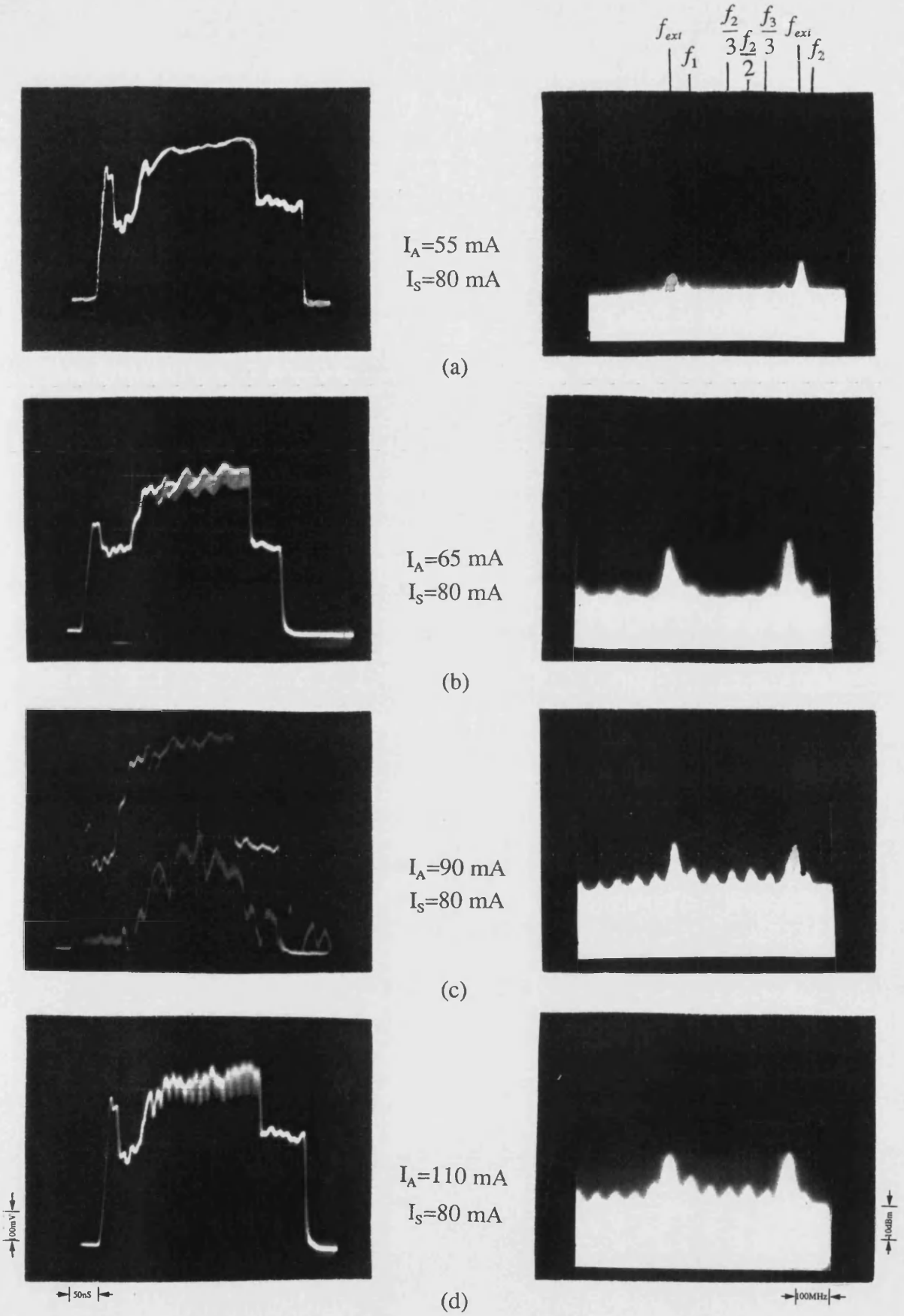

Figure 6.17. Observed subharmonics route to chaos in a AWOA. Left column: fast detector response (upper trace) and output from the monochrometer (lower trace) on time scale. Right column: power spectrum.

where L_{ext} is the length of the external cavity and here it was 39cm. For L_{ext}=39cm, f_{ext} is calculated as 385MHz.

Figure 6.17(b) shows the result at 65mA of the AWOA drive current. As can be seen from figure 6.17(b) (right column), subharmonics start to appear. In all cases, the relationship;

$$f_n = f_1 + (n-1)f_{ext} \tag{6.20}$$

holds. Here n=1,2,3.

As the AWOA biasing increases to 90mA, the appearance of subharmonics becomes clearer, as figure 6.17(c) (right column) shows. Successive subharmonic oscillation up to the third subharmonic of the fundamental oscillations has been observed in the power spectra. The observed power spectra corresponds to f_n/m (where m and n=1,2,3), as shown in figure 6.17. Successive subharmonics appearing at frequency f_n/m are the indication of real oscillations, not noise because the appearance of noise would always be random and the route to chaos is through periodical oscillation [18]. The fast detector output on the oscilloscope appears to take a chaotic shape and is also dominated by subharmonics. Also the output of the monochrometer is shown in figure 6.17(c) and this shows two peaks. This could be due to the coexistence of the two waves of different wavelengths and both of them satisfy the cavity resonance as indicated in reference-19.

At 110mA of the AWOA current, the output of the fast detector on the oscilloscope is changed to one or more frequent pulsations. Figure 6.17(d) shows the result at that particular level of biasing. The frequent pulsation is probably due to the generation of subharmonics as shown in the right column of figure 6.17 where each sub-peak corresponds to the sub-harmonic of particular frequency components (i.e. f_1, f_2,f_3). In the type-2 pulsation, this train of pulsations did not disappear and this has kept the system in region-III of figure 6.20. But for the case of the type-1 pulsation, the frequent train of pulsations disappeared after becoming chaotic in nature (figure 6.11(b)). This suggests that a route to chaos does exist through the subharmonic route in the semiconductor amplifier.

6.5.5.2. Period doubling route to chaos

The period doubling route to chaos was investigated by using the experimental set-up of figure 6.4 and the same experimental procedure of section 6.5.5.1 has been used here. But UB258 was used as the AWOA while UB238 as the source laser because UB258 did not show the existence of subharmonic in figure 6.14(b).

After achieving SSP, the bias current to the AWOA was kept constant at 109mA. The source laser biasing current was reduced to 67mA (corresponding to the no pulsation value) from 80mA (the value for stable pulsations). Figure 6.18(a) shows the results. The source laser current was increased slowly and at 74mA multiple peaks were observed on the monochrometer output, and is shown in left column of figure 6.18(b) (lower trace). This is probably due to coherent collapse of the input radiation and indicates the presence of multiple wavelength oscillations which satisfy the AWOA cavity resonance conditions at the same time. The corresponding output from the fast detector shows an unstable train of pulses with subharmonics (figure 6.18(b), right column, upper trace). On the other hand, the spectrum analyser output shows the two intensity beat noise peaks of the external cavity separated from each other by f_{ext}, as shown in figure 6.18(b). Many small peaks between the main peaks can be seen, and they correspond to different subharmonics. These peaks can be seen more often at 80mA of the source laser biasing current in figure 6.18(c) (right column) but two more main peaks embedded in the subharmonics appear halfway between the beat noise peaks. The output of fast detector on the oscilloscope shows a periodic pulsation and the output of the monochrometer is slightly noisy but generally smooth.

At a slightly higher value of the source laser biasing (85mA), the output of the fast detector on time scale shows the increase in pulsating frequency as shown in figure 6.18(d) (left column). It can be seen that at the end of the train of pulsation, the periodic pulsation becomes chaotic. The output of the monochrometer is not shown because it did not change from its previous position except that it was

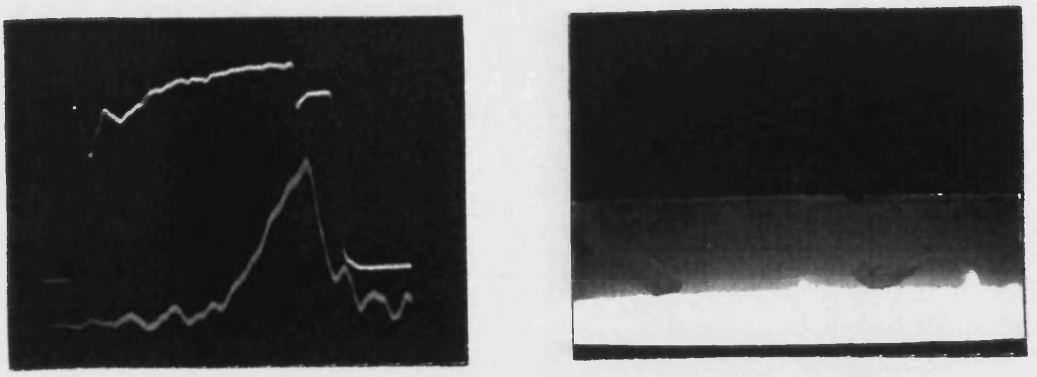

I_S=67 mA, I_A=109 mA

(a)

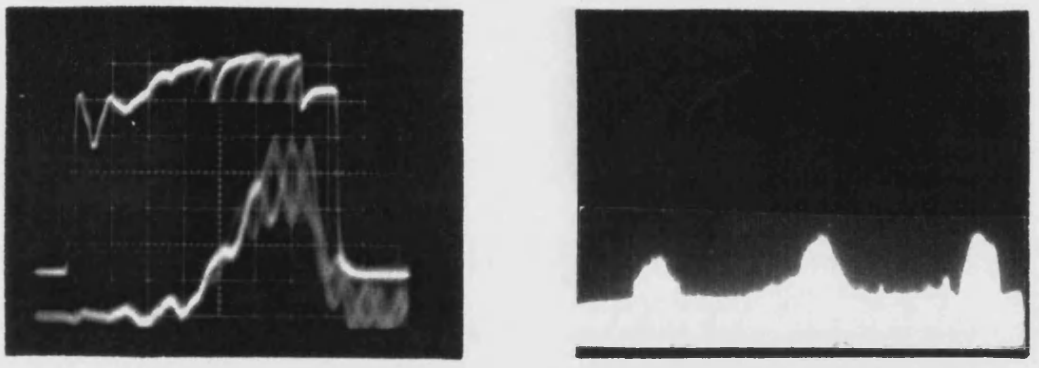

I_S=74 mA, I_A=109 mA

(b)

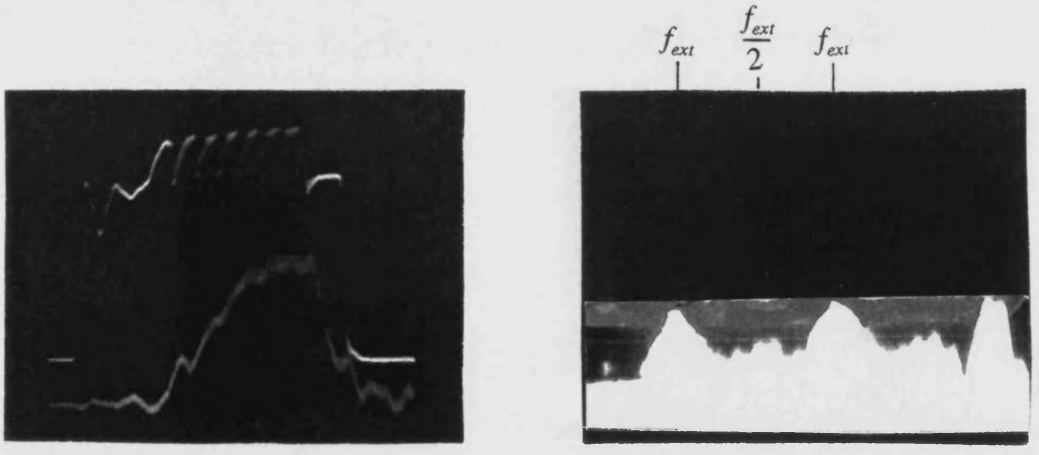

I_S=80 mA, I_A=109 mA

(c)

Figure 6.18 (continue).

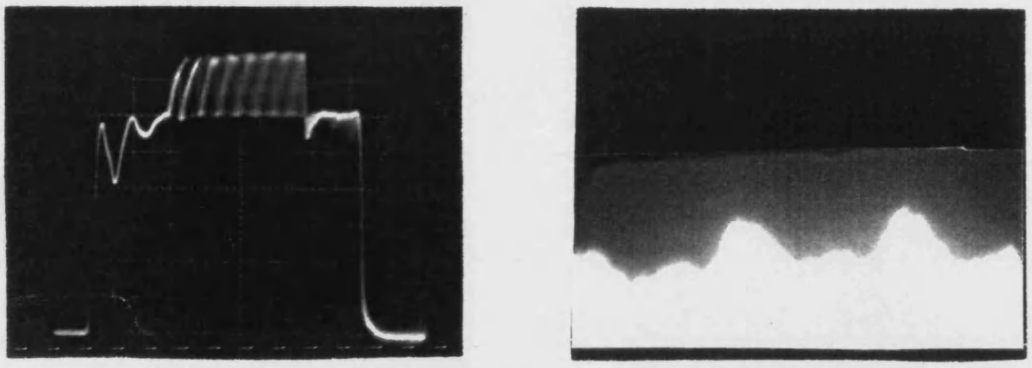

I_S=85 mA, I_A=109 mA

(d)

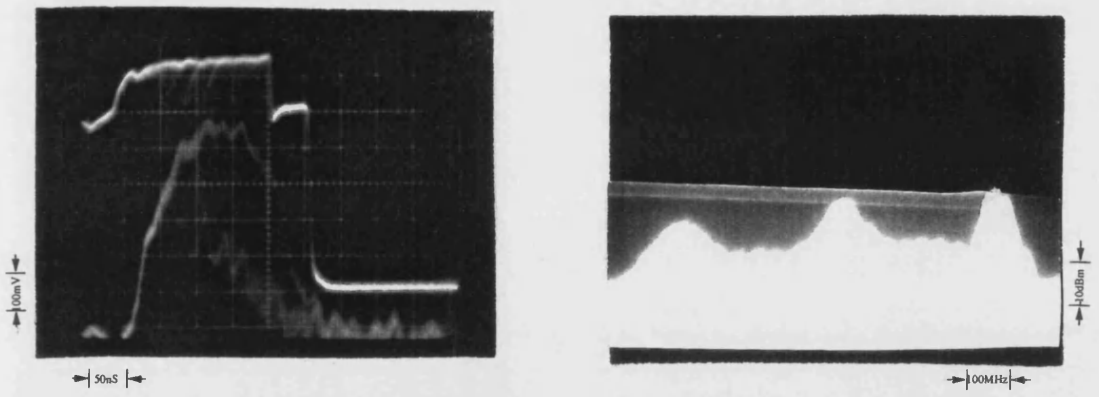

I_S=91 mA, I_A=109 mA

(e)

Figure 6.18. Observed period doubling route to chaos in a AWOA. Left column: fast detector response (upper trace) and output of the monochrometer (lower trace) on time scale. Right column: power spectrum.

shifted slightly towards the left due to a shift in the gain curve as a result of the increase in UB258's current. At the same time, the output of the spectrum analyser starts to become more chaotic. The half-frequency peaks start to disappear but the appearance of subharmonics do not change (figure 6.18(d), right column).

At 91mA, the train of pulsation almost vanishes and taken over by chaos as shown in upper trace (left column) of figure 6.18(e). The lower trace (left column) of figure 6.18(e) shows double waveforms due to the presence of more than one frequency satisfying the resonance frequency of the medium. A similar effect was seen in UB262 during the investigation of route to chaos through subharmonics.

At 100mA of source laser bias current, chaos completely disappears. Figure 6.18 shows the existence of period doubling [6,7,11] (as period $T_{ext}=1/f_{ext}$=2.597nS and at half frequency, time period $T_{ext}=2/f_{ext}$=5.195nS). The phenomena of period doubling can be explained as follows. As the external input increases, the refractive index increases accordingly and causes the asymmetrical scattering of injected stimulated signals into the modes with cavity resonance frequency (as the presence of more than one mode satisfying the cavity can be seen from figures 6.17(c), 6.18(b) and 6.18(e)). The strong external spectral mode suppresses the weak internal modes effectively on the shorter wavelength side than on the longer wavelength side. This gives the additional gain to modes at the lower frequency (higher wavelength) side [20].

This route to chaos looks to be more sensitive to the level of the external optical input. The half-frequency peaks are probably due to the injection of external signals. The presence of subharmonics along with frequency halving peaks is evidence of the coexistence of two routes to chaos in the semiconductor laser amplifier. They could also be due to turbulence, theoretically predicted in single side coated external cavity laser system [21]. These subharmonics are expected to be present as long as the effect of multiple-feedback persists.

It was observed that with an increase in the external optical input, SSP and chaos disappeared. This can be attributed to a change in the peak wavelength of

the lasing source with the injection of carriers. At a particular biasing current to the source laser, the output from the source laser satisfy the resonance conditions of the AWOA. Also the resonance of the AWOA can be tuned by changing the temperature of the AWOA. This means that SSP can be achieved at different combinations of the source and AWOA biasing currents and temperatures. However, during the experimental work reported in this chapter, after achieving the optimum cavity tuning (tuning which gives maximum signal gain), the temperature was kept constant.

6.5.6. Active waveguide response

The fast rise time of type-1 pulsations and the fast decay time of type-2 pulsations can be used to measure the response of the active waveguide. UB258 is found to be more suitable for measuring the active waveguide response because it gives clear periodic self-sustained response with high pulsating frequency and no subharmonic in figure 6.18(c). Therefore, UB258 was used to measure the response of the active waveguide. The experimental set-up of figure 6.4 was used but instead of using an ordinary oscilloscope, a high speed sample and hold oscilloscope with a 25ps Tektronix sampling head was used. After achieving a periodic train of SSP, the output of the fast detector was fed to the sampling and hold oscilloscope. The pulse response of the active waveguide was calculated by measuring the rise time of a pulse from the train of SSP as shown in figure 6.19(a) and was calculated to be around 450pS. In the first instant, it was thought that this slow response was due to the bandwidth limitation of the cable connecting the fast detector and the sampling oscilloscope. So the experiment was repeated using a 12GHz semiflexible cable to connect the fast detector with the sampling oscilloscope. But the same response of around 450pS was obtained. The response time of the active waveguide must be smaller than that measured here as theoretically demonstrated in reference-22. Therefore this slow response time is more likely to be due to the bandwidth limitation of the fast optical detector.

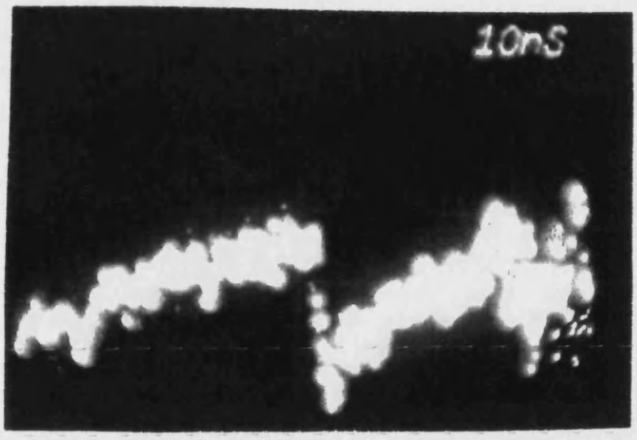

(a)

(b)

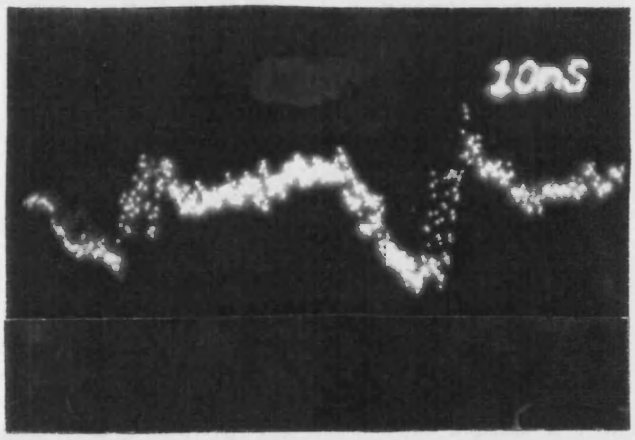

(c)

Figure 6.19. The active waveguide optical amplifier pulse response; (a) UB258, (b) UB259 and (c) UB262.

Similar experiments were repeated using UB259 and UB262 and results are shown in figures 6.19(b) and 6.19(c). Both figures give the same rise time and again support the argument that the slow response time of the active waveguide is due to the bandwidth limitation of the fast optical detector.

6.6. Comparison between experimental results and theory

As mentioned before, no theoretical or experimental work on frustrated instability has been reported so far, but there are a few theoretical models available which deal with this type of instability in the laser amplifier, and the model by Otsuka and Kawaguchi [11] is one of them. They have predicted and demonstrated instabilities in an $LiNdP_4O_{12}$ optical amplifier subjected to only external input signals. They divided their operating characteristics into four regions, depending on the detuning of a system, as;

1. a bistable region with hysteresis
2. a stable lock-in region without bistability and instabilities
3. a dynamically unstable region having pulsating solution
4. a self modulating stable region outside the lock-in range.

Figure 6.20 shows the stability diagram showing all four regions obtained by using equation (6.18) [11]. This diagram can be used to explain some of the experimental results presented in this chapter.

Unfortunately, bistability could not be achieved during the experimental work probably due to the two main reasons;

a. No optical isolator was used between the two laser devices because we were mainly concerned with the investigation of the frustrated instability in butt-coupled integrated components. As a consequence, feedback effects could not be avoided and are not desirable for achieving bistability [23].

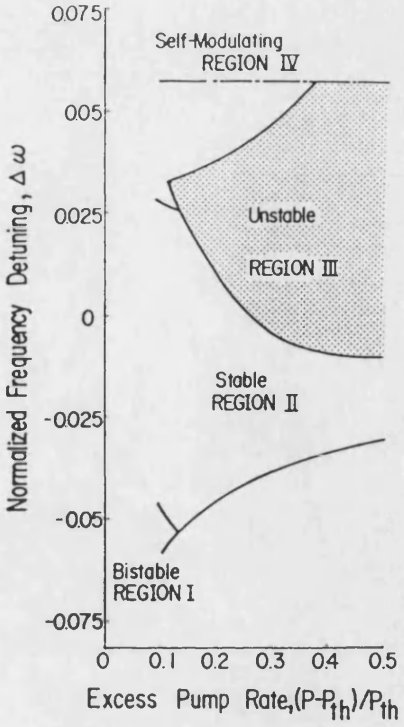

Figure 6.20. The stability diagram of an injection laser amplifier [11].

b. Here a multimode laser source was used whose peak emission wavelength was a function of temperature and drive current. For the observation of bistability, a single wavelength tuneable laser source is required to satisfy the resonance conditions of a single wavelength [23].

Stable region II was more frequently found because the SSP was very sensitive to the position of the AWOA and the source laser drive current. The sensitivity of the system can be justified by looking at figure 6.20 where the appearance of SSPs depends upon the amount of detuning. Detuning is a function of the refractive index and the refractive index depends upon the carrier concentration and temperature. The initial detuning can be achieved at a particular wavelength by changing the resonance of the FP cavity (by changing the temperature). During the experimental work, the temperatures of both the source laser and the AWOA were kept constant, once the SSP was achieved. Therefore, detuning depends on the position of AWOA and the external input.

In this chapter, SSP has been demonstrated quite clearly and this represents region III. In section 6.5.6.2, SSP was found to be a function of the external input power. Because at a constant local pumping rate, any increase in the external input would increase the refractive index of the medium due to the reduction in the carrier density in the active layer, this would in fact, increase the detuning of the system. Therefore, the system would enter into region III. A similar phenomenon was observed during the experimental work and was used to investigate the period doubling route to chaos.

According to figure 6.20, if the local pumping rate is high, then the system can jump to region III from region II quickly because with the increase in the pumping rate of the AWOA, the stable lock-in region become narrower. This was not always the case in the experiments due to the dependence of detuning on temperature. As mentioned before, a multimode laser was used as the source laser whose peak emission wavelength was a function of the carrier concentration. So it was not possible to maintain the same detuning could not have been maintained.

Therefore, whenever resonance matching occurs between the external input and feedback signal and the cavity resonance, SSP was observed.

In this chapter, frustrated instabilities are demonstrated in the form of SSP. The appearance of SSP very much depends upon the initial conditions (as discussed above) of the system being investigated. This is a basic characteristic of chaotic systems and this characteristic has been used for an experimental technique for confidently identifying the chaotic behaviour of a system [18]. This once more gives the evidence that frustrated instabilities give rise to predictable behaviour i.e. chaos.

6.7. Summary

In this chapter, the chaotic dynamics of the active waveguide optical amplifier have been demonstrated. The reasons behind SSP and chaos in a laser system has been outlined using a set of rate equations. The necessary theoretical background in relation to frustrated instabilities has been established and modified rate equations were considered using a coupled-cavity scheme.

The existence of the non-linearity in the AWOA I-L characteristics due to the injection of external optical input has been observed, and the injection of the external input or the presence of another facet was found to reduce the threshold of the FP AWOA. Using non-linearities induced by the external injection of signals and multiple feedback between the source laser and the AWOA, the train of SSP, which eventually leads to chaos, was obtained in all devices. The SSP was found to be very sensitive to externally injected signals and the position of the source laser and the AWOA, as a slight tilt in the position of either device could be made to alter the multiple feedback effects on the AWOA characteristics. The appearance of SSP could be due to the two reasons;

1. noise (such as mode partition noise).
2. frustrated instabilities.

The successive generation of subharmonics (figure 6.17) at frequencies f_n/m

suggest that the observed effects are real oscillations and not due to noise. Furthermore, the periodicity of the pulsations do strengthen this argument and other evidence, such as the slow decay time of the pulse and the appearance of pulsations at the maximum value of feedback, further suggest that the train of SSP is due to the interaction between two stable solutions in the amplifying cavity which results in the frustration of the one or the other.

The two types of pulsation were obtained and found to be 180° out of phase to each other. The observation of the two types of pulsation and the difference in the forward and backward travelling fluxes, suggest the existence of four frequencies i.e. the intrinsic frequency of the active medium, ω_o, frequency components related to external injected signals from the source laser, ω_1 and two frequency components related to feedback signals (between r_2 and r_3 (ω_2) and between r_2 and r_4 (ω_3)) rather than three frequencies predicted in reference-17.

Both the subharmonic and period doubling routes to chaos in the active waveguide optical amplifier in couple cavity scheme have been demonstrated for the first time and the presence of optical turbulence has been predicted because of these coexistence of two routes to chaos. A comparison between the experimental results and the available theory has been carried out. The results obtained in this chapter are found to be in good agreement with theoretical predictions.

The results which are presented in this chapter are of a preliminary nature. They are needed to be analysed in more depth and more intensive theoretical work is needed to confirm these results. However, these results suggest the beginning of a breakthrough in establishing the real understanding of chaotic dynamics in the semiconductor laser systems in order to get rid of undesirable phenomenon of chaos in semiconductor laser systems.

References

1. Ikeda, K., and Mizuno, M., 'Frustrated instabilities in nonlinear optical resonators', Phys. Rev. Letters, vol.53, p.1340, 1984.
2. Otsuka, K., and Yumoto, J., 'Frustrated optical instabilities: Self-induced spatial instabilities', in Optical instabilities, ed: Boyd, R.W., Raymer, M.G., and Narducci, L.M., p.346, Cambridge University press.
3. Buus, J., 'Models of the static and dynamic behaviour of stripe geometry lasers', IEEE J. Quantum Electr., vol. QE-19, p.953, 1983.
4. Agrawal, G.P., and Dutta, N.K., 'Long-wavelength semiconductor lasers', Van Nostrand Reinhold, 1986.
5. Caspersons, L.W., 'Spontaneous coherent pulsation in laser oscillators', IEEE J. Quantum Electr., vol. QE-14, p.756, 1978.
6. Gioggia, R.S., and Abraham, N.B., 'Routes to chaotic output from a single-mode, dc-excited laser', Phys. Rev. Letters, vol.51, p.650, 1983.
7. Wiess, C.O., Godone, A., and Olafsson, A., 'Routes to chaotic emission in a cw He-NE laser', Phys. Rev. A, vol.28, p.892, 1983.
8. See special issue on instabilities in active media, J. Optical Soc. Am. vol.B2, 1985.
9. Chione, N., Aiki, K., and Ito, R., 'Stabilization of semiconductor laser outputs by a mirror close to laser facet', Appl. Phys. Letters, vol.33, p.990, 1978.
10. Liu, H.F., and Kamiya, T., 'Observation of chaos in an inhomogeneously pumped self-pulsating semiconductor laser', Jap. J. of Appl. Phys., vol.28, p.1600, 1989.
11. Otsuka, K., and Kawaguchi, H., 'Period-doubling bifurcation in detuned lasers with injected signals', Phys. Rev. A, vol.29, p.2953, 1984.
12. Winful, H.G., Chen, Y.C., and Liu, J.M., 'Frequency locking, quasiperiodicity, and chaos in modulated self-pulsing semiconductor lasers', Appl. Phys. Letters, vol.48, p.616, 1986.
13. Coldren, L.A., Furuya, K., Miller, B.I., and Rentschler, J.A., 'Etched mirror and groove-coupled GaInAsP/InP laser devices for integrated optics', IEEE J. Quantum Electr., vol. QE-18, p.1679, 1982.
14. Otsuka, K., and Kawaguchi, H., 'New route to optical turbulence in detuned lasers with a compound cavity', Phys. Rev. A, vol.30, p.1575, 1984.
15. Kawaguchi, H., and Otsuka, K., 'A new class of instabilities in a diode laser with an external cavity', Appl. Phys. Letters, vol.45, p.934, 1984.
16. Mukai, T., and Otsuka, K., 'New route to optical chaos: successive-subharmonic-oscillation cascade in a semiconductor laser coupled to an external cavity', Phys. Rev. Letters, vol.51, p.650, 1983.
17. Shore, K.A., 'Non-linear dynamics and semiconductor laser devices', Solid State Electronics, vol.30, p.59, 1987.

18. Derstine, M.W., Gibbs, F.A., Hopf, F.A., and Sanders, L.D., 'Distinguishing chaos from Noise in an optically bistable system', IEEE J. Quantum Electron., vol. QE-21, p.1419, 1985.
19. Binder, J.O., and Cormack, G.D., 'Mode selection and stability of a semiconductor laser with weak optical feedback', IEEE J. Quantum Electron., vol. QE-25, p.2255, 1989.
20. Bogatov, A.P., and Sverdlov, B.N., 'Anomalous interaction of spectral modes in a semiconductor laser', IEEE J. Quantum Electr., vol. QE-11, p.510, 1975.
21. Otsuka , K., and Iwamura, H., 'Theory of optical multistabilities and chaos in a resonant-type semiconductor laser amplifier', Phys. Rev. A, vol.28, p.3153, 1983.
22. Pennington, P.N., and Ormondroyd, R.F., 'Large-signal modulation response of monolithic active integrated-optic waveguides', IEE Proc. J, vol.137, p.11, 1990.
23. Adams, M.J., 'Physics and applications of optical bistability in semiconductor laser amplfiers', Solid State Electronics, vol.30, p.43, 1987.

Chapter-7

General discussion, conclusions and recommendation

7.1. Introduction

The main objective of the research presented in this thesis was to investigate the behaviour of monolithic integrated components to incoming butt-coupled input radiation. In this respect, two optical components, the active waveguide optical detector and the active waveguide optical amplifier have been investigated. In this chapter, the main conclusions of the work reported in this thesis are drawn in section 7.2. During the research, many assumptions were made and several paths have not been pursued due to the limitations of time and technological support. Consequently, this chapter includes suggestions for further work in section 7.3.

7.2. General discussion and Conclusions

From the outset of this research, the problem of excessive heat generation in the 'in-house' fabricated laser devices was encountered. This meant that none of the lasers could be used in CW mode. A detailed study of a number of heat generation sources in the laser diode revealed a significant difference between the heatsink temperature and the active layer temperature. It was shown in chapter 3 that the devices under investigation needed to be operated at a heatsink temperature of around -30°C for CW operation. Using the Peltier cooling pump and existing temperature controlling arrangement, it was very difficult to achieve this range of temperature under CW conditions. Therefore, the devices under investigation, had to be operated in pulse mode to avoid thermal runaway. In future, if the same material is used for the fabrication of the devices of a similar type to the ones investigated in this thesis, junction down (*p* side down) mounting can help in

reducing the active layer temperature and the device could be run in CW mode at higher temperature (higher than -30°C) which would simplify the measurements.

The heat capacity of laser devices was evaluated by measuring the characteristic temperature, T_o in chapter 3. This parameter was used later to investigate the extent of thermal effects in laser devices by measuring the thermal rise time of the devices under investigation. From the results of the thermal rise time, it is found that temperature effects are more prominent in Fabry-Perot devices and the temperature sensitivity is reduced in A.R. coated devices. As a consequence of reduction in this temperature sensitivity, a shift in peak emission wavelength (toward shorter wavelength) is observed in A.R. coated devices. This shift is attributed to (i) reduction in mirror facet heating effects and (ii) an increase in quasi-Fermi level separation due to high current densities. Mirror facet heating effects can be reduced by using segment-contact-scheme [1] in which the carrier density can be controlled by controlling the injection current through each segment. The segment-contact-scheme seems practical since the research in this thesis is concentrated on light propagation in locally pumped active waveguide.

In chapter 3, it was found that free carrier absorption was one of the main heat sources located in the active layer and its close vicinity. In chapter 2 and chapter 3, high absorption losses were measured, which are mainly due to the free carrier absorption. Hill's [2] absorption data has shown that α_{fc} in GaAs increases with temperature or in other words, a higher value of α_{fc} leads to a higher active layer temperature. Therefore, the higher value of α_{fc} is expected to be one of the main reason behind the higher value of α in UB262 rather than optical mode spreading. Free carrier absorption can be altered by controlling the carrier concentration via doping. A lower value of doping gives lower absorption loss and in GaAs it becomes virtually insignificant at carrier concentrations of $10^{17}/cm^3$ or less [3]. Decreasing the doping level in the active layer is of some benefit, but the situation in the case of lasing sources is more complicated, since it is the total concentration of carrier at the lasing threshold which must be considered and a higher

injected carrier density in this case is advantageous.

The saturation intensity, which defines the maximum achievable optical output power of an optical amplifier, also depends on the material gain coefficient. At higher doping levels and for high value of g_m, the saturation intensity is found to reduce, as shown in figure 7.1. The higher values of saturation intensity at low values of g_m is due to low values of the parameter A in equation (5.4). The higher values of saturation intensity at the higher values of g_m is due to the short spontaneous lifetime as a result of increase in the carrier density. At fixed doping levels, the saturation intensity has a minimum at a certain value of g_m. While designing the optical amplifier, this low saturation intensity limit must be avoided by selecting the optimum amplifier structural and material parameters.

Also a higher level of doping increases the responsivity of the AWOD because the absorption coefficient increases with doping density. However, for high frequency applications, the intrinsic layer (the active layer) in the AWOD must be depleted fully and it is only possible when the width of the intrinsic layer lies within the depletion region. The thickness of the depletion region decreases with the increase in doping level (equation (4.13)). The width of the depletion region can also be increased by reverse biasing the AWOD. But in future monolithic OIC, zero bias operation would be preferred over negative bias operation since zero bias operation of the AWOD expected to offer less circuit complexity. In chapter 4 it is seen that high frequency response in our case is limited by electrical circuit capacitance and extra capacitance added by connecting wires.

The radiation detection property of the AWOD was investigated in chapter 4 and this technique was used often to accurately align different active optical components during measurements. The usage of the radiation detection property of a AWOD to align two active components has provided the breakthrough in investigating the source of leakage in butt-coupled devices.

Optical flux leakage introduces an extra source of optical power loss and noise in active waveguide components which could also lead to the distortion of

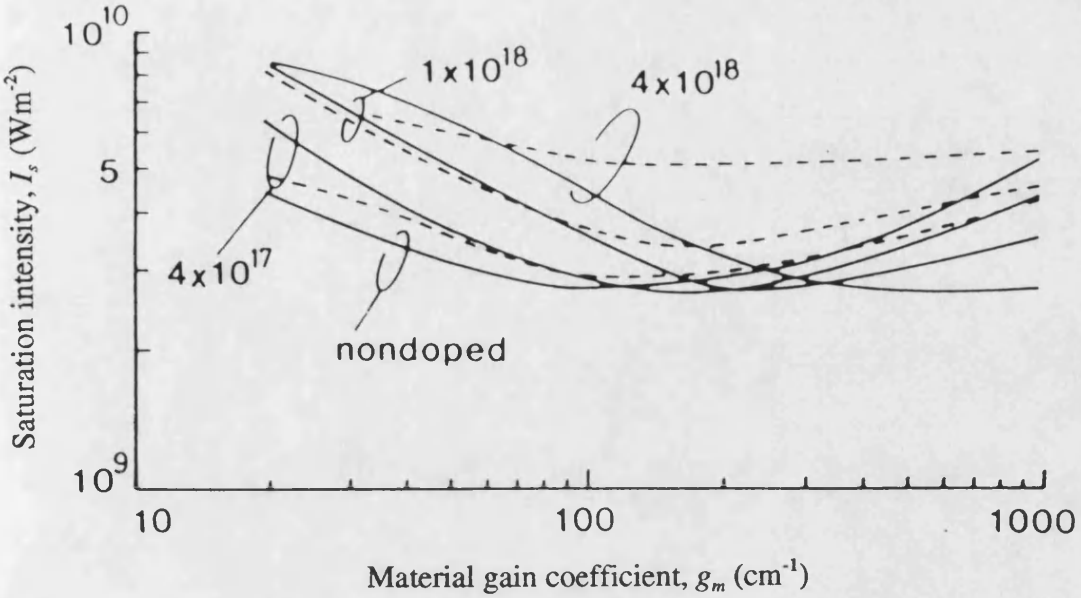

Figure 7.1. Saturation intensity vs the material gain coefficient as a function of doping level. Solid curves *p*-doped and dashed curves *n*-doped materials [4].

optical input signals. The detailed study of optical flux leakage in active waveguide components revealed that the particular monolithic integrated components tested suffered more than the hybrid integrated components as a result of the divergence of the optical beam in etched gap between the two butt-coupled components. This source of leakage of optical flux can only be controlled by controlling the beam divergence process in the etched gap, which was beyond the available fabrication technology. In monolithically integrated components, the amount of the leakage flux depends on etched gap dimensions. It can be reduced by reducing the width of etched gap.

It was also seen in chapter 4 that the coupling of optical radiation to the AWOD is increased as a result of feedback (back reflection) between the source laser and the AWOD butt-coupled facets. The A.R. coated devices were not only used for increasing the internal gain (chapter 5) but they were also used to investigate the effect of backreflection on AWOA characteristics. The effect of backreflection was observed in the AWOA in form of frustrated instabilities (which appears as a self-sustained train of pulsation) and this eventually leads to chaos in the optical amplifiers.

In chapter-6, the effect of detuning as a result of back reflection and the injection of optical input power was investigated, but the effect of detuning on the source laser characteristics was not examined. The source laser is also expected to be effected, since the AWOA and the source laser are butt-coupled and the AWOA is also electrically pumped. The effect of detuning on the source laser characteristics is one area that needs further investigation. However, in future OIC, DFB or DBR lasers are expected to be used rather than the simple FP lasers. Therefore, the effect of detuning on the source laser output will be minimised. But the fabrication of DFB or DBR laser with other active components is beyond the limits of existing technology at Bath.

In chapter-5, the use of the optical amplifier as an integral part of an OIC was considered. Unfortunately, monolithically integrated device, UB136 did not

give satisfactory results because of poor facets in the etched gap. Therefore, the butt-coupled hybrid integrated configuration was used as a substitute for the monolithic case. The use of the external source and AWOA in hybrid approach offers the extra flexibility of using different device combinations (i.e. by changing the facet reflectivity of the AWOA being investigated).

The main purpose of using A.R. coating is to suppress the lasing threshold by suppressing the internal feedback in a laser diode so it can be used as the travelling wave amplifier. This allows it to be used at higher values of pumping current without lasing. However, the increase in the pumping current shifts the peak emission wavelength towards shorter wavelength due to the shift in the gain curve. Shifts in the peak emission wavelength was also observed with the change in heat-sink temperature (chapter-3) and this property was used later in chapter 5 for wavelength tuning of the input radiation to the AWOA resonance wavelength. In chapter-4, it was found that the wavelength dependent response of the AWOD does not change much with the change of the AWOD temperature within the range of wavelengths used in this research. If the temperature of the AWOA is varied during wavelength tuning, the coupling of optical radiation from the source laser to the AWOA can be maintained at optimum value by monitoring the output of the AWOD (as the response of the AWOD does not change significantly with temperature change).

The signal gain of the AWOA in its hybrid configuration was measured by using the saturated output characteristics of the amplifier. The phenomena of gain saturation in the AWOA limits the optical signal gain. The nonlinear phenomena of gain saturation in the AWOA was investigated by measuring non-linear input/output characteristics of the AWOA by using different devices. Non-linearity was found to be strong in UB262 (FP AWOA) and UB258A (single side coated AWOA). The reason behind strong non-linearity between input and output in FP AWOA is probably due to higher temperature sensitivity of that device. However, non-linearity observed in UB258A is thought to be the result of multiple reflection

between the source and the AWOA as result of low input facet reflectivity. In all cases, at low input powers, a dip in the characteristics was observed which was probably due to noise associated with the photoconductive mode of measurement (since the output of the GaAs AWOD was measured in photoconductive mode to have a higher speed of response). As the optical input power increases, the behaviour of the AWOA becomes linear because the source laser frequency tuned with the AWOA resonance frequency. At high input powers, the saturation of the AWOA leads to non-linear operation with compressed output. Hence leading to distortion of optical input signals.

One of the main problems with the locally pumped active waveguides is the ASE (locally generated and associated with input signals). This source of noise limits the gain of the AWOA and it is undesirable in the AWOA. A simple measurement showed that the single side coated device with R_1=0.3 and R_2=0.0448 was worst effected by ASE noise and the device with R_1=0.0448 and R_2=0.3 was less effected. This is due to the significant difference in input and output facet reflectivities, which effects the noise enhancement factor χ (which strongly depends upon input facet reflectivity). Among symmetrical devices, the FP device UB262 has shown higher value of χ due to higher value of input facet reflectivity when compared with the NTW device UB259.

It was seen in chapter 5, that the signal gain of all devices changes with the state of polarization of the input radiation. Although, the polarization sensitivity of the AWOA is reduced in A.R. coated devices, it is not eliminated, and this is mainly due to differences in the confinement factor between TE and TM modes. The difference between the confinement factor can be eliminated by several techniques [5-9] (as mentioned in chapter-5), mainly based on an increase in the device active layer thickness. It would appear from the results that the polarization sensitivity of locally pumped active waveguide will be the one of the main problems for the adoption of monolithic OICs in the future.

To summarise, despite the several problems faced during the research, the

results presented in this thesis demonstrate the feasibility of using the active waveguide in future optical integrated circuits as an attractive solution to routing optical signal, even though it has certain limitation (such as generation of ASE, achievement of vertical etched gap geometry and the effect of backreflection on output characteristics). Although the work presented in this thesis is preliminary, it suggests the beginning of an significant breakthrough in establishing a clear understanding of the propagation characteristics of active waveguides.

7.3. Recommendation for future work

The technology of OICs is still immature (even after two decades of extensive research) and the monolithic integration of several components on a single substrate is still a technological challenge. This technological challenge has been accepted in this thesis.

During the research presented in this thesis, a multilongitudinal mode source is used. For this reason, the internal gain of the AWOA had been measured using saturated output power characteristics approach. Although the results presented here do satisfy the reported results, this new gain measurement technique needs to be further validated in detail. This can be accomplished by using a single wavelength source instead of multiwavelength source and by measuring the internal gain of a particular device from experimentally measured peak-trough ratio and output saturated characteristics and then comparing achieved results.

In chapter-5, the underlying non-linearity as a result of the gain saturation phenomena is shown in the input/output characteristics. However, the saturation-induced nonlinear response of the AWOA was affected by the residual facet reflectivity of the AWOA. The effect of multilongitudinal wavelength input dictate that in order to have a real understanding of nonlinear phenomena in the AWOA, a single wavelength source and extremely low facet reflectivity AWOA are required. The use of a single wavelength source and the use of the AWOA with extremely low facet reflectivity will serve the dual purposes (i.e. it can be used to perform

bistable operation and it can reduce the difference between the TE and TM confinement factor).

In chapter-6, frustrated instabilities were demonstrated experimentally in the hybrid integrated AWOA. It would be interesting to carry out a detail theoretical investigation on frustrated instabilities in monolithic devices, to establish the range of optical input powers over which these effects occur.

Also in chapter 6, the frequency response of the active waveguide was measured to be much slower than the predicted value in reference-10. The reason behind this slower response is the slow response of the optical detector used during measurements. Since extremely high response of the AWOD is predicted (as high as 150GHz [11]), it will be worthwhile to use a properly designed AWOD as the optical detector at output of the AWOA. In this way, a cheap and fast optical detector can be fabricated according to individual needs.

References

1. Herrmann, F.U., Beeck, S., and Abstreiter, G., 'Reduction of mirror temperature in GaAs/AlGaAs quantum well laser diode with segmented contacts', Appl. Phys. Lett., vol.58, p.1007, 1991.
2. Hill, D.E., 'Infrared transmission and fluorescence of doped gallium arsenide', Phys. Rev. vol.133, p.A866, 1964.
3. Pinkas, E., Miller, B.I., Hayashi, I., and Foy, P.W., 'GaAs-$Al_xGa_{1-x}As$ double heterostructure lasers-effect of doping on lasing characteristics of GaAs, J. Appl. Phys., vol.43, p.2827, 1972.
4. Mukai, t., Yamamote, Y., and Kimura, T., 'Optical amplification by semiconductor lasers', in Semiconductor and semimatal vo.E, Ed. Tsang, W.T., p.262, Academic Press, 1985.
5. Vassallo, C., 'Polarization-independent antireflection coatings for semiconductor amplifiers', Electron. Lett., vol.24, p.61, 1988.
6. Olsson, N.A. Kazarinov, R.F., Nordland, W.A., Henry, C.H., Oberg, H.G., White, H.G., Garbinski, P.A. and Savage, A., 'Polarization-independent optical amplifier with buried facet', Electron. Lett., vol.25, p.1048, 1989.
7. Cha, I., Kitamura, M., Honmou, M., and Mito, I., '1.5 *mum* band travelling-wave semiconductor optical amplifiers with window facet structure', Electron. Lett., vol.25, p.1241, 1989.
8. Groβkopf, G., Ludwig, R., Waarts, R.G., and Weber, H.G., 'Optical amplifier configurations with low polarization sensitivity', Electron. Lett., vol.23, p.1387, 1987.
9. Magari, K., Okamoto, M., Yasaka, H., Sato, K., Noguchi, Y., and Mikami, O., 'Polarization insensitive travelling wave type amplifier using strained multiple quantum well structure', IEEE Photonic Tech. Lett., vol.2, p.556, 1990.
10. Pennington, P.N., and Ormondroyd, R.F., 'Large-signal modulation response of monolithic active integrated-optic waveguides', IEE Proc. J, vol.137, p.11, 1990.
11. Alping, A., 'Waveguide *pin* photodetectors: theoretical analyses and design criteria', IEE Proc. J, vol.136, p.177, 1989.